

**Macromolecular Modelling Of Muscle Structure:
A Comparison With
X-Ray Diffraction Results**

by

Catherine V. Miles

Thesis submitted to the University of Leicester

in fulfilment of the requirements

of the degree of Doctor of Philosophy

August 1997

UMI Number: U483798

All rights reserved

INFORMATION TO ALL USERS

The quality of this reproduction is dependent upon the quality of the copy submitted.

In the unlikely event that the author did not send a complete manuscript and there are missing pages, these will be noted. Also, if material had to be removed, a note will indicate the deletion.



UMI U483798

Published by ProQuest LLC 2013. Copyright in the Dissertation held by the Author.
Microform Edition © ProQuest LLC.

All rights reserved. This work is protected against
unauthorized copying under Title 17, United States Code.



ProQuest LLC
789 East Eisenhower Parkway
P.O. Box 1346
Ann Arbor, MI 48106-1346

Macromolecular Modelling Of Muscle Structure: A Comparison With X-Ray Diffraction Results

Catherine V. Miles

During contraction, the molecular arrangement within muscle undergoes large changes which can be traced through corresponding changes in the x-ray diffraction patterns. This thesis investigates the relationship between changes in the muscle structure and those in the resulting diffraction patterns, in order to shed light on the contractile cycle itself.

High resolution x-ray diffraction patterns were obtained from whole frog sartorius muscles using synchrotron radiation. The patterns were obtained at three stages of the contractile cycle: rest, isometric contraction and unloaded shortening.

Three-dimensional computer models were built from the main components of muscle: the proteins actin and myosin arranged in helical filaments. The specific positions and orientations of the protein components were adjusted until the main features of the resulting theoretical diffraction pattern matched those of the experimental x-ray diffraction patterns.

The results of this study indicated that in rest muscle the main mass of the myosin head lies parallel to the muscle's long axis, and the heads are wrapped around the thick filaments from which they protrude forming a compact structure. Introducing disorder into the molecular arrangement revealed that a high degree of azimuthal disorder in the myosin head arrangement was required to reproduce the pattern from isometrically contracting muscle. During unloaded shortening axial filament disorder was the prime candidate.

The main focus of this study was the arrangement of myosin molecules in the thick filaments, but initial studies of the arrangement of actin monomers in the thin filaments indicated that a random cumulative disorder of 10° r.m.s. is present in the helical arrangement of the actin monomers.

Acknowledgements

First and foremost, my thanks are due to my supervisor, Agneta Svensson, for her advice, support and encouragement throughout the course of this work. I would also like to acknowledge the BBSRC and the SERC for providing me with this studentship.

A sincere thank you goes to Joan Bordas and the Non Crystalline Diffraction group at CCLRC Daresbury Laboratory for many useful discussions and for all their help during beamtime. In particular to Greg Diakun for all his support during my time at Daresbury; it was, and is, much appreciated. Also to my partner in crime Jonathan Gandy for keeping me sane and entertained.

Thanks to the station staff at Daresbury Laboratory for all their help during the experimental work, especially to Elizabeth Towns-Andrews and Susan Slawson for taking the time to show me the ropes.

I am particularly grateful to Guillermo Diaz-Banos and Manolis Pantos for their help and advice on the computer modelling aspects of this project, as well as useful chunks of code.

Thanks also to Geoff Mant and Richard Denny who also gave up their free time to help me get my data. And to Marisa Martin Fernandez and John Harries for making me so welcome and introducing me to the wonderful world of x-ray diffraction.

In Leicester, I would like to thank the Physics Department and members of the Condensed Matter Physics group at Leicester University for their continued support and friendship. I could not have wished for a better group of people to share the last three years with. Especially to Richard Bayliss, carry on the good work.

Finally, the biggest thank you goes to my family for their constant support and encouragement throughout this time, without which I would certainly not have reached this point. Thanks also to my friends for putting up with me and waiting so patiently; yes, I can come out and play now.

Catherine Miles

August 1997

“The beginning of knowledge is the discovery of something we do not understand.”

Frank Herbert

“A conclusion is the place where you got tired thinking.”

Martin H. Fischer

CONTENTS

| | Page |
|--|------|
| Chapter 1: Introduction To Muscle Diffraction | 1 |
| Chapter 2: Muscle Structure And Contraction | 3 |
| 2.1: Introduction | 4 |
| 2.2: Muscle Physiology and Energy Supply | 4 |
| 2.3: Vertebrate Skeletal Muscle | 6 |
| 2.4: Thin Filament Structure | 11 |
| 2.5: Thick Filament Structure | 12 |
| 2.6: Filament Interaction | 14 |
| 2.7: Contraction Theories | 18 |
| 2.7.1: Crossbridge Cycle Models | 18 |
| 2.7.2: Weak and Strong Binding States | 19 |
| 2.7.3: Tilting Crossbridge Controversy | 22 |
| 2.7.4: Step Size | 23 |
| 2.7.5: Non-Crossbridge Cycle Models | 24 |
| 2.8: Summary | 26 |
| Chapter 3: Helical Diffraction Theory | 27 |
| 3.1: Introduction | 28 |
| 3.2: Basic Diffraction Theory | 28 |
| 3.3: Crystalline Diffraction | 31 |
| 3.4: Helical Diffraction | 33 |
| 3.4.1: Diffraction from an Infinite Continuous Helix | 33 |
| 3.4.2: Diffraction from a Helix of Discrete Atoms | 37 |
| 3.5: Application to Muscle | 41 |
| 3.5.1: Multi-stranded Helices | 42 |
| 3.5.2: Two Dimensional Hexagonal Lattice | 43 |
| 3.6: Disorder Effects | 44 |
| 3.6.1: Helical Disorders | 45 |
| 3.6.2: Lattice Disorders | 46 |
| 3.7: Summary | 48 |
| Chapter 4: X-Ray Diffraction Experimental Techniques | 49 |
| 4.1: Introduction | 50 |
| 4.2: Synchrotron Radiation and the SRS | 50 |

| | |
|---|-----|
| 4.3: Wiggler Magnets | 53 |
| 4.4: Optical System | 54 |
| 4.5: Experimental Station 16.1 | 59 |
| 4.6: Detectors | 60 |
| 4.6.1: Gas Filled Multi-Wire Proportional Counters | 60 |
| 4.6.2: Imaging Plate System | 62 |
| 4.6.3: Spatial Calibration of the Image Plate System | 63 |
| 4.6.4: Determination of the Dynamic Range of the Image Plate System | 65 |
| 4.7: Experimental Procedure | 69 |
| 4.7.1: Sample Preparation | 69 |
| 4.7.2: Diffraction Protocols | 72 |
| 4.8: Data Reduction | 73 |
| | |
| Chapter 5: Diffraction Results | 77 |
| 5.1: Introduction | 78 |
| 5.2: Rest Data | 78 |
| 5.2.1: Myosin Reflections | 81 |
| 5.2.2: Actin Reflections | 91 |
| 5.2.3: Other Reflections | 94 |
| 5.3: Isometric Contraction Data | 94 |
| 5.4: Unloaded Shortening at Zero Tension Data | 101 |
| 5.5 Summary | 102 |
| | |
| Chapter 6: Computer Modelling Procedures | 103 |
| 6.1: Introduction | 104 |
| 6.2: Scope of the Model | 104 |
| 6.3: Previous Modelling Studies | 105 |
| 6.4: General Modelling of Muscle Structure | 109 |
| 6.4.1: Building a Three Dimensional Model | 111 |
| 6.4.2: Mass Projection into a 2D Plane | 116 |
| 6.4.3: Fourier Transform of the Model | 118 |
| 6.4: Modifications to the Basic Model | 120 |
| | |
| Chapter 7: Modelling of Rest Muscle | 123 |
| 7.1: Introduction | 124 |
| 7.2: Reproducing the Actin Filament Pattern | 124 |
| 7.3: Myosin Filament Pattern - Low Resolution Myosin Head | 127 |
| 7.3.1: Meridional Reflections | 127 |

| | |
|--|-----|
| 7.3.2: Layer Line Profiles | 133 |
| 7.3.3: Relative Intensity of the Layer Lines | 135 |
| 7.4: Myosin Filament Pattern - High Resolution Myosin Head | 142 |
| 7.4.1: Meridional Reflections | 144 |
| 7.4.2: Layer Lines | 144 |
| 7.5: Discussion of Results | 151 |
| | |
| Chapter 8: Modelling of Contracting Muscle | 157 |
| 8.1: Introduction | 158 |
| 8.2: Studies of Disorder | 158 |
| 8.2.1: Disorder Within the Helix | 158 |
| 8.2.2: Disorder Between Helices | 171 |
| 8.3: Isometrically Contracting Muscle | 174 |
| 8.3.1: Meridional Intensity Distribution | 174 |
| 8.3.2: Spatial Considerations | 177 |
| 8.4: Unloaded Shortening at Zero Tension | 180 |
| 8.5: Summary | 181 |
| | |
| Chapter 9: Conclusions and Further Work | 183 |
| | |
| Publications | 186 |
| References | 187 |

Chapter 1: Introduction To Muscle Diffraction

The conversion of chemical energy into mechanical work is one of the most important issues in biology today. Since this is the primary function of muscle during contraction, it is an ideal system through which to investigate the energy conversion process. Considerable effort has been spent studying muscle contraction using various methods including electron microscopy, x-ray diffraction studies, and biochemical and kinetic analyses, but the exact sequence of molecular events which result in the generation of macroscopic force is still unknown.

Changes in the molecular structure of muscle give important clues as to how the contraction mechanism works. If the molecular structure can be determined at key stages of the contractile cycle, the physical changes from one state to the next can be correlated with the level of force production. Scattering of x-rays of wavelength $\lambda \sim 0.1\text{nm}$ from muscle samples gives rise to characteristic diffraction patterns, since the protein molecules found in muscle are of a similar size to the wavelength; the basic elements of muscle are the contractile proteins actin and myosin, whose molecular lengths are $\sim 5.5\text{nm}$ and 160nm respectively. The positions and intensities of the reflections in the pattern represent the average structural arrangement of the protein molecules at the time of scattering; thus changes in the diffraction pattern throughout a complete contraction reflect changes in the average molecular structure.

Muscle fibres are not truly crystallographic structures, but they do contain regular helical repeats which give rise to distinctive x-ray diffraction patterns. Like most biological samples, muscle is a poor scatterer which needs a very intense source of x-rays to produce good quality diffraction images. The experiments described in this work used synchrotron radiation to obtain diffraction patterns from highly ordered frog sartorius muscle samples.

In principle, since the diffraction pattern is determined by the Fourier Transform of the diffracting structure, it should be possible to reverse the process and obtain the original structure from an inverse Fourier Transform of the diffraction pattern (Chapter 3). However, the recorded patterns contain no phase information, so the underlying muscle structure cannot be determined in this way. Instead, theoretical transforms from

macromolecular models must be compared with experimental data. Simplified representations of the protein molecules are built into three dimensional structures which approximate the gross structure of muscle as we know it. The models are mass projected, and the mass projections Fourier transformed and squared to give a two dimensional intensity distribution comparable to the X-ray diffraction patterns. A “trial and error” method is then employed, modifying the models to improve the match between calculated and experimental results.

An introduction to the theory of muscle contraction is presented in Chapter 2, including the structure of the protein molecules, their arrangement within the muscle fibres, and a discussion of the more popular proposed mechanisms of interaction and force generation. The theory of x-ray diffraction is described in Chapter 3. Chapter 4 describes the experimental procedure for obtaining low angle diffraction patterns from whole muscle samples, with the resulting data presented in Chapter 5. In Chapter 6, three dimensional computer modelling procedures are discussed, with emphasis on the methods used in this work. The results from modelling the structure of muscle at rest are presented in Chapter 7, followed by investigations into the structure of the isometric plateau and unloaded shortening states in Chapter 8. Chapter 9 summarises the results of this modelling, with conclusions and suggestions for further work.

Chapter 2: Muscle Structure And Contraction

2.1: Introduction

2.2: Muscle Physiology and Energy Supply

2.3: Vertebrate Skeletal Muscle

2.4: Thin filament Structure

2.5: Thick Filament Structure

2.6: Filament Interaction

2.7: Contraction Theories

2.7.1: Crossbridge Cycle Models

2.7.2: Weak and Strong Binding States

2.7.3: Tilting Crossbridge Controversy

2.7.4: Step Size

2.7.5: Non-Crossbridge Cycle Models

2.8: Summary

2.1 Introduction

Through evolution, the structure and properties of different muscle types have diversified to perform a wide range of functions, adapting to such criteria as speed or strength. The elements of the underlying contraction process which are common to all muscles are revealed by the similarities between different types, whilst the differences mean that suitable samples may be found for varied investigation techniques. Although the molecular structure may differ between muscle types, the insights into the contractile cycle which are gained from such varied methods as structural studies and biochemical or kinetic analyses can be applied to muscle in general.

All vertebrate muscles can be classed as either smooth or striated muscle. Smooth muscle is found in the internal organs of the body, and contracts involuntarily: it gets its name from its smooth appearance under an optical microscope. In contrast, striated muscle is crossed by alternating dark and light bands when viewed through an optical microscope. Striated muscle can be further divided into cardiac muscle and skeletal muscle: cardiac muscle is found in the heart, and is capable of sustaining regular, involuntary contractions; skeletal muscle is attached to the skeleton and causes motion of the body under voluntary stimulation.

Vertebrate skeletal muscle is the most ordered of these muscle groups, making it ideal for x-ray diffraction studies which require good structural order. Whole muscles consist of fibres arranged roughly parallel to the long axis of the muscle, so that when the muscle contracts, the force acts along its length. This lengthways contraction simplifies experimental tension and length measurements on a macroscopic scale.

2.2 Muscle Physiology and Energy Supply

Skeletal muscle contraction is triggered *in vivo* by the nervous system, via the nerve attached to each muscle. The sarcolemma membrane surrounds the muscle fibres and periodically forms T-tubules leading to the interior of the fibre. The stimulus is a momentary

depolarisation of the nerve membrane, which propagates as a voltage change through the T-tubules to the sarcoplasmic reticulum. When the voltage change reaches the sarcoplasmic reticulum calcium ions (Ca^{2+}) are released, and the increased Ca^{2+} concentration induces contraction. When the stimulus is removed, the Ca^{2+} ions are recovered to the sarcoplasmic reticulum and the muscle relaxes.

In an *isotonic* contraction, the muscle produces macroscopic work by shortening against a load. However, if the load is equal to the maximum force the muscle can produce and its length is effectively fixed, the muscle will produce internal tension instead of doing work, and the contraction is said to be *isometric*. The energy supply to do work or produce tension comes from the hydrolysis of ATP (adenosine 5'-triphosphate) to ADP (adenosine diphosphate) and inorganic phosphate:



ATP is initially replaced by a creatine kinase buffer system, and in the long term by glycolysis or oxidative phosphorylation.

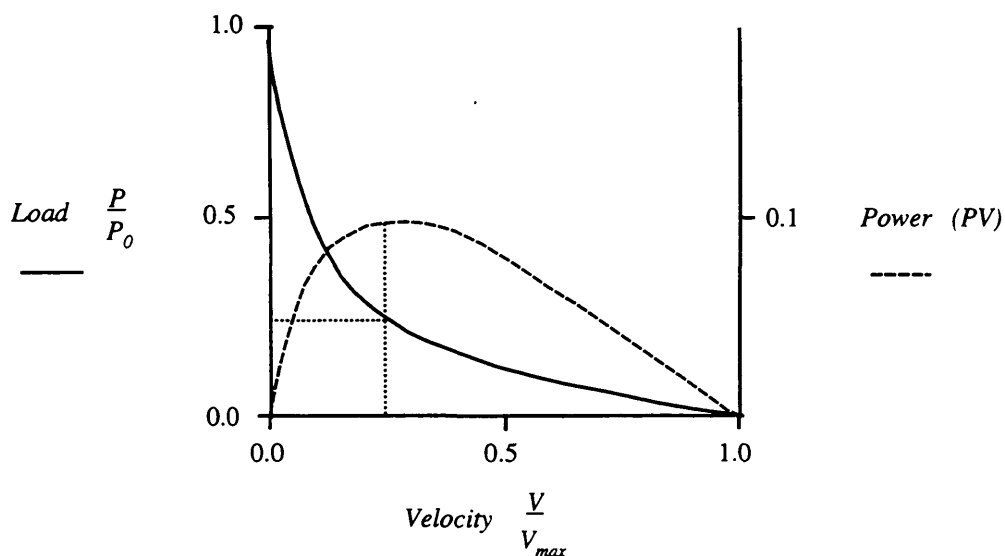


Figure 2.1: Relation Between Load, Velocity of Shortening and Power Output [8]

The power output is at a maximum when both shortening velocity and load are one third of their maximum values, and falls to zero when either quantity is zero.

The chemical energy released by the ATPase reaction is converted into the mechanical force responsible for muscle contraction, plus generated heat energy. The amount of work done depends on the shortening velocity of the muscle, which in turn depends on the load against which the muscle works. Figure 2.1 shows the relationship between shortening velocity and load [54, 55] (after Bagshaw [8]); the velocity is at a maximum for unloaded shortening, and is zero for isometric contraction. The power output (PV - also shown) peaks when the shortening velocity and load are about one third of their maximum values [54, 55], and falls to zero during both the unloaded shortening ($P=0$) and isometric contraction ($V=0$) phases.

2.3 Vertebrate Skeletal Muscle

A whole vertebrate skeletal muscle consists of bundles of fibres sheathed by connective tissue (fig. 2.2). This tissue forms tendons at either end of the muscle which attach the muscle to the skeleton. Each muscle fibre contains about a thousand striated myofibrils, which are strictly aligned to give the fibre an overall banded appearance. The origin of the striations is an alternating series of high and low protein density bands repeating lengthways along the myofibril. The basic repeating unit, the sarcomere, is typically 2-3 μm long depending on the state of the muscle (fig. 2.2), and contains both contractile proteins which are actively involved in the force generating process, and structural proteins which hold the sarcomere structure in place.

The sarcomere consists of two sets of interdigitated filaments, called the thick and thin filaments. The region where the two sets of filaments overlap forms a band of high protein density. This band appears dark under an optical microscope and is labelled the A-band because it has a relatively anisotropic refractive index (fig. 2.3a). The thin filaments alone form a light, low density region which is the relatively isotropic I-band. The thick filaments alone form the slightly darker H-band.

A cross-section through the myofibril at overlap (fig. 2.3b) shows that the thick filaments form a hexagonal array, with the thin filaments occupying the trigonal points of

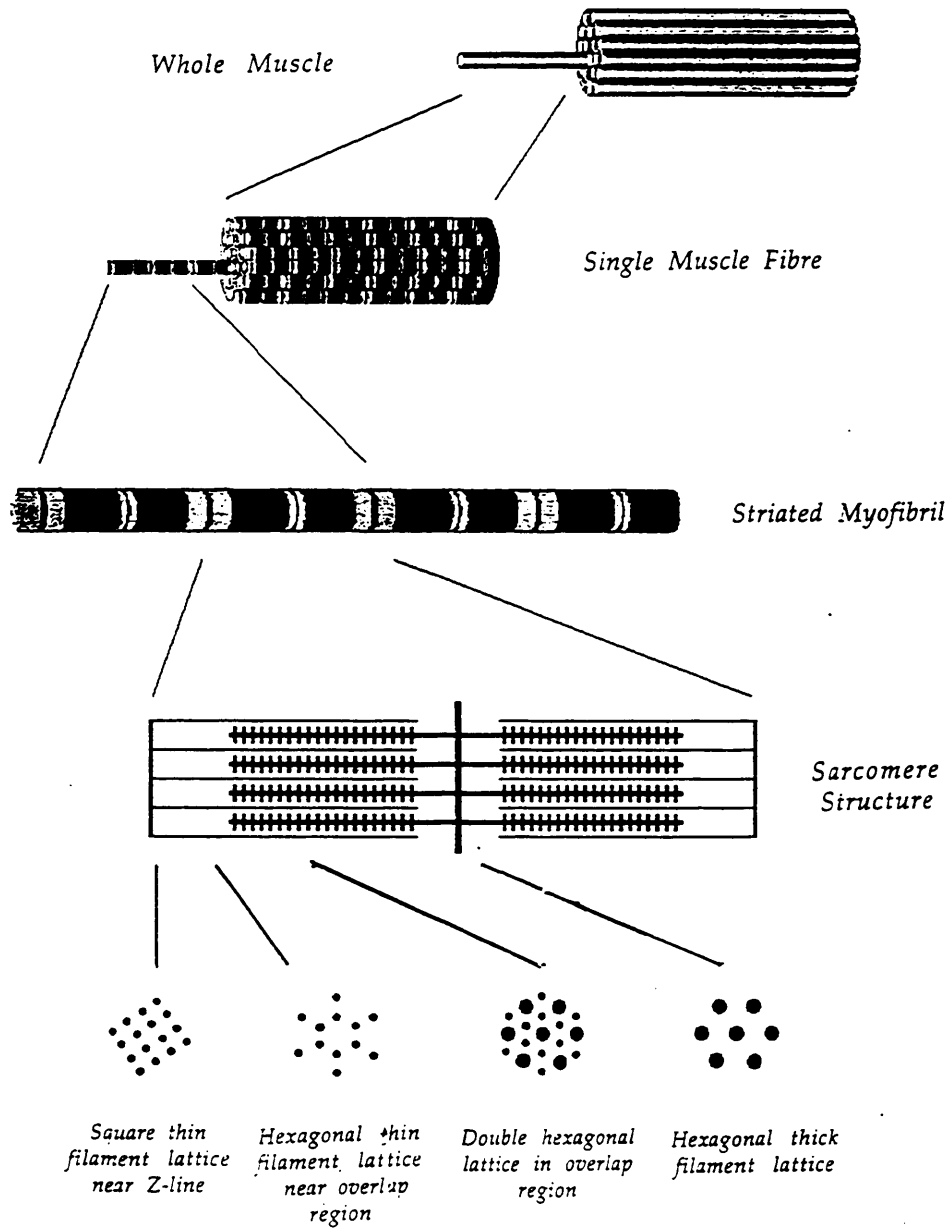


Figure 2.2: Skeletal Muscle Structure (courtesy R.I.Bayliss)

Figure 2.3: *Electron Micrographs of Frog Sartorius Muscle (courtesy R.I.Bayliss)*

- (a) *Longitudinal slice through a muscle fibre showing the sarcomere structure with its alternating light and dark striations.*

Magnification: x 14,100 times

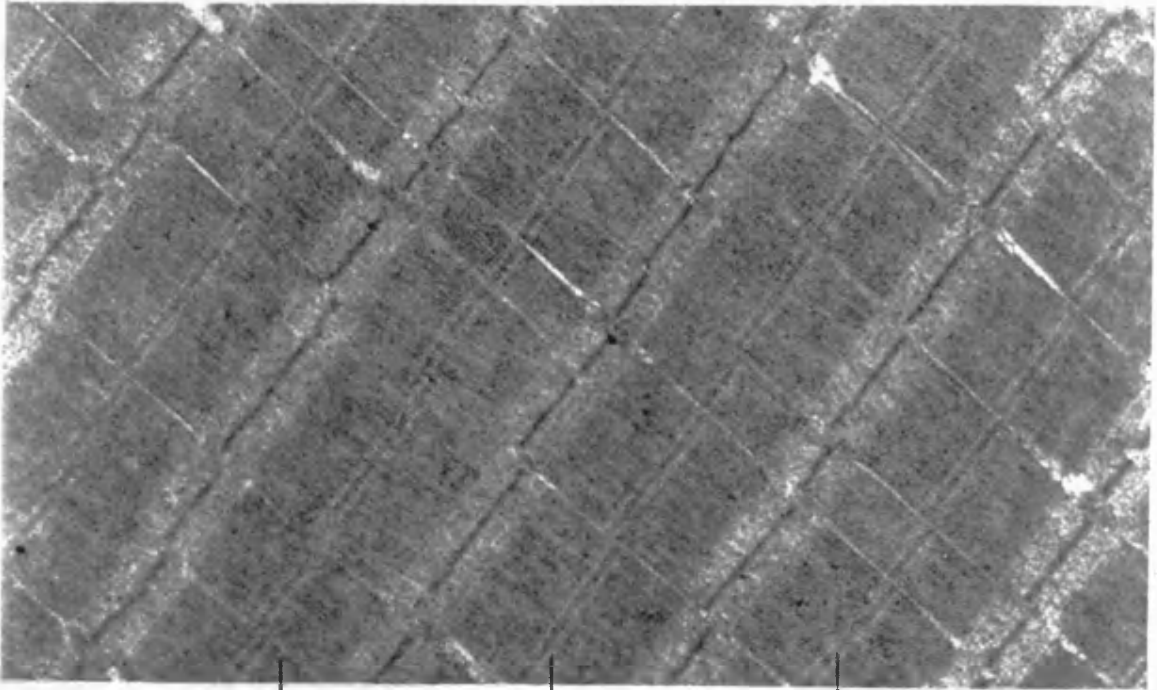
- (b) *Cross sectional slice through a muscle fibre showing various regions of the sarcomere:*

O: Full overlap region

M: M-line

H: H-band

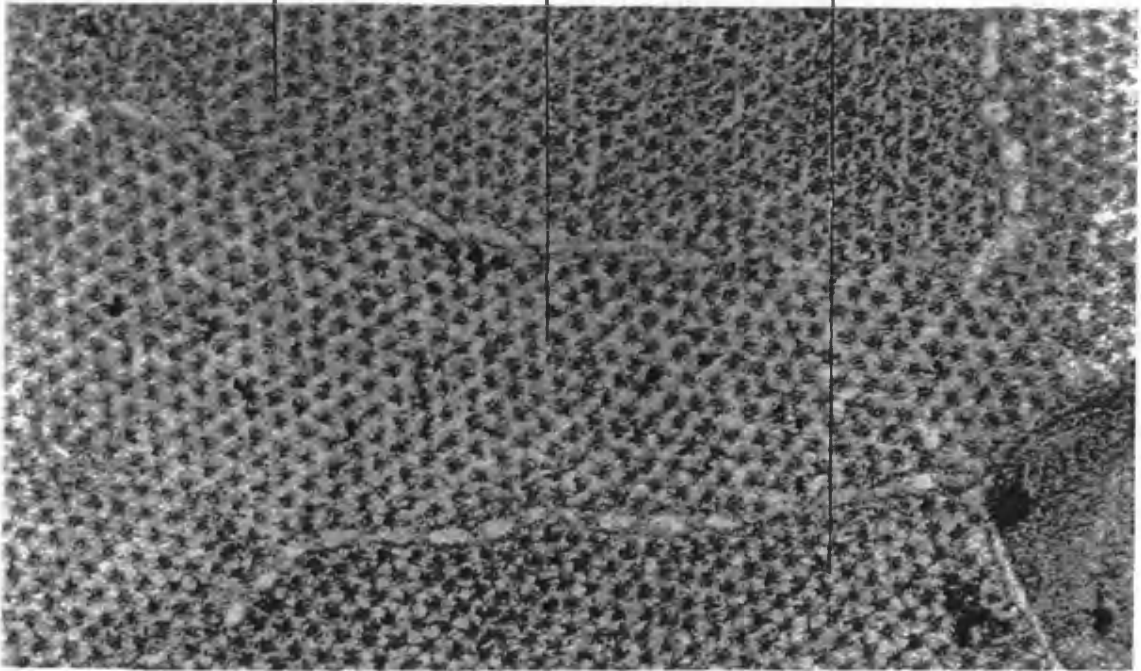
Magnification: x 85,000 times



0

I

2

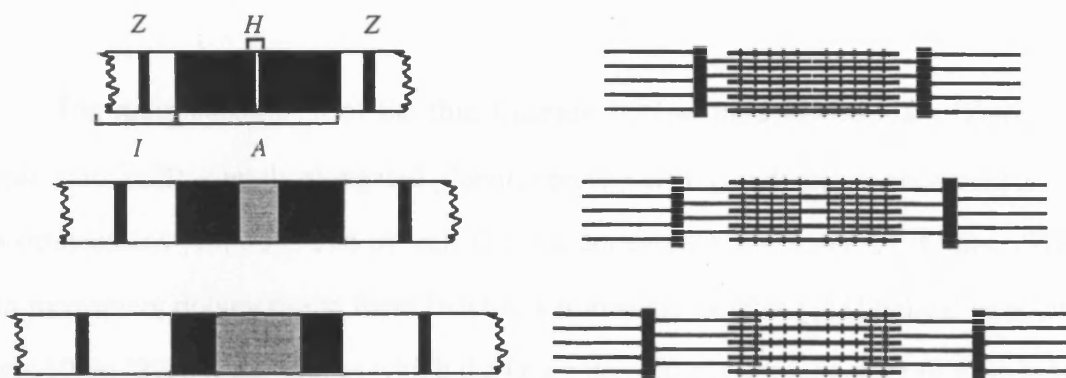


the lattice. The individual sets of filaments are held in register across the myofibril by structural protein arrangements. The M-lines connect the centres of the thick filaments [82], whilst the Z-lines join the centres of the thin filaments. The filament separation is balanced between the elastic attraction forces of these structural formations, and the electrostatic repulsion between the filaments. From the overlapping ends of the thin filaments towards the central Z-line, the thin filament lattice gradually changes to become more square than hexagonal.

Microscopy studies have shown that the macroscopic shortening of a muscle during contraction is the result of each of the sarcomeres shortening in length. Observations show that the A-band remains at a constant length and the I-band shortens [63, 72], which suggests that the length of the individual filaments remains constant during contraction whilst the degree of filament overlap increases (fig. 2.4a). This is the *Sliding Filament Theory* put forward by A.F.Huxley in 1954 [63].

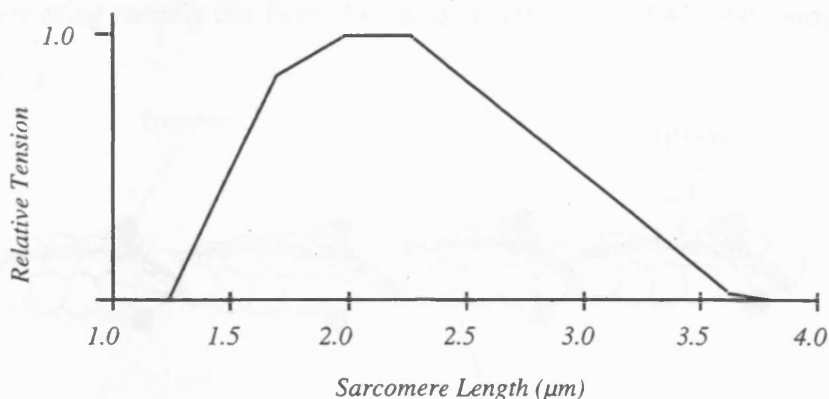
Crossbridges regularly protrude from the surface of the thick filament [67], except for a bare region around the centre of the filaments, and move out to interact with the thin filaments during contraction. This interaction, together with the sliding filament theory, explains why the maximum tension reached by a given muscle during isometric contraction varies strongly with the sarcomere length before stimulation (fig. 2.4b). At sarcomere lengths over $3.5\mu\text{m}$ the thick and thin filaments do not overlap at all and no crossbridge interaction can occur. As the sarcomere length decreases, the filament overlap and therefore the number of crossbridges interacting with the thin filaments increases, corresponding to an increase in force production. This trend continues until the sarcomere length is such that the thin filaments overlap the bare region of the thick filaments. The number of interactions does not change since there is no new crossbridge overlap, and the force produced during contraction also remains constant. At still shorter sarcomere lengths, the thin filaments start to interfere with the interactions in the other half of the sarcomere, and the force decreases rapidly.

The interaction between the crossbridges of the thick filaments and the thin filaments results in filament sliding, and is therefore the key to the force generation process.



(a) Sarcomere Shortening Under an Optical Microscope

Sarcomere Shortening in Terms of the Sliding Filament Theory



(b) Variation of Isometric Tension with Sarcomere Length (after Squire [133])

Figure 2.4: The Sliding Filament Theory

(a) The changing length of the striations under an optical microscope can be explained in terms of the degree of filament overlap present as a muscle contracts.

(b) Similarly, the peak isometric tension produced by a muscle can be explained by the degree of overlap between filaments. The amount of overlap depends on the sarcomere length at which the isometric contraction takes place.

2.4 Thin Filament Structure

The main constituent of the thin filament is G-actin, a 42kDa (1Da (Dalton) \equiv 1 atomic mass unit), slightly elongated globular protein with two domains, each consisting of two subdomains [79, 32]. The overall G-actin dimensions are 5.5nm by 3.5nm. The G-actin monomers polymerise to form F-actin, a somewhat flexible [111] helical structure of radius 10nm [29, 31, 32, 156] in which the larger domain of each monomer lies towards the centre of the helix [105, 59]. The genetic structure of F-actin is a left-handed helix, with a pitch of 5.9nm and an axial translation of 2.73nm (fig. 2.5). Alternatively, it can be visualised as a long two-stranded helix where each strand has a pitch of 73.0nm, an axial translation of 5.46nm, and is staggered with respect to the other strand by 2.73nm [46, 70, 104, 44]. The actin monomers are all oriented the same way within a filament, with the long axis roughly pointing radially out from the filament axis [156, 104], bestowing polarity on the thin filaments.

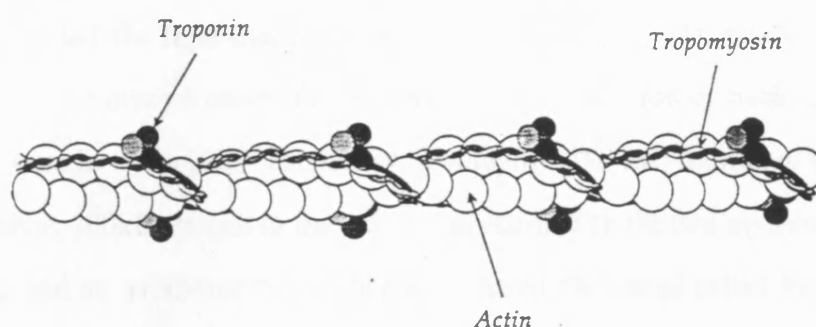


Figure 2.5: Thin Filament Structure [8]

The regulatory proteins tropomyosin and troponin also contribute significantly to the thin filament structure. The tropomyosin molecule is a 66kDa two-stranded helix, 40nm long [145, 162]. The tropomyosin winds around the groove of the long actin helix with a pitch of 38.5nm, with each molecule covering seven actin monomers [113, 114]. Adjacent molecules overlap to form a junction [115], which is strengthened by a molecule of troponin [127].

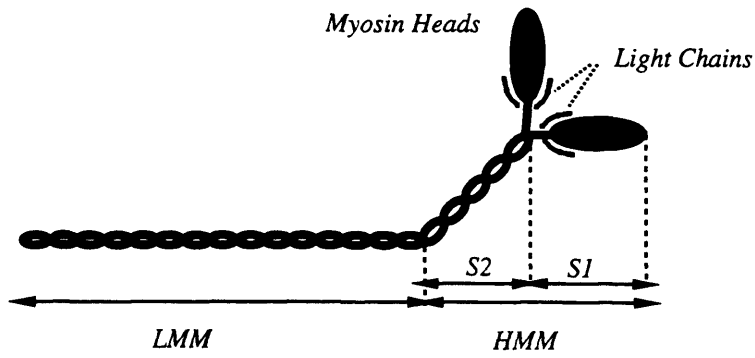
Troponin is an 80kDa globular protein [28] which is strongly affected by the Ca^{2+} ion concentration, and together with tropomyosin regulates the interaction between thick and

thin filaments. The troponin molecule (TN) is composed of three parts, TN-I, TN-C, and TN-T. TN-I binds to the actin helix, inhibiting actin-myosin interaction [160, 53, 121]; TN-C binds to Ca^{2+} in proportion to the Ca^{2+} concentration, reversing the inhibitory effect of TN-I at high Ca^{2+} concentrations [20]; and TN-T binds to tropomyosin [111], bridging the junction between adjacent tropomyosin molecules, and holding them at the edge of the actin groove at low Ca^{2+} concentrations [36, 112]. Thus the precise position of tropomyosin with respect to the actin helix is determined by its interaction with troponin, which depends on the physiological conditions [114]. The regulation process is discussed further in §2.6.

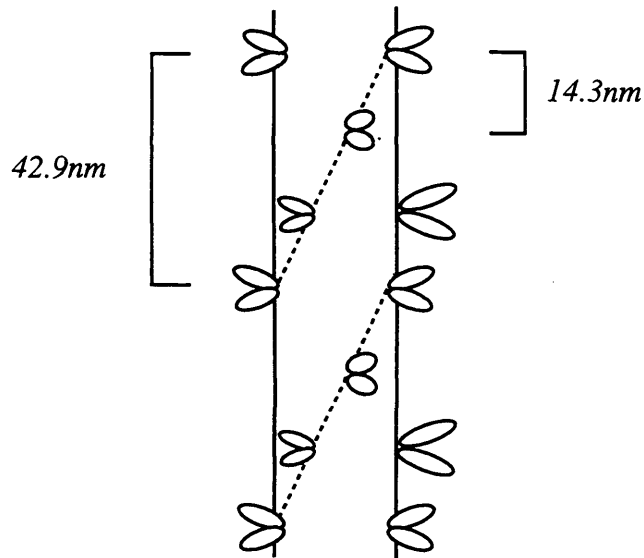
2.5 Thick Filament Structure

The thick filaments are primarily an aggregation of molecules of the 520kDa protein myosin [92]. Each myosin molecule consists of two chains which coil around each other to form a double helical chain with two globular heads (fig. 2.6a). The larger 166kDa section of this chain, called the light meromyosin chain (LMM) [93, 34], binds strongly to its counterpart in other myosin molecules to give rise to a thick rod or backbone of myosin molecules 17.6nm in width [83]. The heavy meromyosin (HMM) section of each molecule consists of a short 100kDa length of the coiled coil chain (S2), the two myosin heads (S1) of 120kDa each, and an additional two ~20kDa chains on each head called the essential and regulatory light chains which are thought to be involved in the regulation of the ATP hydrolysis [107]. The HMM sections of the myosin molecules protrude from the backbone to form the observed crossbridges [68].

The myosin molecules aggregate such that the pairs of myosin heads form a triple helix of pitch 42.9nm on the filament surface (fig. 2.6b) [80, 135, 136]. Head levels are separated axially by an average of 14.3nm, and each level contains three pairs of heads [72]. A slight distortion from the perfect helix has a significant effect on the resulting diffraction patterns [144]. The thick filaments are also bipolar, with the molecules aligned such that the heads point in opposite directions on either side of the M-band. This results in a bare zone around the M-band, where there are no crossbridges [8, 133].



(a) *The Myosin Molecule*



(b) *Arrangement of Myosin Molecules in the Thick Filament*

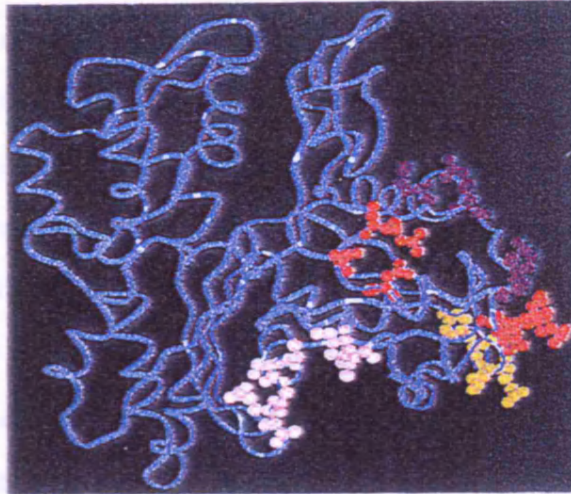
Figure 2.6: Thick Filament Structure

The thick filaments also contain significant amounts of C-protein, a 150kDa rod shaped protein approximately 40nm by 2nm [108]. The C-protein molecules bind strongly to the thick filament backbone in seven strips on each side of the filament M-line, with an axial repeat of 44nm. The slight distortion in the triple helix may be attributable to the presence of C-protein molecules [17]. The backbone structure is undetermined at present, though recent modelling studies have suggested that the myosin molecules pack closely in a curved molecular crystalline layer, with a small tilt of 1-3° from the filament axis [17].

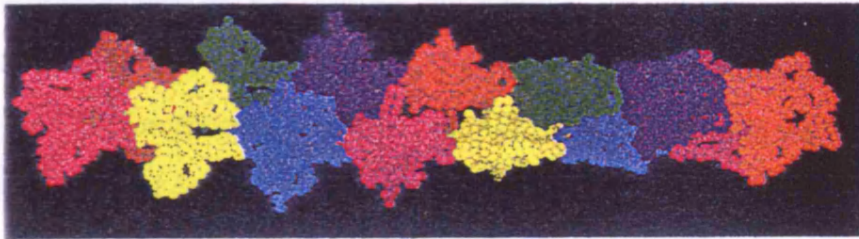
2.6 Filament Interaction

Structural studies have shown that after stimulation of a muscle, but before any force is produced, the myosin heads move out radially towards the thin filaments. This enables the myosin heads to interact with the actin monomers; a prerequisite for filament sliding. There is evidence that the S2 chain is very flexible at both the HMM-LMM and the S2-S1 junctions [155, 83]. The flexibility and elasticity of the S2 chain confers a certain freedom of movement on the myosin heads, allowing the heads to change their position and orientation without altering the backbone structure; additional backbone rearrangement is possible but it is not a requirement for myosin head movement.

The crystallographic co-ordinates of the atoms in the actin filament (fig. 2.7) [79, 59, 91] and the myosin head (fig. 2.8) [124] have recently been determined. The positions of the myosin binding sites on the actin monomers, and the ATP and actin binding sites on the myosin heads, have been established [152]. This breakthrough has allowed Molecular Dynamics calculations to investigate the actin-myosin interactions in detail [122, 49, 25]. These calculations indicate that the interaction between the thin filaments and the myosin heads is likely to be an electrostatic one, rather than a physical connection between the two: the actin filament is primarily surrounded by a negative potential, and the interaction sites on the myosin head are positively charged [25]. In this work, the term “bonding” will refer to the actin-myosin interaction, whatever form it takes.



(a) *G-Actin Monomer*



(b) *F-Actin Filament*

Figure 2.7: Crystallographic Structure of Actin (courtesy J.Harries)

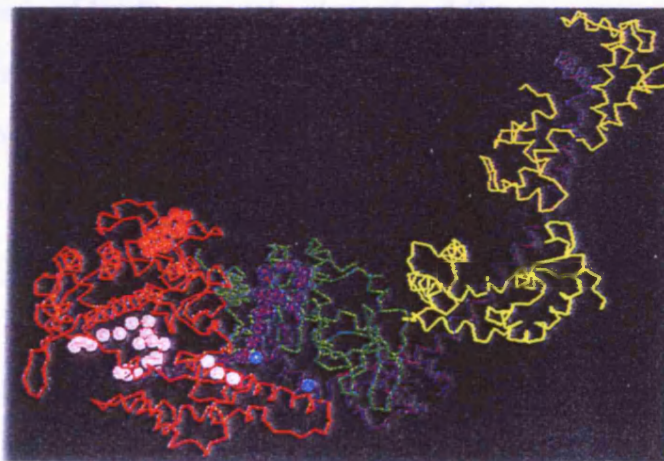


Figure 2.8: Crystallographic structure of the Myosin Head (courtesy J.Harries)

The first step in the contraction process is the release of Ca^{2+} ions from the sarcoplasmic reticulum, as described in §2.2. Troponin and tropomyosin, the regulatory proteins found in the thin filament, are strongly affected by the Ca^{2+} ion concentration; the *Steric Blocking Mechanism* describes how the presence of these ions may initiate contraction as follows [134, 138, 87].

In the presence of a low concentration of Ca^{2+} ions, the tropomyosin molecules follow the groove of the long actin helix as described in §2.4, weakly linked to each of the seven corresponding actin monomers. X-ray diffraction and electron microscopy studies have shown that the preferred myosin head binding site is on the outer face of the actin monomer. Therefore in the low $[\text{Ca}^{2+}]$ of the rest state, the tropomyosin molecules block this site (fig. 2.9a) inhibiting the actin-myosin interaction.

Troponin molecules have a high affinity for both actin and tropomyosin in the presence of low Ca^{2+} ion concentrations, and they pull the tropomyosin into the blocking position towards the outer domain of the actin monomer. In high concentrations of Ca^{2+} the troponin loses its affinity for actin and it no longer holds the tropomyosin in position. The weak links between the actin monomers and the tropomyosin molecules pull the tropomyosin further into the F-actin groove to follow the actin symmetry more closely, leaving most of the outer face of the actin monomer accessible to the myosin head. Thus the tropomyosin inhibition is removed and binding can take place (fig. 2.9b).

However, recent studies have shown that this is not the whole story by determining that each myosin head actually binds to two sites on the actin filament [5, 6]. The major interaction is with the outer domain of one monomer as described above, while another interaction takes place between the tip of the myosin head and the inner domain of the adjacent actin monomer. According to the simple steric blocking model, this second site is still blocked by the tropomyosin molecules. Clearly some further movement of the tropomyosin is necessary to allow a full interaction. It has been suggested that this extra movement may be caused by some internal rearrangement of the inner domain of the actin monomer, or by the presence of myosin heads in the vicinity of the thin filament. Whatever the cause, this additional step supports the proposal of a two stage interaction between thin

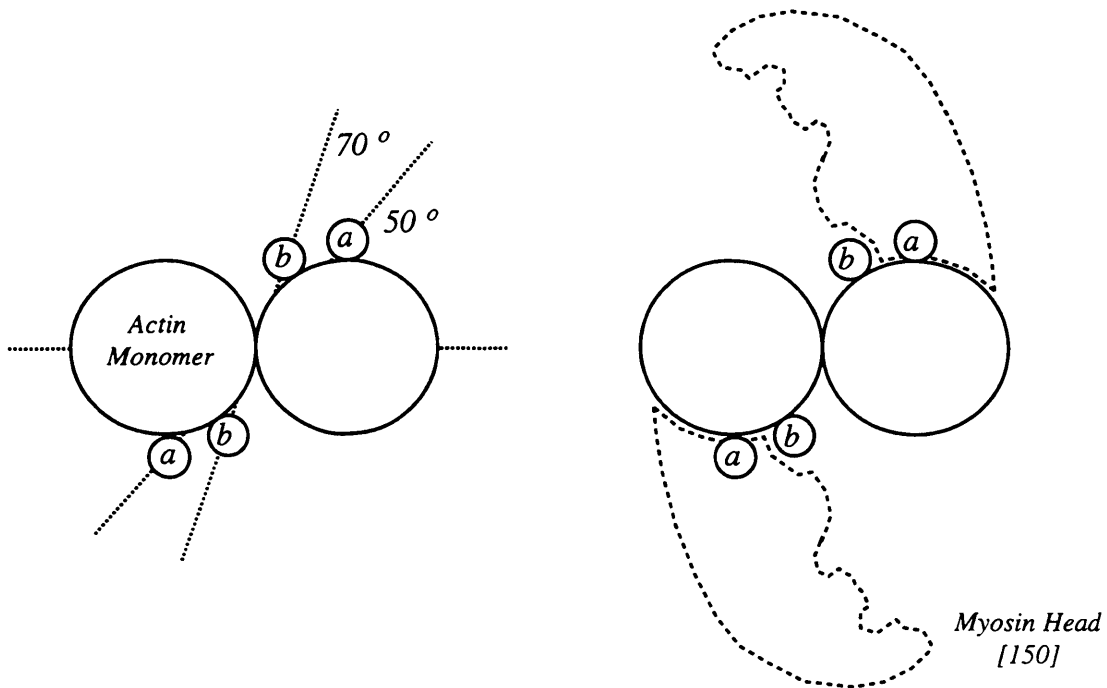


Figure 2.9: The Steric Blocking Mechanism (after Squire [133])

- (a) *In unactivated muscle, the tropomyosin molecules take positions at 50° to the line joining adjacent monomers, blocking the favoured myosin binding site.*
- (b) *In activated muscle, the tropomyosin moves further into the groove of the F-actin helix to an angle of 70° , uncovering the binding site.*

filaments and the myosin heads. This topic will be returned to in the next section.

2.7 Contraction Theories

Numerous theories have been proposed to describe the contraction mechanism, ranging from the plausible to the probable. Surveying the comprehensive reviews which compare and contrast various models [78, 27, 66], it is interesting to note that although the theories themselves vary widely, there are some common elements which keep recurring, and are therefore likely to be involved in the real mechanism. This section describes the key elements of some of the more popular theories which attempt to explain how the interaction between thick and thin filaments generates a force which result in the filaments sliding past each other.

2.7.1 Crossbridge Cycle Models

Most models fall into one of two categories: those involving a crossbridge cycle, and those which offer an alternative cause of filament sliding. The first group are based on the *Cycling Head* model proposed by H.E.Huxley in 1969 [69], combined with the Lymn-Taylor ATP hydrolysis cycle [94]. In its simplest form, this theory suggests that the myosin head attaches to an actin monomer in a particular orientation, and then the attached head moves to take on a distinct orientation. Since the head is still bound to the thin filament, they slide relative to one another (fig. 2.10). The head then detaches from the actin filament and the release of energy from ATP hydrolysis results in its reorientation, ready to attach to the next actin monomer in the thin filament and repeat the process, hence the term *cycling* head. The bipolar nature of the thick filaments ensures that the relative sliding moves the thin filaments in both halves of the sarcomere towards the M-band in the centre, and the summed effects of many heads asynchronously cycling result in macroscopic shortening.

The precise relation between the ATPase cycle and the crossbridge cycle is not confirmed, but in the basic Lymn-Taylor model the hydrolysis of one ATP molecule is linked to one crossbridge cycle [94]. If the cycle is interrupted by blocking the recovery of

ATP after hydrolysis, the myosin head cannot release the actin monomer and is trapped at the end of the power stroke. The muscle is then said to be in the *rigor* state, where the majority of the myosin heads are bound to the thin filaments, but are unable to cycle. The high proportion of bound heads makes the muscle stiff and gives a high passive tension, but the trapped state means it is unable to generate tension upon stimulation.

In this model the rigor state is equivalent to the conformation at the end of the power stroke, though other models may differ in their interpretation. It is clear that muscle requires both Ca^{2+} and ATP to contract and generate force; without Ca^{2+} the heads do not bind significantly to the actin monomers, and without ATP they cannot release at the end of the cycle. In both cases, no force is generated.

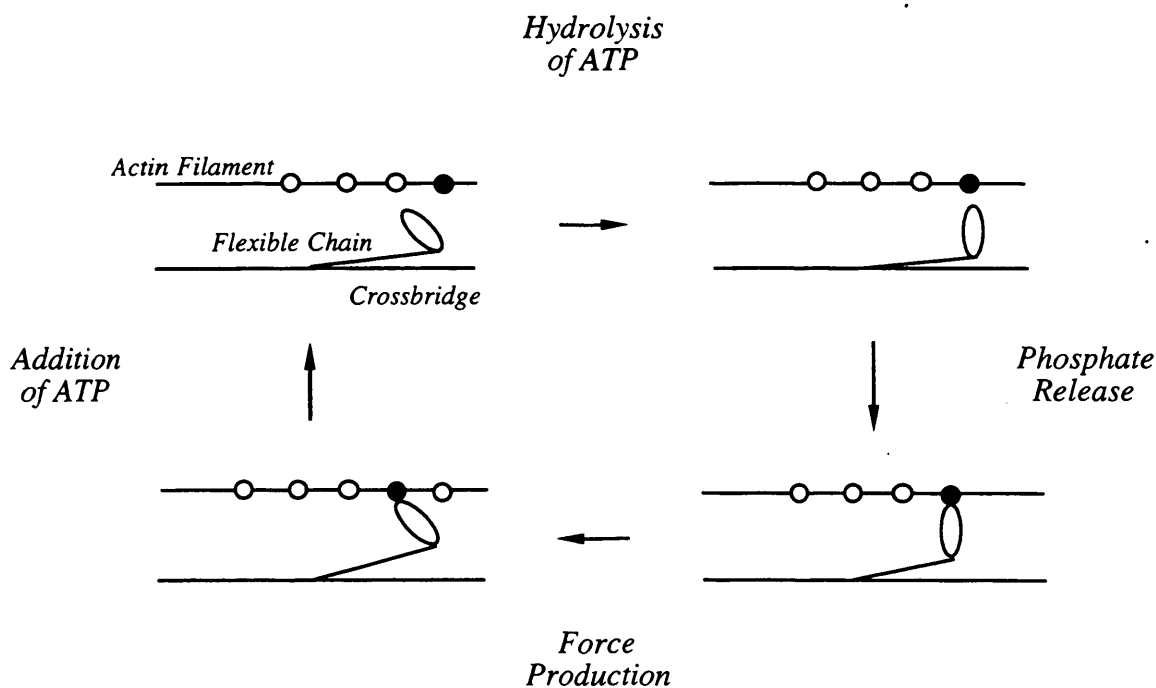


Figure 2.10: Basis Of The Cycling Head Model

See text for details.

2.7.2 Weak and Strong Binding States

The cycling head model has been modified as research provides new information, but this simple mechanism still forms the basis of many current theories. The Lymn-Taylor

cycle has been modified to allow for the fact that ATPase does not inevitably lead to detachment of the actin-myosin bond [142, 33]. In the modified cycle, the crossbridges alternate between a weak binding state and a strong binding state, which returns to the proposal of a two stage interaction suggested in §2.6. The central supposition of this theory is that the myosin heads initially bind weakly to the thin filaments, then undergo a conformational change to form a stereospecific strong bond. This strongly bound conformation is a strained one, and the power stroke releases the strain energy, returning the head to a weak binding conformation.

Many heads are weakly bound at any one time and are in rapid equilibrium with the detached state; only a small portion of these heads go on to become strongly bound. The mechanism by which the transfer from one state to the other is realised may be modulated by the specific nucleotide present at the ATPase site. The concept of two binding states and a power stroke transfer between them is attracting a lot of attention, and there is structural and biochemical evidence to support the theory [40, 58, 120, 151, 123].

The mechanism of transfer between states could be explained by a model where the release of inorganic phosphate triggers the change from weak to strong binding [123]. The cycle starts with the myosin head strongly bound to the thin filament, after relative sliding has taken place (fig. 2.11). The first step involves a molecule of ATP attaching to the ATPase site in a cleft on the myosin head, causing the bond to change from a strong bond to a weak one. This results in a reorientation of the head to partially close the ATPase cleft, which completely detaches the myosin head from the thin filament. The reorientation causes the hydrolysis of ATP, and the ADP and inorganic phosphate hydrolysis products remain in the cleft: the phosphate is only released when the head rebinds to the thin filament, triggering the power stroke and resulting in relative sliding of the filaments. The power stroke also reopens the ATPase cleft, allowing another molecule of ATP to bind to the myosin head to start the cycle again.

Again, if ATP recovery is blocked, the rigor state is reached. In this model, the rigor state is therefore equivalent to the strong binding state at the end of the power stroke. However, there is another puzzle regarding the diffraction data: strongly defined layer lines

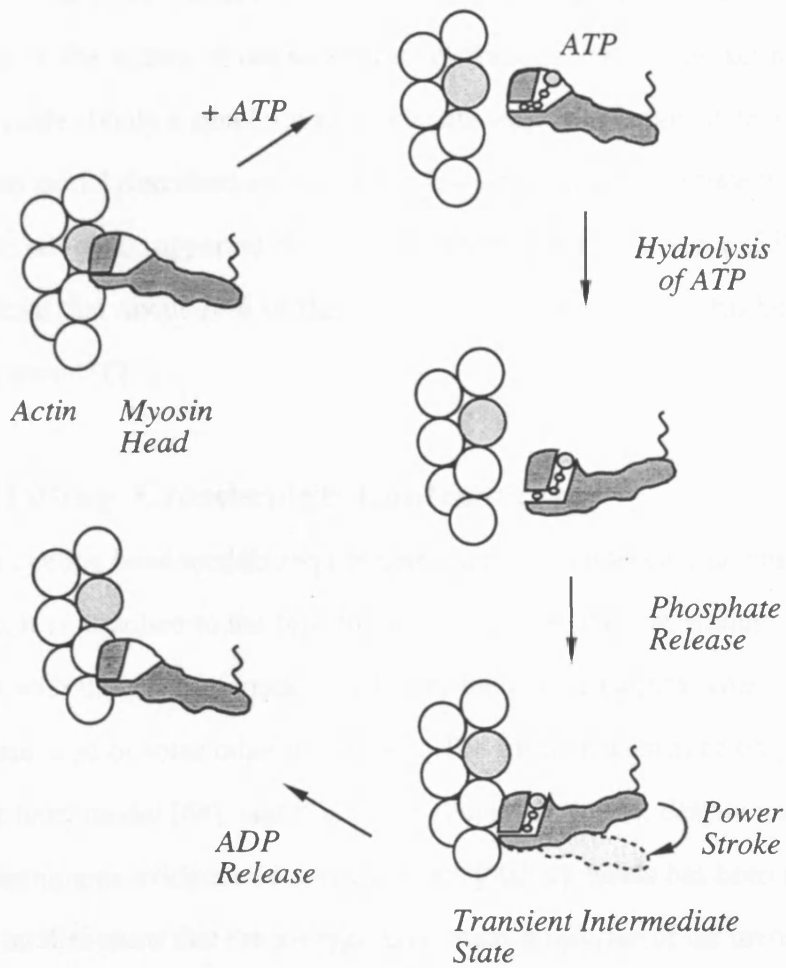


Figure 2.11: Modified Model Of Contraction Cycle (after Rayment [123])

See text for details.

from muscles in rigor take on the spacing of the actin helical repeats, revealing a significant amount of binding to actin, but no trace of similar rigor layer lines are observed in contracting muscle patterns [70]. If the strong binding state is indeed equivalent to the rigor state, why is no rigor pattern observed? In fact, because the diffracted intensity is proportional to the square of the number of diffracting centres, no actin-based rigor lines would be visible if only a small number of heads were in the rigor state at any one time. In the two-state model described above, only a few heads at any one time were in the strongly bound state, which is supported by electron paramagnetic resonance (EPR) measurements which indicate that about 20% of the myosin heads are strongly attached in isometrically contracting muscle [21].

2.7.3 Tilting Crossbridge Controversy

The cycling head models require some sort of conformational change in the myosin head whilst it is attached to the thin filament to cause filament sliding. The predominant uncertainty with this class of model is whether the conformational change involves a tilting of the myosin head or some other movement. The tilting head was an original supposition of the cycling head model [64], and it is a neat theory; however, despite many attempts to do so, no unambiguous evidence of asynchronously tilting heads has been uncovered. X-ray diffraction studies show that the average axial mass projection of the myosin heads becomes more spread out during contraction, indicating that the heads have become less perpendicular to the filament axis and/or are less axially ordered than at rest. The results could be explained equally well by tilting crossbridges, or in terms of a simple axial motion of the attached heads without tilting, which is easily provided for by the elasticity in the S2 chains joining the heads to the thick filament backbone [76, 169, 172]. Electron microscopy studies appear to give conflicting evidence; some indicate that both the weakly bound heads and rigor heads are tilted [119]; others suggest that heads during isometric contraction take a range of values whose average is perpendicular to the filament axis, whilst at rigor the heads are regularly tilted [57, 56].

A high degree of axial order remains during contraction [70, 13]. Further time

resolved diffraction studies suggest that changes in the axial orientation of the heads may be the effect of the strain imposed on them by tension generation, rather than the cause of the tension generation itself [13, 76]. The suggestion is that only a small fraction of the total number of diffracting heads and/or a small fraction of their mass performs random axial motions [98]. Physiological studies show that at least 70% of the myosin heads are attached in isometrically contracting frog muscle [116], which indicates that only small sections of the myosin head are reoriented during force generation.

Several small mobile loops have been identified in the myosin head structure [12, 23, 128, 123, 124] which are affected by the nature of the attached nucleotide and the presence of actin. Diaz Baños *et al* [25] have used molecular dynamics calculations to study these flexible loops, and their conclusion is that it is possible to visualise a mechanism of contraction whereby these mobile loops are the small sections of the head which are rearranged during the force generation process; several possible interaction states exist where transfer from one state to the next would result in a firmer bond and a more strained orientation.

2.7.4 Step Size

Another controversial area is the step size of the contractile cycle; this is usually defined as the amount of relative sliding between filaments per molecule of ATP hydrolysed. If one molecule of ATP is hydrolysed per myosin head cycle, then this is equivalent to the power stroke of the myosin head. On this basis, early tilting crossbridge models set an upper limit to the step size of the maximum swing of the myosin head, then estimated at 40nm (twice the length of the head) [69]. Since then, studies have placed the step size between 10 and 20 nm [62, 37, 64, 117]. More recent suggestions have ranged from smaller values of 4nm [73], to greater than 200nm [170, 171].

Much of the controversy may arise from the relationship between step size and ATP coupling, as well as from the different conditions under which experiments are carried out (reviewed by Burton [15]) [15, 39]. The ATP coupling is usually assumed to be one myosin head cycle per molecule of ATP hydrolysed, but Yanagida's results could be

explained if many head cycles took place for one ATPase: thus the total amount of sliding per ATPase would be many times the amount moved by a single head. This suggests that ATP hydrolysis is not necessary for detachment of the actin-myosin bond, a theory which has had support in the past [117, 118, 65, 60]. The step mechanism itself also remains unclear; if the myosin heads are acting asynchronously, those heads which are at the end of their working stroke but are still attached may well affect the working heads. The effect of two myosin heads on the same S2 chain must also be considered.

Recently, myosin steps of 12nm have been observed directly, and support for one to one ATP coupling remains strong [35]. However, given the history of controversy over the step size, a lot more work needs to be done before the uncertainty can be removed.

2.7.5 Non-Crossbridge Cycle Models

This section briefly introduces several of the alternatives to the popular crossbridge cycle discussed in the previous sections. One model suggests that the contraction force is actually generated by a change in the length of the actin filaments [45, 7]. The theory is that the binding of myosin to actin induces a change in the structure of the actin helix. ADP is exchanged for ATP, which is subsequently hydrolysed. The actin structure reverts to its original state, at which point the myosin dissociates from the actin filament [147, 149].

A more recent version of the actin force generator model has proposed that the change in the actin helix structure is a transformation between ribbon and helix states [129, 130, 131]. After hydrolysis of ATP on the myosin head, the head binds to the actin filament inducing a transformation of that section of actin helix to a ribbon state, whose repeat is commensurate with the myosin repeat, and breaking the actin - tropomyosin bond.

The contraction force is produced when the actin segment reverts to the helix structure and shortens. The inextensible tropomyosin/troponin complex takes on the role which actin holds in the crossbridge cycling models: that of summing the force generated from each actin segment, and transmitting the total force to the Z-disc, resulting in filament sliding. The actin segment is anchored by the myosin head, and as it shortens during helicalisation, the tropomyosin pulls the Z-disc towards the centre of the sarcomere. The

twisting of the actin helix during the transformation results in the breaking of the actin-myosin bond. This theory can explain many of the mechanical observations related to the contraction process, and is a perfectly valid model which should be investigated further.

Another interesting approach to contraction involves electric dipole field theory [77]. The myosin heads are considered to act as an array of electric dipoles, negatively charged at the backbone end and positively charged at the tip. The myosin dipoles induce a charge on the rod-like thin filaments in much the same way as a magnetic dipole induces magnetism in a ferromagnetic rod. The dielectric constant of the surrounding material determines whether the induced charge attracts the rod or repels it, which introduces a dependence on the concentration of free ions, i.e. Ca^{2+} , in the surrounding environment.

The contractile force is generated by the coulombic interaction between the dipoles and the charged rod, and is proportional to the energy density at the tip of the thin filament. The electric dipole on the myosin head is formed when it binds ATP, and the ATPase cycle allows multiple ATP binding to one head. The rigor state is not considered to be part of the active contraction cycle, and is instead a completely separate state where the myosin heads and actin monomers are physically cross linked: the active cycle states involve electrostatic interaction rather than physical contact between the two components.

The last model to be discussed here is the liquid crystal model of contraction [158]. This involves the formation of a trigonal channel by three adjacent myosin filaments and the internal actin filament. In relaxed muscle, the myosin heads are situated close to the backbone and the thick filaments appear to be approximately cylindrical. Although the thick and thin filaments have different periodicities, as quasi-cylinders the difference is negligible and the structure is stable. The symmetry is lost, however, when the myosin heads move outwards towards the thin filaments upon activation, and the differences in periodicity become apparent. The resulting non-equilibrium state causes the filaments to move relative to one another, and the polar nature of the filaments ensures unidirectional motion in each half of the sarcomere.

Although the crossbridge cycle model is very intuitive, there is as yet no direct evidence for it which cannot be explained by an alternative theory. This section has shown

that a crossbridge cycle is by no means the only possible cause of filament sliding, and all the models stated here are theoretically capable of explaining many aspects of the behaviour of muscle.

2.8 Summary

The information in this chapter reveals that the basic structural components of vertebrate skeletal muscle are helical filaments, occupying a two dimensional hexagonal lattice: this then is the starting point for building a model. The structure can be treated as a collection of chain molecules, and diffraction from such a structure is discussed in Chapter 3.

The mechanical force of contraction is believed to originate in an interaction between the myosin heads on the thick filaments and actin monomers in the thin filaments. The interaction involves both Ca^{2+} , without which the troponin/tropomyosin complex blocks the binding sites on the actin helix and myosin heads cannot bind significantly to the thin filaments, and ATP, without which the heads cannot release the bonds and are trapped in the *rigor* state. With both elements present, the myosin heads bind to the thin filaments and generate the contraction force, causing the thick and thin filaments to slide past each other.

Several mechanisms of contraction were discussed in this chapter, giving examples of how the observed behaviour of muscle can be explained without invoking a crossbridge cycle. However, the crossbridge cycle is the generally accepted basis of muscle contraction. The interpretation of the modelling results in this work was approached with the crossbridge cycle in mind, although no assumptions were made about the contraction process in the actual modelling process.

Chapter 3: Helical Diffraction Theory

3.1: Introduction

3.2: Basic Diffraction Theory

3.3: Crystalline Diffraction

3.4: Helical Diffraction

3.4.1: Diffraction From An Infinite Continuous Helix

3.4.2: Diffraction From A Helix of Discrete Atoms

3.5: Application to Muscle

3.5.1: Multistranded Helices

3.5.2: Two Dimensional Hexagonal Lattice

3.6: Disorder Effects

3.6.1: Helical Disorders

3.6.2: Lattice Disorders

3.7: Summary

3.1 Introduction

A monochromatic, coherent beam of x-rays falling onto a periodic collection of atoms is preferentially scattered in certain directions according to the structure of the collection. The x-rays are actually scattered by the electrons in the atoms, and the resulting scattered intensity distribution is determined by the Fourier transform of the structure's electron density distribution, $F(\underline{S})$:

$$I(\underline{S}) = F(\underline{S})^* F(\underline{S}) = |F(\underline{S})|^2 \quad \text{eqn. (3.1)}$$

where:

\underline{S} = reciprocal space coordinate

$I(\underline{S})$ = intensity distribution given by a structure

$F(\underline{S})$ = Fourier transform of the electron density distribution of the structure

$F(\underline{S})$ is defined in § 3.2

Muscle is a polycrystalline structure: the lattice is well defined in small crystallite regions which are themselves randomly oriented throughout the muscle fibre. The diffraction pattern combines components from both the helical and crystal lattice arrangements in muscle [102]. The primary contributions to the low angle x-ray diffraction pattern from muscle come from the helical actin and myosin structures within the thin and thick filaments, with less intense contributions from other proteins. Thus the majority of the pattern can be interpreted in terms of the scattering from a two dimensional array of helical structures. This chapter develops the theory necessary to reconstruct such scattering, with special reference to the molecular arrangement in muscle [157, 19, 81].

3.2 Basic Diffraction Theory

When a wave of wavelength λ is elastically scattered by an atom, the scattered wave at a distance r from the atom is of the form [157]:

$$Ae^{i(kr+\phi)} \quad \text{eqn. (3.2)}$$

where:

ϕ = the initial phase of the wave

$$\underline{k} = \frac{2\pi}{\lambda} \hat{k}$$

= the incident wavevector

$$k = |\underline{k}| = \frac{2\pi}{\lambda}$$

Radiation is scattered equally in all directions, and the scattering power of the atom is independent of the direction of observation. However, when the atom is replaced by a collection of atoms, the individual waves interfere with each other to produce a scattering pattern whose intensity depends on the direction of scattering. For a pair of atoms separated by r (fig. 3.1) the resultant scattered wave is of the form:

$$f e^{i(\underline{k} - \underline{k}_0) \cdot \underline{r}} \quad \text{eqn. (3.3)}$$

where:

f = the scattering power of a single atom

\underline{k}_0 = the incident wavevector

\underline{k} = the scattered wavevector at 2θ to the incident direction

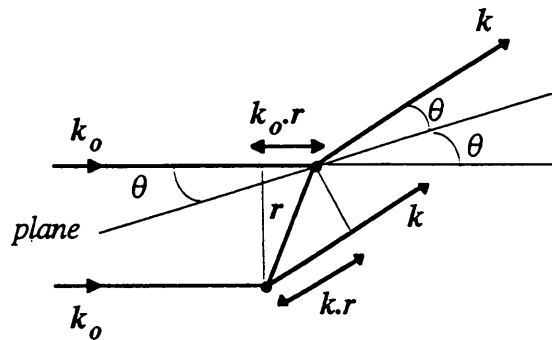


Figure 3.1: Scattering From Two Atoms

Incident x-rays (\underline{k}_0) are scattered (\underline{k}) by two atoms separated by r . The rays are parallel until the bottom ray is scattered by the lower atom, and again after the top ray is scattered by the upper atom. During the time that the rays are non-parallel, the top ray travels $\underline{k}_0 \cdot \underline{r}$ whilst the bottom ray travels $\underline{k} \cdot \underline{r}$. Thus the path difference between the two rays is $(\underline{k} - \underline{k}_0) \cdot \underline{r}$.

Note that if the wavelength is much larger than the separation of the atoms, then the two scattered waves are almost in phase in all directions, and no interference pattern is

observed. This explains why x-rays are suitable for diffraction from atomic structures; the wavelength is of the same order of magnitude as the atomic scale.

Bragg scattering occurs in the special case where the atoms form a series of planes (fig. 3.2). For constructive interference to give a peak in the interference pattern, the waves from the two planes must be in phase, which means that the path difference between the two waves must be a whole number of wavelengths. The path difference is the distance ABC in figure 3.2: the geometry of this diagram results in the Bragg scattering condition:

$$2d \sin \theta = n\lambda \quad \text{eqn. (3.4)}$$

where:

- d = separation of the planes
- θ = angle of incidence
- λ = incident wavelength
- n = integer order 0, 1, 2,...

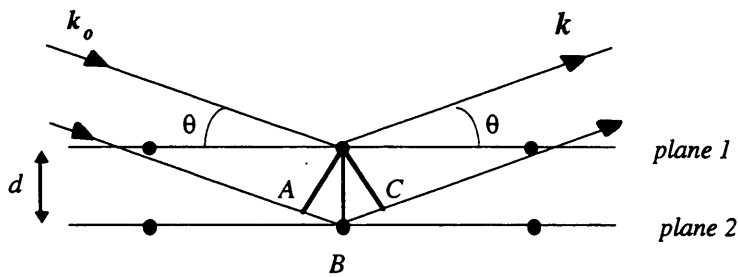


Figure 3.2: Bragg Scattering From A Set Of Planes

Incident x-rays (k_0) are scattered (k) from two planes separated by a distance d . The bottom ray travels a distance ABC further than the top ray, leading to a path difference of ABC between the two rays. This length is dependent on the angle between the incident x-rays and the scattering planes.

In general the atoms do not form planes, and the simple Bragg condition does not hold. In this case the individual interference effects from each atom with respect to an origin atom of the form given in equation (3.3) are summed to give the scattering factor for the collection of atoms:

$$F(\underline{S}) = \sum_{j=1}^n f_j e^{i2\pi \underline{S} \cdot \underline{r}_j} \quad \text{eqn. (3.5)}$$

where:

n = number of atoms

f_j = scattering power of a single atom

$$\underline{S} = \frac{(\underline{k} - \underline{k}_0)}{2\pi}$$

= the scattering vector

Finally, the discrete scattering units may be replaced by a continuous electron density function which allows for atomic structure, rather than treating the atom as a point source. This also allows the introduction of scattering centres other than a single atom such as molecules or other particles. This generalisation results in equation (3.5) becoming:

$$F(\underline{S}) = \int_V \rho(\underline{r}) e^{2\pi i \underline{S} \cdot \underline{r}} dV \quad \text{eqn. (3.6)}$$

where:

$\rho(\underline{r})$ = electron density distribution of the scattering structure

dV = volume element

This is the definition of the Fourier transform of the electron density distribution. Thus the scattering function of a collection of scattering units is the Fourier transform of the electron density distribution function, and by equation (3.1) the resulting intensity distribution is the square of the modulus of the Fourier transform.

3.3 Crystalline Diffraction

A three dimensional crystal structure consists of a basic unit cell which repeats throughout the whole structure. The unit cell can be described in terms of its three vectors (fig. 3.3); the repeating nature of the structure means that any point in the crystal can be reached by an integer combination of these vectors. The structure factor of the crystal is determined by that of the unit cell. Equation (3.6) can be expanded using vectorial components:

$$F(XYZ) = \iiint \rho(xyz) e^{2\pi i(Xx+Yy+Zz)} dx dy dz \quad \text{eqn. (3.7)}$$

where:

$\underline{r} = x, y, z$ = real space coordinates

$\underline{S} = X, Y, Z$ = reciprocal space coordinates

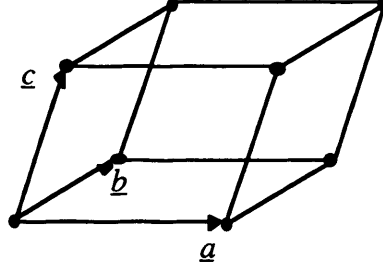


Figure 3.3: General Unit Cell Vectors

Any point in a lattice based on this unit cell can be reached by an integer combination of the unit cell vectors \underline{a} , \underline{b} , and \underline{c} .

For a single unit cell, the electron distribution function need only be considered between the cell limits. Introducing Miller indices $[hkl]$ to describe the set of planes intersecting the unit cell vectors at $\frac{1}{h}\underline{a}$, $\frac{1}{k}\underline{b}$ and $\frac{1}{l}\underline{c}$, the corresponding structure factor for the unit cell is:

$$F_{hkl} = \int_0^a \int_0^b \int_0^c \rho(xyz) e^{2\pi i(ha^*x + kb^*y + lc^*z)} dx dy dz \quad \text{eqn. (3.8)}$$

where:

F_{hkl} = structure factor arising from the hkl planes in one unit cell

$\rho(xyz)$ = electron distribution function for the unit cell

$\underline{a}^*, \underline{b}^*, \underline{c}^*$ = reciprocal space unit cell vectors:

$$\underline{a}^* = \frac{\underline{b} \times \underline{c}}{\underline{a} \cdot \underline{b} \times \underline{c}}; \quad \underline{b}^* = \frac{\underline{c} \times \underline{a}}{\underline{a} \cdot \underline{b} \times \underline{c}}; \quad \underline{c}^* = \frac{\underline{a} \times \underline{b}}{\underline{a} \cdot \underline{b} \times \underline{c}}$$

F_{hkl} is only non-zero for integer values of $[hkl]$, so the diffraction pattern is a set of discrete spots. These reflections form the reciprocal space lattice for the crystal. The lengths of the reciprocal lattice unit cell vectors are inversely proportional to the corresponding real space vectors.

For the whole crystal, the structure factor is the sum over all unit cells:

$$F_{hkl} = \sum_j f_j e^{2\pi i(\frac{h}{a}x_j + \frac{k}{b}y_j + \frac{l}{c}z_j)} \quad \text{eqn. (3.9)}$$

where:

$f_j = \text{structure factor for one unit cell}$

By analogy to the three dimensional case, a two dimensional real space crystal lattice has a reciprocal lattice consisting of a set of rods perpendicular to the lattice plane, separated by a distance inversely proportional to the real space lattice spacing. The reciprocal lattice for a one dimensional array of points is a set of planes perpendicular to the one dimensional array, separated by a distance inversely proportional to the point spacing.

3.4 Helical Diffraction

3.4.1 Diffraction From An Infinite Continuous Helix

An infinite continuous helix is more easily described in cylindrical polar coordinates (r, θ, z) than in Cartesian coordinates (x, y, z) (fig. 3.4).

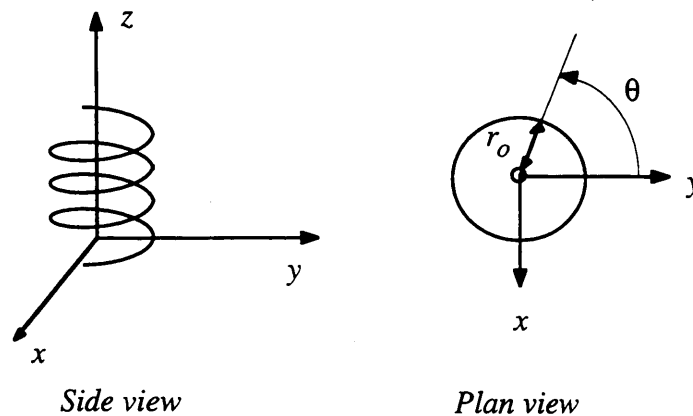


Figure 3.4: Cartesian and Cylindrical Polar Coordinates

Any point on the cylindrical helix can be converted to Cartesian coordinates by:

$$\begin{aligned}
x &= r_o \cos \theta \\
y &= r_o \sin \theta \\
z &= \frac{p \cdot (\theta - \theta_o)}{2\pi}
\end{aligned}
\tag{eqn. (3.10)}$$

where:

- r_o = radius of the helix
- θ_o = angular position of the helix at $z = 0$
- p = pitch of the helix

An infinite continuous helix can be defined as the convolution of a single turn of a helix with an infinite set of points separated by the helix pitch [157, 81, 19, 132]:

$$h_{\infty}(r\theta z) = h_1(r\theta z) * P(xyz) \tag{eqn. (3.11)}$$

where:

- $h_{\infty}(r\theta z)$ = infinite continuous helix
- $h_1(r\theta z)$ = single turn of a helix
- $P(xyz)$ = pitch function

Thus by the convolution theorem, the Fourier transform of the infinite continuous helix is given by:

$$F(h_{\infty}) = F(h_1) \cdot F(P) \tag{eqn. (3.12)}$$

The pitch function is confined to a one dimensional set of points in the z direction separated by a distance p , by the equation:

$$P(xyz) = \delta(x)\delta(y) \sum_{n=-\infty}^{+\infty} \delta(z - np) \tag{eqn. (3.13)}$$

The Fourier transform of this function is:

$$\begin{aligned}
F(P) &= \int_{\nu} P(r) e^{ik \cdot r} dr \\
&= \sum_n \delta(k_z - \frac{2n\pi}{p})
\end{aligned}
\tag{eqn. (3.14)}$$

As described in §3.3, this is a set of planes perpendicular to the helix axis, separated by a distance $\frac{2\pi}{p}$.

Considering the helical definition in equation (3.10), a single turn of a continuous helix is defined by:

$$h_I(r\theta z) = \delta(r - r_0)\delta\left(z - \frac{P(\theta - \theta_0)}{2\pi}\right) \quad \text{eqn. (3.15)}$$

Thus the Fourier transform is:

$$F(h_I) = r_0 \int_0^{2\pi} e^{i(k_x r_0 \cos\theta + k_y r_0 \sin\theta + k_z \frac{P(\theta - \theta_0)}{2\pi})} d\theta \quad \text{eqn. (3.16)}$$

From equation (3.11), the Fourier transform of the infinite continuous helix is therefore the product of equations (3.14) and (3.16):

$$F(h_\infty) = \sum_n r_0 \int_0^{2\pi} e^{i(k_x r_0 \cos\theta + k_y r_0 \sin\theta + n(\theta - \theta_0))} d\theta \quad \text{eqn. (3.17)}$$

Converting this to reciprocal space cylindrical coordinates (R, ψ, ζ) , defined by:

$$X = 2\pi R \cos\psi$$

$$Y = 2\pi R \sin\psi$$

$$Z = 2\pi\zeta$$

and substituting for:

$$\Omega = \theta - \psi$$

we find:

$$F(h_\infty) = \sum_n r_0 e^{in(\psi - \theta_0)} \int_0^{2\pi} e^{2\pi i R r_0 \cos\Omega} e^{in\Omega} d\Omega \quad \text{eqn. (3.18)}$$

Comparing this equation to the definition of a Bessel function of order n :

$$2\pi i^n J_n(X) = \int_0^{2\pi} e^{iX \cos \Omega} e^{in\Omega} d\Omega \quad \text{eqn. (3.19)}$$

and substituting for $i^n = e^{\frac{i n \pi}{2}}$ we find that the Fourier transform of an infinite continuous helix becomes:

$$F(h_\infty) = \sum_n r_0 e^{in(\psi + \frac{\pi}{2} - \theta_0)} J_n(2\pi R r_0) \quad \text{eqn. (3.20)}$$

and thus the intensity of the diffraction pattern is:

$$I_\infty = |F(h_\infty)|^2 = \sum_n r_0^2 J_n^2(2\pi R r_0) \quad \text{eqn. (3.21)}$$

In real terms, this is a series of n discrete planes in reciprocal space at axial spacings of $Z = \frac{2\pi n}{p}$. The intensity is cylindrically symmetric: for a given value of n , the intensity distribution depends only on R , and is independent of ψ . This means that all the intensity information can be recorded in one two dimensional plane, but all phase information is lost.

In general, the original diffracting structure can be recovered from its Fourier transform by performing an inverse Fourier transform on $F(\underline{S})$, where the inverse Fourier transform is defined as:

$$\begin{aligned} F(\underline{S}) &= \int_v \rho(\underline{r}) e^{2\pi i \underline{S} \cdot \underline{r}} dV && \text{Fourier transform} \\ \rho(\underline{r}) &= \int_V F(\underline{S}) e^{-2\pi i \underline{S} \cdot \underline{r}} dV && \text{Inverse Fourier transform} \end{aligned} \quad \text{eqn. (3.22)}$$

However, the phase information which is lost in the recorded diffraction pattern is required to perform the inverse transform, which means that the original structure cannot be recovered by inverse transforming the diffraction pattern in this way.

The two dimensional diffraction pattern, then, is a series of layer lines perpendicular to the helix axis whose intensity distribution is determined by the helical arrangement of the scattering units. The central layer line where $n=0$ is called the *equator*, and since

$J_{-n}^2(X) = J_n^2(X)$, the diffraction pattern is symmetrical about the equator. The equator is actually determined by the mass projection onto the lattice plane (i.e. along the helix axis) and is insensitive to any changes to the helical structure in the axial direction. The pattern is also symmetrical about the Z -axis or *meridian*, due to the cylindrical symmetry of the Bessel functions. The meridian is sensitive to changes in the axial mass distribution and is unaffected by any variations in the plane perpendicular to the muscle axis.

Bessel functions have many interesting properties and their behaviour is well documented [157, 132]. The variation of $J_n(2\pi Rr_0)$ with R and n is shown in figure 3.5. The R -axis position of the first peak increases with n , which results in the distinctive helical “X” diffraction pattern.

3.4.2 Diffraction From A Helix of Discrete Atoms

Most helices of practical interest are not infinite or continuous, but are in fact made up of a series of units at regular intervals along the helical track. The repeating units may be atoms, molecules, or groups of molecules. To introduce discontinuity to an infinite continuous helix, the helix is multiplied by a series of planes perpendicular to the helix axis, separated by the axial subunit translation, t . The planes sample the infinite continuous helix, resulting in a discontinuous helix of points separated by t .

The convolution theorem is invoked again to give:

$$F(h_d) = F(h_\infty) * F(P) \quad \text{eqn. (3.23)}$$

where:

$$F(h_d) = \text{discontinuous helix of points}$$

$$F(P) = \text{plane function}$$

The plane function is defined by:

$$P(xyz) = \sum_m \delta(z - z_0 - mt) \quad \text{eqn. (3.24)}$$

which is Fourier transformed to:

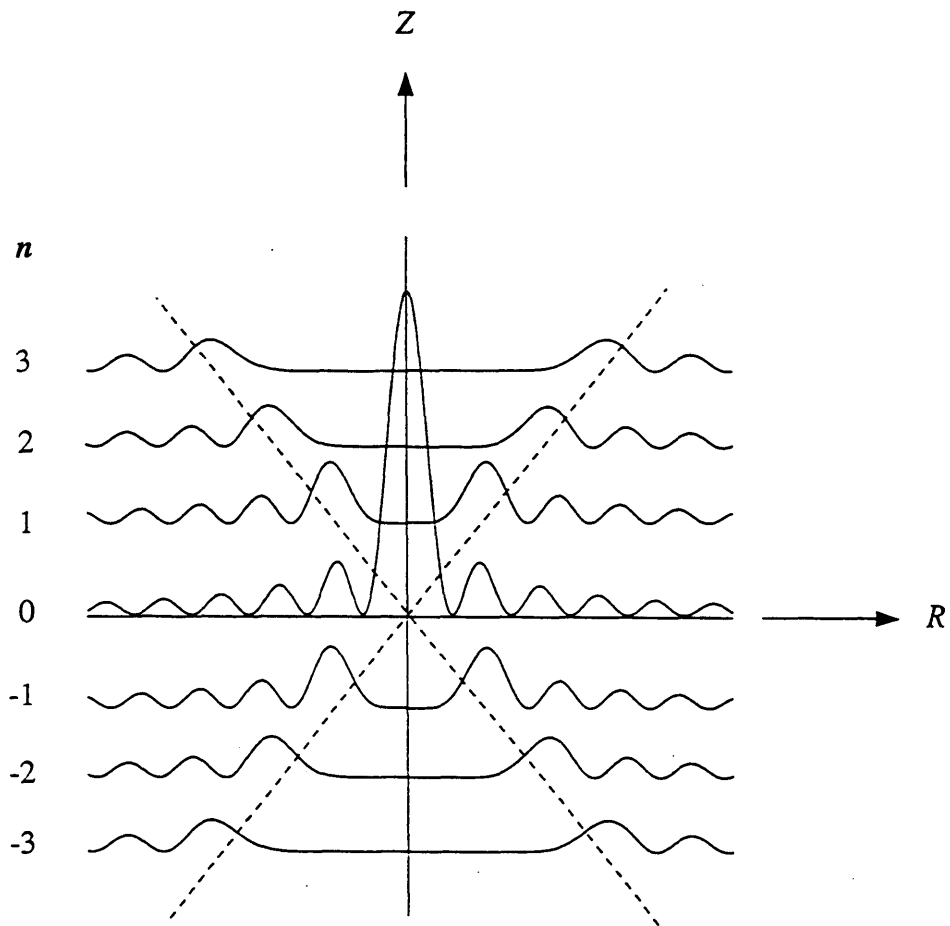


Figure 3.5: Squared Bessel Functions J_n^2 for $-3 < n < 3$

$$F(P) = \delta(k_x)\delta(k_y)e^{ik_z z_0} \sum_m \delta(k_z - \frac{2m\pi}{t}) \quad \text{eqn. (3.25)}$$

This expression represents a series of points along the Z-axis in reciprocal space at axial spacings of $\frac{2m\pi}{t}$.

Using the form of $F(h_\infty)$ calculated in equation (3.20), the discontinuous helix Fourier transform is given by:

$$F(h_d) = \left\{ \sum_n r_0 e^{in(\psi + \frac{\pi}{2} - \theta_0)} J_n(2\pi R r_0) \right\} * \left\{ \delta(k_x)\delta(k_y)e^{ik_z z_0} \sum_m \delta(k_z - \frac{2m\pi}{t}) \right\} \quad \text{eqn. (3.26)}$$

This is mathematically complicated but physically simple: the distinctive cross of layer lines from the continuous helix described above is distributed at each of the series of points along the Z-axis derived from the plane function. The result is a series of crosses centred on the meridian at axial spacings of $\frac{2\pi m}{t}$. Each individual cross is identical to the continuous result, with layer lines separated by $\frac{2\pi}{p}$.

For a helix where the axial subunit translation is much smaller than the pitch, the crosses are spread out along the meridian and do not overlap. However, as the subunit translation increases, the cross separation decreases and the different sets of layer lines overlap. This means that the layer lines can no longer be described by the integer n , but must also be described with reference to the cross from which they arise (fig. 3.6). The helical selection rule simplifies this description, whilst allowing for easy calculation of the Bessel function contributions to each layer line.

The selection rule assumes that a helix of pitch p and subunit translation t can always be approximated to an integer helix, where:

$$\frac{p}{t} = \frac{a}{b} \quad \text{for integer } a \text{ and } b \quad \text{eqn. (3.27)}$$

and in this case, the l th layer line from the equator contains contributions from the n th layer line of the m th X centred on $\frac{2m\pi}{t}$ for combinations of m and n which obey the rule:

$$l = am + bn \quad \text{eqn. (3.28)}$$

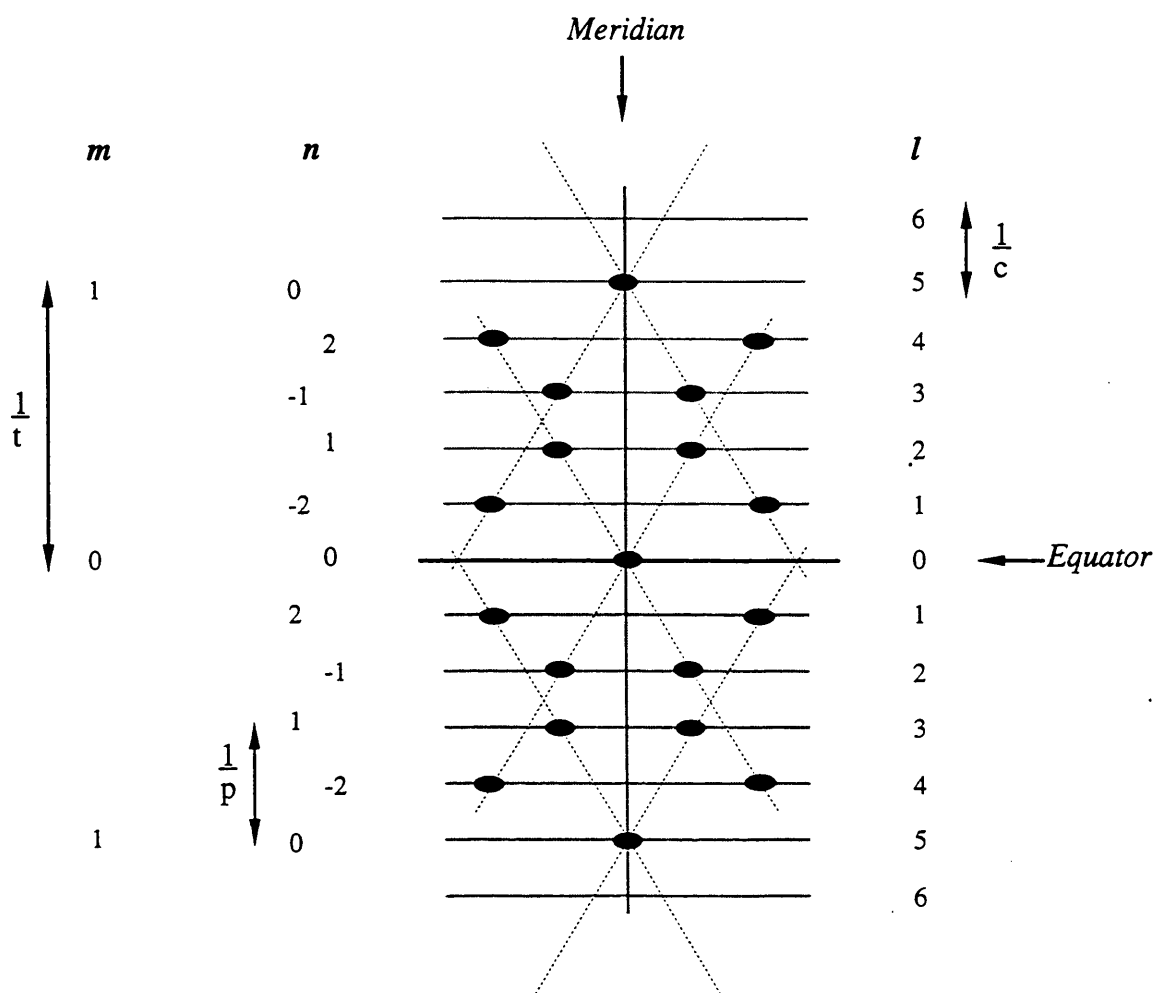


Figure 3.6: Layer Line Labelling

For helices with larger axial translations, the separate diffraction crosses distributed along the meridian begin to overlap. When this happens, the layer line labelled l consists of contributions from the n th layer line of the m th cross, where l , m and n obey the selection rule:

$$l = am + bn$$

In this example the helix has a pitch p , axial translation t , a true repeat c , and $a/b = p/t = 5/2$.

Since the intensity of the first peak of each squared Bessel Function decreases rapidly with n , only the first few values of n which contribute need be considered.

The introduction of a new parameter, $c = pb = ah$, which describes the true repeat of the helix taking account of the positions of the discrete units as well as the helical track itself, enables this rather complex Fourier transform to be written mathematically:

$$F(h_d) = \sum_l e^{\frac{2\pi ilz_0}{c}} \sum_n r_0 e^{in(\psi + \frac{\pi}{2} - \theta_0)} J_n(2\pi Rr_0) \quad \text{eqn. (3.29)}$$

The corresponding intensity distribution is a series of layer lines at axial positions of $Z = \frac{2\pi l}{c}$, and with contributions from Bessel functions n which obey the selection rule.

i.e.
$$I = \sum_l \delta(Z - \frac{2\pi l}{c}) \sum_n r_0^2 J_n^2(2\pi Rr_0) \quad \text{eqn. (3.30)}$$

for n satisfying equation (3.28).

When an identical finite structure is placed at each discrete point of the helix by convoluting the structure functions, the corresponding Fourier transforms are multiplied:

$$F(h_a) = F(h_d) \cdot F(atom) \quad \text{eqn. (3.31)}$$

which, for the simplest case of a single atom, is simply the atomic scattering factor for that atom, f_a . The result is that the whole diffraction pattern is sampled by the structure factor of the repeating unit, which tends to fade the pattern towards higher R values.

3.5 Application to Muscle

The molecular structure of muscle is an array of approximately parallel helical molecules placed in a two dimensional lattice which occupies a plane perpendicular to the long axis of the molecules. This structure is reproduced by convoluting one helical molecule with a two dimensional point lattice; the Fourier transform of the structure is therefore the

product of the individual transforms of one helix and the lattice. Thus the diffraction pattern is given by the helical transform sampled by a set of interference lines running parallel to the helix axis. The positions of the interference peaks arising from the lattice provide information about the molecular packing of the helices in the structure.

The reflection notation is adapted from the three dimensional crystal case where $[hkl]$ referred to the reflection from the three dimensional $[hkl]$ planes. In terms of helical arrays, $[hkl]$ refers to the reflection arising from the $[hk]$ set of planes in the two dimensional lattice, and the l th layer line from the helical structure.

3.5.1 Multistranded Helices

As described in Chapter 2, both the thick and thin filaments are multistranded helices: a double actin helix in the case of thin filaments and a triple myosin in the thick filaments. An N -fold multistranded helix of true pitch p has an effective pitch which is $\frac{p}{N}$. The intensity distribution for an infinite continuous helix was determined by equation (3.21) to be a series of layer lines at axial spacings of $Z = \frac{2\pi n}{p}$ where n is the order of the layer line.

$$I_{\infty} = |F(h_{\infty})|^2 = \sum_n r_o^2 J_n^2(2\pi R r_o) \quad \text{eqn. (3.21)}$$

The multistranded helix pitch of $\frac{p}{N}$ means that the layer lines now occur at spacings of $Z = \frac{2\pi n}{p} * N$, where p is the true pitch of one strand. Thus all layer lines are removed except those for which n is an integer multiple of N .

In the thin filament actin helix, a single strand of true pitch 73nm would produce layer lines at $Z = \frac{2\pi n}{73} \text{ nm}^{-1}$. The double helix with an effective pitch of $\frac{73}{2} \text{ nm}$ gives rise to layer lines at $Z = \frac{4\pi n}{73} \text{ nm}^{-1}$, twice the spacing of the n th layer line expected from a single strand of the helix. The result is that all the layer lines arising from the single strand helix are removed except those which were labelled $n = 2 \times \text{integer}$.

The triple myosin helix has a true pitch of 128.7nm. The effective pitch of $\frac{128.7}{3} \text{ nm}$ produces a set of layer lines at $Z = \frac{6\pi n}{128.7} \text{ nm}^{-1}$, effectively removing all layer lines except those which were labelled $n = 3 \times \text{integer}$ in the single strand pattern.

The remaining layer lines are numbered according to the effective pitch, rather than the single helix true pitch. Thus, layer lines occur at $Z = \frac{2\pi n}{36.5} \text{nm}^{-1}$ from the thin filament helix and at $Z = \frac{2\pi n}{42.9} \text{nm}^{-1}$ from the thick filament helix, where $n=0,1,2,3\dots$. This gives rise to a significant uncertainty in determining the pitch and number of strands in a helix from the diffraction pattern; if the number of strands is unknown, the Bessel function corresponding to a given layer line is also unknown. Thus the centre of mass of the diffracting structures cannot be determined unambiguously. A layer line at a spacing of $\frac{1}{R}$ could be produced by any structure where $\frac{N}{P} = \frac{1}{R}$. As a result, the Bessel function order n is unknown and cannot be used to determine the radius of the helix, and vice versa [157, 133, 132].

3.5.2 Two Dimensional Hexagonal Lattice

The two dimensional muscle lattice is basically hexagonal: the thick filaments form an hexagonal lattice with thin filaments at the trigonal points (§2.3). However, in frog sartorius muscle it is not a simple hexagonal lattice; the thick filaments take one of two orientations which results in a superlattice arrangement. The unit cells for the simple and super lattices are shown in figure 3.7 [133, 70].

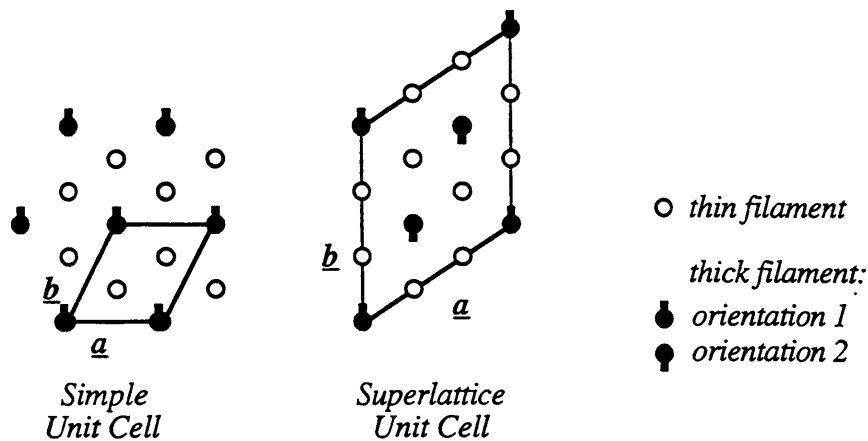


Figure 3.7: Unit Cells for Simple and Super Lattices

The thick filaments take on one of two distinct orientations in the superlattice unit cell as illustrated by this example configuration.

Because the vectors of the unit cell define the [hk] plane notation, the same planes are labelled differently in each lattice case; the [11] superlattice planes are equivalent to the

[10] planes in the simple hexagonal lattice, and the [10] superlattice planes are equivalent to the [11] simple lattice planes. Figure 3.8 displays the major planes in both notations. For consistency, all lattice planes in this text will be labelled with reference to the simple unit cell unless otherwise specified.

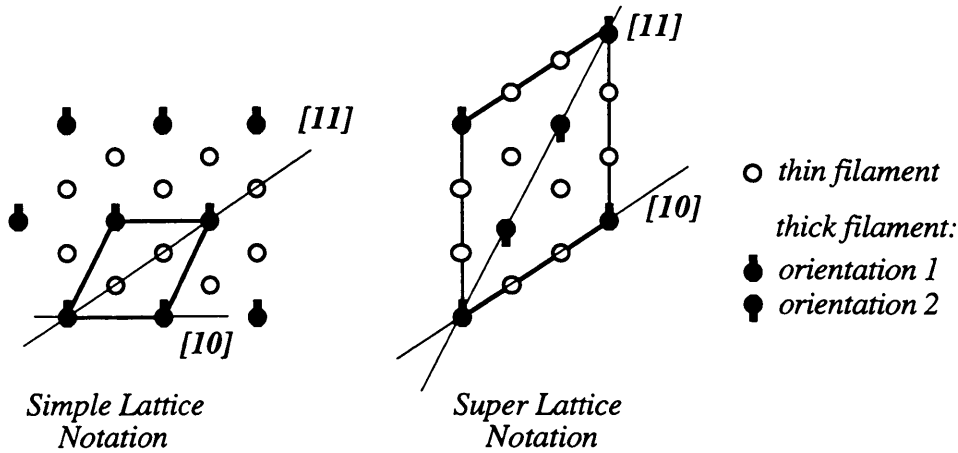


Figure 3.8: Plane Notation in Simple and Super Lattices

The [10] and [11] reflections on the equator of the diffraction pattern are the strongest reflections in the muscle pattern; as discussed in §3.4, the equator is sensitive to the mass projection onto a plane perpendicular to the helix axis (i.e. projected along the helix axis). The relative intensities of the [10] and [11] reflections provide information on the amount of mass in close proximity to the thick and thin filaments. The [10] planes contain only thick filaments, so a strong [10] reflection indicates that there is a lot of mass near the thick filaments lattice positions. Since the [11] planes contain both thick and thin filaments, a stronger [11] reflection would indicate more mass close to the thin filament positions. A more detailed account of the behaviour of these reflections, and the structure and effects of the superlattice, are presented in Chapters 5 and 7 respectively.

3.6 Disorder Effects

A diffraction pattern actually represents the averaged diffracting structure, and any information obtained from the data is averaged over the whole structure. If the scattering

units in a helical structure are not precisely helical in their distribution because of variation in their position, orientation or atomic arrangement, an averaged electron density can be assumed which does repeat regularly. One side effect of this is that the more variation there is in a parameter, the more averaged the data will be, resulting in increased smearing of the diffraction pattern.

3.6.1 Helical Disorders

The subunits within a helical molecule rarely occupy the ideal helix positions; all of the helical parameters are vulnerable to disorder where the actual values of the parameter take a range of values about the ideal value. Within a single helix disorder may appear in the position and/or orientation of the subunits; in practice, any combination of the disorders discussed here may be observed.

Disorder in the axial translation between subunits has a strong effect on the axial mass projection, and therefore is most obvious in the meridional intensities. Axial motion also upsets the helical projections and thus affects the layer line intensities. However, the mass projection onto the lattice plane is insensitive to axial changes in a perpendicular plane, resulting in an unmodified equatorial distribution [164]. Conversely, changes in the radius of the centre of mass of each subunit are observed in the equator and layer lines, without affecting the meridian [164].

The angular position of the subunits may be subject to disorder which strongly affects the intensity distribution along the layer lines [28, 29]. The helical projections are disordered whilst the axial and lattice plane projections are largely unchanged, leaving the meridional and equatorial reflections unaffected. The subunits may also take a variety of orientations, axially and/or azimuthally whilst maintaining the same position of their centres of mass.

The effects of helical disorders on the diffraction pattern are generally similar. The reflections are centred on the position given by the corresponding averaged parameter, and the intensity is spread out according to the amount of the disorder; large disorders result in low, broad peaks. The disorder may be cumulative or non-cumulative; non-cumulative disorders cause all reflection orders with the same structural origin to smear by a similar

amount; cumulative disorders result in the smearing effects increasing in the higher order reflections.

3.6.2 Lattice Disorders

There are three important types of disorder which can effect the lattice structure: net distortions, filament shifts and filament rotations. Bending of the filaments is also possible, but it is beyond the scope of this thesis to include such a distortion.

Net distortions occur where the filaments are randomly displaced from their perfect lattice positions. *Disorder of the first kind* displaces each filament from its ideal location by an amount randomly drawn from a Gaussian distribution of displacements; thus the probability of a certain displacement decreases as the displacement gets larger. Long range order is maintained and the amount of disorder is independent of the position of the filament with respect to the lattice origin; on average the array retains crystalline order throughout the lattice.

Disorder of the second kind is a more complex case where disorder is cumulative; the position of each filament is affected by the displacements suffered by the surrounding filaments. There is a statistical probability that the translations between adjacent filaments will be the unit cell vectors, but any long range order is completely lost. Figure 3.9 illustrates the difference between first and second type disorders [157, 101, 146, 147]. Both types result in similar broadening of the Bragg diffraction peaks and redistribution of the intensity along the layer line continuous helical transform, but differ in that the broadening from disorder of the first type is similar for all layer lines, and increases at higher reciprocal spacings for disorder of the second type.

An axial shift between filaments causes an averaging of the ideal axial mass projection, and a corresponding smearing of the meridional reflections [18]. The loss of helical order resulting from the shift removes the Bragg diffraction peaks on all layer lines except for the equator, whose lattice projection is insensitive to axial changes [101, 146, 147]. The effects are worse for higher order Bessel functions and the corresponding layer lines.

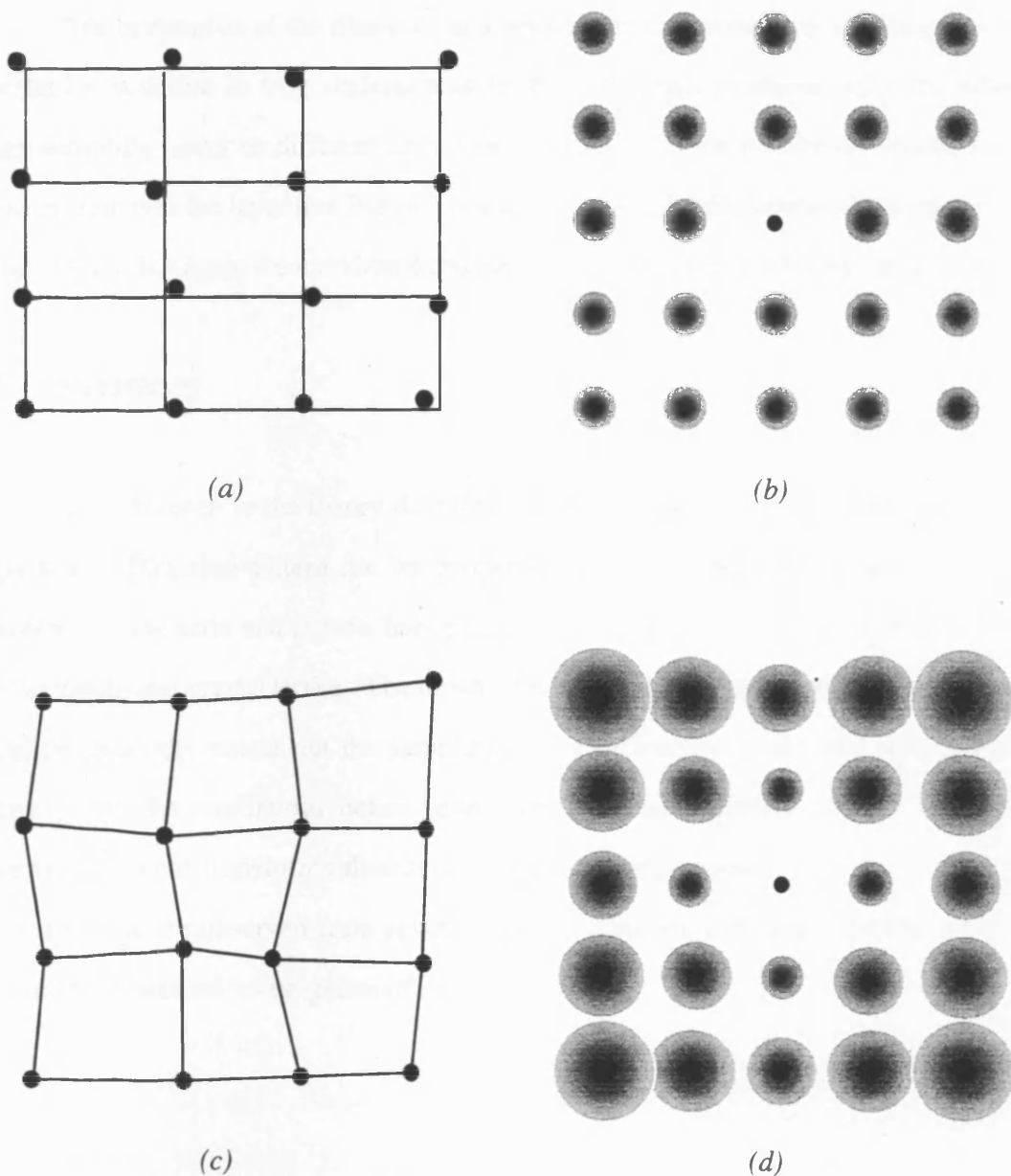


Figure 3.9: Comparison of Disorders of the First and Second Kinds (after Vainshtein [153])

Molecular arrangement compared to the ideal lattice positions for (a) disorder of the first kind and (c) disorder of the second kind. In (a) the lattice vectors repeat perfectly and the molecules are displaced about their ideal positions, whereas in (c) the lattice vectors themselves are distorted from their ideal values.

Resulting smearing of the diffraction pattern reflections for (b) Disorder of the first kind and (d) disorder of the second kind. In (b) the retention of long range order results in a similar smearing at all diffraction points; in (d) the long range order is lost and the outer reflections are smeared to a far greater extent than those closer to the pattern centre.

The orientation of the filaments as a whole is an important factor, giving rise to the superlattice structure in frog skeletal muscle (§3.5.2) which produces radically different Bragg sampling peaks on different layer lines. Variation in the precise orientations of the filaments removes the layer line Bragg diffraction peaks and redistributes the intensity along the layer lines, but again the meridional and equatorial projections are largely unaffected.

3.7 Summary

By reference to the theory developed in this chapter, the reflections from the low angle x-ray diffraction pattern can be interpreted to provide information about the helical parameters of the actin and myosin helices, as well as the molecular packing of these helices into the hexagonal crystal lattice. The broad effects of disorders have been discussed: lattice disorders generally smear out the sampling Bragg diffraction peaks and redistribute the intensity into the continuous helical transforms; helical disorders tend to broaden the underlying helical transforms themselves, redistributing intensity into the background. Similar effects are observed from several types of disorder, and more specific results are required for a detailed investigation of muscle structure.

Chapter 4: X-ray Diffraction Experimental Techniques

4.1: Introduction

4.2: Synchrotron Radiation and the SRS

4.3: Wiggler Magnets

4.4: Optical System

4.5: Experimental Station 16.1

4.6: Detectors

4.6.1: Gas Filled Multi-Wire Proportional Counters

4.6.2: Imaging Plate System

4.6.3: Spatial Calibration of the Image Plate System

4.6.4: Determination of the Dynamic Range of the Image Plate System

4.7: Experimental Procedure

4.7.1: Sample Preparation

4.7.2: Diffraction Protocols

4.8: Data Reduction

4.1 Introduction

In order to capture transient structural states during muscle contraction, the sample must be exposed to X-rays for periods of milliseconds at a time, summed over many individual contractions. To obtain high quality, accurate patterns in such low exposure times a very high intensity source is required, together with a fast, sensitive detection system. Synchrotron radiation is the most intense source of x-rays available for experimental work, and, as §4.2 illustrates, it is well suited to producing good quality diffraction patterns from muscle.

The experiments described in this thesis were carried out on stations 16.1 and 2.1 of the Synchrotron Radiation Source (SRS), Daresbury, UK, and station BL4 (insertion device II) of the European Synchrotron Radiation Facility (ESRF), Grenoble, France. Station 16.1 of the SRS is described in this chapter as a typical example of a small angle X-ray diffraction station.

4.2 Synchrotron Radiation and the SRS

Synchrotron radiation (SR) is emitted by charged particles when they are accelerated at relativistic speeds; at the SRS the charged particles are relativistic electrons, travelling in a near circular orbit and emitting radiation in a direction perpendicular to their centripetal acceleration [86]. The charged particles circulate under a vacuum of better than 10^{-9} torr: this prevents unwanted scattering of the electrons by particles in the air which would reduce the intensity of the SR emission. The SR is almost totally linearly polarised in the plane of the orbit, and is naturally collimated so that the bulk of the emission is tangential to the orbit.

Figure 4.1(a) shows the classical angular distribution or dipole pattern of emitted intensity from a slow moving electron ($v \ll c$ where $c =$ speed of light) [153, 161]. When the electron speed approaches relativistic velocities ($v \approx c$) the angular distribution is distorted into a narrow cone in the forward direction, largely polarising the radiation in this direction (fig 4.1(b)). The half width of the cone is determined by the velocity:

$$\Gamma = \sqrt{1 - \beta^2}$$

where:

$$\beta = \frac{v}{c}$$

The emitted spectrum is strongly Doppler shifted as the relativistic particles orbit, which leads to a continuous distribution of intensity with wavelength [84]. Thus SR is white radiation, but if monochromatic radiation is required a particular wavelength can be selected by a monochromator. The beam size can be made very small (on the scale of mm or smaller), which results in good peak to peak resolution even from poorly scattering biological samples. The intensity of the various reflections from muscle diffraction differ by several orders of magnitude, and the high intensity of SR ensures that even the weakest parts of the pattern are clearly visible. Like most organic samples muscle suffers radiation damage, and the shorter exposures permitted by SR reduce the structural damage which causes pattern features to be lost.

The radius of orbit R (m) of an electron in a field B (Tesla) at energy E (GeV) is

$$R = \frac{10^9 E}{cB} \quad c = \text{speed of light}$$

Given the radius of the ring as a fixed constraint, the Energy reached by the electrons depends solely on the strength of the magnetic field obtainable: this is limited by cost, practical handling considerations, and technical ability. The power radiated (kW) by a single relativistic electron travelling with an energy E (GeV) is given by:

$$P = \frac{2ce^2 E^4}{3R^2 (m_o c^2)^4} \quad \begin{array}{l} e = \text{charge on an electron} \\ m_o = \text{rest mass of an electron} \end{array}$$

Thus the total power (kW) radiated for a current of I (A) in a field B is:

$$P_{total} = 26.6 E^3 B I$$

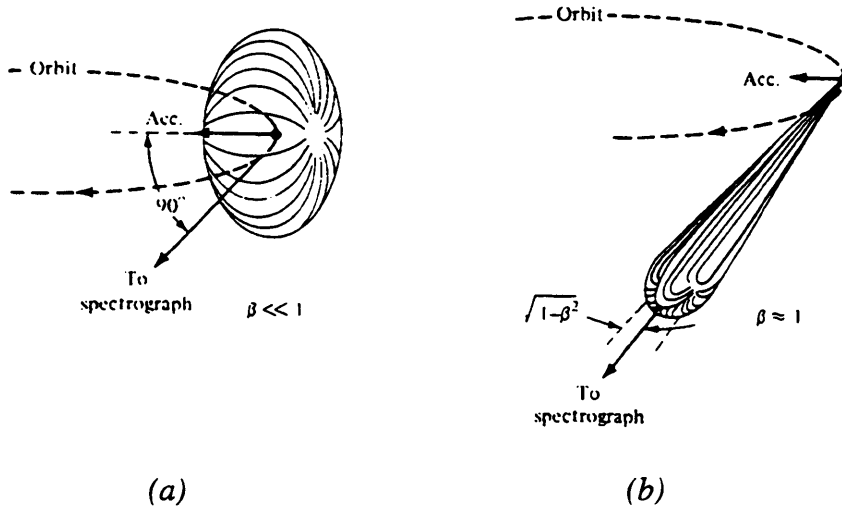


Figure 4.1: Dipole Patterns for (a) Classical and (b) Relativistic Electrons [153]

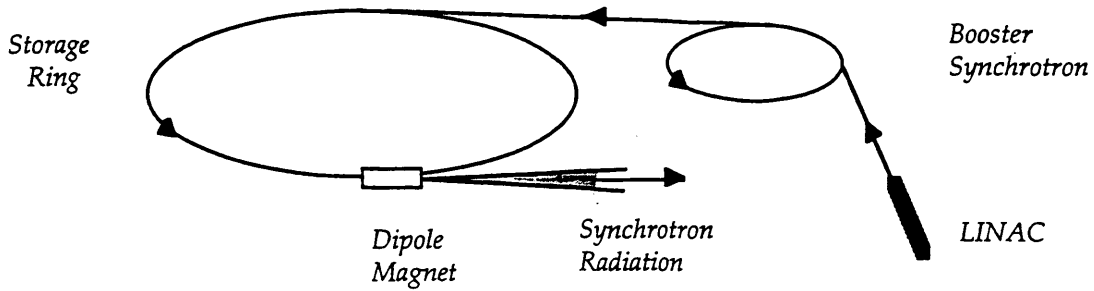


Figure 4.2: Schematic of the Synchrotron Radiation Source

Electrons are accelerated to 12MeV in the LINAC, transferred to the booster synchrotron for initial acceleration to 600MeV, and finally accelerated to 2GeV in the main storage ring.

The SRS is a three stage accelerator (fig. 4.2). Electrons are initially accelerated to 12MeV in a linear accelerator (LINAC). They are then transferred to a booster synchrotron ring (radius 5.1m) and accelerated to 600MeV. Finally, they are injected into the main storage ring (radius 15.3m), where they are accelerated to 2GeV. The current travelling through the synchrotron at injection is 250-300mA, but this value decreases as electrons are continuously lost through collisions with the storage ring walls. Losses are minimised by a set of sixteen quadrupole magnets which keep the electron beam tightly focused. Fine tuning and stabilisation of the beam is provided by the High Brilliance Lattice, a further set of sixteen multipole magnets [86].

The synchrotron ring is roughly circular, being formed from straight sections of pipe incorporating the quadrupole and multipole magnets, joined by sixteen dipole magnets which actually bend the electron beam path and thus accelerate the electrons. The electrons are only accelerated when they are being deflected in the magnets, and it is here that they emit SR at a tangent to the deflection curve. The radiation from each magnet is collected at the *tangent point* by vacuum beamline pipes, which lead to experimental stations.

Energy is continuously being lost through synchrotron radiation, at a rate of δE (keV) per electron per orbit, where:

$$\delta E = \frac{88.5E^4}{R}$$

This energy loss is restored by 500MHz radio frequency cavities synchronised to the passage of the electrons, which results in the electron beam becoming pulsed: a series of electron bunches separated by ~2ns.

4.3 Wiggler Magnets

The characteristic wavelength of a spectrum, λ_c , is defined as the point where half the power is radiated at longer wavelengths and half at shorter wavelengths. The characteristic wavelength in Ångstroms of the SR emission spectrum from a magnet of strength B (Tesla) travelling with an energy E (GeV) in an orbit radius R (m) is given by:

$$\lambda_c = \frac{18.64}{BE^2} = \frac{5.59R}{E^3}$$

and is therefore inversely proportional to the strength of the magnetic field. For a 1.2T bending magnet, λ_c is 3.9Å (fig. 4.3). In order to raise the flux at lower wavelengths, typically about 1Å for muscle experiments, a higher magnetic field is required. This is provided by incorporating a liquid helium cooled, superconducting magnet array into the straight section before the bending magnet [84].

Wiggler 2 at the SRS is a three pole array, producing a peak field of 6T [126, 10]. The resulting emission spectrum has a characteristic wavelength of 0.78Å (fig. 4.3). The two outer poles of the array are half the strength of the central pole, and opposite in polarity. The resulting beam path through the array is a characteristic horizontal ‘wiggler’ (fig. 4.4). This arrangement allows a localised field increase within the magnet, whilst the beam exits the array with no net displacement. The tangent point where the emitted radiation is drawn off is at the peak of the central pole, where the radius of curvature of the beam is greatest.

Radiation is also emitted at the two outer poles, as well as from the bending magnet directly after the wiggler magnet. The exact positioning of the tangent point determines the spectrum of radiation exiting through the corresponding beamline. On the 16.1 beamline, the tangent point has been chosen to superimpose the emission from the central peak and one of the outer peaks, thus increasing the intensity output [10, 11]. Although the shape of each diffraction spot is determined by the shape of the beam cross section, in this case the two sources are so well superimposed that no trace of a double spot has been observed.

4.4 Optical System

The multi-wavelength white SR drawn off along the beamline passes through a series of optical elements designed to focus the beam and to select a specific wavelength if monochromatic radiation is required. Station 16.1 at the SRS is a fixed wavelength non-crystalline diffraction (NCD) station, selecting a wavelength of 1.4Å [11]. The source, as

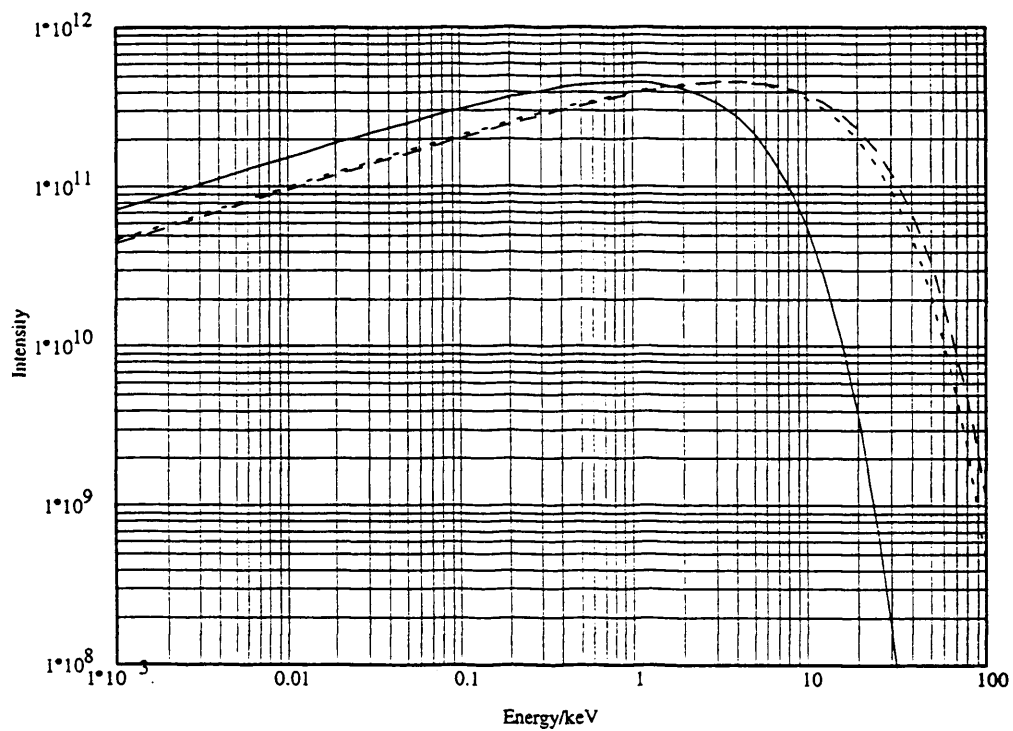


Figure 4.3: *Radiation Spectrum emitted from SRS Magnet Sources*

- Spectrum from a 1.2T dipole magnet
- - - Spectrum from a 5T wiggler magnet
- · - Spectrum from a 6T wiggler magnet

Intensity is measured in units of photons/sec/mrad_r/mA/1% bandpass

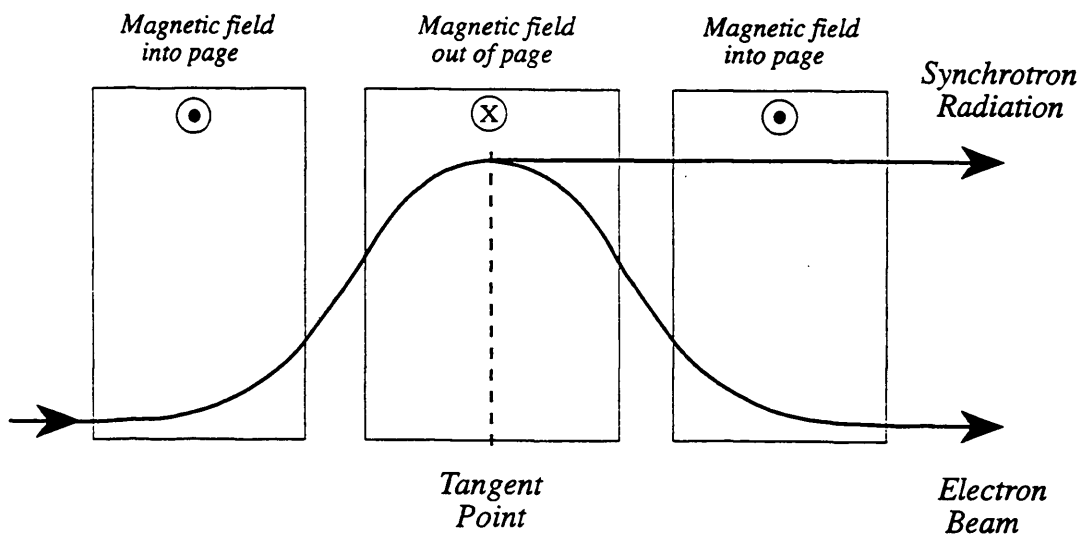


Figure 4.4: Path of the Electron Beam Through a Wiggler Magnet Array

described above, is the tangent point of a 6T wiggler magnet. After the tangent point, horizontal and vertical apertures limit the angular divergence of the accepted radiation to 12mrad by 0.9mrad respectively.

The optical system consists of a monochromator, a mirror, and defining slits (fig. 4.5). Small angle X-ray diffraction optics are usually based on the double focusing X-ray camera [52]. The mirror focuses the radiation beam vertically, whilst the monochromator selects the required wavelength and focuses the beam horizontally. The original arrangement put the mirror upstream of the monochromator so that it accepted white radiation, but these components are reversed in the 16.1 system. Here, monochromatic radiation falls on the mirror, reducing both the heat load and the damage it causes to the mirror surface, and providing a very stable focal point [14, 154]. However, this rearrangement means that only one wavelength can be selected once the optical system is built. The monochromator uses Bragg diffraction to select the required wavelength and reflect it onto the mirror. Once the mirror is in position, the angle of diffraction cannot be altered, and thus the wavelength is fixed.

The optical elements are adjustable to give the optimum focus, and are precisely positioned by computer controlled motors. The vacuum chambers are built on vibration isolation systems to prevent motor vibrations interfering with their operation.

The monochromator in the 16.1 optical system is a triangular Germanium 111 crystal, situated 9.74m from the tangent point. The crystal is 40 x 290 x 1.5 mm (base, height, width). The 111 planes are cut asymmetrically (10.5°) to reduce the output cross-section [85]. The immense heat load on the monochromator cannot be diffused in a vacuum, so the crystal sits in a copper bath of GaInSn (eutectic) which cools it. A piece of ceramic behind the monochromator fluoresces when x-rays fly over the crystal tip and hit it, providing the only direct observation of the beam. A ceramic cam-wheel at the tip of the crystal bends the monochromator, enabling the beam to be focused horizontally.

The mirror is a 1.2 x 0.08 x 0.04m platinum coated rectangle, situated 11.25m from the tangent point. It reflects 80% of the vertical aperture falling on it and can be tilted and bent to focus the beam vertically [11].

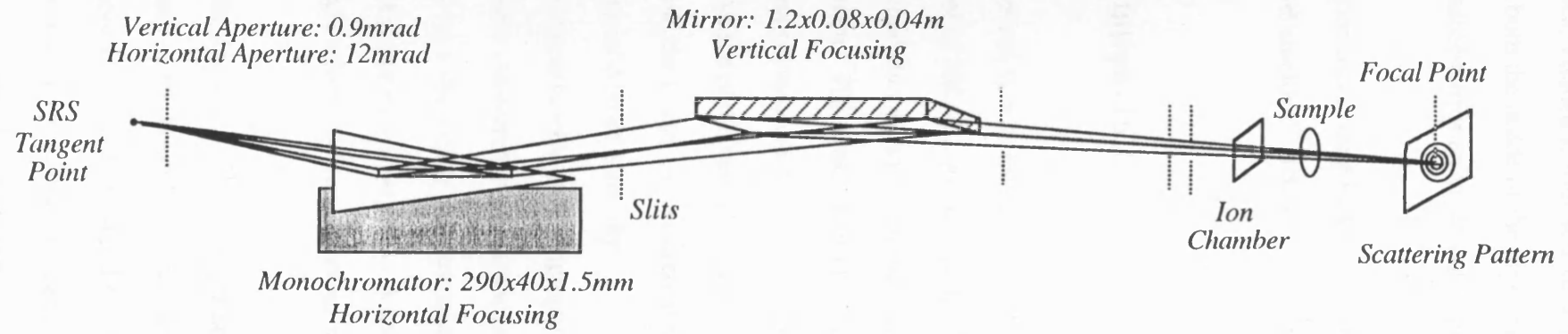


Figure 4.5: Optical System on SRS Station 16.1

In addition to the optical elements, four sets of defining slits positioned along the beamline reduce scatter from both the inside of the pipe and the optical elements. The slits combine with the monochromator-mirror arrangement to give a very clean background and high output fluxes [154].

In order to prevent station users being exposed to dangerous radiation emissions, the optical system is inside a lead shielded hutch which must be sealed before the beam can enter.

4.5 Experimental Station 16.1

Passage through the optical system reduces the radiation flux by about two orders of magnitude: for a beam current of 300mA, this brings the flux on 16.1 down to the order of 10^{12} photons/second. The actual flux at any given moment is measured by an ion chamber at the end of the optical system. The cross section of the usable beam depends on the beamline in question: the cross section and divergence of the original source, the length of the beamline, and the configuration of the optical system all affect the final output beam. In the experiments described here, the beam was focused at the detector where the beam size was typically 4mm horizontally by 0.5mm vertically.

For muscle diffraction experiments, the equipment arrangement is shown in figure 4.6. The X-rays pass through the ion chamber, and are scattered by the muscle sample in its cell (§4.7). The scattered X-rays then enter an aluminium camera tube, which is under vacuum to prevent further scattering by air particles. A lead beamstop at the far end of the camera blocks the intense unscattered beam to prevent saturation or overloading of the detector.

The peak to peak resolution of the diffraction patterns was determined by the length of the camera tube and the size of the beam focal spot, whilst the maximum extent of the patterns depends on the camera tube diameter and the detection area. In general, a short camera gives a low resolution, wide angle diffraction pattern, whereas a long camera gives a higher resolution, low angle pattern. For example, in conjunction with a 200x200mm

detection area and a 300mm diameter camera tube, a 2.25m camera gives a resolution of $1 \times 10^{-3} \text{ nm}^{-1}$ per pixel for peaks spaced between $1/30 \text{ nm}^{-1}$ and $1/4 \text{ nm}^{-1}$. In comparison, a 6.25m camera with the same configuration gives a resolution of $0.4 \times 10^{-3} \text{ nm}^{-1}$ per pixel for peaks between $1/65 \text{ nm}^{-1}$ and $1/10 \text{ nm}^{-1}$. The minimum spacings given here correspond to the width of the beamstop in the axial direction; the beamstop is wider in the equatorial direction which results in a larger minimum observable spacing.

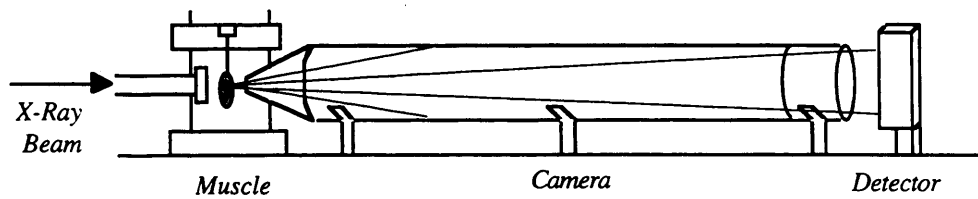


Figure 4.6: X-ray Camera

X-rays pass through the muscle sample, and are scattered down the camera tube. The length of the tube determines the range of the resulting pattern.

4.6 Detectors.

There are several detector systems available for muscle diffraction experiments, including film, image plates, and multi-wire proportional counters. The detector must have good spatial resolution, low distortion, low parallax, and a uniform response to ensure accurate positioning of the reflections. Accurate peak to peak intensity ratios require a linear response over a large dynamic range, a low fog level, and a high count rate. In these experiments, both image plates and proportional counters have been used and are described here.

4.6.1 Gas Filled Multi-Wire Proportional Counters (MWPC)

MWPCs were first developed in 1977 [38], and have been in constant use since then [163,89]. Their responses and characteristics are well documented and they are often used as standards against which new detectors are tested (table 4.1) [88]. The detection area of a gas-filled MWPC consists of three sets of orthogonal wires and a volume of gas (fig. 4.7).

When a photon enters through the two dimensional mesh of wires it ionises a gas molecule and starts a charge avalanche. Signals are sent in both directions along each set of wires when the avalanche reaches them, and the difference in time between the pulses reaching either end of the wire allows the position of the originating charge to be determined. The sets of wires are perpendicular which makes the system position sensitive in both X and Y dimensions.

| | MWPC Parameters |
|--------------------------------------|-----------------|
| Spatial Resolution (μm) | 200 |
| Dynamic Range | 10^7 |
| Linear Range | 10^7 |
| Count Rate Limit (ph/s) | 10^6 |
| Fog Level (ph/ mm^2) | <1 |

Table 4.1: MWPC Parameters [88]

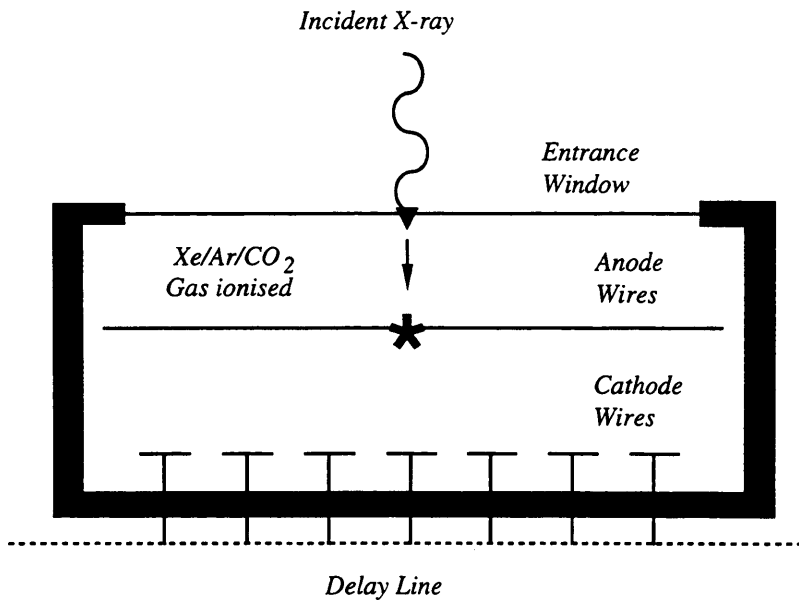


Figure 4.7: Principles of a Gas Filled Multi-Wire Proportional Counter (after Lewis [88])

As an x-ray enters the gas volume it ionises the gas, starting a charge avalanche. When the charge reaches a pair of crossed wires, signals are sent in both directions along each of the perpendicular wires, and the time difference between the pulses reaching either end of a given wire determines the exact position of the originating charge along that wire.

The MWPC detector has a high count rate, limited only by the electronic dead-time between events. It has good spatial resolution and a large linear dynamic range, as well as a negligible fog level. However, the depth of the gas volume gives rise to a significant amount of parallax, and there is some non-uniformity to the response across the detector. These can be corrected for somewhat by regularly exposing the detector to a known uniform source through a metal grid. The spatial distortion of the detector can be determined by the displacement of the grid points from their true positions, and any non-uniformity in intensity measurement can be calculated. The corrections necessary to convert the measured image from the uniform source to a true uniform image are then applied to the diffraction images themselves. The radiation detected is recorded in user-defined time frames, so that time resolution on the scale of <1ms is possible. This is an important requirement for capturing transient states of the contraction cycle.

4.6.2 Imaging Plate System

The development of the image plate detection system is relatively recent, and the system response is not as well-documented as that of the MWPC [106, 3, 2]: table 4:2 shows parameters compiled from various references. The main advantage over the MWPC is the increased spatial resolution. The image plate is an integrating detector which collects any radiation that falls on it; thus the count rate is only limited by the saturation of the plate. Time resolved data collection is not possible, but a selected time window during the contraction can be collected using a shutter to block the X-rays during most of the contractile cycle, and opening it to capture the desired state.

Because of the unfamiliarity of this system, its response was calibrated using that of a MWPC as standard. The dynamic range, fog level, and spatial distortion were investigated (§4.6.3/§4.6.4) in order to confirm its suitability for these experiments, using a Molecular Dynamics Image Plate system.

The image plate detection system collects two-dimensional patterns using the principle of photostimulable light (fig. 4.8). The surface of the image plate consists of a film of photostimulable phosphor crystals (BaFBr:Eu²⁺) combined with an organic binder.

When incident radiation falls on the plate, some electrons are excited to the conduction band of the phosphor crystals where they become trapped in bromine vacancies within the crystals, forming temporary colour centres.

| | Image Plate Parameters |
|--------------------------------------|------------------------|
| Spatial Resolution (μm) | 88 |
| Dynamic Range | 10^5 |
| Linear Range | 10^4 |
| Count Rate Limit (ph/s) | none* |
| Fog Level (ph/mm ²) | 750 |

Table 4.2: Image Plate Parameters

**Although the image plate system has no count rate limit, there is an inherent upper limit bound by the saturation level of the plate*

When red light from a 633 nm He-Ne laser falls on the phosphor, the trapped electrons are released back into the conduction band to form excited Eu^{2+} ions. These emit photostimulated luminescence (PSL) of wavelength 390 nm (blue light). The number of trapped electrons excited, and therefore the light energy emitted, is proportional to the original incident radiation intensity in that area.

The PSL is collected by a photomultiplier tube, which converts the light signal to a current. The current is converted to a linear digital voltage signal, which is stored on computer as the intensity in Scanner Units. The image plate can be erased by exposing to strong, visible white light, and reused.

4.6.3 Spatial Calibration of the Image Plate System

The scanning of the image plate introduces a significant amount of spatial distortion to the diffraction patterns which must be corrected for. To determine the extent of the spatial distortions, the image plate was exposed to a uniform x-ray source through a two dimensional grid of holes (2mm separation). The measured positions of the intensity peaks on the plate were compared with the positions of the holes in the mask [140, 146, 42].

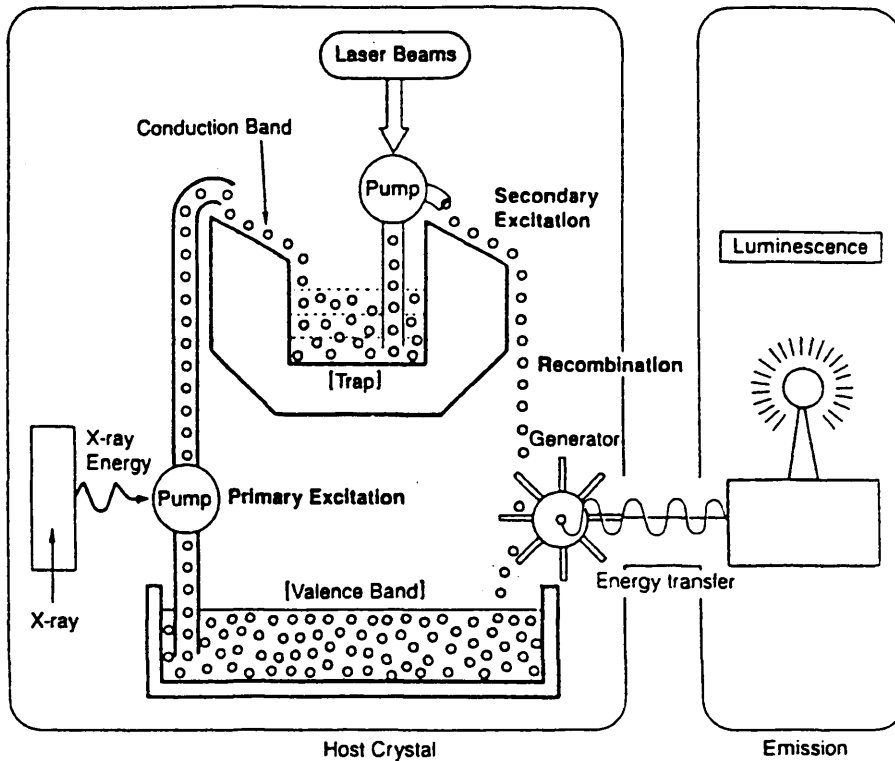


Figure 4.8: The principles of Photostimulated Luminescence [4]

Incident x-rays falling onto a surface containing $[BaFBr:Eu^{2+}]$ phosphor crystals excite electrons into the conduction band of the crystals, where they become trapped in bromine vacancies. Light from a He-Ne laser releases the electrons, which recombine with the phosphor crystals, emitting photostimulated light as they do so.

Figure 4.9 shows the displacement of the intensity peaks for each mask hole, in each of the two dimensions.

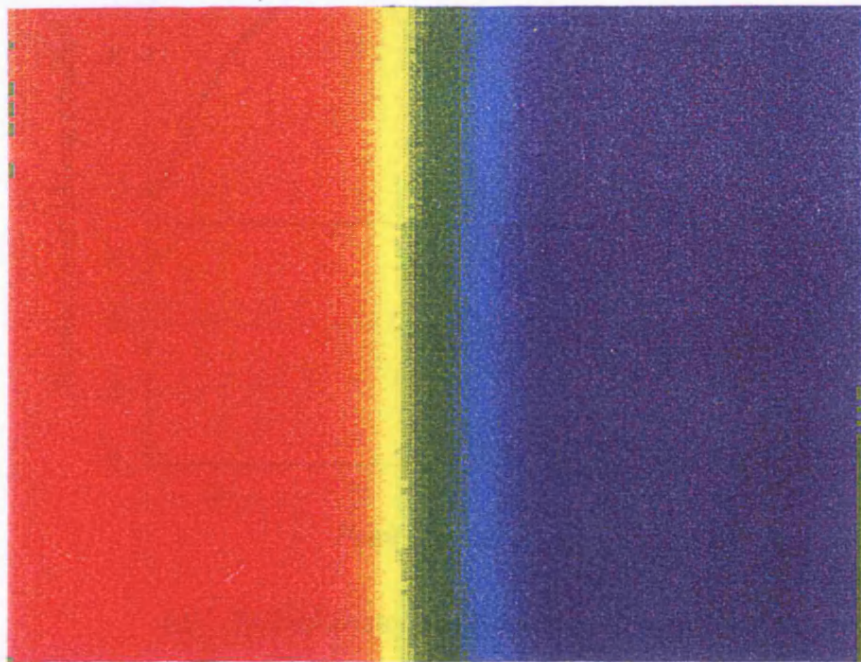
In the X-direction across the plate, the amount of displacement varies sinusoidally. It arises from the circular motion of the scanning laser as it is directed across the plate by a galvanometer controlled mirror. The exact distortion varies with time, but it is reproducible over the period of the diffraction experiments (~2 weeks). This means that a single calibration mask exposure per experiment allows the distortion to be predicted and corrected for using the FIT2D suite of programs. Typical maximum displacements are 15 x [88 μ m] pixels (fig. 4.10), which can be corrected for to better than 1 pixel.

In the Y-direction along the plate, the displacements do not follow a regular pattern, and cannot be reproduced over any length of time. This irregularity arises from the way the plate is mechanically pulled past the scanning laser/mirror arrangement. The displacement of any given peak could be as much as 5 x [88 μ m] pixels in places. So although this distortion is smaller than in the X-direction, it cannot realistically be corrected for to better than 3 pixels.

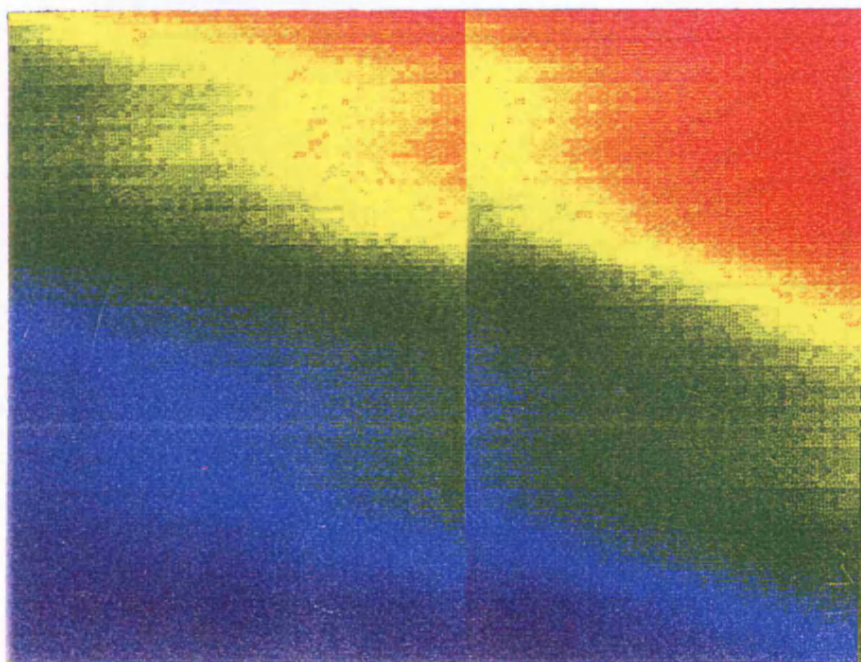
4.6.4 Determination of the Dynamic Range of the Image Plate System

The dynamic range of the image plate system is limited at the lower end by the fog level of the image plate and at the upper end by its saturation level. It is quoted as 10^5 , which is the minimum range that would collect both the strongest and weakest diffraction features from a muscle sample. This range was tested by calibrating the image plate system against an MWPC which is known to be linear over a dynamic range of 10^7 .

Both the MWPC and the image plate recorded the diffraction from a collagen sample, for a range of exposure times. The intensity of each collagen peak was calculated in photons per mm^2 for the MWPC and in Scanner Units per mm^2 for the image plate. A further standard correction transformed the Scanner Units into Molecular Dynamics Units (MDU). A plot of MDU per mm^2 against the corresponding intensity in photons per mm^2 (fig. 4.11)

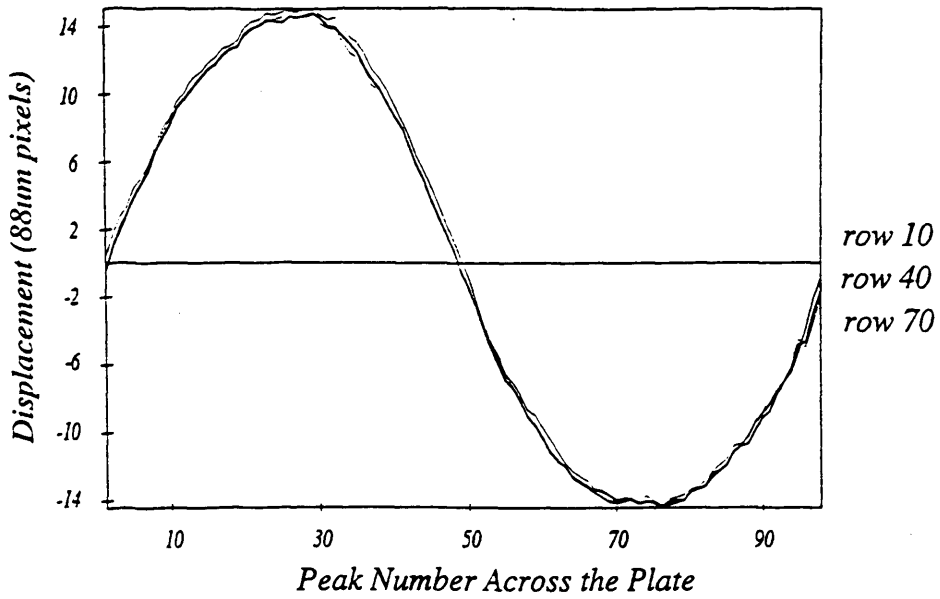


(a) Displacement of each grid point from its ideal position in the x-direction (across the plate) in $88\mu\text{m}$ pixels. Maximum Red=+15 pixels; Minimum Blue=-15 pixels



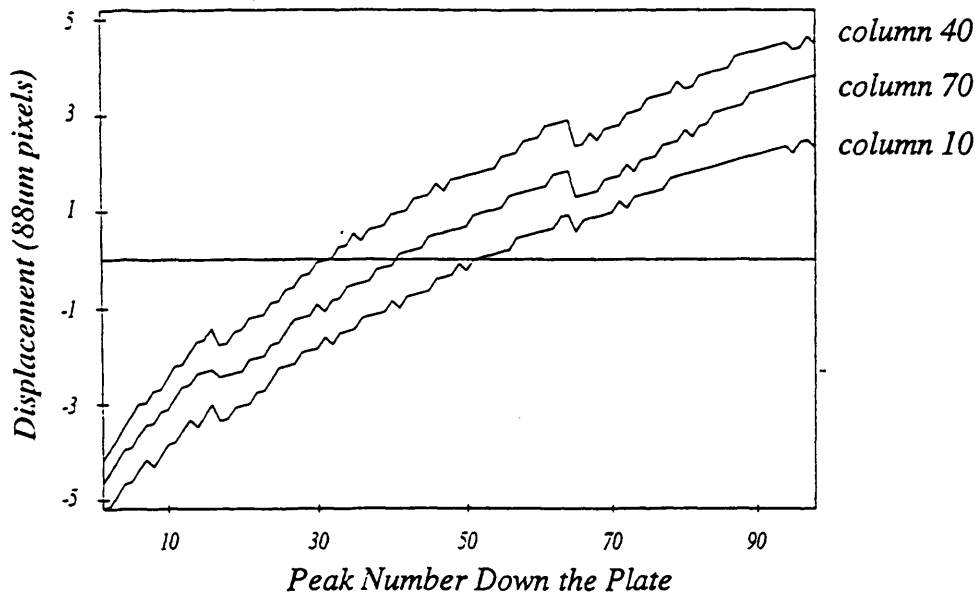
(b) Displacement of each grid point from its ideal position in the y-direction (down the plate) in pixels. Maximum Red=+5 pixels; Minimum Blue=-5 pixels.

Figure 4.9: Spatial Distortion in the Image Plate System



(a) *Spatial Distortion Across the Image Plate (x)*

The displacements are illustrated for three rows taken from the top, middle and bottom of the image plate. Their similarity indicates the reproducibility of the spatial distortion in this direction.



(b) *Spatial Distortion Down the Image Plate (y)*

The displacements are shown for three columns taken from the left, middle and right of the image plate. The distortion varies across the plate and cannot be reproduced accurately.

Figure 4.10: *Spatial Distortion in the Image Plate System*

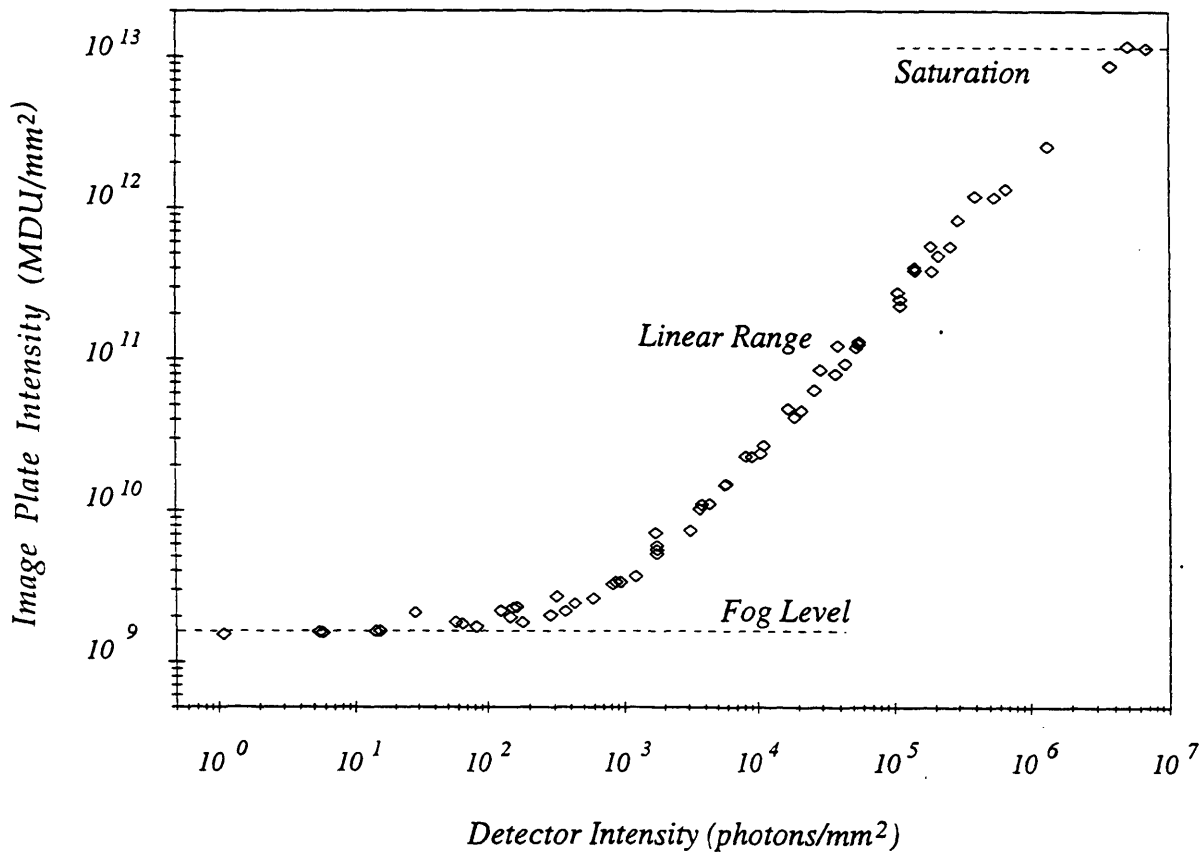


Figure 4.11: Calibration of the Image Plate

The dynamic range is limited at the bottom by a fog level of 900 ± 50 photons/mm², and at the top by a saturation level of $6.5 \times 10^6 \pm 0.5 \times 10^6$ photons/mm². The conversion factor from MDU/mm² to photons/mm², given by the gradient of the linear part of the plot, is calculated to be 1.95×10^6 MDU/photon.

clearly shows the linear range of the image plate, and the conversion factor from MDU to photons over this range.

The range as shown in figure 4.11 is only 10^4 which is much lower than the quoted $>10^5$. The discrepancy is due to the definition of dynamic range. The quoted value can be obtained if the plate is scanned at two photomultiplier tube voltages and the results combined. Research has shown that since scanning the image with a laser releases the trapped electrons the image cannot be scanned again without degradation of the stored data. This means that the image plates must be re-exposed before scanning at the higher PMT voltage, effectively doubling the exposure time required to get the same intensity compared to the MWPC.

There is a more insurmountable problem in that the fog level of the image plate is 900 ± 50 photons/mm². For most exposures, this is low enough that it does not affect the diffraction patterns. However, for the more transient states which exist for 10s of milliseconds or less, some diffraction features cannot be seen above the fog level. For this reason, those experiments which involve the transient release state (§4.7.2) used a MWPC detector, whilst higher resolution image plate data was collected for the longer lasting rest and isometric plateau states.

4.7 Experimental Procedure

4.7.1 Sample Preparation

Sartorius muscles from healthy *Rana Temporaria* frogs were dissected and clamped at the pelvic end into a perspex cell, cooled by a water bath (fig. 4.12). The muscles, typically 35mm long by 5mm wide by 2mm thick, were bathed in Ringer's solution [70] and supplied with oxygen to reproduce the natural ionic environment found inside the body. The muscles were stimulated by transmitting electrical pulses through two platinum electrodes, which ran the length of the cell to ensure even stimulation. A train of 15V square pulses at a frequency of >50 Hz applied to a fixed length muscle resulted in a fused isometric tetanus, where the tension produced reached a plateau which was considerably higher than the peak

reached by a single pulse (fig. 4.13). At this plateau a maximum number of cells within the muscle were being activated which makes it one of the most useful states to study.

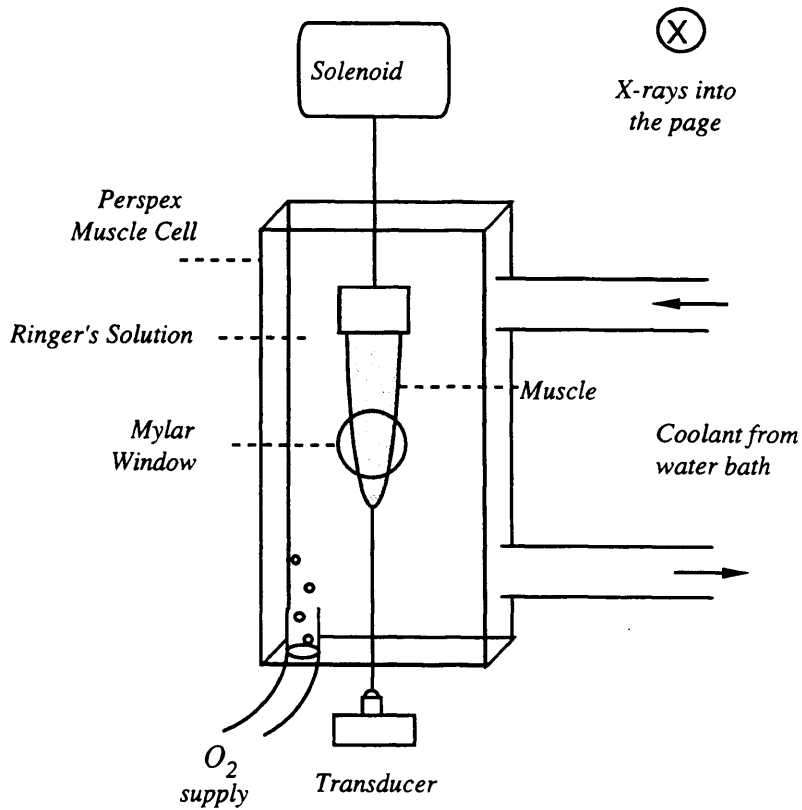


Figure 4.12: *The Muscle Environment*

The natural muscle environment is reproduced by bathing the muscle in Ringer's solution, pumping oxygen through the solution, and cooling it to 8°C with a water bath

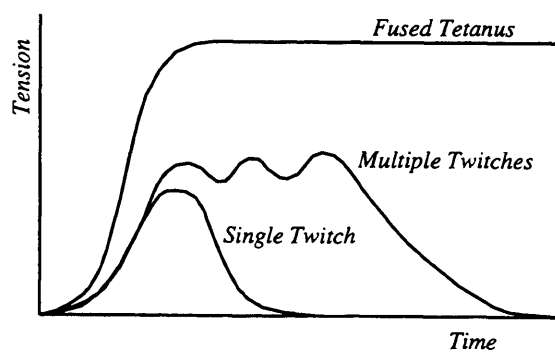


Figure 4.13: *Fused Tetanus*

Multiple twitches at a rate >50Hz produce a fused tetanus in the muscle.

The optimum temperature for these experiments was 8°C, where a smooth, flat plateau was reached within 300ms. Figure 4.14 shows the dependence of the tension development on temperature: at higher temperatures a high plateau was reached quickly but did not flatten out, whilst at lower temperatures the tension developed much more slowly to reach a lower plateau tension. The plateau continued until the stimulus was removed or the muscle became fatigued, typically after about one second. One muscle contained enough fuel reserves for hundreds of isometric contractions, provided a recovery period was allowed after each stimulation. When the peak tension had fallen to 85% of the original plateau tension, the muscle was replaced.

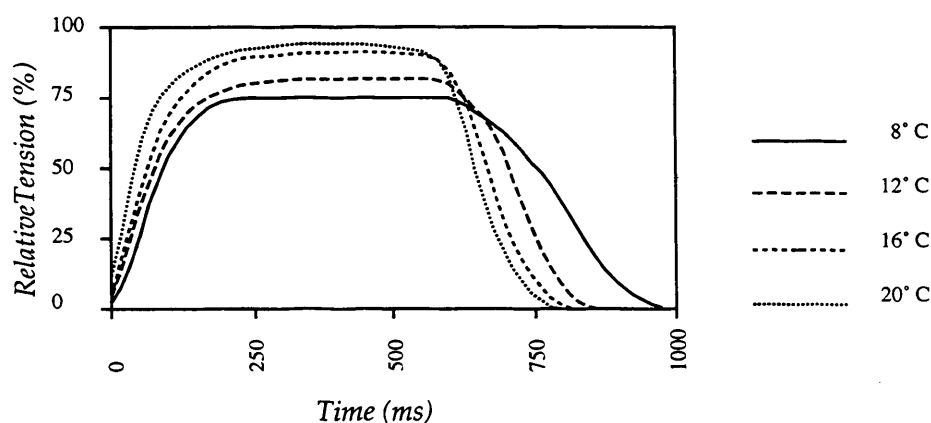


Figure 4.14: Variation of Tension Trace with Temperature

The optimum temperature is 8°C. Above this temperature an isometric contraction will not produce a flat tension trace, and at lower temperatures the muscle response is slow and it produces less tension.

The muscle cell was placed between the station shutter and the x-ray camera tube, in a frame which allowed the muscle to be positioned accurately to intercept the beam. The long axis of the muscle was vertical, and the x-ray beam passed through the thinnest dimension of the muscle, through small (1cm diameter) Mylar windows on either side of the muscle cell. The windows were much thinner than the perspex cell and allowed transmission of the x-rays without great attenuation. They were screwed in and out to allow adjustment for different thicknesses of muscle with a minimum of attenuation from the surrounding solution. The cell was oscillated vertically in the x-ray beam during contraction

to reduce radiation damage to a localised region of the muscle. In addition, a fast shutter which could block the x-ray beam in ~ 1 ms was closed whenever possible to reduce unnecessary muscle exposure when data was not being collected.

4.7.2 Diffraction Protocols

Two sets of experiments are described here, using different protocols. The first protocol involved collecting diffraction patterns from muscles at rest and during isometric contraction. The muscle was stimulated at a fixed rest length, defined by a sarcomere length of $2.3\mu\text{m}$. The sarcomere length was determined by diffraction of a He-Ne laser by the sarcomere boundaries. When isometric plateau was reached, the shutter was opened and the x-ray diffraction pattern was collected by the detector. A time frame generator synchronised the stimulation of the muscle and the opening of the fast shutter to ensure that data was collected during the required periods of the contraction.

In the second set of experiments, the muscle was allowed to reach isometric plateau as in the first protocol. A length change was then applied to the muscle during contraction. A sudden decrease in the overall muscle length of around 1mm in 1ms was applied, followed by a slower ramp of a few mm in ~ 30 ms. These macroscopic length changes correspond to 30 nm and 100 nm of shortening per half-sarcomere respectively. The tension dropped almost to rest value after the sharp length change, and then remained isotonicly close to rest during the ramp (fig. 4.15); data was collected during 15ms of this flat period. When the ramp had finished, the muscle remained at the shorter length, whilst the tension recovered to the isometric plateau value.

The required length change was programmed into a wavefunction generator to be input into a solenoid control box. The solenoid itself was attached to one end of the muscle by a vertical arm running perpendicularly between a light source and a photodiode. The amount of light detected by the photodiode depended on the exact vertical position of a small flag attached to the solenoid arm. This feedback mechanism allowed accurate determination of the solenoid position, and therefore of the muscle length, at any time. The length change

initiation was controlled by the time frame generator to ensure correct timing of the shutter operation (fig. 4.16).

The rest and plateau states were relatively static compared to the 30ms period of unloaded shortening, so many more contractions were required to get adequate statistics and good resolution patterns for this state than for either the rest or plateau states. The time frame generator stored the diffraction data collected during each state in separate memory bins, which were then added together over thousands of contractions to improve the signal to noise statistics.

The tension generated by the muscle was converted into a voltage signal for inspection on an oscilloscope, before being converted to a frequency for storage. The tension traces revealed any abnormal contractions (i.e. showing muscle slippage or fatigue) and the corresponding x-ray data were discarded.

4.8 Data Reduction

The first step in analysing the diffraction data was to determine which patterns were usable, and which should be discarded because of poor diffraction, fatigued muscles, or slippage during the contraction. The tension traces from each set of contractions were examined for any sign of an abnormal contraction, which might have been caused by slippage of the knots holding the muscle in place, or incorrect stimulation of the muscle. The diffraction patterns from the remaining contractions were examined for deterioration of data quality. The unloaded shortening tension traces were also carefully checked to ensure that the tension remained level at a value below 10% of the plateau tension during the shortening period.

The suitable two dimensional diffraction patterns were then divided by the normalised detector's response to a uniform intensity Fe^{55} source (§4.6.1) to remove any non-uniformities in the detector's intensity measurements. The spatial distortion was calculated by exposing the detector through a uniform grid of holes, as described for the image plate system in §4.6.1, and corrected using the FIT2D program [42, 141].

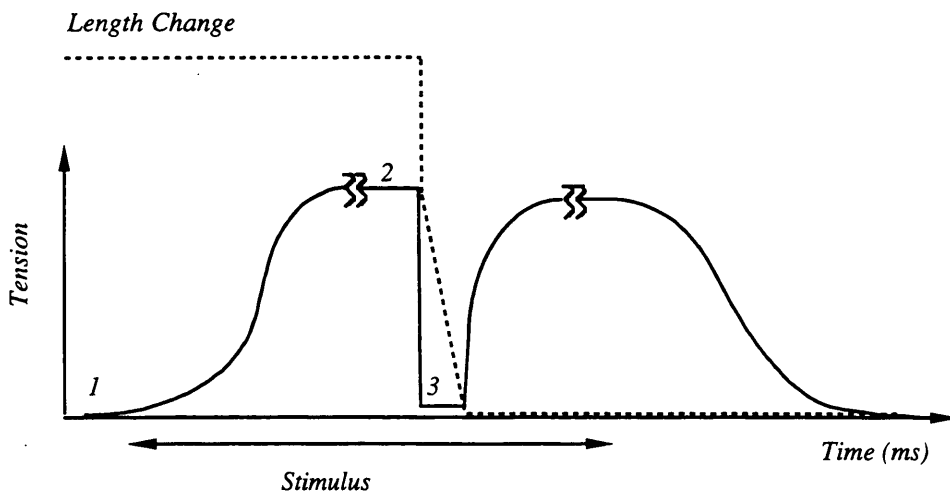


Figure 4.15: Protocol for Length Change Experiments

Shutter is open to collect diffraction data at the following points during the contraction cycle:

- 1: Rest pattern*
- 2: Isometric contraction pattern*
- 3: Unloaded shortening pattern*

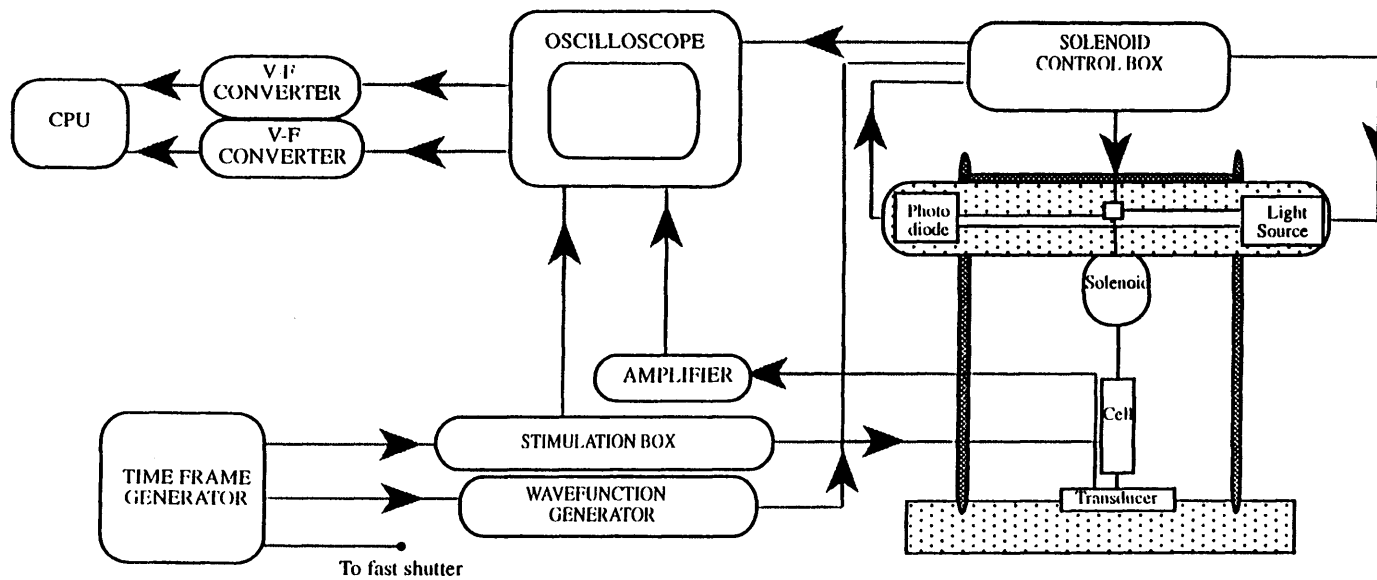


Figure 4.16: Simultaneous Tension Measurement and X-Ray Diffraction Equipment

Once the individual patterns were corrected, they had to be summed to give a total for each muscle state; data manipulation was carried out using the BSL [9] and OTOKO [97] programs. Small changes in the orientation of the muscle from one sample to another occurred despite precautions taken to mount all samples vertically, and the corresponding patterns were rotated about their centres until the correct vertical orientation was obtained. The centres of the rotated patterns were accurately determined and the 2D patterns shifted until all centres coincided.

The patterns were then normalised, so that the relative contributions from each muscle were equal. The patterns were added together to produce a single diffraction pattern for each of the three states: rest, isometric plateau, and unloaded shortening. The sloping background was subtracted from these three patterns using the CCP13 program TBACK [24] to reveal the actual data arising from the molecular arrangement within muscle. The resulting patterns were ready for detailed analysis, as described in the next chapter.

Chapter 5:

Results - Diffraction Patterns

5.1: Introduction

5.2: Rest Data

5.2.1: Myosin Reflections

5.2.2: Actin Reflections

5.2.3: Other Reflections

5.3: Isometric Contraction Data

5.4: Unloaded Shortening at Zero Tension Data

5.5: Summary

5.1 Introduction

The data presented in this chapter were obtained from the x-ray diffraction experiments described in Chapter 4, and have undergone elementary data reduction. The two dimensional patterns are shown in figure 5.1 for the three key states: rest, peak of isometric contraction and unloaded shortening.

Unless otherwise stated, all spacing measurements are subject to a maximum error of $\pm 2\%$. Although the percentage reading error decreases at larger spacings, this is offset by the increased difficulty in determining the centre of the peaks themselves which broaden due to disorder effects; thus the overall error remains approximately constant.

One dimensional intensity plots were produced from the two dimensional patterns by integrating in radial and axial directions as illustrated in figure 5.1(c). Radial integration over the meridional region produces a one dimensional plot illustrating the meridional intensity distribution. A similar radial integration over a region parallel to the meridian but shifted to cover the [10] and [11] equatorial reflections illustrates the relative intensities of the layer lines. Axial integration over a particular layer line produces the intensity profile along that layer line.

5.2 Rest Data

Relaxed frog skeletal muscles produce a very distinctive diffraction pattern, the origins of which are discussed in Chapter 3. The main feature is a series of layer lines arising from the helical distribution of myosin heads in the thick filaments. Another set of layer lines is produced by the helical arrangement of actin monomers in the thin filaments. Both sets of layer lines are sampled by peaks arising from Bragg scattering off the planes in the filament lattice. Other reflections come from lesser components of the muscle structure, such as troponin, tropomyosin, and C-protein.

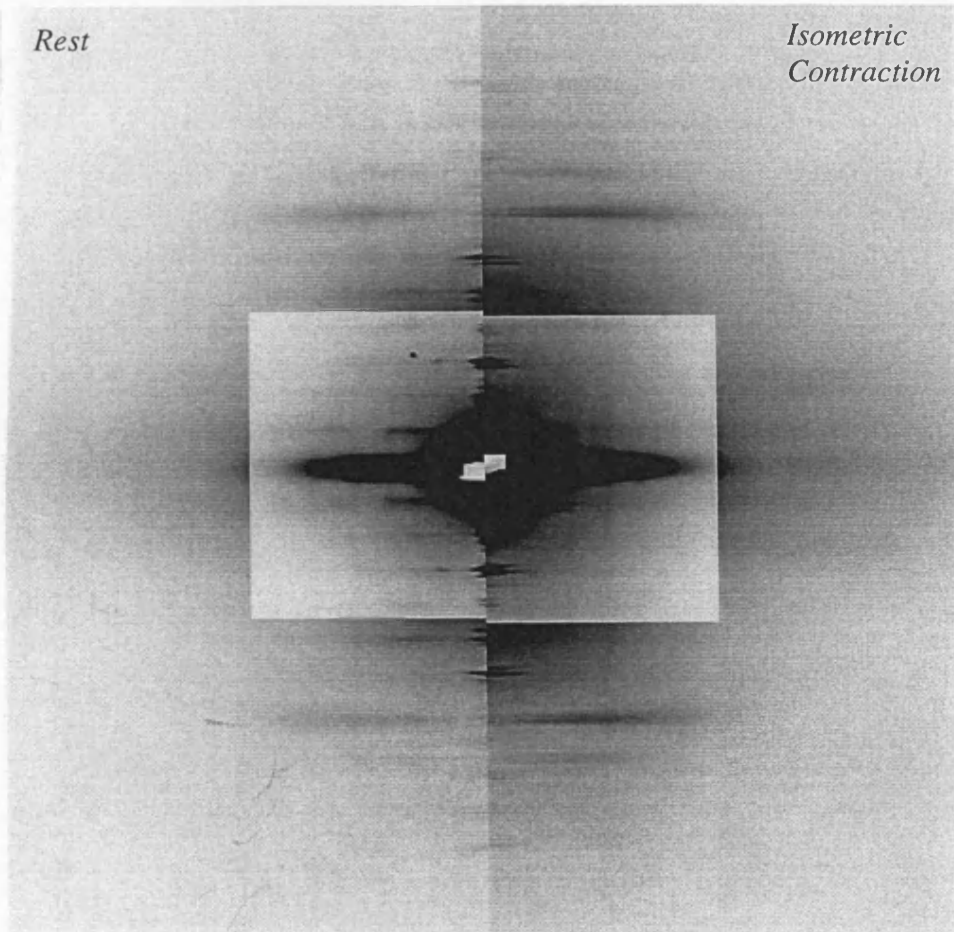


Figure 5.1: Two-Dimensional Diffraction Patterns

(a) From muscle at rest (left) and during the peak of isometric Contraction (right).



Figure 5.1: Two-Dimensional Diffraction Patterns

(b) From muscle at rest (left) and during unloaded shortening at zero tension (right).

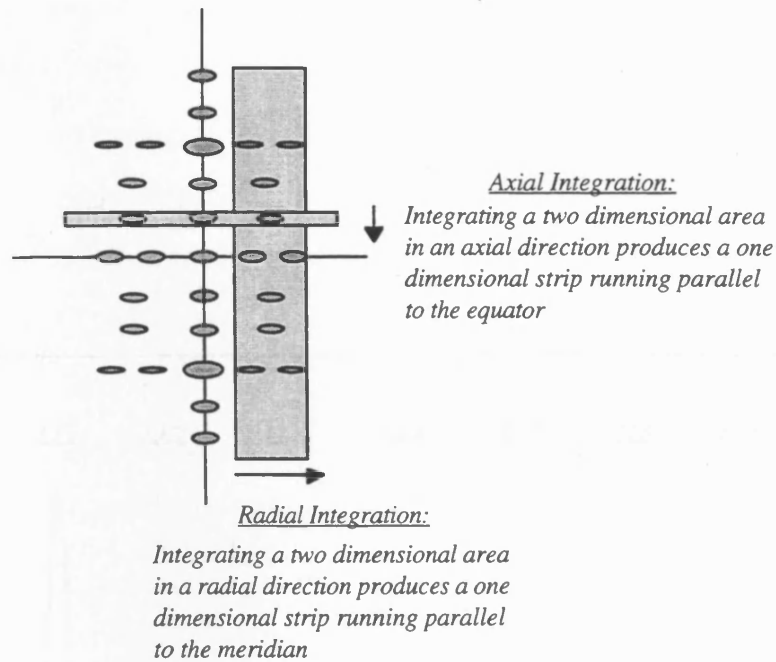


Figure 5.1(c): Integration of the Two Dimensional Patterns

Radially integrated strips illustrate the intensity distribution along the meridian and the relative intensities of the layer lines. Axially integrated strips illustrate the intensity profiles along the equator or the layer lines.

5.2.1 Myosin Reflections

The series of regularly spaced layer lines attributed to scattering from the myosin heads in the thick filaments appear at axial intervals of $1/42.9 \text{ nm}^{-1}$: radial integration of an axial strip through the layer lines in the region of the [10] equatorial reflection shows their relative intensities (fig. 5.2). The 1st layer line at $1/42.9 \text{ nm}^{-1}$ (LL1) and the meridional reflection of the 3rd layer line at $1/14.3 \text{ nm}^{-1}$ (3M) are particularly strong. Although the very distinct low angle pattern reveals a high degree of structural order exists, the pattern weakens towards higher spacings (i.e. above $1/5 \text{ nm}^{-1}$) indicating some disorder must be present in the myosin head distribution.

A triple helix with an effective pitch of 42.9 nm and an axial translation of 14.3 nm would be expected to produce a series of layer lines separated by $1/42.9 \text{ nm}^{-1}$, with meridional reflections only appearing at spacings of $1/14.3 \text{ nm}^{-1}$. Radial integration of an axial strip between the iso-intensity points on either side of the third myosin meridional

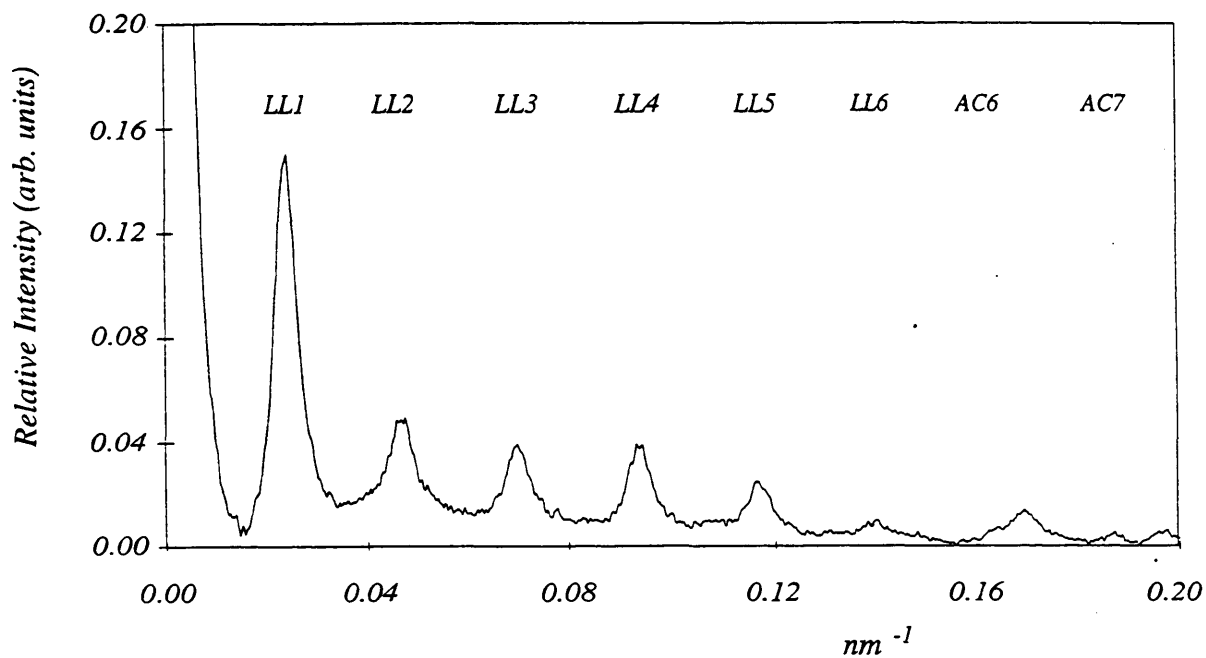


Figure 5.2: Radially Integrated Strip Running Parallel to the Meridian in the Region of the [10] and [11] Equatorial Reflections of the Rest Pattern

The myosin layer lines labelled LL1 etc. are clearly visible at $1/42.9 \text{ nm}^{-1}$ intervals. The sixth and seventh actin layer lines labelled AC6 and AC7 appear at $1/5.9 \text{ nm}^{-1}$ and $1/5.1 \text{ nm}^{-1}$ respectively.

reflection clearly shows the presence of significant meridional reflections at additional spacings of $1/42.9 \text{ nm}^{-1}$ (fig. 5.3).

The unexpected meridional reflections indicate that the 14.3nm axial translation is not perfectly held throughout the myosin helix. A random distortion in the axial translation would redistribute intensity from the $1/14.3 \text{ nm}^{-1}$ peak into the background, whilst a regular distortion repeating at 43nm intervals would contribute to the meridional reflections at $1/42.9 \text{ nm}^{-1}$, as observed. This suggests that the perturbation can be visualised in terms of a distortion group of three myosin head levels, within which the axial rise is distorted from, but averages out to, 14.3nm; the distortion group itself is repeated at 42.9nm intervals along the myosin helix.

The width of the myosin meridional reflections is a measure of the extent over which the myosin heads are kept in close order. The heads are held in register over a range of hundreds of nm; the 3M axial width corresponds to $\sim 1000\text{nm}$, and the radial width to $\sim 400\text{nm}$. The axial width of the myosin layer lines similarly indicates that helical order is maintained over $\sim 500\text{nm}$. The meridional reflections are axially sampled by an interference function which arises from interference between the myosin heads in each half of the sarcomere; the separation of the two sets of heads across the M-line is of the order of 900 nm [70].

Axial integration of a radial strip between the iso-intensity points on either side of the [10] equatorial reflection reveals the equatorial profile. The reflections from the [10] and [11] lattice planes appear at radial spacings of $1/36.0 \text{ nm}^{-1}$ and $1/20.8 \text{ nm}^{-1}$ (fig. 5.4), representing the respective interplanar separations d_{10} and d_{11} . The hexagonal lattice spacing is calculated to be 41.6 nm using the relationships:

$$d_{10} = \frac{\sqrt{3}}{2} a \quad \text{and} \quad d_{11} = \frac{a}{2}$$

Whereas the different helical repeats of the thick and thin filaments allow the two sets of layer lines to be separated easily, the equatorial reflections are the result of the mass distribution in the lattice plane, and are affected by both the actin and myosin filament

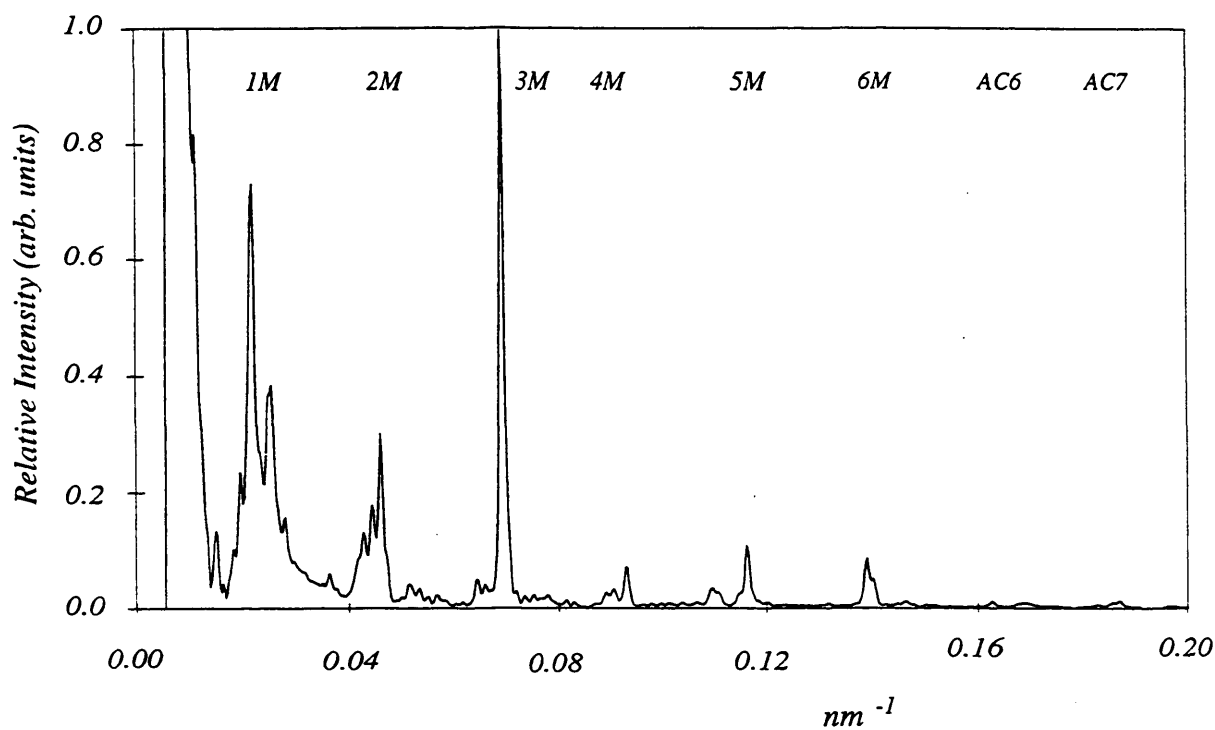


Figure 5.3: A Radially Integrated Strip along the Meridian of the Rest Pattern

The myosin meridional reflections labelled 1M etc. are clearly visible at $1/42.9 \text{ nm}^{-1}$ intervals. The sixth and seventh actin meridional reflections labelled AC6 and AC7 appear at $1/5.9 \text{ nm}^{-1}$ and $1/5.1 \text{ nm}^{-1}$ respectively.

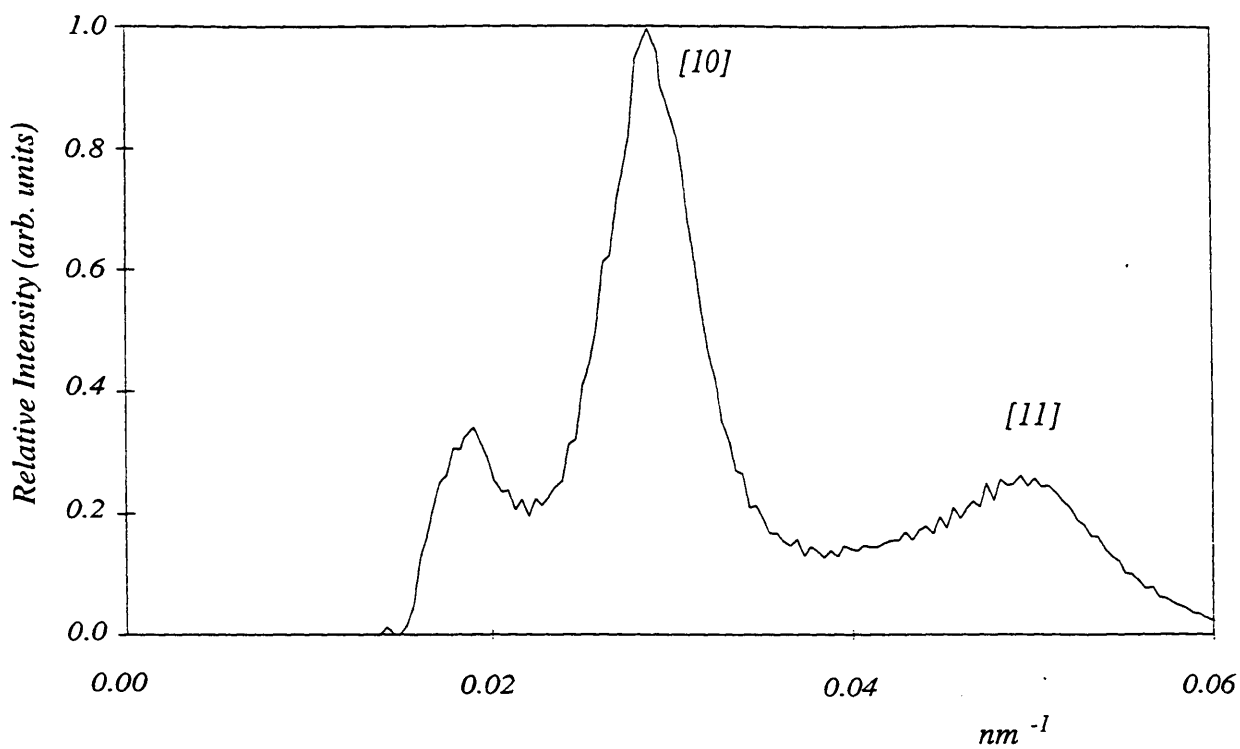


Figure 5.4: An Axially Integrated Strip Along the Equator of the Rest Pattern

The [10] and [11] lattice reflections appear at spacings of $1/36.0$ and $1/20.8 \text{ nm}^{-1}$ respectively (simple unit cell notation is used throughout this work as described in Chapter 3.)

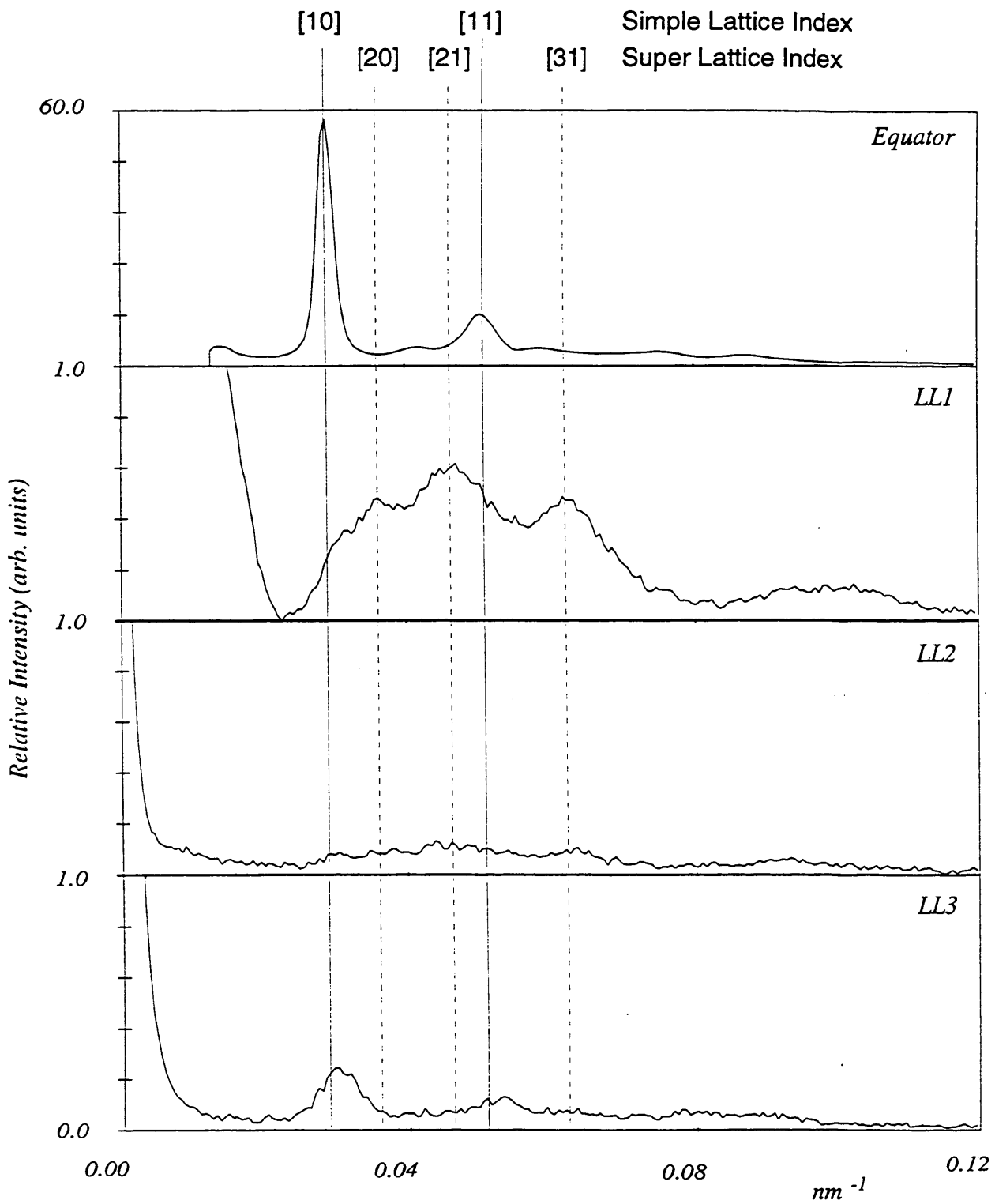


Figure 5.5: Myosin Layer Line Profiles at Rest

The Bragg peaks on the first and second myosin layer lines are different to those on the equator and the third layer line, illustrating the presence of a superlattice arrangement in the muscle lattice. The main reflections are indexed as described in table 5.1.

distributions. The [10] peak reflects the amount of mass at the thick filament sites, and the [11] peak reflects the mass at both sets of filaments (§3.5.2).

The myosin layer line profiles, obtained by axial integration of the corresponding layer lines (fig. 5.5), clearly illustrate the positions of the lattice sampling peaks on the different layer lines; the peaks on the third layer line coincide with those on the equator, but are at different spacings to the peaks on the first and second layer lines (and the fourth and fifth - data not shown) (table 5.1). A simple hexagonal lattice structure would produce the same sampling peaks on all layer lines, so the different sampling distributions indicate the presence of a superlattice structure which is undetectable in certain projections (i.e. the equatorial projection).

| Simple Lattice Index | Super Lattice Index | Calculated Spacing (nm) | Measured Peak Position (nm) | |
|----------------------|---------------------|-------------------------|-----------------------------|------------------|
| | | | Equator | Layer Line 1 |
| 10 | 10 | 62.4 | | |
| | 11 | 36.0 | 35.9 | 36.4 <i>weak</i> |
| | 20 | 31.2 | | 30.6 |
| | | | 25.1 | |
| 11 | 21 | 23.6 | | 23.4 |
| | 30 | 20.8 | 21.0 | |
| 20 | 22 | 18.0 | 17.9 <i>weak</i> | |
| | 31 | 17.3 | | 17.2 |
| | 40 | 15.6 | | |
| 21 | 41 | 13.6 | 14.1 <i>weak</i> | |
| | 50 | 12.5 | | |
| 30 | 33 | 12.0 | 12.3 <i>weak</i> | |

Table 5.1: Indexing of Layer Line Sampling Peaks

The calculated spacings are determined for a lattice with a myosin-myosin nearest neighbour separation of 41.6nm. Those measurements marked 'weak' are estimated positions of the centre of the reflection.

The sampling peaks on the equator can be indexed on a simple hexagonal unit cell of side 41.6 nm, whereas the peaks on the first layer line can only be indexed on a larger unit cell of side 72.1 nm, $\sqrt{3}$ times the simple unit cell side; table 5.1 indexes the sampling peaks from both lattices in terms of lattice planes. The superlattice is not maintained beyond a few unit cell repeats, as indicated by the diffusion of the sampling peaks with higher layer line number. Since the equatorial reflections are the product of the projection of the muscle lattice

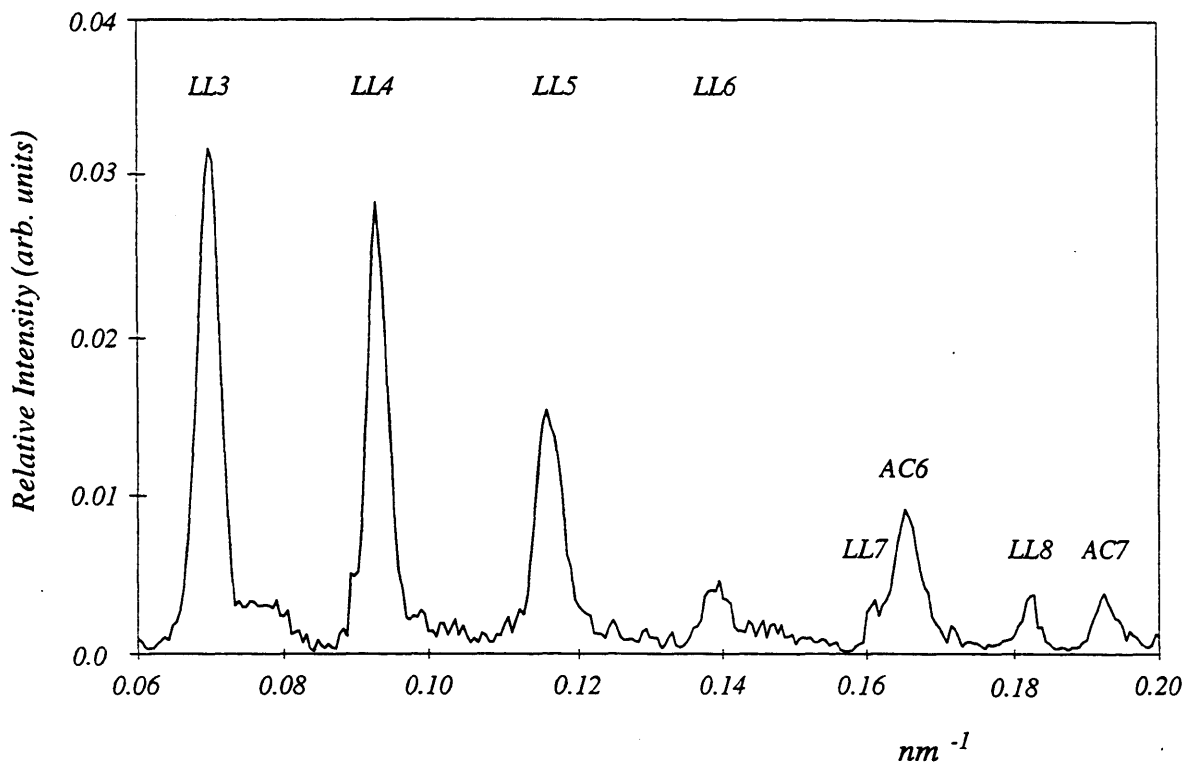


Figure 5.6: Radially Integrated Strip Running Parallel to the Meridian in the Region of the [10] and [11] Equatorial Reflections of the Rest Pattern

The sixth actin layer line (AC6) at $1/5.9 \text{ nm}^{-1}$ closely overlaps the seventh myosin layer line (LL7) at $1/6.1 \text{ nm}^{-1}$. The seventh actin layer line (AC7) appears at $1/5.1 \text{ nm}^{-1}$.

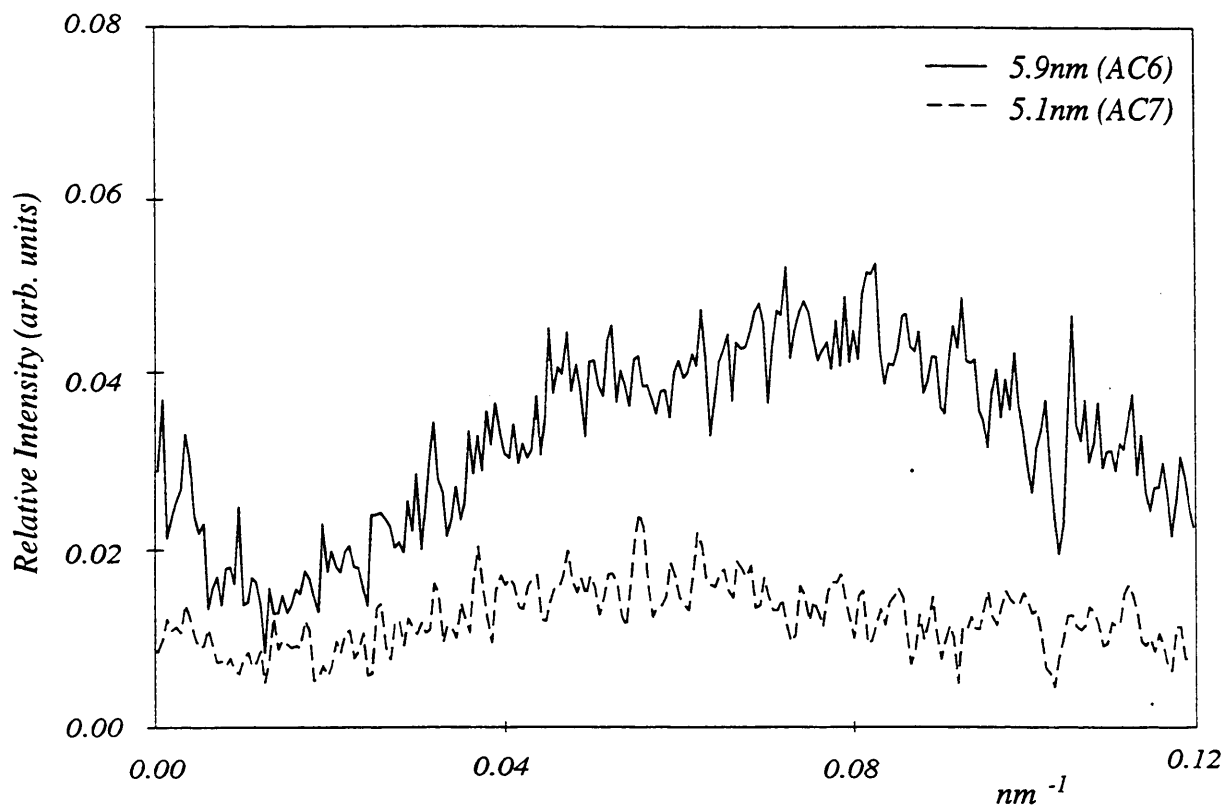


Figure 5.7: Actin Layer Line Profiles at Rest

The sixth and seventh actin layer lines are faint in comparison to the first six myosin layer lines, resulting in a lower signal to noise ratio as seen here.

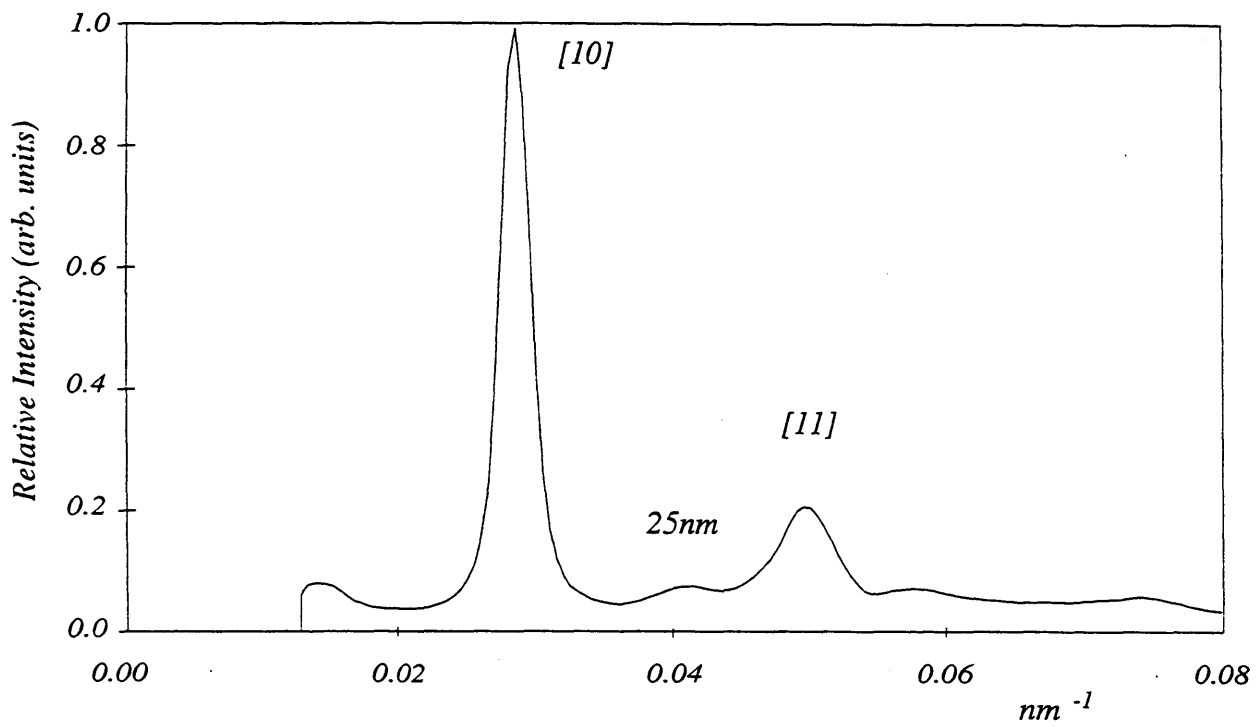


Figure 5.8: Rest Equator Showing Peak due to Square Lattice

An extra peak is observed in some muscle samples: the peak appears at $\sim 1/25 \text{ nm}^{-1}$, and corresponds to the spacing of the square lattice which the thin filaments form near the sarcomere Z-line. The example shown here was produced by a single muscle sample.

along the filament axis, the fact that the equatorial plot gives no indication of the larger unit cell reveals that whatever the non-identical factor is between the nearest neighbour filaments, it must be undetectable in this end-on view, which suggests an axial displacement or rotation between filaments.

The fact that the Bragg peaks are still clearly present on the third layer line indicates that a considerable amount of three-dimensional ordering is maintained in the myosin filament lattice, both in axial register and orientation.

5.2.2 Actin Reflections

The actin layer lines observed in the rest pattern can be indexed on a helix of pitch $\sim 36\text{nm}$, which is the effective pitch of the double actin helix. Radial integration of an axial strip in the region of the [11] reflection shows that the strongest layer lines as indexed on this helix are the sixth at an axial spacing of $1/5.9\text{nm}^{-1}$ and the seventh at $1/5.1\text{nm}^{-1}$ (fig. 5.6). The first actin layer line at $1/36\text{nm}^{-1}$ closely overlaps the first myosin layer line at $1/43\text{nm}^{-1}$, which makes it difficult to determine its position and profile accurately.

The strong sixth actin layer line arises from the left-handed genetic helix of pitch 5.9nm , and its peak at 0.08nm^{-1} corresponds to a J_1 Bessel function of radius 3.5nm (fig. 5.7). Similarly, the seventh layer line arises from the alternative right-handed genetic helix of pitch 5.1nm .

There is no evidence of radial sampling of the actin layer lines, possibly because of the presence of large amounts of disorder in the actin filament lattice. The actin filaments are lighter and more flexible than the myosin filaments, and it is likely that they will be more easily displaced from their ideal lattice positions than the thick filaments; especially when the gradual change from square (Z-disk) to hexagonal (A-band) thin filament lattices is considered.

Several individual muscles gave rise to an additional equatorial reflection at a radial spacing of $\sim 25\text{nm}$, believed to arise from the thin filament lattice near the Z-line: in this region the thin filaments occupy a square lattice of side 26nm [174, 70]. This reflection is not evident in all diffraction patterns, but only particularly clear examples (fig. 5.8).

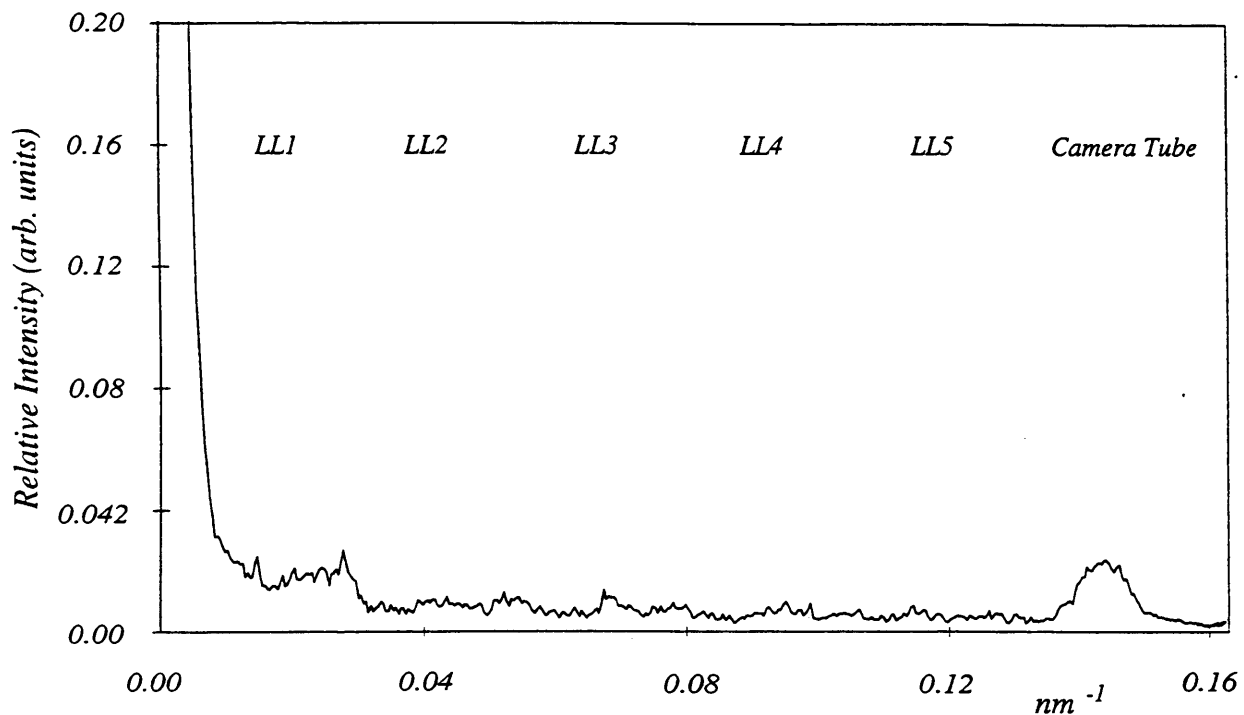


Figure 5.9: A Radially Integrated Strip Running Parallel to the Meridian in the Region of the [10] Equatorial Reflection Taken at the Peak of Isometric Contraction

The positions of the first five myosin layer lines appearing in the pattern from rest muscle are indicated. During isometric contraction the myosin layer lines all but disappear, leaving a trace of the first layer line which is too diffuse to accurately place. The large peak at $\sim 0.145\text{nm}^{-1}$ is an artefact arising from the edge of the camera tube in this particular set of experiments.

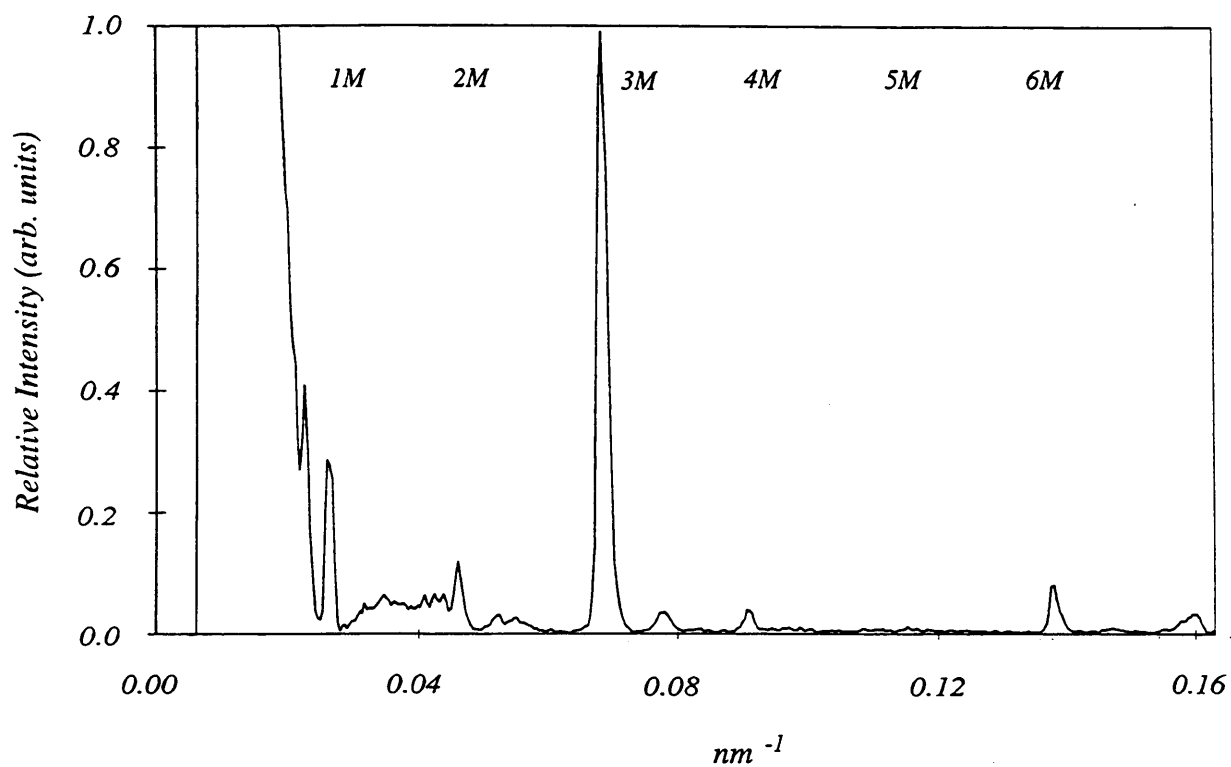


Figure 5.10: A Radially Integrated Strip along the Meridian of the Peak of Isometric Contraction Pattern

The positions of the myosin meridional reflections in rest muscle are indicated (nm). During isometric contraction the third (3M) and sixth (6M) meridional reflections remain strong, but the forbidden reflections (1M, 2M, 4M, 5M) all but disappear.

5.2.3 Other Reflections

A series of meridional reflections which occur at spacings of $1/44.2 \text{ nm}^{-1}$ is attributed to the distribution of C-protein within the thick filaments [125]. An interference function between the two sets of C-protein molecules in either half of the sarcomere samples the C-protein peaks by $1/710 \text{ nm}^{-1}$.

A further series of meridional reflections is attributed to the axial distribution of the troponin molecules in the thin filaments. The reflections index onto an axial repeat of 38.2nm. Similarly, the tropomyosin molecules give rise to a series of layer lines corresponding to the helical arrangement of the molecules, with a pitch of 38.2nm.

5.3 Isometric Contraction Data

The obvious change between the patterns from rest muscle and muscle contracting isometrically is the complete loss of three dimensional helical order evidenced by the loss of the off-meridional myosin layer lines (fig. 5.9). A faint first layer line remains, but it is too diffuse to accurately determine its spacing.

Along the meridian, the forbidden reflections all but disappear, leaving just the 3M and 6M peaks (fig. 5.10). This indicates that the regular distortion which gave rise to the forbidden meridionals is almost completely removed, but does not necessarily mean that the thick filaments become more ordered. When taken with the overall loss of helical order in the whole pattern, it is more likely to represent the conversion of the regular distortion into a random disorder. This would also have the effect of broadening the meridional reflections axially, which is indeed observed; the axial width of the 3M and 6M meridional reflections almost double when compared to the corresponding widths at rest, indicating that the myosin head order is now maintained over a much smaller axial length. The large increase in the radial widths of the 3M and 6M peaks also point to the loss of helical order in the myosin head arrangement.

The myosin meridional peaks also change their axial spacings to reflect a new axial repeat of $\sim 14.5 \text{ nm}$ (fig.5.11). In fact, the 3M peak can be split into a doublet at $1/14.4 \text{ nm}^{-1}$

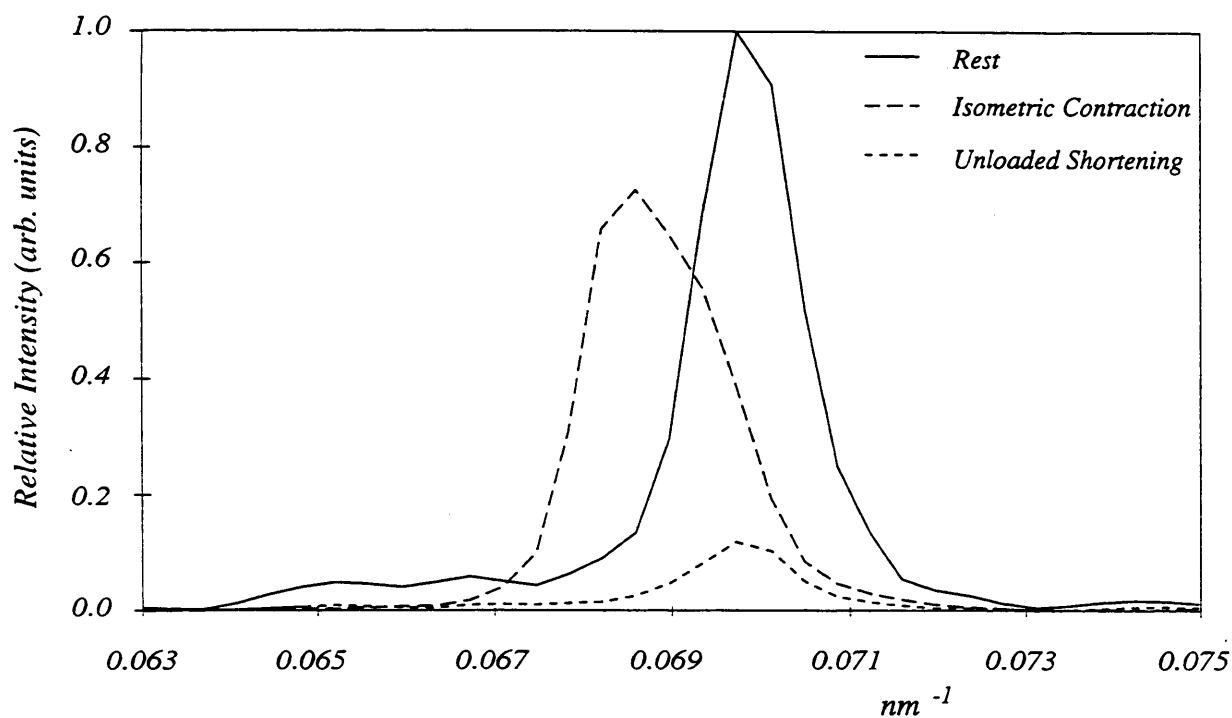


Figure 5.11: A Comparison of the Third Myosin Meridional in Different Muscle States

The third myosin meridional reflection appears at $1/14.3\text{nm}^{-1}$ in rest muscle. During isometric contraction the peak widens and shifts to a spacing of $1/14.5\text{nm}^{-1}$: sampling of the wider peak results in the formation of two peaks at $1/14.4\text{nm}^{-1}$ and $1/14.6\text{nm}^{-1}$. During unloaded shortening, the third myosin meridional returns to a single peak at a spacing of $1/14.3\text{nm}^{-1}$, but with a much lower intensity.

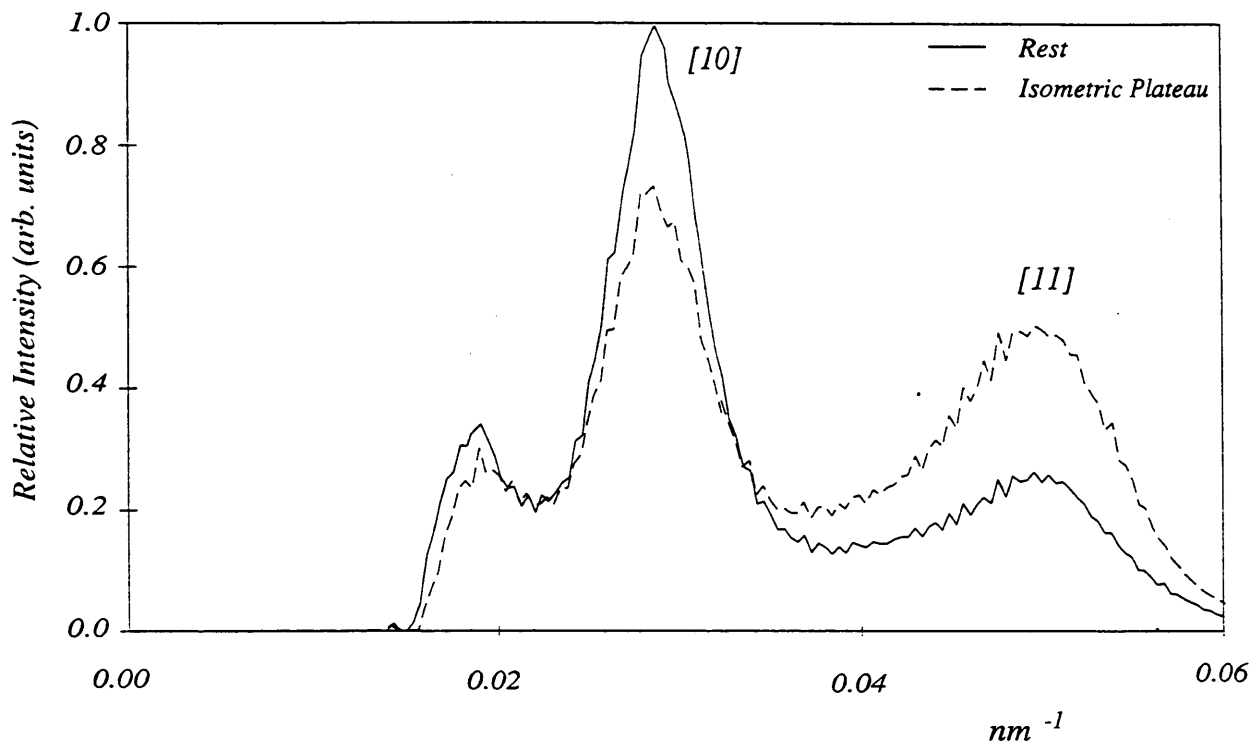


Figure 5.12: The Equatorial Intensity Reversal at During Isometric Contraction

At the peak of isometric contraction the intensity of the [10] equatorial reflection decreases relative to its intensity at rest, and the [11] reflection increases relative to its rest value.

and $1/14.6 \text{ nm}^{-1}$, probably due to sampling of the now much broader meridional reflection by the myosin head interference function.

On the equator, the [10] and [11] lattice reflections change both in intensity and position. The spacing change is small, and is due to the constant volume of the muscle; as it shortens its length, which happens a little even in isometric contractions because of the compliance of the muscle tendon, the lattice swells to maintain a constant volume. Conversely, the intensity change is considerable; the [10] reflection decreases whilst the [11] reflection increases, resulting in a reversal of relative intensity (fig. 5.12). At rest the ratio of $I_{10}:I_{11}$ is 3.0, compared to 1.2 during isometric contraction. The interpretation of this reversal is that mass has been transferred from the thick filaments, which contribute to both sets of planes, to the thin filaments, which contribute to just the [11] planes.

There are equally important, if less dramatic, changes in the thin filament pattern during isometric contraction. The sixth and seventh actin layer lines increase in intensity, which can be taken in consideration with the equatorial intensity reversal to indicate that myosin heads are moving away from the thick filaments towards the thin filaments and binding, thus increasing the mass taking the actin helix repeat, and the corresponding intensity of the thin filament layer lines. The helical order of the thin filaments is fairly well maintained, since the actin layer lines are still present.

During contraction the left handed actin helix is actually twisted a little more tightly than at rest, modifying the 5.9nm helix from an 80/37 helix (2.162 subunits per turn) at rest to a 54/25 helix (2.16 subunits per turn) at isometric plateau, and the right handed helix untwists to change the 5.1nm helix to a 54/29 helix (1.86 subunits per turn). This change is probably triggered by the binding of Ca^{2+} ions to the troponin upon activation [159]. The modified actin axial rise is then commensurate with the myosin repeat.

The C-protein and troponin meridional reflections are maintained during isometric contraction, though their intensities are slightly decreased, probably due to general disorder in the filament arrangement.

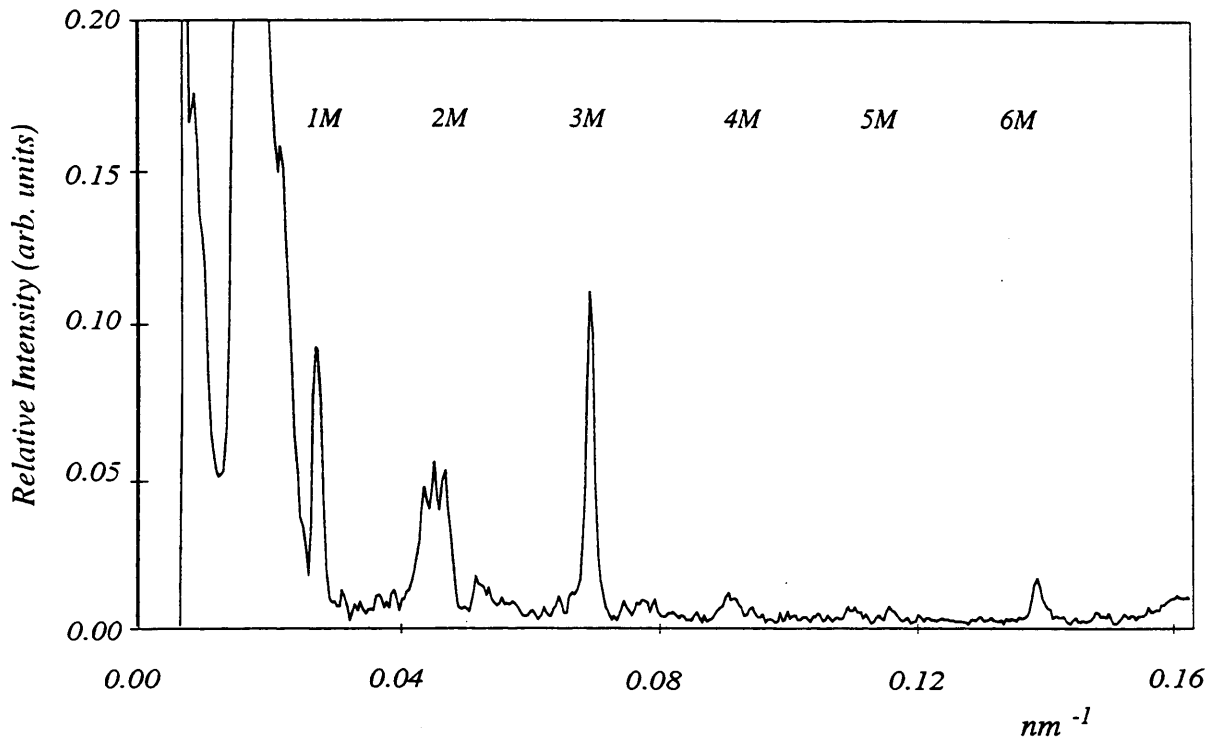


Figure 5.13: A Radially Integrated Strip along the Meridian of the Unloaded Shortening Pattern

The positions of the myosin meridional reflections in rest muscle are indicated (nm). During unloaded shortening the meridional intensity distribution is very similar to the meridian from rest muscle, though the overall intensity is greatly decreased relative to the rest meridian.

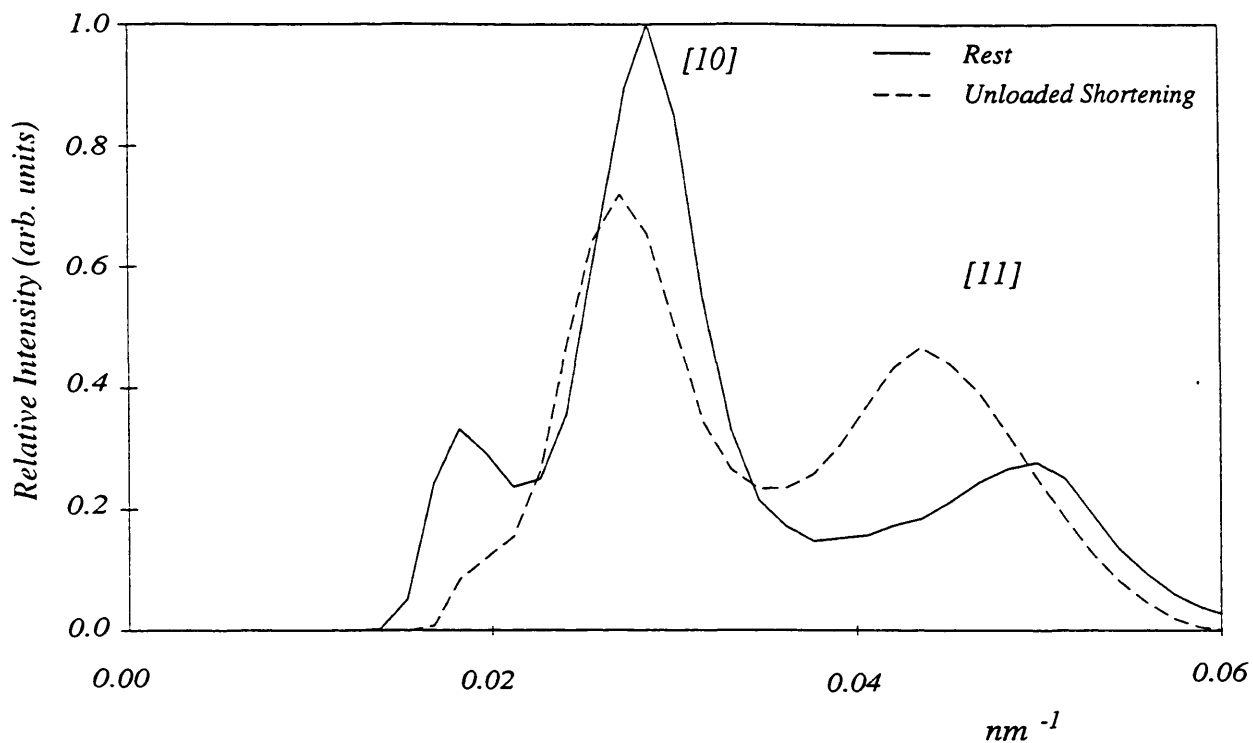


Figure 5.14: Changes in the Equatorial Reflections During Unloaded Shortening

During unloaded shortening the equatorial reflections recover some way towards the rest intensity distribution, which was reversed during the peak of isometric contraction. The [10] and [11] reflections also move to larger spacings as the conservation of muscle volume causes the hexagonal lattice of the shortening muscle to increase its spacing.

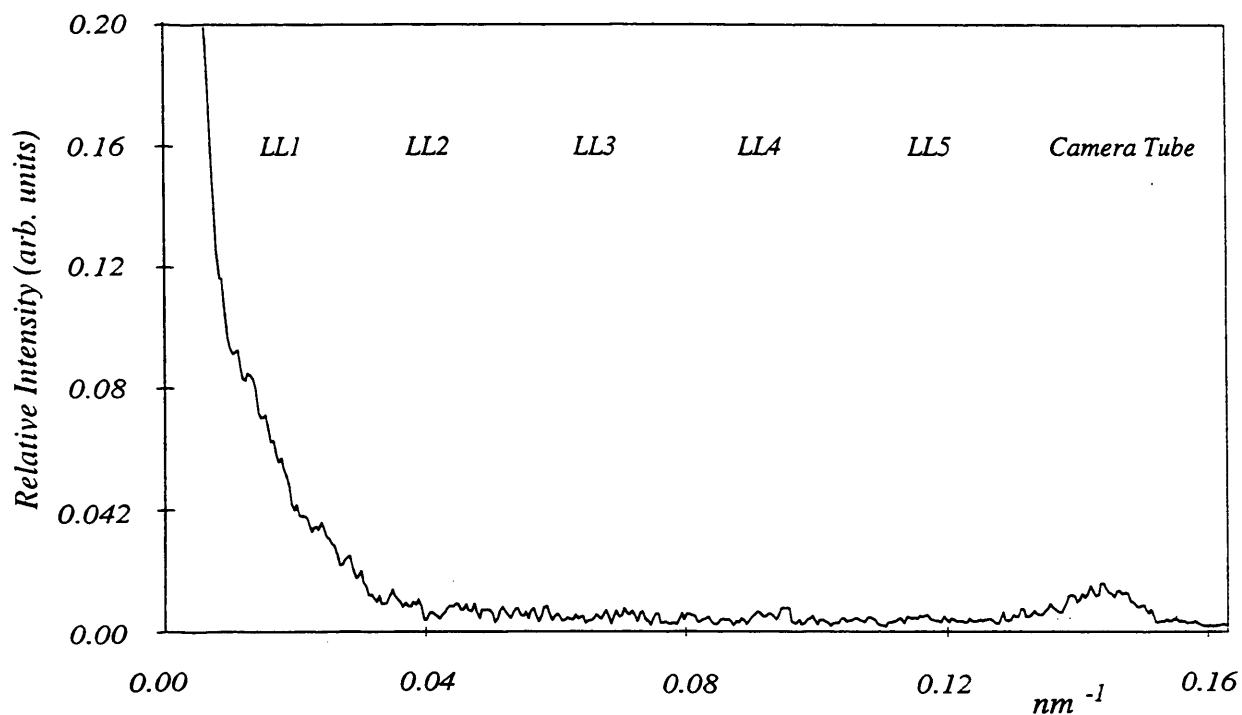


Figure 5.15: A Radially Integrated Strip Running Parallel to the Meridian in the Region of the [10] Equatorial Reflection Taken During Unloaded Shortening of the Muscle.

The positions of the first five myosin layer lines appearing in the pattern from rest muscle are indicated. During unloaded shortening there is no trace of the myosin layer lines. This could in part be because of the lower signal to noise ratio arising from the shorter exposure times required to capture this transient state, although the layer lines would have to be very faint to fall below the noise level. The peak at $\sim 0.145\text{nm}^{-1}$ is an artefact arising from the edge of the camera tube in this set of experiments.

5.4 Unloaded Shortening at Zero Tension Data

The unloaded shortening diffraction pattern represents the average structure of the muscle during the 30ms of data collection where the tension produced remained level at approximately zero. It should be noted that the total exposure of the unloaded shortening state is just 1/20 of the total exposure of the rest state, because of the difficulty in maintaining near-zero tension for any length of time. Therefore the statistics for the unloaded shortening pattern are poorer than for the rest or isometric contraction patterns.

The diffraction pattern from muscle which is shortening at zero tension combines features from both the rest and isometric contraction patterns. The meridional region of the pattern closely resembles the rest pattern meridian, albeit with a much lower intensity, whilst the lack of layer line structure in the off-meridional pattern follows the isometric contraction case.

During unloaded shortening the meridional reflections largely return to the rest distribution, complete with forbidden meridionals (fig. 5.13). The third myosin meridional, which moved to a larger spacing of $1/14.58 \text{ nm}^{-1}$ during isometric contraction, returns to a single peak at $1/14.34 \text{ nm}^{-1}$, and the relative intensities of all the myosin meridionals return to the rest ratios. However, the absolute intensity of the meridional reflections falls to a fraction (~ 0.1) of the rest meridian, probably due to axial displacement of the filaments caused by the rapid shortening of the muscle. In addition, the troponin reflection at 38.2 nm which is prominent in the rest meridian disappears, to be replaced by a new peak at 36.4 nm (1T). The new peak, scaled to the 3M reflection, is more intense than the rest reflection at 38.2 nm , though it is likely that its origin is still the troponin/tropomyosin complex.

The [10] and [11] equatorial reflections return some way towards the intensity ratio present at rest, and stop half way between the rest and isometric contraction ratios at $I_{10}:I_{11}=1.2$, suggesting that the myosin heads may be leaving the vicinity of the thin filaments and pausing between the thin and thick filaments (fig. 5.14). The spacing change of the equatorial peaks to [10] at $1/37.9 \text{ nm}^{-1}$ and [11] at $1/21.9 \text{ nm}^{-1}$ again reflects the constant

volume of the muscle: this time it is more noticeable than at isometric contraction, because the amount of shortening is much more marked.

The off-meridional layer lines, which disappeared during the isometric phase of the contraction, either reappear at such a low intensity that they cannot be distinguished from the background at this resolution, or do not reappear at all. The latter is more likely since the row line profile (fig. 5.15) shows an increased background near the equator: this in itself indicates an increase in disorder within the structure. The continued absence of the layer lines indicates that although the tension produced by the muscle is negligible, three dimensional order has not returned to the structure.

5.5 Summary

From the changes discussed in this chapter, some basic details about the contraction cycle emerge. The equatorial intensity reversal is taken to represent the myosin heads moving away from the thick filament backbone, towards the thin filament. In the process of moving, they lose their helical order, resulting in the loss of the myosin layer lines. The myosin heads bind to the thin filaments, taking on the helical repeat of the actin helix and increasing the intensity of the actin layer lines. In addition, the myosin heads are redistributed axially such that the regular perturbation is removed, and the average axial spacing of the heads increases significantly.

During unloaded shortening, when the muscle is producing no tension, the myosin heads appear to leave the vicinity of the thin filaments, and partially, though not completely, return towards the thick filament backbone. The heads recover an axial structure which is very similar to the rest pattern, but azimuthally the helical order is not recovered.

The information derived in this chapter is used to create a basic model of the actin and myosin filaments which can be modified until the precise arrangements of protein molecules which give rise to the patterns described here are determined.

Chapter 6: Computer Modelling Procedures

6.1: Introduction

6.2: Scope Of The Model

6.3: Previous Modelling Studies

6.4: General Modelling of Muscle Structure

6.4.1: Building a Three Dimensional Model

6.4.2: Mass Projection into a 2D Plane

6.4.3: Fourier Transform of the Model

6.5: Modifications To The Basic Model

6.1 Introduction

The aim of this modelling work is to investigate the arrangement of the actin and myosin molecules in muscle at different stages of the contraction cycle, so that structural changes between the modelled states can be correlated to the corresponding level of force production. The three states to be modelled are rest, peak of isometric contraction, and unloaded shortening at zero tension.

The rest muscle structure contains substantial three dimensional order (§5.2), resulting in the observed sharp peaks in the diffraction pattern. The presence of such detail makes any attempt to model the pattern easier than modelling an indistinct pattern, such as that obtained from isometrically contracting muscle (§5.3). In short, a pattern with poorly defined features can usually be reproduced by a number of different structural models, usually including various disordered components. To overcome this ambiguity, rather than try to model uniquely the contracting muscle structure, the isometric contraction and unloaded shortening states have been probed by studying the effects of introducing various forms of disorder to the model.

This chapter describes the methods used to model the muscle structure, including the pseudo-code for the various programming subroutines; the full code for the modelling program can be found on a disk at the back of this volume. Computational and time constraints are discussed, and the scope of the model is defined within these limits. The starting model based on the dimensions obtained from the rest diffraction pattern is outlined, and used to describe the mass projection and Fourier transform sections of the program. Detailed results from the modelling exercise are presented and discussed in Chapters 7 and 8.

6.2 Scope Of The Model

Ideally, a model of the structure of muscle would include every atom of every protein molecule, for a region equivalent in size to a whole muscle sample. The filaments would form sarcomere structures, and the sarcomeres would be organised into myofibrils and fibres. Only then could the model be expected to reproduce perfectly the experimental

patterns. In reality, there are two concerns which make this kind of detailed modelling unfeasible: the limits set by computational time and memory, and the sheer number of parameters which could be varied in such a model. The model components are built up of spheres of various sizes, and the greater the resolution required, the more smaller spheres must be used, increasing both the computational requirements and the complexity of the model. On the other hand, if the model is too simplified it cannot be relied upon to provide an accurate representation of the muscle structure. Thus a compromise is reached between the practical computational limits and the resolution required to give a realistic model.

The simplified model consists of three components: actin monomers, myosin heads, and thick filament backbones. The actin monomers and myosin heads are represented by spheres occupying a similar mass/space distribution to the real subunits, and the thick filament backbones are modelled by solid cylinders.

This work concentrated on reproducing the major features of the diffraction patterns, most notably the meridional intensity distribution, the equatorial reflections, and the profiles and relative intensities of the myosin layer lines, and to a lesser extent the actin layer lines. Detailed modelling of the thin filament structure was not made a priority; approximate intensities comparable to the experimental values could be obtained using the simple helix described, and several recent studies have already modelled the thin filament structure with interesting results as discussed in the next section. Other components such as C-protein, troponin and tropomyosin are not included since they are not believed to contribute greatly to the actin and myosin reflections which are the main focus of this work. Lastly, no attempt was made to reproduce the sampling effects along the meridian by introducing a sarcomere structure to the model.

6.3 Previous Modelling Studies

Computer modelling of muscle structure is a growing area of research, becoming more accessible as computers increase in speed and memory capacity. The thin filament structure has been modelled in great detail using x-ray diffraction, crystallography and electron microscopy data. The F-actin structure and the position of the troponin and

tropomyosin proteins relative to the actin helix have been investigated, modelling the actin monomer either as four small spheres representing the four subdomains, or using the full atomic structure [79, 59, 100, 120, 139, 1]. The tropomyosin and troponin molecules are modelled explicitly, and the changes in their position during contraction support the steric blocking model of regulation (§2.6); the tropomyosin molecules appear to shift into the groove of the F-actin helix upon activation, revealing the myosin binding sites in the thin filament.

The generally accepted thin filament model in rest muscle, then, is one where the long axis of the elongated actin monomers lies roughly perpendicular to the filament axis, and the tropomyosin molecules lie to one side of the F-actin helix groove [90]. One conclusion which is particularly relevant to this work is that the actin helix contains a significant degree of cumulative rotational disorder, which strongly affects the intensities of the actin layer lines [29, 31].

Detailed modelling of the thick filament diffraction pattern is harder to find, though two studies are of particular interest with regard to modelling the myosin filaments of frog muscle. Both use frog muscles which have been stretched until the thick and thin filaments no longer overlap, and lattice order is removed; such muscles produce a diffraction pattern devoid of lattice sampling, which greatly simplifies the modelling process since the myosin layer lines can be modelled by a single myosin filament and no lattice effects need be considered.

The first of these studies by Haselgrove [50] concentrated on reproducing the shape and relative intensities of the myosin off-meridional layer lines, and made no attempt to include the meridional components of the layer lines, or the equatorial reflections. The myosin head was modelled by seven overlapping spheres as first proposed by Miller and Tregear [103].

The main conclusion from this study was that the myosin filament could not be modelled with just one myosin head at each subunit position. The best model was reached when the two myosin heads of each subunit pointed in opposite axial directions at angles of $\pm 30^\circ$ to the normal to the muscle axis, and were wrapped around the filament at an azimuthal angle of about 80° to the normal to the backbone (fig. 6.1). In addition, an isotropic

“thermal disorder” component was required to reduce the higher order layer lines to a satisfactory intensity. A refined model of the myosin head based on the curved head proposed by Moore et al. [173] had little effect on the model’s theoretical diffraction, which led to the further conclusion that “the exact shape of the crossbridges is unimportant provided they are elongated”.

Malinchik & Lednev [96] used the same basic approach to model the myosin layer lines from stretched frog muscle, but expanded the work to include detailed modelling of the meridian. Their results supported Haselgrove’s work; the best rest model placed the myosin heads at axial angles of $\pm 27^\circ$, and wrapped them around the backbone at an azimuthal angle of 80° .

The axial distribution of the myosin heads was modelled by a one dimensional mass distribution of units, each unit representing one head level. The head levels were grouped into triplets 42.9nm apart. Within each triplet, the head levels were displaced such that the units were 13nm apart, rather than 14.3 nm (fig. 6.2). This arrangement represents the distortion group giving rise to the forbidden meridional reflections (§6.5.1). The best result was reached when the distortion group did not extend over the whole length of the thick filament, and further contributions from C-protein and the backbone were included [96].

This thesis differs from the above studies in that it aims to reproduce the actin and myosin reflections of the two dimensional diffraction pattern from unstretched resting and contracting muscle, including lattice effects [137]. The meridional and off-meridional contributions are integrated rather than being regarded as independent models.

There is a dearth of published work on modelling the structure of contracting muscle, and what there is seems to concentrate on the individual effects of various types of structural disorder on fibre diffraction [164, 18, 101, 146, 147, 157].

In particular, Malinchik & Yu [95] discussed various factors which could be responsible for the equatorial intensity reversal observed in isometrically contracting muscle. Their results indicate that the ratio of the intensities of the [10] and [11] equatorial reflections is strongly affected by lattice disorder. Disorder in the thick filament lattice lowers the [10] intensity, leaving the [11] largely unaffected; in contrast, disordering the thin filament lattice raises the [10] intensity and lowers that of the [11] reflection. They observed that if the

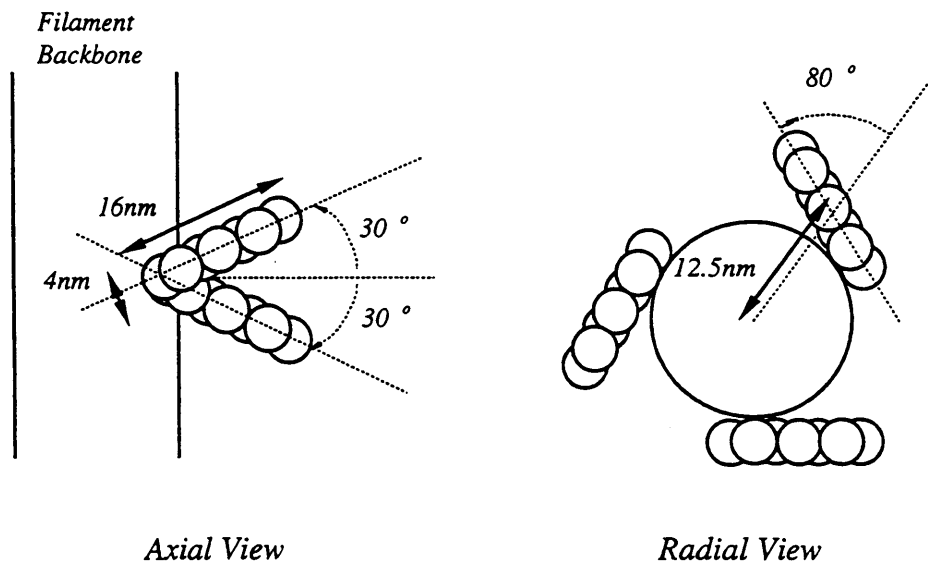


Figure 6.1: Haselgrove's Model Subunit Arrangement [50]

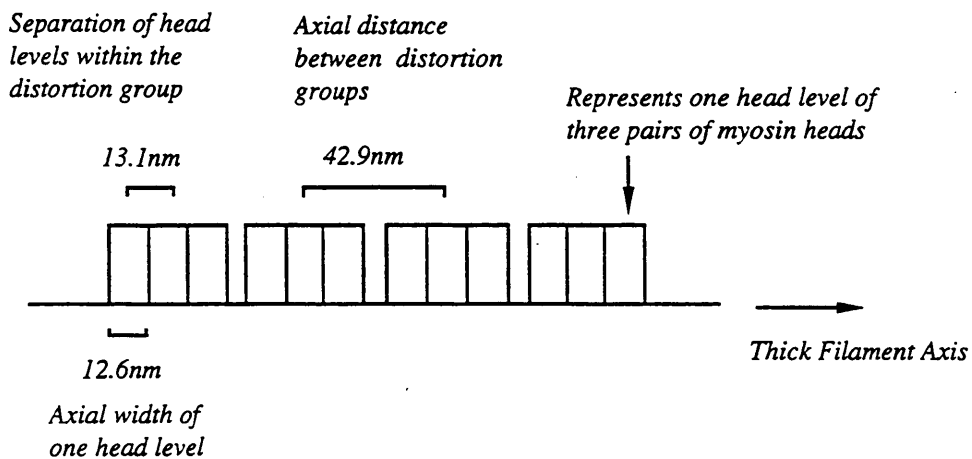


Figure 6.2: Axial Mass Distribution in the Perturbed Region of Malinchik & Lednev's Best Model of the Thick Filament in Rest Muscle [96]

In this model, the perturbed region of the myosin head arrangement does not extend over the whole length of the thick filament. The best rest model also includes contributions from C-protein and backbone structures.

disorder is thermal in origin, the mass difference is likely to result in a larger average amplitude of displacement for the thin filaments than for the thick filaments: an amplitude ratio of 1.6:1 was suggested. Taking account of this ratio when combining both lattice disorders, the overall effect is to raise the [10]:[11] intensity ratio.

The characteristic feature of the isometric contraction pattern is the lack of sampling indicating the presence of large amounts of disorder, particularly in the myosin head arrangement. It is important to distinguish between the effects of the different types of disorder so that those which are most likely to contribute to the observed effects can be investigated in greater detail. This work differs from the studies referenced above in that the disorders are applied specifically to the myosin head arrangement and the filament lattice, rather than being generalised discussions.

6.4 General Modelling of Muscle Structure

The general procedure for producing theoretical diffraction patterns can be divided into three steps: building the three dimensional model, mass projecting the model structures, and Fourier transforming the mass projections (fig. 6.3). The sum of the squared transforms for a range of projections covering one complete revolution around the muscle axis is equivalent to an experimental x-ray diffraction pattern, though it should be convoluted with a two dimensional Gaussian, representing the cross-section of the experimental x-ray beam, before a direct comparison can be made. The computer programs which produce the result in this thesis make use of methods based on a set of earlier programs written by Diaz and Pantos [26] at the SRS. The mass projection and Fourier transform methods are implemented in the same way, but the model building section has been completely rewritten.

The basic model used in this work is a three dimensional model of the overlap region of the sarcomere (fig. 6.4), consisting of parallel thick and thin filaments in a hexagonal lattice. The lattice lies in the x - y plane, and the filament axis is the z -dimension. The extent of the modelled region is variable, as is the resolution of the model defined as the number of pixels per nm.

```

Input model parameters
BUILD: builds the three dimensional model
FOR each projection angle
    PROJECT: mass project the model into a 2D buffer
    TRANSFORM: Fourier transform the 2D mass projection buffer
    Square transforms
ENDFOR
Accumulate Intensity

```

Figure 6.3: Pseudo-Code for Complete Modelling Program

The resolution is determined by the extent of the model and the number of pixels in the mass projection buffer, which in practice can only take a limited number of values: the Fourier transform uses an optimised fast Fourier transform routine which requires that the input mass projection must be square, and that the number of pixels along each side must be a power of two. In addition, there is an upper limit to the size of the mass projection buffer set by the computational memory and time required to Fourier transform it; a 1024 x 1024 pixel buffer (2^{10}) takes 1.5 minutes, compared to 8 minutes for the next allowable buffer size - 2048 x 2048 pixels (2^{11}).

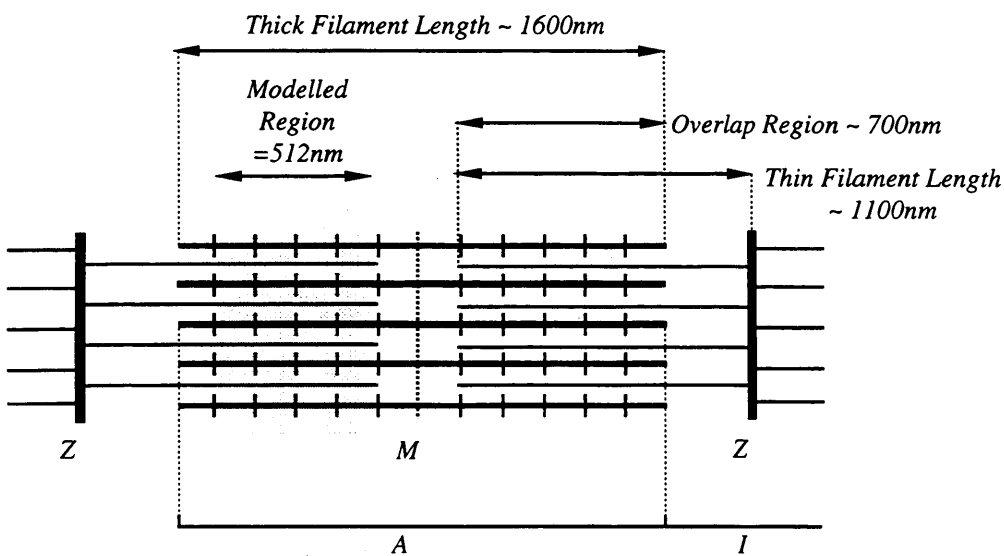


Figure 6.4: Modelled Region In Relation To A Full Sarcomere

For a given mass projection buffer size, the extent of the modelled region can only be increased by decreasing the resolution of the model, making the spheres smaller in terms of pixels. This has its own problems in that it can cause pixelation errors, because the position of each sphere is not exact but is in fact centred on the nearest pixel to its exact position. At low resolutions, this rounding action can involve a significant displacement from the calculated position, distorting the structural repeats. As a result, the diffraction pattern may exhibit spurious peaks or incorrect intensities.

So the models used here are limited in size by the time it would take to run the program, and in resolution by pixelation errors. A compromise was reached using a 1024 x 1024 pixel buffer, and a maximum model size of 512nm, giving a resolution of 2 pixels per nm.

6.4.1 Building a Three Dimensional Model

The basic model structure is built using the parameters presented in table 6.1, and setting all undefined parameters, such as the angles taken by the myosin heads, to a default value of zero. In the modelling process, various parameters are modified to obtain a good fit to the experimental data. Different subroutines are called by the modelling program according to the status of the muscle; the set of routines available when the model status is *contracting* is a superset of the *rest* subroutines, allowing for increased disorders and bonding calculations. The pseudo-code for building the rest status model shows the general steps split into various subroutines (fig. 6.5).

The first procedure is to define the two dimensional hexagonal lattice which the filaments occupy. It is actually built on a rectangular framework, which allows both the thick filaments in the simple hexagonal lattice and the thin filaments at the trigonal points to be reached with the same lattice vectors. The rectangular lattice vectors are 12nm in the *x*-direction, and 20.8nm in the *y*-direction (fig. 6.6), giving a nearest neighbour hexagonal lattice spacing of 41.6nm. The program automatically removes any thick filaments which are not surrounded by six thin filaments, to give all myosin heads every opportunity to bond fully.

```

LATTICE: Calculate co-ordinates of each thin filament lattice point
      Calculate co-ordinates of each thick filament lattice point

FOR each thin filament
      Calculate orientation of the whole filament
      Centre one actin helix on the lattice site
ENDFOR

FOR each thick filament
      Calculate orientation of the whole filament (superlattice formation)
      Centre three myosin helices on the lattice site, rotated by 120° relative to one
      another
      Calculate orientation of each individual myosin helix in the filament
ENDFOR

SUBUNIT: Input parameters of the subunit models

FOR each actin helix
      HELIX_ACTIN: Calculate co-ordinates of every subunit in actin helix
ENDFOR

FOR each myosin helix
      HELIX_MYOSIN: Calculate co-ordinates of each subunit in myosin helix
ENDFOR

FOR each actin helix
      Calculate full 3D co-ordinates of each actin subunit
      Store co-ordinates with actin sphere type
ENDFOR

```

continued overpage...

```

FOR each thick filament
    Calculate full co-ordinates of each backbone segment
    Store co-ordinates with backbone cylinder type
ENDFOR

FOR each myosin helix
    FOR each subunit
        Calculate full co-ordinates of the bases of the two myosin heads
    ENDFOR
ENDFOR

IF status is contracting
    BOND: Define chosen bonds and calculate corresponding head orientation
ENDIF

FOR each thick filament
    FOR each subunit
        FOR each of the two myosin heads
            POSITION: Calculate the full co-ordinates of each sphere in the
                    head given the orientation and the co-ordinates of the
                    base subunit
            Store co-ordinates with myosin head sphere type
        ENDFOR
    ENDFOR
ENDFOR

```

Figure 6.5: Pseudocode For Building Section Of Modelling Program

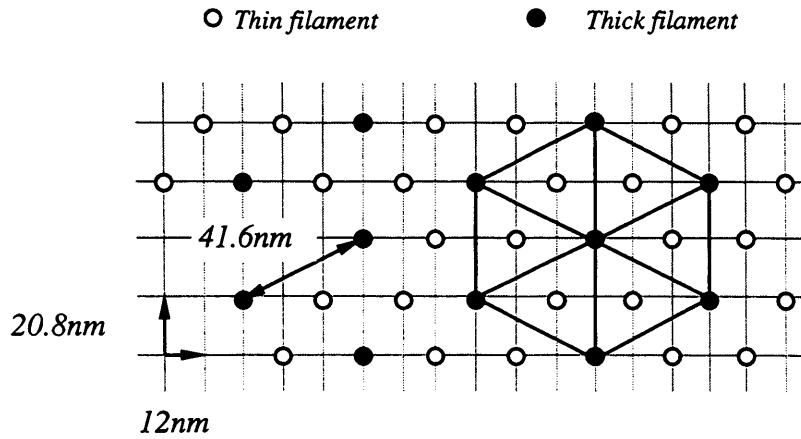


Figure 6.6: *Framework Of The Hexagonal Lattice*

Good lattice order is held over ~400 nm (§5.2.1), which is well within the 512nm maximum extent of the lattice (§6.4). The mass projection buffer size restricts the all three dimensions of the model, limiting the filament length to 512 nm. This is shorter than the overlap region of the sarcomere in rest length muscle (700nm), but is sufficiently long to model the meridional reflections correctly.

| PARAMETER | VALUE |
|-------------------|-----------|
| Lattice spacing | 42.0nm |
| Myosin Helix: | |
| Pitch | 43.0nm |
| Axial translation | 14.3nm |
| No. subunits/turn | 9 |
| Radius | 7.5nm |
| Actin Helix: | |
| Pitch | 36.0nm |
| Axial translation | 27.3nm |
| No. subunits/turn | 0.2162162 |
| Radius | 2.5nm |

Table 6.1: *Initial Model Parameters*

The helical filaments are built to the specifications in table 6.1, with each subunit representing one monomer in the actin helix and one pair of myosin heads in the myosin helix. Three myosin helices are combined at orientations of 0°, 120° and 240° to produce the triple helix structure. In the basic model, all the filaments of each type are identical and have

the same orientation, though every helix is generated individually to allow for later inclusion of disorder within the helix structure (§6.5.3). The subunit co-ordinates are added to the corresponding lattice co-ordinates of each filament, effectively placing the thick and thin filaments at the correct lattice sites.

The actin monomer is modelled by a single sphere of radius 2.5nm, centred on the co-ordinates of each actin subunit (fig. 6.7a), closely approximating the real elongated monomer: the consequences of the spherical approximation are not significant enough to warrant more in depth modelling at this stage, and are discussed in the next chapter.

The myosin subunit model is more complex, representing two myosin heads which are far from spherical. The individual myosin heads are modelled by a group of spheres arranged in one of two structures of different resolution. The simplest model is a low resolution head identical to that first suggested by Miller & Tregear [103]. The model consists of seven spheres each of radius 2nm, whose centres are separated by 2nm in a straight line giving overall dimensions of 16 x 4 x 4 nm for each head (fig. 6.7b). The full subunit representation comprises two head models, with the first sphere of each head centred on the subunit co-ordinates.

The second head model is a much higher resolution structure, consisting of fifty-nine spheres, each of radius 0.8nm, arranged so as to closely mirror the crystalline myosin head structure determined by Rayment et al. (fig. 6.7c) [124]. The dimensions of this model head are 16.5 x 6.5 x 4.5 nm, and its Fourier transform was almost identical to that of the full head structure. Again, each subunit comprises two model heads, and the tertiary sphere is centred on the subunit co-ordinates.

The backbone elements of the thick filaments are modelled by uniform cylinders: it is assumed that the backbone structure does not change during contraction, since there is little evidence to suggest otherwise. The cylinders are built in 14.3nm long sections of radius 7.5nm, centred at the thick filament lattice sites and at 14.3nm intervals along the length of the filament (fig. 6.7d).

The basic model parameters stay largely the same throughout the modelling process and give rise to the fundamental diffraction pattern. Matching this pattern to the experimental data is done by modifying the distribution and orientation of the subunits within the helices,

and the arrangement of the filaments in the lattice. These modifications are discussed in detail in the next chapter. When all the components have been arranged, the position of each building block in the structure is stored along with its type: sphere or cylinder.

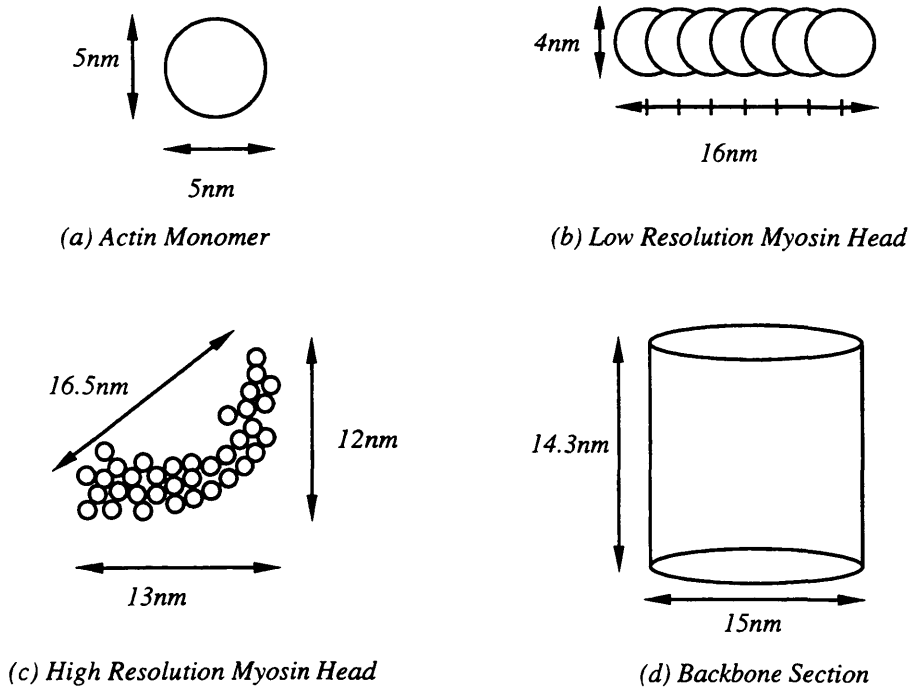


Figure 6.7: Modelled Representations of the Basic Subunits

6.4.2 Mass Projection into a 2D Plane

The three dimensional model co-ordinates are transferred into a two dimensional mass projection buffer using rotation matrices, according to the angle of the projection, though transferring the subunits themselves to two-dimensional mass projections is a little more complex. In general, the mass projection of the subunit will depend on the projection angle, which is where the advantage of using spheres for building the model becomes apparent; the two dimensional mass projection of a sphere is independent of the incident projection angle. Thus a single two dimensional mass projected sphere template can be built for each type of sphere used in the model, and simply pasted into the mass projection buffer at the required projected co-ordinates (fig. 6.8). Since the backbone sections are also spherically symmetric in the lattice plane, which is perpendicular to all projections in this program, the template method is still valid.

To make the templates, each sphere is normalised to the size of the full mass projection buffer, and pixels that fall within the sphere outline are weighted by the depth of the sphere at that point, taking into account the relative density of the sphere type. The same method is employed for the backbone sections, projecting the mass into a depth-weighted longitudinal slice. This need only be done once for each sphere type, and the resulting templates stored for further use.

The relative densities of the three components - the actin, myosin head and backbone subunits - are crucial to generating the correct relative intensities of the actin and myosin layer line sets, which vary as the square of the corresponding density. The model density of each component was calculated from the known mass and the modelled volume of the subunit.

Table 6.2 presents the figures used in these calculations: the sources of the quoted actin and myosin head masses are found in Chapter 2. For the actin subunit, the mass of one G-actin monomer (42kDa) was used. The mass of one myosin head consists of one myosin S1 unit (120kDa) plus two light chains (20kDa each), giving a total mass of 160 kDa.

| | Actin Monomer | Myosin Head 1 | Myosin Head 2 | Backbone Section |
|---|----------------------|----------------------|----------------------|-------------------------|
| Model Unit | 1 sphere | 7 spheres | 59 spheres | 1 cylinder |
| Radius (nm) | 2.5 | 2.0 | 0.8 | 7.5 |
| Length (nm) | - | - | - | 14.3 |
| Unit Volume (\AA^3) | 6.545×10^4 | 2.346×10^5 | 1.265×10^5 | 2.527×10^6 |
| Mass (kDa) | 42 | 160 | 160 | 836 |
| Unit Density ($\text{Da}/\text{\AA}^3$) | 0.642 | 0.682 | 1.264 | 0.331 |

Table 6.2: Parameters of the Basic Modelling Units

Each cylindrical backbone section corresponds to one level of three myosin head pairs, equivalent to three myosin molecules. The mass of this section was taken as the sum of the LMM (160 kDa) and S2 (100 kDa) chain sections of three molecules. In addition, a third (56 kDa) of a C-protein molecule is incorporated into each section, calculated by averaging the mass of seven C-protein molecules ($7 \times 150\text{kDa}$) over a half sarcomere length. C-protein is a significant proportion of the thick filament mass but does not contribute to the helical diffraction of the myosin heads. Evenly distributing its mass over the backbone

ensures that it contributes to the equatorial reflections but not the myosin layer lines; however, the uniform distribution of mass also means that the meridional reflections which arise from the C-protein arrangement do not appear either.

This raises a question over the contribution of the troponin and tropomyosin proteins to the thin filament mass, and how it might affect the calculated actin monomer density. Their contributions to the actin and myosin layer lines are negligible: the tropomyosin helix gives rise to its own set of layer lines, whereas the troponin molecules produce a set of reflections on the meridian. However, the extra mass centred at each of the thin filaments can be expected to have a significant effect on the equatorial reflections and cannot be ignored. Distributing the mass evenly over the actin helix would falsely raise the layer line intensities, but unlike the thick filaments, there is no backbone component to deal with this problem. Without explicitly modelling the regulatory proteins, the simplest way to deal with the extra mass is to evenly distribute it over the actin helix when determining the equatorial reflections, and leave it out for the layer line calculations. So for the equatorial calculations, two troponin molecules at 80kDa each and two tropomyosin molecules at 66kDa each were added for every 14 actin monomers: a total extra mass of 21kDa per actin monomer, which increases the density to $0.960 \text{ Da}/\text{\AA}^3$.

The number of projection angles used is a compromise between the required resolution and the total computational time necessary to Fourier transform the set of projections. The minimum number of mass projections required to reproduce the model completely must cover half of one complete revolution about the muscle axis: the symmetry of the model means that this is equivalent to one complete revolution in real terms. A standard of 5° increments between 0° and 180° was determined to produce a set of reflections with almost identical relative intensities to the ideal case, whilst reducing the computational time involved to about one hour; the Fourier transform of a set of 36 projections at 1.5 minutes each.

6.4.3 Fourier Transform of the Model

Each of the mass projection buffers are Fourier transformed individually using an optimised fast Fourier transform routine, which limits the input buffer to a square buffer

```

Input projection angles
FOR each type of sphere used in the model
    TEMPLATE: generate a projection template
ENDFOR

FOR each projection angle
    FOR each myosin head in the model
        MASS_PROJECTION: Rotate 3D model to projection angle required
            Mass project co-ordinates of each sphere
            Paste assigned template onto projected co-ordinates
    ENDFOR

FOR each thick filament backbone
    MASS_PROJECTION: Rotate 3D model to projection angle required
        Mass project co-ordinates of each cylinder segment
        Paste assigned template onto projected co-ordinates
    ENDFOR

FOR each actin helix
    MASS_PROJECTION: Rotate 3D model to projection angle required
        Mass project co-ordinates of each sphere
        Paste assigned template onto projected co-ordinates
    ENDFOR

TRANSFORM: Fourier transform the mass projection buffer
    Square FT buffer
    Accumulate running total of intensity over all projections
ENDFOR

Store accumulated intensity as a 2D image file

```

Figure 6.8: Pseudocode For Mass Projection And Fourier Transform Sections Of The Modelling Program

with a side of 2^n pixels. The routine was tested against a standard NAG library routine and gave identical results. The individual transformed buffers are squared and summed over the entire set of projections to reproduce the intensity distribution of the diffraction pattern.

6.5: Modifications to the Basic Model

Most modifications to the basic model described in the previous section involve changing parameters and dimensions, but there are a few structural modifications which require explicit programming. Incorporation of the distortion group which produces regular perturbations in the axial translation of the myosin helix is one such case. The distortion group is defined by the number of head levels in the group and the displacement of each level from its ideal position. The displacements are added to the ideal axial positions at the myosin helix building stage, and are non-cumulative. The capacity to model filament extensibility is incorporated by translating a percentage filament extension to an increase in the corresponding helix pitch before the building stage.

In modelling the superlattice structure, it is assumed that the thick filaments take one of two orientations, 0° or 60° , which is equivalent to a 180° relative rotation because of the trigonal symmetry [133]. Every thick filament is assigned an angle, which is added to the orientation angles of each of the three myosin helices in the filament: thus the triple helix structure is maintained.

The introduction of disorder to the model also requires specific programming, and can take one of several forms. The modelling program includes the possibility of displacing whole filaments laterally or axially within the hexagonal lattice, and randomly orienting them about their long axis. Bending of filaments and axial tilting are rather more complex and are not included in the programming. Within a given helix, the individual subunits can be axially, radially or azimuthally displaced, and/or randomly oriented. In the following discussion, the term displacement may refer to a lateral, axial, or angular displacement from the ideal value of a parameter.

Random isotropic disorder is the simplest case: the parameter in question is allowed to vary in the range $p-a < p < p+a$, where the amplitude a is the maximum allowable

displacement of the parameter from its ideal value. Within this range, the displacements are chosen randomly and are all equally likely; the disorder is defined by the statistical rms displacement.

Disorder of the first kind is similar, but the displacements are randomly drawn from a Gaussian distribution of displacements centred on the ideal position, rather than a uniform distribution. The amount of disorder is defined by the half width of the Gaussian distribution of displacements. The distribution is normalised to the full number of filaments in the model, and the displacements randomly assigned to each filament.

The modelling process is a little more complicated than for the isotropic disorder, because of the necessity of drawing the displacements from a defined distribution. The effect on the diffraction pattern is similar in most instances, so for simplicity, isotropic disorder is used rather than disorder of the first kind. The option of using the more complex disorder is retained for modelling lattice disorder, where its effects are slightly more visible. Both disorders are non-cumulative, so the displacement of one unit is independent of the displacements of adjacent units.

Disorder of the second kind is still more complex, since it is a cumulative disorder. The displacement of each unit from its ideal position is affected by the displacements of the adjacent units, destroying long range order. Modelling a structure which contains cumulative disorder is more involved, because the disorder has to be incorporated as the structure is built, rather than building a perfect structure and adding the disorder afterwards. In this program, disorder of the second kind was only used in modelling the lattice disorder, where the lattice was built point by point from the centre out, using randomly distorted lattice vectors to reach the next point.

Much of the contracting muscle diffraction pattern can be modelled empirically by introducing various disorders, but there is still a need to study the bonding process by forming specific actin-myosin bonds. The program uses specified physical criteria to define a suitable bond, and uses this information to choose the most favourable bonds for the model. The subroutine BOND deals with determining which bonds are favourable for each myosin head, taking account of its position before binding takes place, and moves the heads to the orientation they would take in that bond. Control is then passed back to the main

BUILD routine with the repositioned myosin heads, ready to be mass projected and Fourier transformed (fig. 6.9).

```
BOND: (called from main BUILD section when muscle status is contracting)
FOR each myosin helix
    Determine the surrounding six actin chains
    FOR each myosin head
        POSITION: Calculate initial position of each myosin sphere
        Define myosin-actin bond criteria
        Determine which bonds fall within these criteria
        Select a bond for this myosin head
        Determine new orientation of bound myosin head
    ENDFOR
ENDFOR
Determine statistics for bond parameters
Return to BUILD which uses new orientation in model
```

Figure 6.9: Pseudocode For Bonding Procedure

Chapter 7: Modelling Of Rest Muscle

7.1: Introduction

7.2: Reproducing the Actin Filament Pattern

7.3: Myosin Filament Pattern - Low Resolution Myosin Head

7.3.1: Meridional Reflections

7.3.2: Layer Line Profiles

7.3.3: Relative Intensity of the Layer Lines

7.4: Myosin Filament Pattern - High Resolution Myosin Head

7.4.1: Meridional Reflections

7.4.2: Layer Lines

7.5: Discussion of Results

7.1 Introduction

This chapter presents an investigation of the structure of rest muscle using the programs described in the previous chapter. Results obtained using both the low resolution (7 sphere) and high resolution (59 sphere) models of the myosin head are described with regard to their suitability for modelling work on this scale.

Subject to the limitations discussed in §6.4/§6.4.1, the standard model size was defined as a 360nm by 360nm lattice of 512nm long filaments, incorporating 70 myosin filaments and 176 actin filaments. Each actin filament contained 187 subunits, and each myosin filament 35 head levels, giving a total of 14700 myosin heads.

Where an R-factor is calculated as a measure of goodness of fit, the following definition was used:

$$R = \frac{\sum (I_{\text{calculated}} - I_{\text{observed}})^2}{\sum I_{\text{observed}}^2} \quad I = \text{intensity}$$

7.2 Modelling The Actin Filaments

Modelling the thin filament as a helix of 2.5nm spheres, as described in §6.4.1, produced a set of layer lines at the correct spacings, with the most intense layer lines being the sixth at $1/5.9 \text{ nm}^{-1}$, the seventh at $1/5.1 \text{ nm}^{-1}$, and the first at $1/36 \text{ nm}^{-1}$, as observed in the experimental data. The modelling was not intended to reproduce the thin filament pattern in any great detail, but the initial model could be improved within the bounds of the spherical actin monomer approximation.

The first problem involved the relative intensities of the actin layer lines. The first actin layer line was much too intense with respect to the sixth and seventh layer lines, as well as when compared to the first myosin layer line at $1/43 \text{ nm}^{-1}$. The first actin and myosin layer lines overlap considerably which makes determination of the exact relative intensities impossible, but at rest the first actin layer line is significantly lower in intensity than the first myosin layer line; in this initial model, the reverse was true. The sixth and seventh layer lines were also more intense than the sixth myosin layer line, whereas in the experimental data they were less intense.

Since the model actin subunits are spherical, their orientation is immaterial: this leaves the exact position of the subunits in the helix and the position of the filaments in the lattice to play with. One disorder which would have the desired effect is a random cumulative rotational disorder which disturbs the helical order of the actin subunits: this type of distortion is undetectable to the axial or equatorial mass distributions, so its effects would only be seen in the off-meridional layer lines. There is evidence to support such a disorder in the actin helix [29], which causes the rotational angle between adjacent subunits to vary by a random amount whilst leaving the axial translation unaffected. The effect is cumulative so the rotational displacement of a given monomer from its ideal position affects the displacement of the next. The result is to alter the position of the cross-over points of the long, double actin helix; instead of crossing at regular 36nm intervals, the double helix crosses at irregular intervals (fig. 7.1) [43]. The effect on the diffraction pattern is to reduce the intensity of all the actin layer lines, but preferentially the lower order ones.

Various amounts of disorder were added to the actin helices, and the minimum value which sufficiently reduced the actin layer lines was $\delta_{\text{rms}} \approx 10^\circ$: approximately 6% of the perfect subunit rotation of 166° . The resulting change in layer line intensities decreased the first actin layer line to a level comparable with the experimental data, and the sixth and seventh actin layer lines also decreased relative to the sixth myosin layer line (fig. 7.2). The rotational disorder did not, however, improve the relative intensities of the sixth and seventh layer lines relative to each other, which at $I_{5,1}:I_{5,9} \sim 1:2$ was significantly higher than the experimental ratio of 1:4.

It is likely that the difference in relative intensity is due to the elongated shape of the real actin monomer, which is ignored in this simple model. The elongated axis is believed to lie approximately at right angles to the thin filament axis [30, 105], which could reinforce the left handed 5.9nm pitch helix in preference to the right handed 5.1nm pitch helix, thus increasing the intensity of the sixth layer line at the cost of the seventh. In addition, the radius of the centre of mass of the actin monomers would increase from the modelled 2.5 nm to nearer 3.5nm, resulting in a shift of the radial profile of the actin layer lines to better fit the experimental data. However, a more complicated monomer representation than this program offers is required to study these effects.

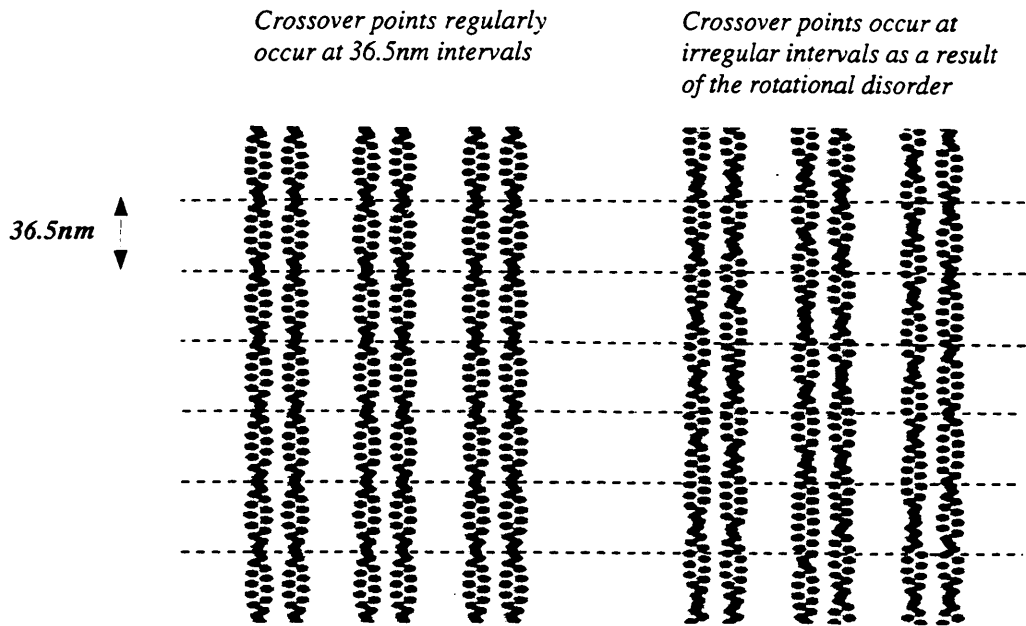


Figure 7.1: The Effect of Cumulative Rotational Disorder on the Actin Helix

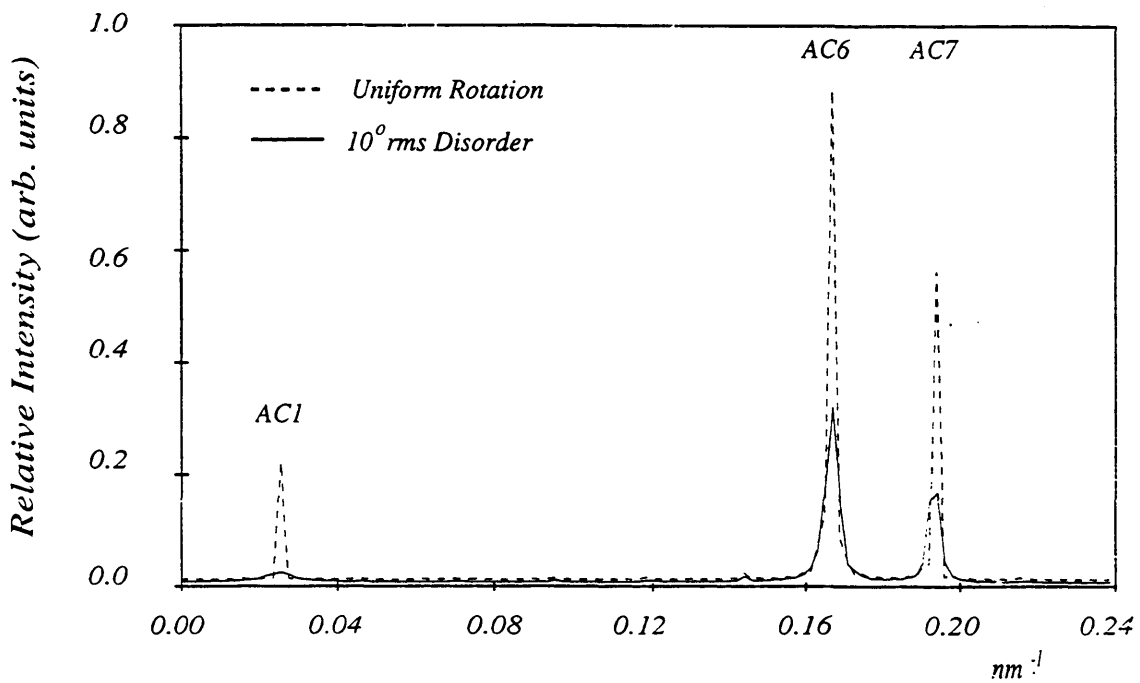


Figure 7.2: The Effect of Cumulative Rotational Disorder on the Actin Layer Lines AC1, AC6, and AC7

The actin layer line profiles show sharp sampling peaks which are not present in the experimental rest patterns. The peaks were greatly reduced by introducing random isotropic disorder to the thin filament lattice of the order of 2.5nm rms.

7.3 Myosin Filament Pattern - Low Resolution Myosin Head

The basic structure of the thick filaments was modelled as described in §6.4.1. The backbone components of the thick filaments were assumed to maintain the same cylindrical structure in all models, leaving the flexibility of the model in the arrangement of the myosin heads. The modelling programs allow many of the parameters to be varied, specifying the position and orientation of the two myosin heads in each subunit individually.

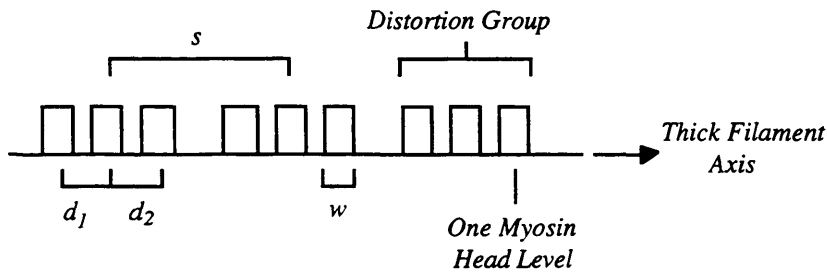
The significant number of flexible parameters requires a systematic method of investigating the myosin head arrangement. This approach is aided by the fact that the meridional region of the diffraction pattern only depends on the axial mass distribution of the model. In other words, any model parameter which does not affect the axial mass distribution can be varied without changing the meridian of the diffraction pattern. Thus the meridian can be modelled independently from the rest of the pattern by altering those parameters which modify the axial mass distribution, and setting all others to a default value. Once the meridian has been reproduced, these parameters can be fixed and the remaining parameters brought into play to model the off-meridional region of the pattern.

7.3.1 Meridional Reflections

The relative intensity of the meridional myosin reflections is determined by the axial mass distribution averaged over all the thick filaments in the model. An approximation of the distribution can be defined in terms of units representing one myosin head level, containing six myosin heads. Figure 7.3 illustrates the case for a distortion group of three head levels, represented as uniform functions, though in the model, as in reality, the shape of the function would depend on the mass distribution over the head level.

The axial mass distribution is defined by the width, w , (and shape) of the head level unit, the configuration of the distortion group, d , and the distribution of the distortion group

along the thick filament axis. In initial modelling of the distortion group, the myosin heads of each subunit were set to their default arrangement, superimposed on each other and both oriented perpendicular to the filament axis.



w = axial width of each myosin head level
 d_1, d_2 = axial separation of head levels within the distortion group
 s = axial separation of centres of distortion groups

Figure 7.3: Definition of the Axial Mass Distribution

It was assumed that there were three head levels in each distortion group [70, 144], and the group repeated at 43nm intervals along every thick filament; thus the overall 43nm pitch of the myosin helix was maintained. Within the distortion group, the myosin head levels were displaced from their ideal positions, where $d_1=d_2=14.3\text{nm}$. The displacements of each of the three heads, Δ_1 , Δ_2 , and Δ_3 , were added to the ideal positions to calculate the distorted d values (fig. 7.4).

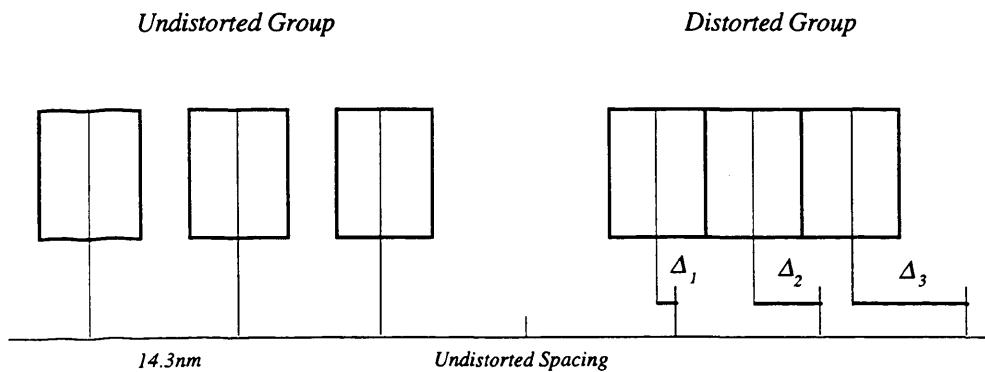


Figure 7.4: Description of the Distortion Group

The distortion group was modelled both with positive Δ values, expanding the head separation within the group, and with negative Δ values, compressing the group. Displacements of the order of 1nm were required to produce significant peaks at the positions of the 1M and 2M forbidden reflections. Compressing the head levels within the distortion group produced slightly better relative intensities than expanding them, and with slightly lower displacements. Best results were obtained when the first myosin head level was assumed to be in its ideal position ($\Delta_1=0$), and the other two levels were displaced by negative amounts of the order of 1nm ($\Delta_2= -1\text{nm}$, $\Delta_3= -2\text{nm}$). An interesting result was that the average spacing $d=(d_1+d_2)/2$ is more important than the individual spacings: thus the best result was when $d_1=d_2=13.1\text{nm} \pm 0.2\text{nm}$.

For larger spacings ($d \geq 13.3\text{nm}$; smaller displacements) the intensities of the forbidden peaks were too low compared to the true 3M and 6M reflections; the 1M and 2M reflections in particular were negligible. Smaller spacings ($d \leq 12.8\text{nm}$; larger displacements) caused the forbidden reflections to become too prominent; at displacements greater than $\Delta_1=0$, $\Delta_2=-3\text{nm}$, $\Delta_3=-6\text{nm}$, they dominated the true peaks.

The shape and width of the head unit level is determined by the arrangement of the two heads in the myosin subunit, and of the three subunits in each level. Initially, it was assumed that the three subunits were identical, and azimuthally separated by 120° . The simple myosin head subunit is defined axially by three parameters: the axial angles of each of the two heads, and the vertical offset between them (fig. 7.5). The axial angles α_1 and α_2 are defined with $\alpha=0^\circ$ when the heads are perpendicular to the filament axis, and $\alpha=90^\circ$ when they are parallel to the axis.

The axial angles of the heads were varied independently of each other, and in combination with the regular perturbations Δ discussed above. As α increased and the myosin head became more parallel to the filament backbone, the mass distribution changed from sharply defined high mass concentrations to a more spread out arrangement where the mass concentrations overlapped. This resulted in the higher order diffraction peaks decreasing in intensity with respect to the lower order peaks, though not uniformly so.

The myosin meridional reflections sample an underlying interference function, the shape of which is determined by the shape of the myosin subunit [98]. The function arises

from the interference between the centre of mass of each head in the pair, which becomes especially noticeable when the myosin heads point in opposite directions along the myosin filament. The first peak of the function appears at an axial spacing which is the inverse of the centre of mass separation. The exact shape of the function depends on the relative contributions of the axial angles and the offset to the total centre of mass separation (fig. 7.6), and has a significant effect on the meridional diffraction pattern; for the same total separation, the combination of smaller axial angles and a larger vertical offset produced a function with more well-defined minima and maxima.

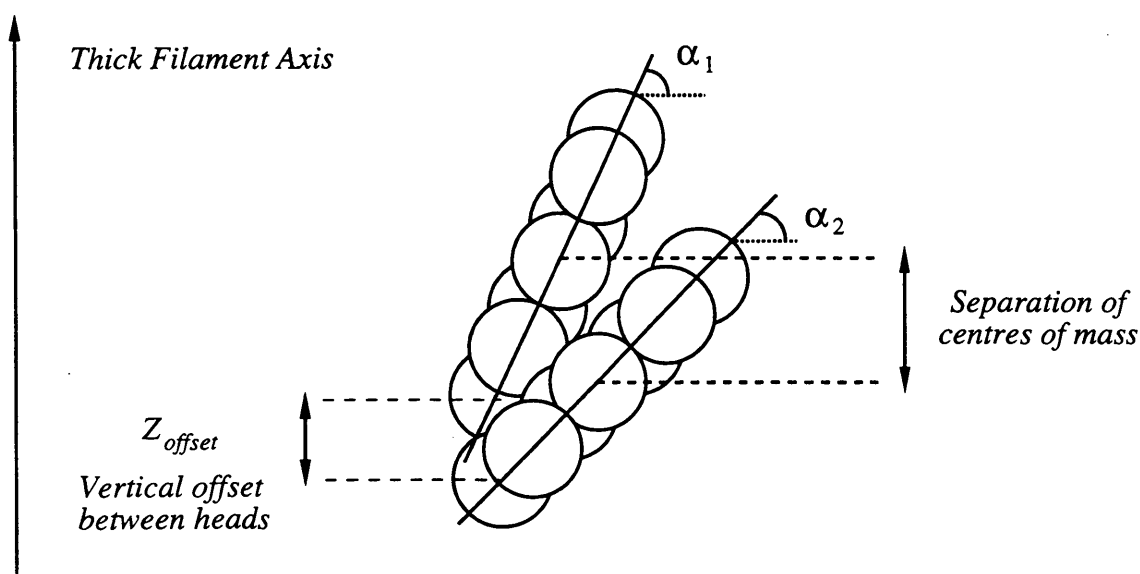


Figure 7.5: Parameters Defining the Axial Myosin Subunit

The two best matches to the meridional diffraction pattern, U1 and U2 described below, both have similar axial distributions, though in model U1 the two heads of each subunit point in the same direction along the filament axis, and in model U2 they point in opposite directions. The axial width in each case is $13.5\text{nm} \pm 0.3\text{nm}$. The best model, model U1, is where the two heads point in the same direction along the filament axis, taking angles of $\alpha_1 = 60^\circ \pm 1^\circ$, $\alpha_2 = 55^\circ \pm 1^\circ$, and the second head is offset vertically by $1.5\text{nm} \pm 0.2\text{nm}$. In model U2, the second best model, the heads point in opposite directions with $\alpha_1 = 24^\circ \pm 1^\circ$, $\alpha_2 = -24^\circ \pm 1^\circ$, and a vertical offset between them of $-0.8\text{nm} \pm 0.2\text{nm}$. In both models, the distortion group separations were $d_1 = d_2 = 13.31\text{nm} \pm 0.2\text{nm}$. The meridional intensity plot produced by model U1, with R-factor of 35%, is shown in figure 7.7.

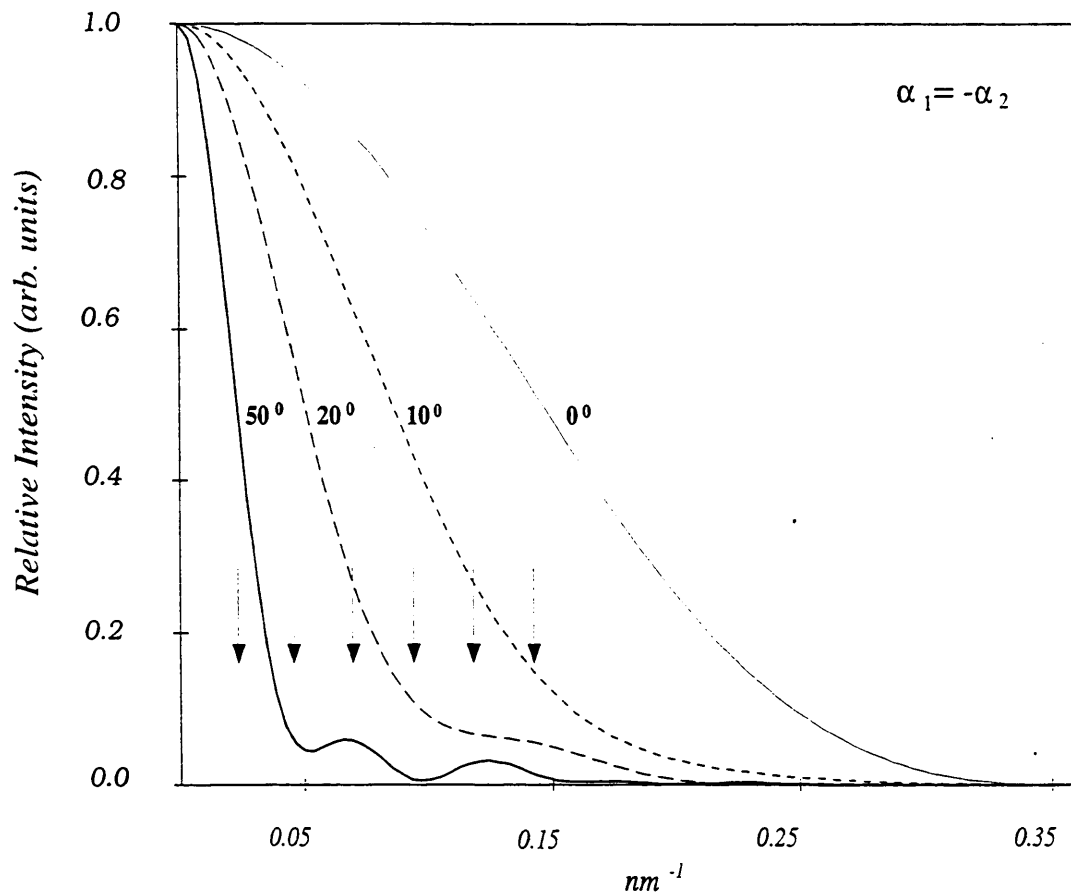


Figure 7.6: Meridional Strip of the Subunit Interference Function

The intensity functions shown here illustrate the effect of varying the separation of the myosin heads' centres of mass within a single myosin subunit. In each case, the axial angles taken by the two myosin heads are $\alpha_1 = -\alpha_2$, so that the heads point in opposite directions along the thick filament axis.

The separation of their centres of mass becomes significant for larger angles ($\sim 8\text{nm}$ for $\alpha = 25^\circ$): the structure of the resulting interference function strongly affects the intensity of the myosin meridional reflections, whose positions are marked by the arrows.

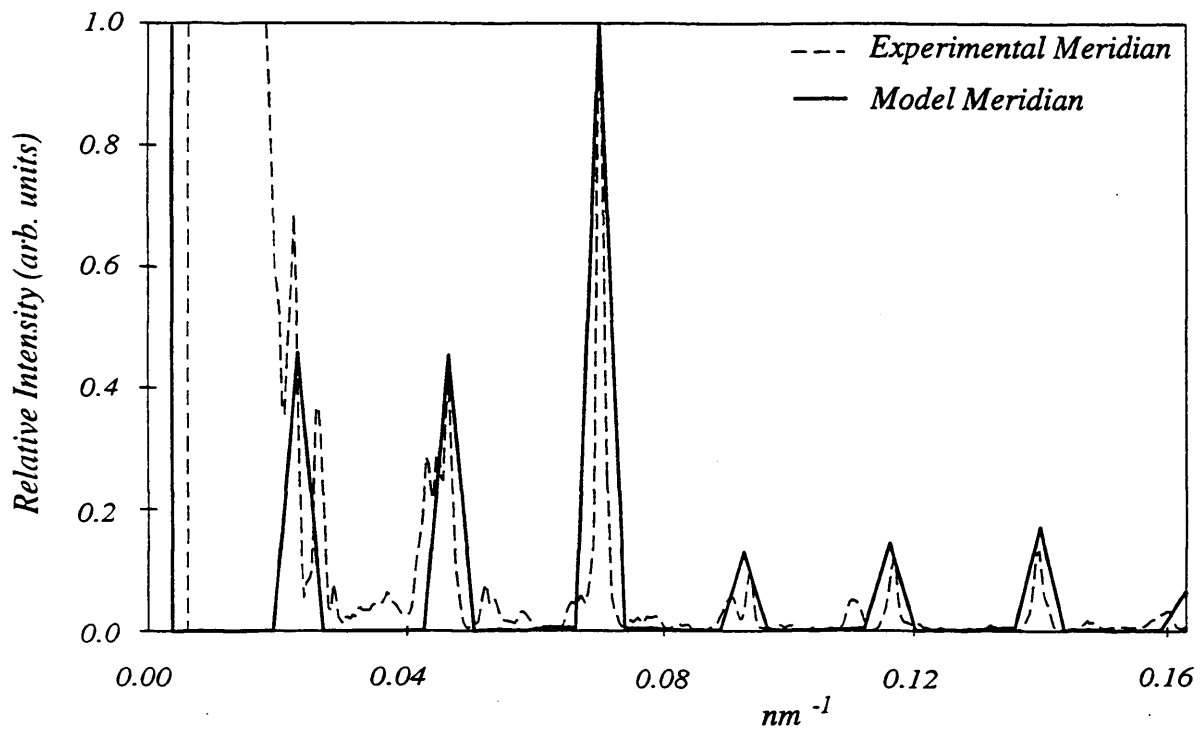


Figure 7.7: Comparison of the Experimental Meridian with the Best Rest Model Obtained Using the Simple Myosin Head Model (U1)

7.3.2 Layer Line Profiles

When modelling the off-meridional pattern, the axial mass distribution was alternately set to model U1 or U2, the two best rest models determined in the previous section. The defining parameters (α_1 , α_2 , Z_{offset} , d , s) were kept constant during the modelling, and only those parameters which had no effect on the axial distribution, and were only detected in the helical or equatorial projections, were varied.

The layer line profiles are shaped by the combination of a broad continuous peak arising from the helical structure of the thick filaments, sampled by Bragg diffraction peaks from the lattice planes. The function underlying the first myosin layer line is a third order squared Bessel function, J_3^2 . Calculations for J_3^2 Bessel functions of radius $10\text{nm} \leq r_c \leq 15\text{nm}$ showed that the best fit to the layer line profile was with a radius of $13.3\text{nm} \pm 0.3\text{nm}$ (fig. 7.8).

The radius of centre of mass also had a strong effect on the equatorial intensity distribution. As the mass of the myosin heads moved away from the filament backbone, the mass in the [10] planes decreased relative to the mass in the [11] planes, decreasing the [10]:[11] ratio. The ratio was also affected slightly by the azimuthal angle taken by the heads, even when the radius of centre of mass was unchanged (§7.3.3).

The Bragg peaks on the first and second layer lines can be indexed onto a superlattice cell of side $\sqrt{3}$ x the lattice spacing (§5.2.1). Various models based on this superlattice shape were tested, all involving the basic unit cell proposed by Squire [133], where the corner filaments and one of the internal filaments take one orientation, and second internal filament is rotated by 60° (fig. 7.9). In the first model, this basic unit cell was perfectly repeated over the whole lattice. The resulting sampling peaks on the first layer line were far too intense and completely overshadowed the underlying continuous peak (fig. 7.10a). Another model built several unit cells, each with a slightly different distribution of the two filament orientations, and distributed the unit cells regularly over the lattice. The results were strikingly different, though in neither case did the relative intensities of the sampling peaks match the experimental first layer line profile.

Better relative sampling on the myosin layer lines was obtained using a semi-random superlattice. The corner filaments of the basic unit cell were all set to the same

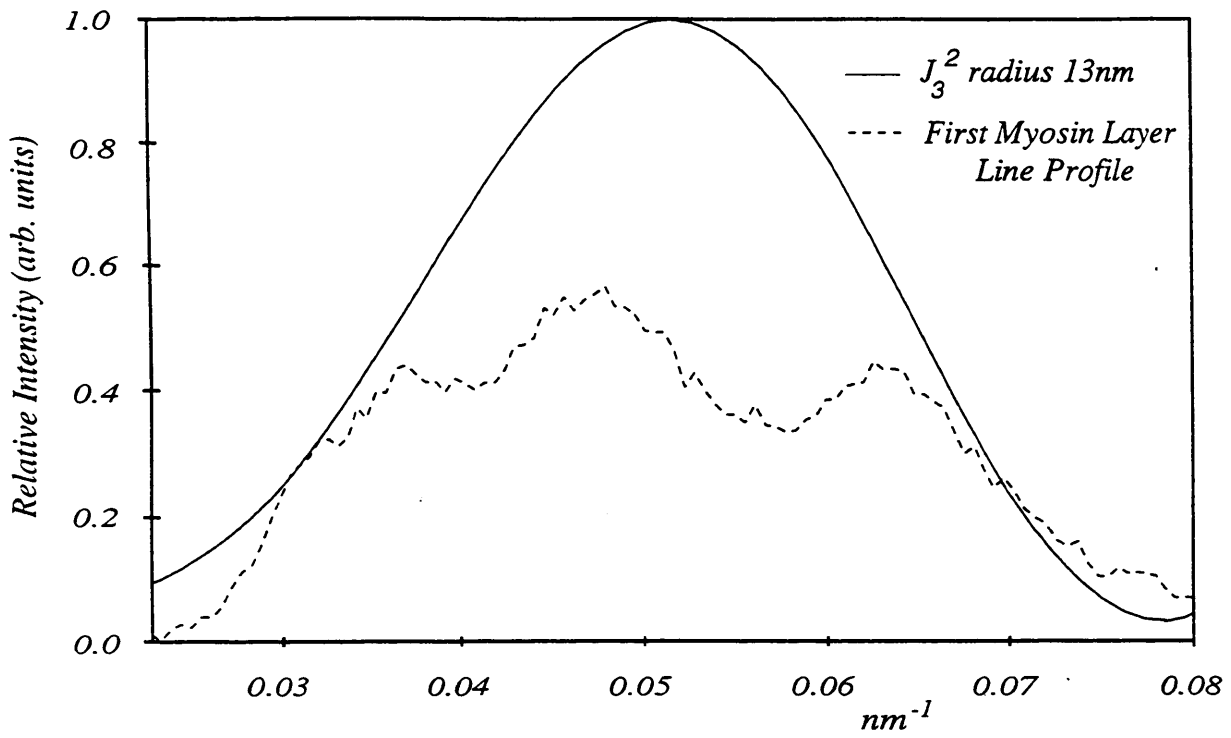


Figure 7.8: J_3^2 Bessel Function Fitted to the First Layer Line Profile

This fit was obtained using a J_3 Bessel function of radius 13nm, which indicates that the average centre of mass of the myosin heads is close to 13nm.

orientation (0°), and the two internal filaments were allowed to randomly take one of the two orientations, on the further premise that no three nearest-neighbour filaments could have the same orientation. A slight improvement was found by rotating every filament by a further 10° such that the absolute orientations were either -10° or 50° (fig. 7.11).

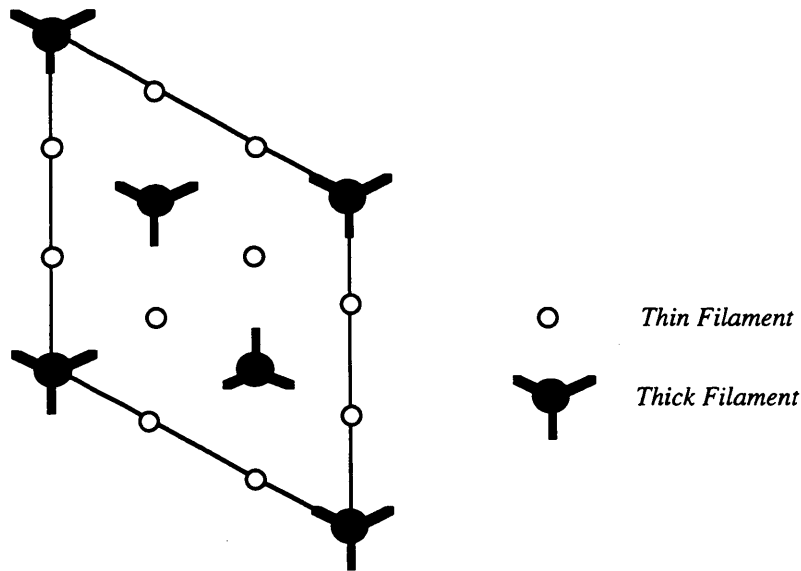


Figure 7.9: Basic Unit Cell Configuration

In addition, a small amount of isotropic myosin lattice disorder was found to lower the relative intensities of the Bragg peaks and the background continuous diffraction. Levels of the order of 1.7nm rms. significantly improved the match to the experimental layer line profile (fig. 7.10b).

7.3.3 Relative Layer Line Intensity

With the meridional intensity distribution and the first layer line intensity modelled, attempts were made to produce higher order layer lines with approximately correct relative intensities (§5.2). The relative intensities of the myosin layer lines are largely determined by the orientation of the myosin heads in the helix; with the axial angles already fixed to give a good match to the meridional pattern, this depended primarily on the azimuthal angle of the heads around the backbone. The azimuthal angles, θ_1 and θ_2 , are defined as 0° when perpendicular to the filament backbone, and 90° when tangential to the backbone surface (fig. 7.12).

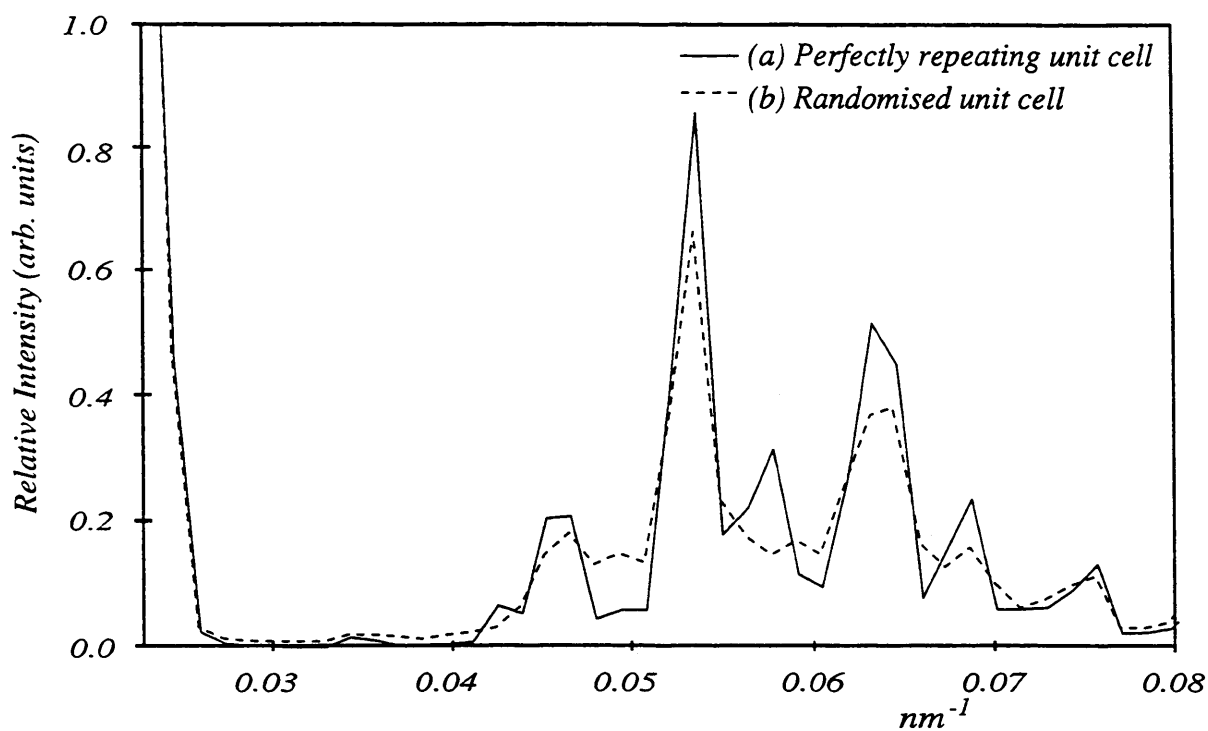


Figure 7.10: Profiles of the First Layer Line for Different Superlattice Arrangements

(a) The unit cell shown in figure 7.9 is perfectly repeated throughout the lattice

(b) The lattice is made up of cells of the same dimensions as that in figure 7.9, but the two central thick filaments are randomly distributed between the two available orientations such that there are an equal number of filaments of each orientation in the whole lattice.

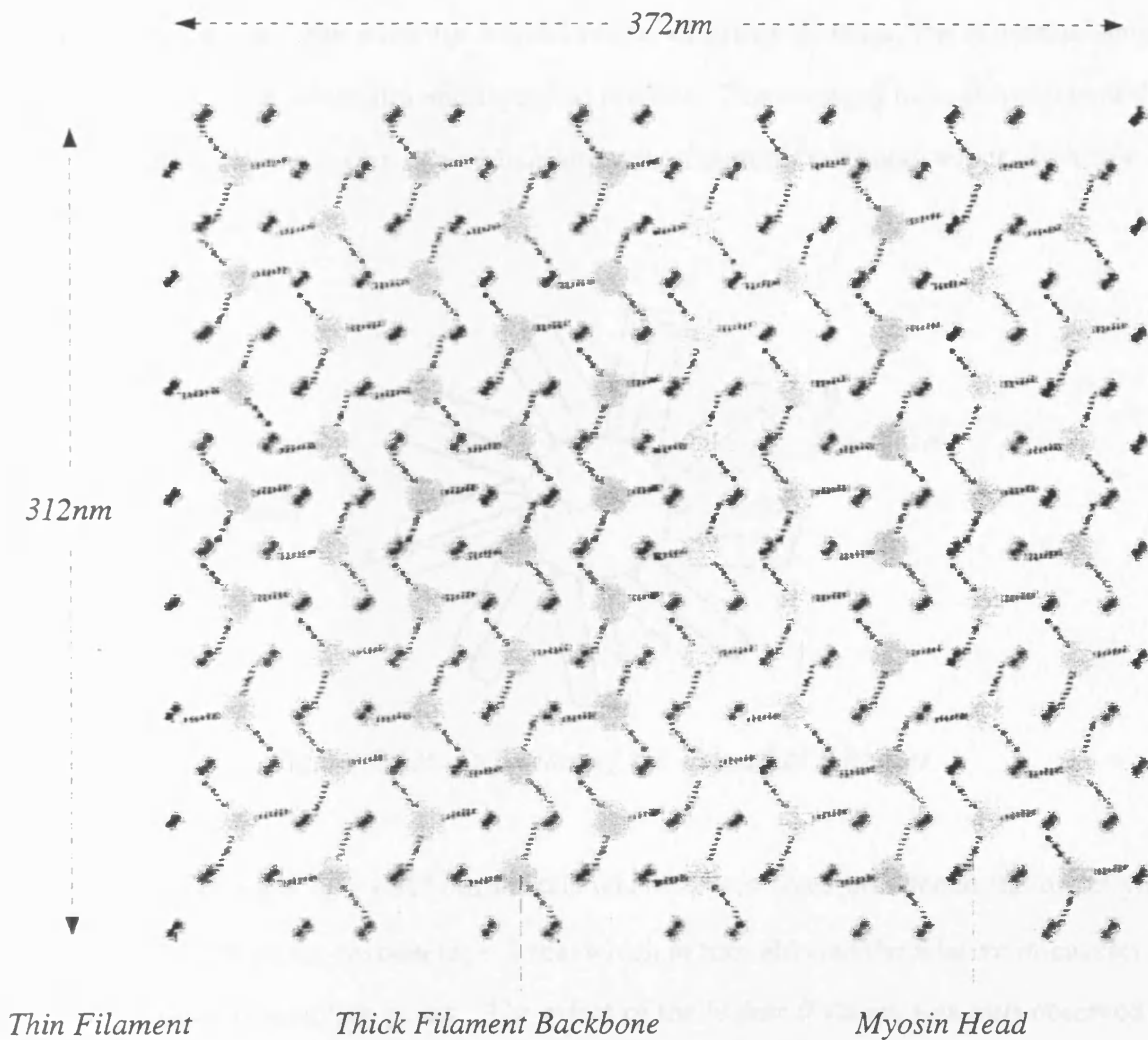


Figure 7.11: Cross Section Through Model Showing the Superlattice Structure

A 14.3nm wide slice is shown with a single myosin head placed at each myosin subunit position and oriented perpendicular to the surface of the thick filament backbone. This representation illustrates the distribution of the two possible filament orientations 60° apart, and the offset of the whole lattice by 10° from the horizontal.

The most obvious way in which varying the azimuthal angle affects the model is in altering the radius of centre of mass of the myosin heads, r_c ; the centre of mass of a head which is fixed to the backbone at one end is at a maximum radius when the head is perpendicular to the backbone ($\theta = 0^\circ$), and decreases as θ increases and the head wraps around the filament. But even for a fixed radius of centre of mass, the azimuthal angle affects the equatorial intensities and layer line profiles. The averaged mass projection of the myosin heads occupies a ring of width dr about the filament backbone, which is narrow at high θ angles (fig. 7.13).

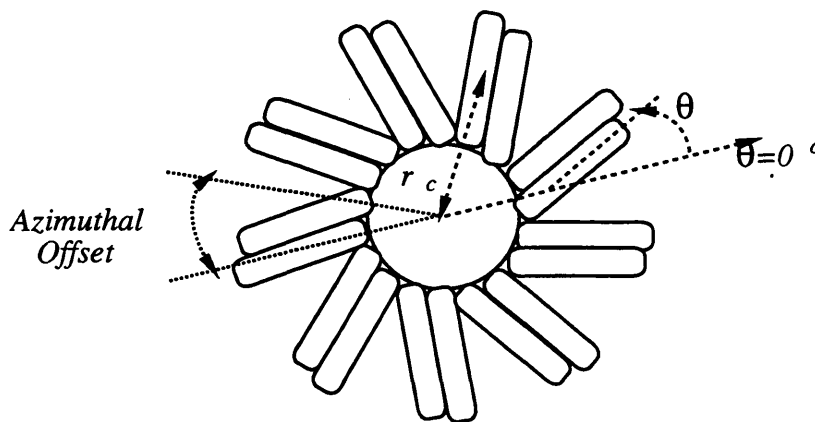


Figure 7.12: Definition of the Azimuthal θ Angles

Increasing θ ($\theta \rightarrow 90^\circ$) in models where r_c was fixed broadened the underlying continuous peaks on the myosin layer lines, which in turn affected the relative intensities of the superimposed sampling peaks. The effect of the higher θ values was also observed in the equatorial profile; for a given r_c , an increase in θ moved mass away from the backbone towards the radius of centre of mass, reducing the [10] intensity slightly. As a result, it was not possible to model the layer line profiles and relative layer line intensities independently: rather they must be considered in combination.

For the axial models U1 and U2, the azimuthal orientations of the two myosin heads in each subunit were varied independently, and in combination with various centre of mass radii. In both cases, the closest approximations were obtained for high azimuthal angles of $\theta_1 \sim \theta_2 \sim 65^\circ \pm 15^\circ$, though neither model gave ideal layer line intensity ratios; none of the models tested could give a reasonable match to the rest pattern layer line intensity distributions.

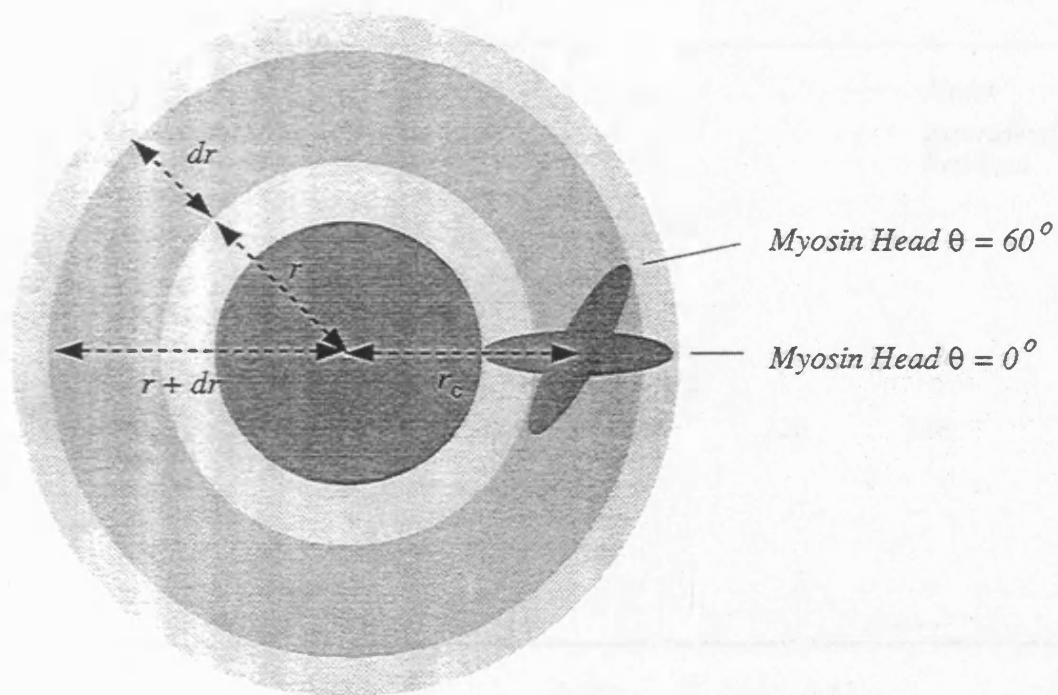


Figure 7.13: *The Effect of the Azimuthal θ Angle on the Averaged Thick Filament Mass Projection*

For a given radius of centre of mass (r_c), an increase in the azimuthal angle of the myosin head forces the projected mass into a narrower ring about the thick filament backbone (dr). The peaks of the continuous Bessel functions underlying the myosin layer lines broaden as a result of this change, increasing the intensity of those Bragg reflections which fall on the sloping sides of the Bessel function peaks relative to those falling near the centres of the Bessel function peaks.

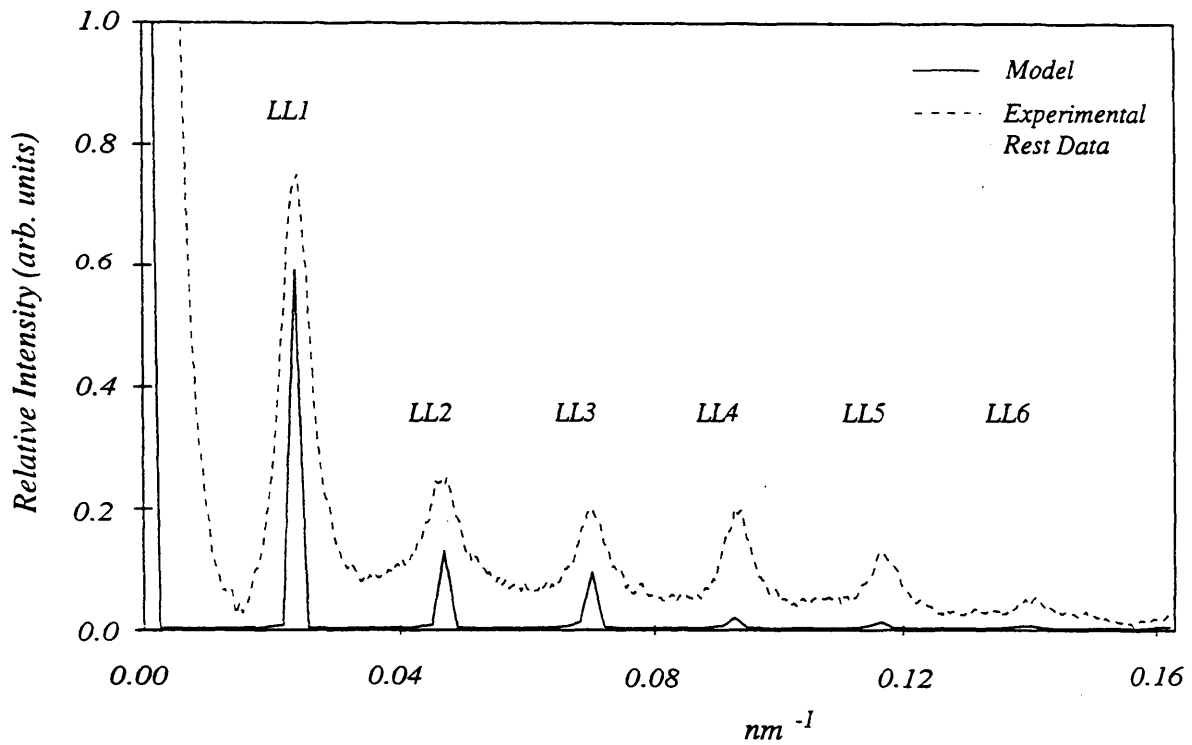


Figure 7.14: Relative Intensities of the Myosin Layer Lines in Model U1a

A radially integrated strip running parallel to the meridian in the region of the [10] equatorial reflection shows the relative intensities of the myosin layer lines. The first three layer lines have comparable relative intensities to the experimental rest pattern, but the higher order layer lines are too low in intensity.

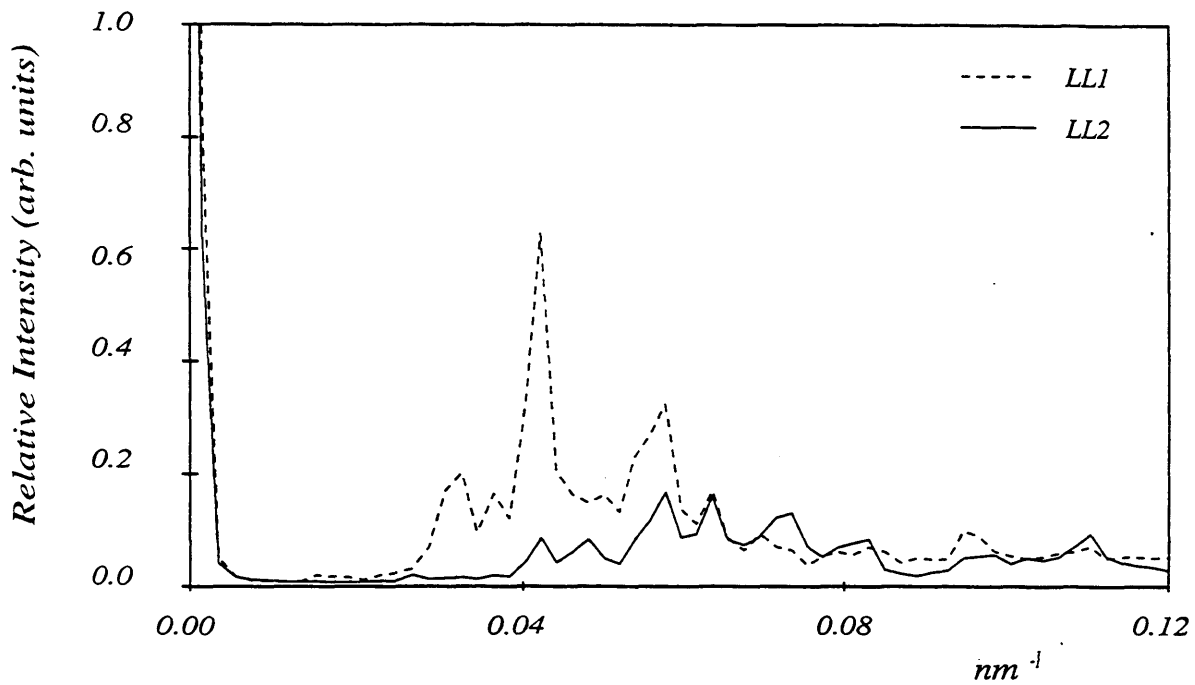


Figure 7.15: *The First and Second Layer Lines from Rest Model U2a*

The second layer line peaks at too high a radius, which gives it a different shape when compared to the first layer line.

Model U1a, the best match to the experimental data using axial model U1 where both heads pointed in the same direction, produced good relative intensities for the first three myosin layer lines. However, the intensity dropped off sharply at this point, and the higher order layer lines were much weaker than expected (fig. 7.14).

With model U2a, the best model using axial model U2 with both heads pointing in opposite directions, the relative intensities of the first six layer lines were of the right order. However, the second and fourth myosin layer lines were the wrong shape; the underlying continuous function peaked at a higher radius than on the first and fifth layer lines (fig. 7.15). The equatorial intensity plots were a good fit to the experimental data for both models U1a and U2a.

7.4 Results With High Resolution Myosin Head

The higher resolution myosin head is far more complex than the simple seven sphere model used up to this point. The positions of the fifty-nine spheres reproduce the crystalline structure of the myosin head [124]. With the simple symmetrical head model, there were few parameters which needed to be considered, but the introduction of this non-uniform head requires the definition of more parameters. The high resolution head model is shaped rather like the head of a golf club, with most of the mass in the head and the rest in the stick. The default position of the myosin head was defined as that where the minor part of the mass lies parallel to the filament backbone, and the majority of the mass is perpendicular to the filament surface (fig. 7.16). The axial angle, α , and the azimuthal angle, θ , were defined as being zero in this position, and a third angle, β , was introduced, to allow for rotation of the myosin head about the normal to the filament surface. All the other parameters remain the same as with the previous head model.

With the introduction of the β rotation, and the non-uniform shape of the myosin head, the axial and azimuthal angles can no longer be simply visualised; in general, the head is no longer perpendicular to the filament backbone when $\alpha=0^\circ$, and the azimuthal angle is no longer perpendicular to the backbone when $\theta = 0^\circ$, unless $\beta=0^\circ$.

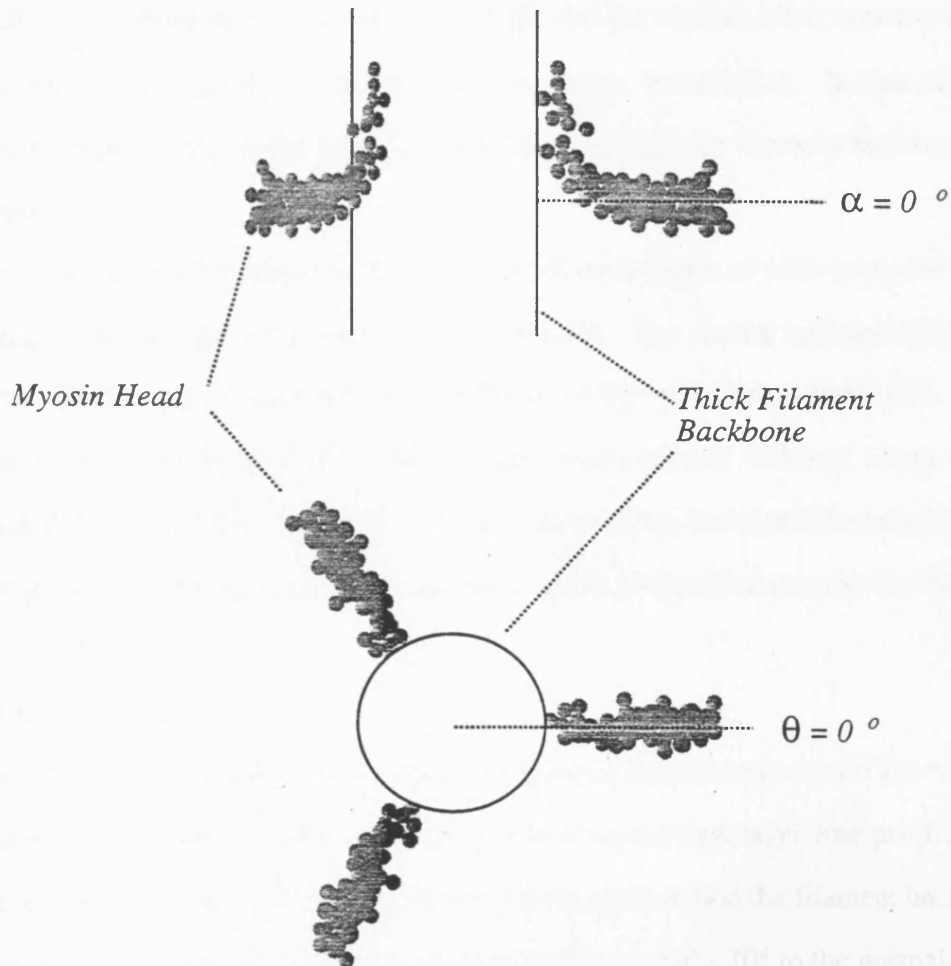


Figure 7.16: Default Orientation for the Complex Myosin Head Model

This is the orientation of the myosin head at $\alpha = 0^\circ$; $\beta = 0^\circ$; $\theta = 0^\circ$. For clarity, only one myosin head has been placed at each point in the helix in this figure.

7.4.1 Meridional Reflections

The α and β angles, and the vertical offset between the two myosin heads, were varied in combination to produce a good meridional intensity match. A similar distortion group to that found with the simple head model was determined, with $d_1=d_2=13.3\text{nm}$. The best fit meridian was obtained with $\alpha_1=\alpha_2=90^\circ$, $\beta=0^\circ$, and the vertical offset between heads in a subunit was 2.5nm , giving an axial width of $\sim 14\text{nm}$ (model C1). In this subunit arrangement, the main mass of the myosin head lies parallel to the filament backbone, as shown in figure 7.17.

This was the best fit meridian (fig. 7.18), with an R-factor of 13% (over the $0.03\text{-}0.15\text{nm}^{-1}$ range), but not the only one to give a good fit. The second best meridian was obtained when $\beta=90^\circ$, $\alpha=0^\circ$, and the offset between heads was 6nm (model C2). This arrangement is shown in figure 7.19, with a similar axial subunit width of 14nm , but a slightly worse R-factor of 15% (fig. 7.20). The myosin head has been turned around so that the golf club shape now lies in the equatorial plane, roughly perpendicular to the best model.

7.4.2 Layer Lines

The off-meridional patterns for both meridional models were tested for various azimuthal angles and centre of mass radii. In model C1a, the best layer line profiles and relative intensities were obtained when the two heads wrapped around the filament backbone so that the main mass of the heads made azimuthal angles of $\sim 50^\circ - 70^\circ$ to the normal to the backbone (fig. 7.17, 7.21). The direction of wrapping was significant too; wrapping the same amount but in the opposite (negative θ) sense gave poor layer line intensities. Indeed, as the myosin heads moved away from the best azimuthal angle towards and past the normal to the backbone, the relative intensities of the layer lines steadily worsened.

In model C2a (fig. 7.19), the azimuthal arrangement was quite different: the best layer line profiles and relative intensities were obtained when the myosin heads crossed over and were approximately tangential to the backbone surface. The resulting pattern (fig. 7.22) is a reasonable match, although not as good as model C1a, especially at higher resolutions.

The semi-random superlattice cell was used again, with good results. An interesting observation is that the lattice disorder needed to reduce the Bragg sampling peaks

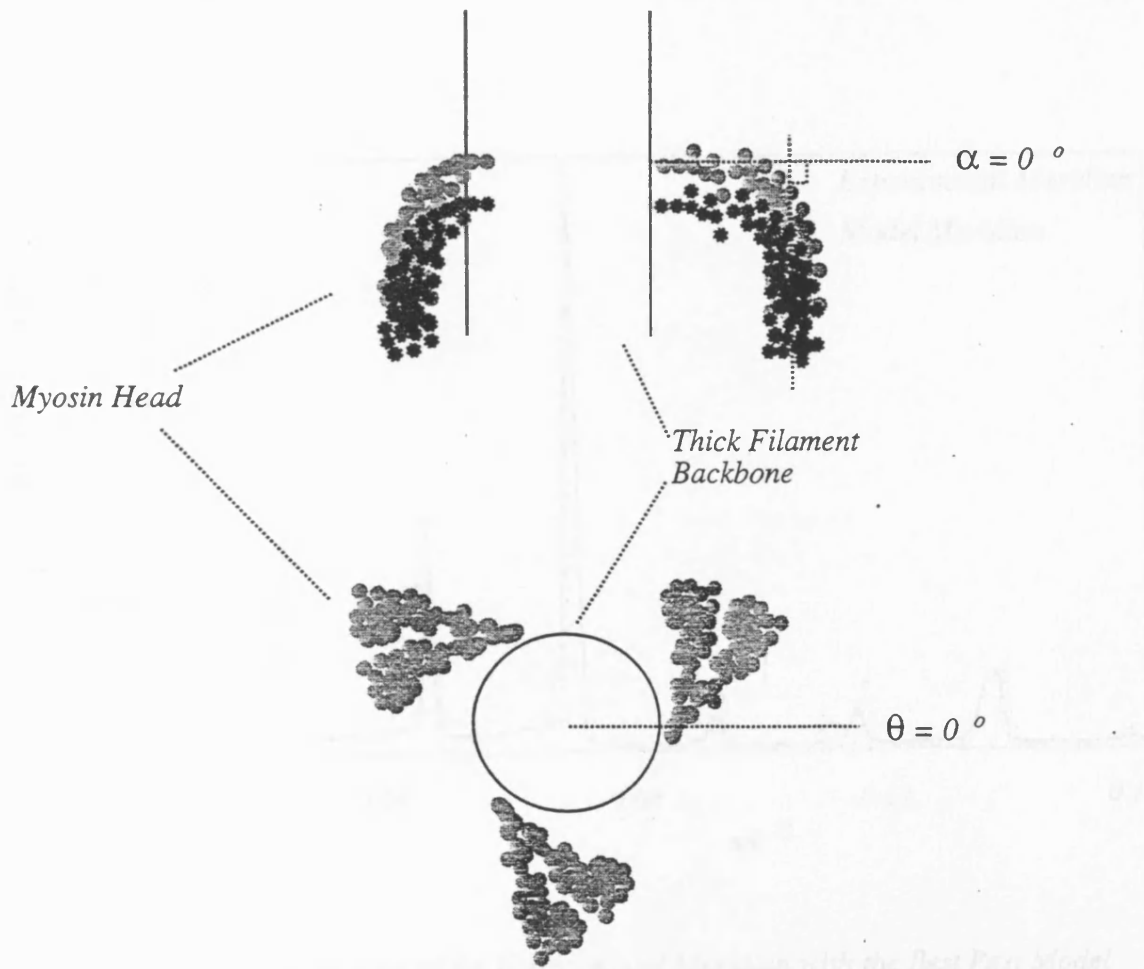


Figure 7.17: Orientation of the Complex Myosin Head in the Best Rest Model C1a

For the sake of clarity, the lower of the two heads pictured here is represented by darker spheres.

$$\alpha = 90^\circ$$

$$\beta = 0^\circ$$

$$\theta = 50^\circ ; 70^\circ$$

Vertical offset between heads is 2.5nm;

Azimuthal offset between heads is 2.0nm.

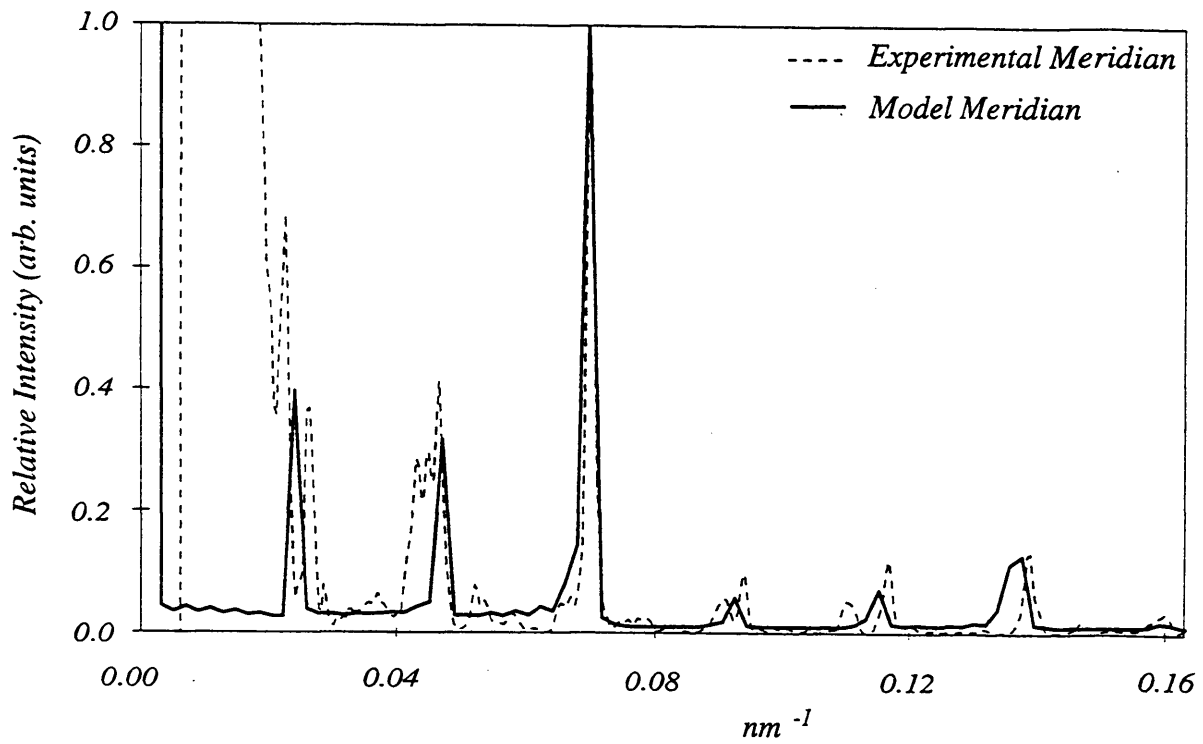


Figure 7.18: Comparison of the Experimental Meridian with the Best Rest Model Obtained using the Complex Myosin Head Model: Model C1

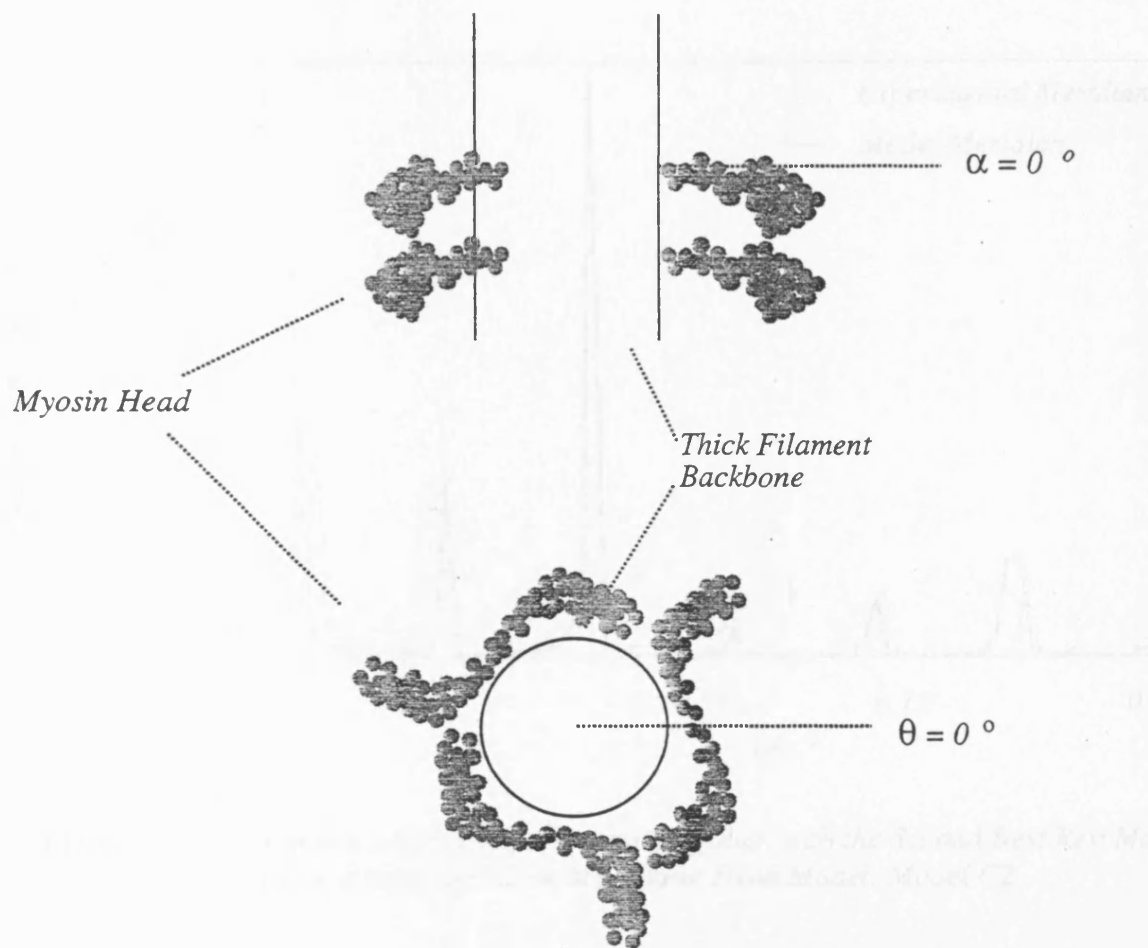


Figure 7.19: Orientation of the Complex Myosin Head in the Second Best Rest Model C2a

$\alpha = 0^\circ$
 $\beta = 90^\circ$
 $\theta = -90^\circ; 90^\circ$
 Vertical offset between heads is 6.0nm;
 Azimuthal offset between heads is 0nm.

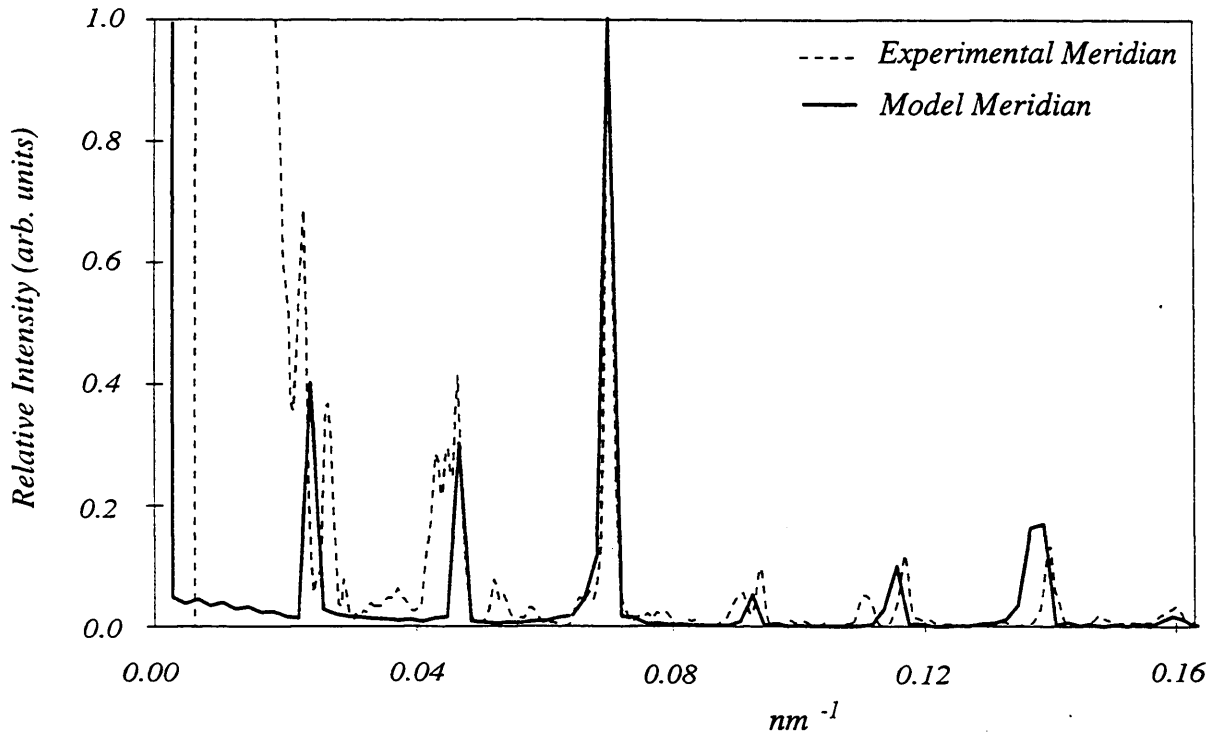


Figure 7.20: Comparison of the Experimental Meridian with the Second Best Rest Model Obtained using the Complex Myosin Head Model: Model C2

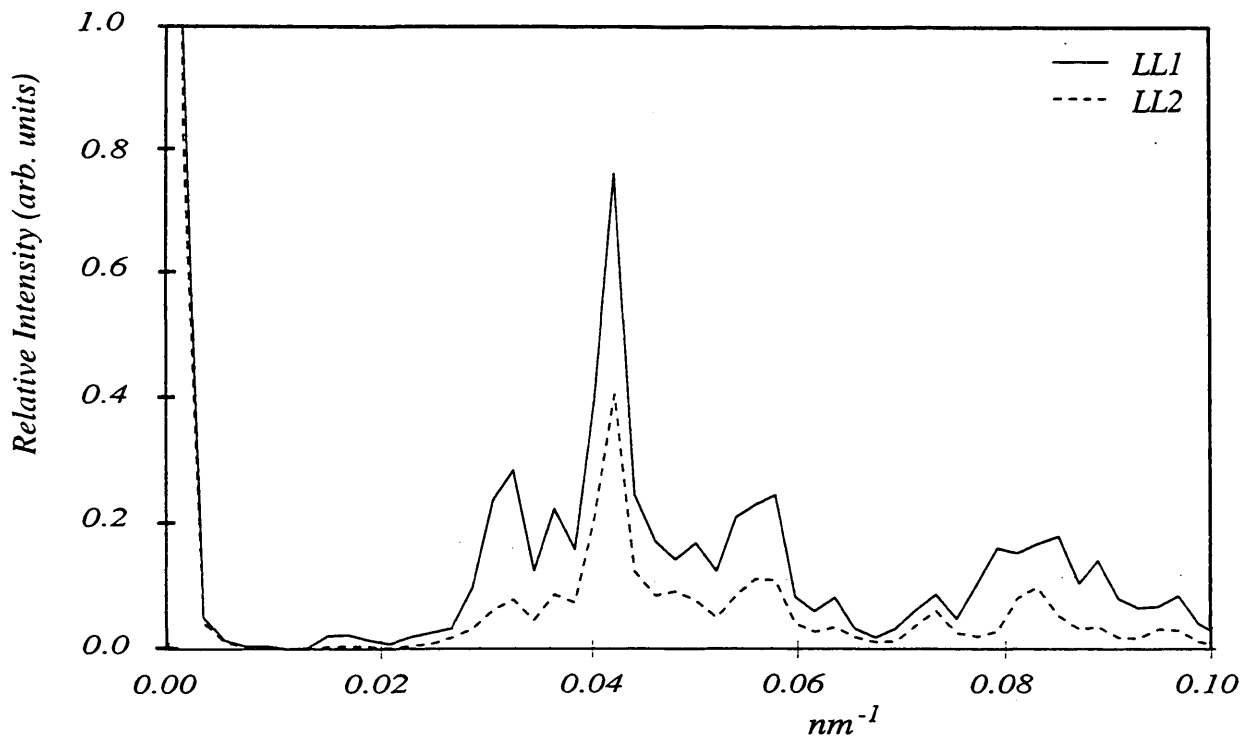


Figure 7.21: First and Second Myosin Layer Lines from the Best Rest Model obtained using the Complex Myosin Head: Model C1a

Both layer lines show a good profile, with three main Bragg peaks sampling the broad Bessel function underneath. LL2 is approximately half the intensity of LL1 (c.f. experimental data in Chapter 5).

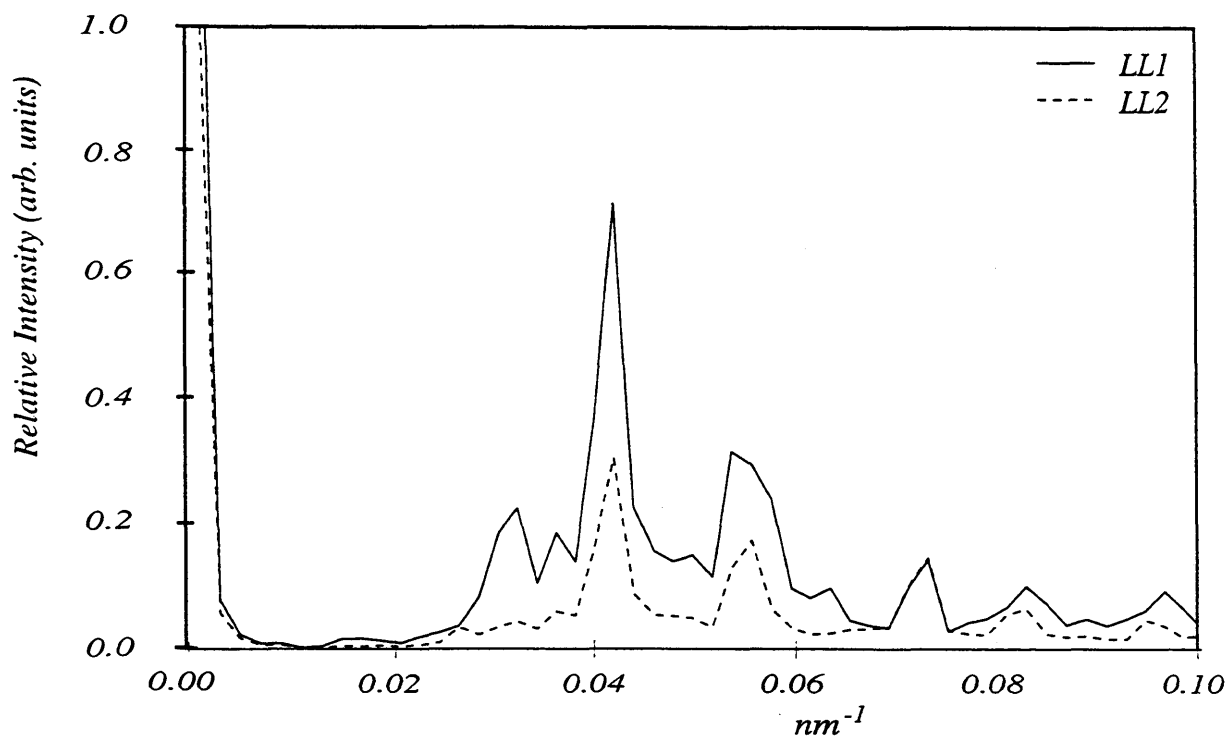


Figure 7.22: First and Second Myosin Layer Lines from the Second Best Rest Model obtained using the Complex Myosin Head: Model C2a

Both layer lines show a good profile, though not as well defined as that from model C1a. Again, the three main Bragg peaks sample the broad Bessel function underneath. LL2 is approximately half the intensity of LL1 (c.f. experimental data in Chapter 5).

to reasonable levels in models U1a and U2a, both based on the simple myosin head, was no longer necessary. Indeed, lattice disorder seemed to have a much less significant effect on the layer line sampling with the high resolution head model; lattice disorders will be investigated in detail in the next chapter. The equatorial plots produced the correct [10]:[11] intensity ratios with both models C1a and C2a.

The width of the reflections in the experimental diffraction patterns indicate that the myosin heads are held in helical order over about 400nm. The cross-sectional area of a typical skeletal muscle myofibril is of the order of 10^6 nm^2 , equivalent to a few cells of this size, and there are thousands of myofibrils in each muscle fibre. This program models a single cell and could not be expected to reproduce the correct absolute widths of the meridional peaks, but a comparison between various cell sizes and the effects on the meridional widths was a useful study.

Using the myosin head arrangement from model C1a, cells of various size were modelled and their meridional widths compared. Figure 7.23 shows the profile of the first layer line corresponding to cells of diameter 400nm and 200nm. In each case, the number of cells was arranged so that the total number of myosin filaments is the same in both models (210). The profile for the model of three large cells of 70 filaments produced a much sharper meridional peak than the model of seven small cells of 30 filaments each. In addition, the intensity of the meridional peak was relatively higher than the rest of the layer line profile for the large cell model. From this exercise, it is clear that the area of the model has a significant effect on the diffraction features produced, and should be carefully considered, especially when comparing different models.

7.5 Discussion of Results

The key factors in modelling the meridional pattern appear to be the axial width of the subunits and their distribution in the distortion group. The best meridional intensity plots (U1, U2, C1, C2) were consistently those produced by an axial subunit width between 13.5 and 14nm, distributed in a compressed distortion group where the myosin head levels were

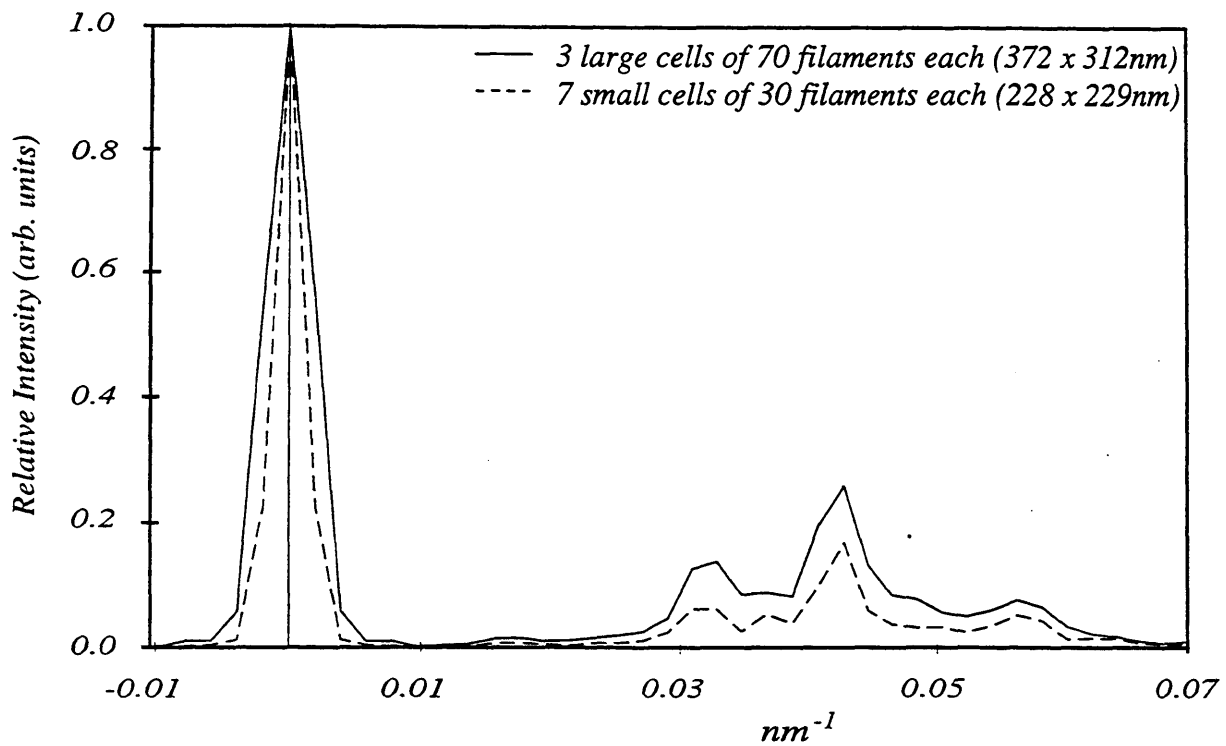


Figure 7.23: Effect of Cell Size on the First Myosin Layer Line Profile

- (a) Profile obtained using large cells, corresponding to long-range order in the filament lattice structure;
- (b) Profile using smaller cells, corresponding to good order being maintained over a smaller area of the lattice.

In each case, the number of filaments in the total number of cells is 210, to maintain an identical total mass overall.

separated by $d_1=d_2=13.3\text{nm}$. The first head of the next distortion group was offset by 16.3nm, producing a distortion group repeat of 43nm.

Other studies support this favoured distortion group: the equivalent spacings in our terminology from various sources are displayed in table 7.1. Malinchik & Lednev's modelling found a good meridional match with an axial separation of $d_1=d_2=13.1\text{nm}$; they also agreed with the finding that the actual head level separations in the distortion group are not as important as the average separation [96]. Stewart & Kensler's electron microscopy analysis of frog skeletal muscle [144] determined that the corresponding spacings were $d_1=12.9\text{nm}$, $d_2=13.5\text{nm}$, and the distortion group repeated at 42.9nm intervals. The average separation within the group is therefore 13.2nm. Another modelling study, by Squire [140] determined the spacings to be $d_1=12.8\text{nm}$, $d_2=13.8\text{nm}$, giving an average spacing of 13.3nm. These results are all similar to the best distortion group modelled here.

The above models all found that the best match was a compressed distortion group, but a few studies favoured an expanded group where the average spacing was $d > 14.3\text{nm}$. Squire's alternative model where $d_1=15.3\text{nm}$ and $d_2=16.3\text{nm}$ gave an average spacing of 15.8nm. Yagi [166] suggested a distribution where $d_1=d_2=16.1\text{nm}$. The displacements from the ideal separations of 14.3nm are therefore of the order of $>1.5\text{nm}$, supporting the finding that to give similar results, somewhat larger displacements are required for an expanded distortion group than for a compressed group.

| Source | Subunit Spacings (nm) | | |
|-------------------------|-----------------------|----------------|---------------|
| | d_1 | d_2 | $d_{average}$ |
| Our Models | 13.3 ± 0.2 | 13.3 ± 0.2 | 13.3 |
| Malinchik & Lednev [96] | 13.1 | 13.1 | 13.1 |
| Stewart & Kensler [144] | 12.9 | 13.5 | 13.2 |
| Squire et al. (1) [140] | 12.8 | 13.8 | 13.3 |
| Squire et al. (2) [140] | 16.3 | 15.3 | 15.8 |
| Yagi et al. [166] | 16.1 | 16.1 | 16.1 |

Table 7.1: Comparison of Distortion Group Spacings

The compressed distortion group seems to have more support than an expanded group. It remains to be seen whether the regular perturbation causing the distortion group

formation has any implications for the internal structure of the thick filament backbone or the arrangement of other thick filament proteins, especially C-protein, in the filament [17]. An interesting observation is that the compressed arrangement spacing of 13.3nm is a close match to the actin axial translation; 13.6nm corresponds to five actin monomers with an axial rise of 2.73nm. It has been pointed out that if three myosin heads attach to the fifth, tenth and sixteenth actin monomers in a sixteen monomer length of thin filament (5-5-6 model; fig. 7.24), the average myosin head separation over the whole thick filament is 14.5nm - close to the 14.3nm experimental value. The resulting separations within the distortion group would then be $d_1=d_2=13.6$ nm. This could indicate that there is some actin-myosin interaction in rest muscle, perhaps weak binding, which is aided by the compressed distortion group. Further discussion of the 5-5-6 model is presented in §8.3.

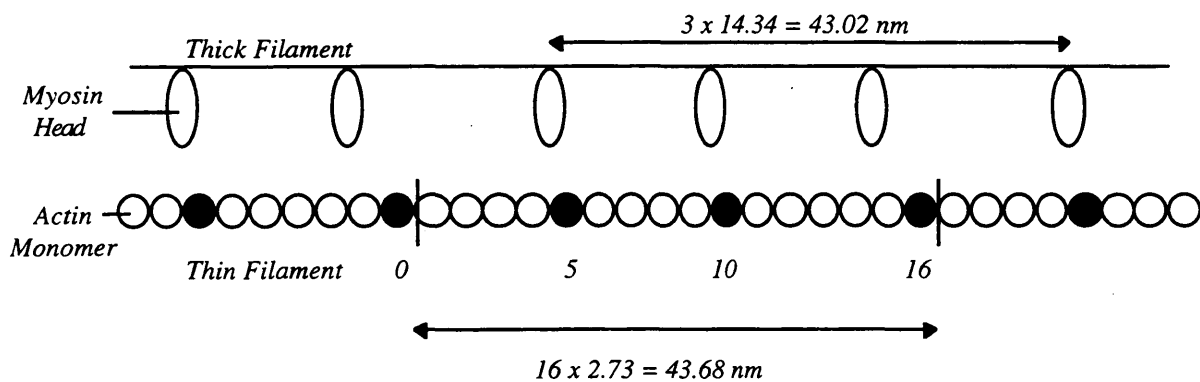


Figure 7.24: Near Matching of Thick and Thin Filament Repeats Allows the Formation of a 5-5-6 model (see text).

The 14nm axial width of the best model, C1a, is slightly larger than the 12.6nm axial width of Malinchik & Lednev [96]. This is probably related to the fact that they approximated each myosin head level to a uniform function. Our whole model representation would result in a more realistic axial shape, with the mass distributed less evenly over the axial width. An interesting observation is that the axial width of each subunit (14nm) is greater than the separation of the three heads within each distortion group (13.3nm), leading to the conclusion that the heads from one level probably overlap slightly with the heads from adjacent levels. Previous studies on tarantula thick filaments have made

similar observations [171, 176], and Offer et al. went further by proposing an interaction between the overlapping heads [175].

The axial width does not, however, give any indication about whether the myosin heads in each subunit point in opposite directions along the filament axis, or in the same direction. Public opinion is divided on this point: a number of electron microscopy studies have put the myosin heads pointing in opposite directions along the backbone [22, 50, 144, 96], whilst others disagree [16]. The modelling results presented here support the latter case. The high azimuthal angles taken by the myosin heads indicate that the thick filaments form compact structures in rest muscle, a view supported by other modelling studies [50, 96].

The large effect which the azimuthal angles have on the relative intensities of the layer lines can be explained in terms of the helix net shown in figure 7.25. The axial orientation of the myosin head determines the extent of the head when it is projected onto the helical net; the azimuthal angle determines which of the sets of helical planes the head points along. The more parallel the projected head is to a given set of planes, the more intense the corresponding layer line will be. An azimuthal angle of around 60° in model C1a (fig. 7.17) results in most of the mass pointing along the set of planes which give rise to the first layer line, and across all the other sets to some extent. Thus the first layer line is much more intense than the other layer lines.

It is interesting to note that despite the completely different azimuthal arrangements of the myosin heads in model C2a (fig. 7.19), the majority of the mass in the myosin heads still follows the same helical planes as the best model (C1a). This explains why two apparently different models give very similar diffraction patterns.

This study also indicates that the thin filament lattice is more disordered than the thick filament lattice, as evidenced by the lack of sampling on the actin layer lines compared to the clear sampling on the myosin layer lines. The ratio of thin:thick filament rms. disorder in the best model is 1.6:1; this ratio is in agreement with Malinchik & Yu's result, and supports their suggestion that the mass ratio of the filaments, which would be expected to affect any thermal disorder in the model, governs this ratio [95].

The best fits to the experimental data are all obtained from models where the average centre of mass of the myosin heads is typically at 13.5nm. This is slightly higher than the generally accepted 12.5-13nm [70, 50]; Huxley & Brown originally determined that the outer radius of the myosin heads measured from the first layer line profile was ~13nm [50]. The present modelling work supports their further suggestion that this was not actually the outer radius, but the point after which the mass became smeared out due to disorder.

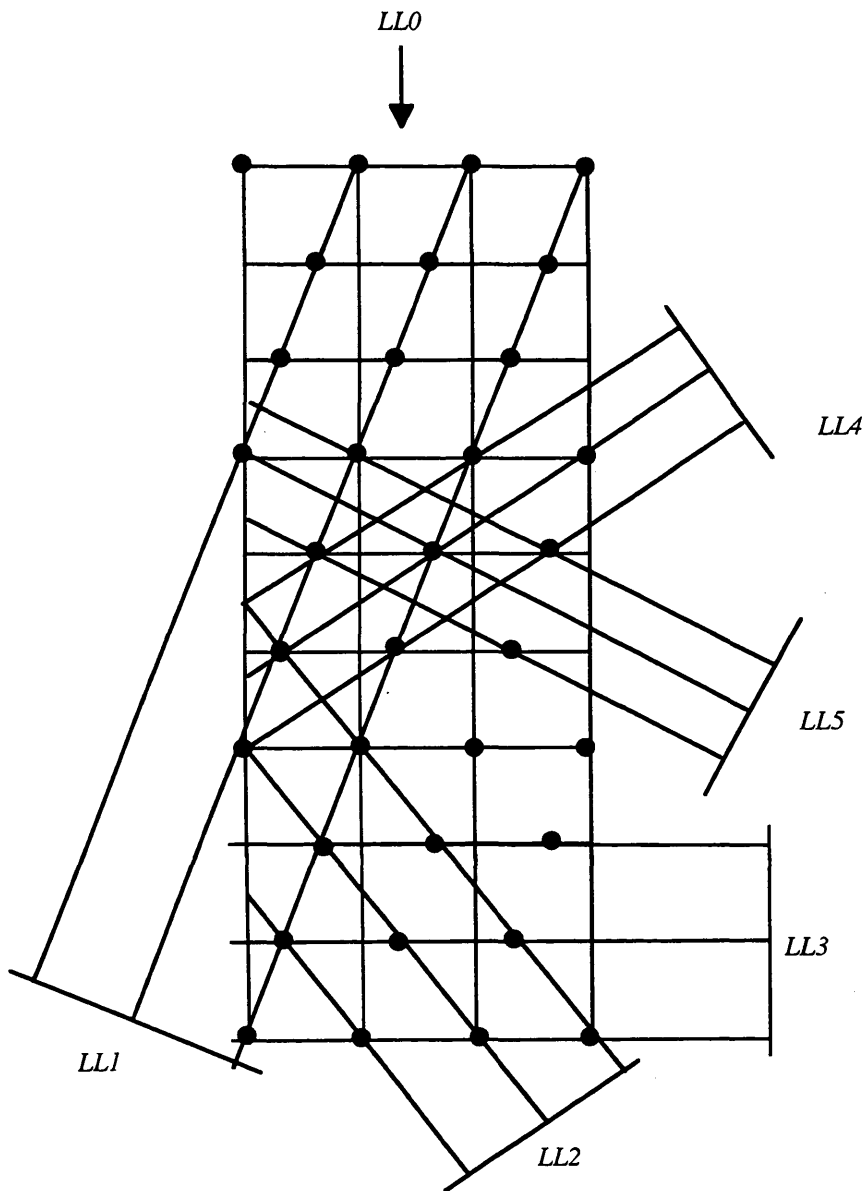


Figure 7.25: *Helix Net: Example of Helix Planes (after Squire [133])*

The set of planes labelled LLn gives rise to the nth myosin layer line in the diffraction pattern

Chapter 8: Modelling of Contracting Muscle

8.1: Introduction

8.2: Studies of Disorder

8.2.1: Disorder Within the Helix

8.2.2: Disorder Between Helices

8.3: Isometrically Contracting Muscle

8.3.1: Meridional Intensity Distribution

8.3.2: Spatial Considerations

8.4: Unloaded Shortening at Zero Tension

8.5: Summary

8.1 Introduction

This chapter follows on from the work done in the previous chapter to determine the macromolecular rest muscle structure. Using the best rest model obtained with the uniform myosin head representation, U1a (§7.3) as a basis, further investigation was made into the structural changes which might take place during contraction. The first part of this investigation involved studying the effect of introducing disorder to the key parameters defining the model structure. The results of this study were then applied to the specific cases of muscle structure at the peak of isometric contraction and during unloaded shortening at zero tension. The overall aim was to probe the effects of various disorders and determine how effectively they could be modelled, rather than to reproduce the experimental data from the isometrically contracting or unloaded shortening muscle closely.

The effects of the different disorders were essentially the same for both models of the myosin head, though they were slightly less significant in the case of the more complex myosin head model. This can probably be attributed to the fact that the complex head model had a non-uniform structure to start with, which would be less sensitive to small changes in head orientation than the uniform rod of the simple head model. The simple myosin head was used in the disorder study because its uniform structure made it easier to visualise the structural effects of the physical changes involved.

8.2 Studies of Disorder

In practice, disorders in polycrystalline materials, such as muscle, fall into one of two categories: disorder between whole filaments, and disorder within the filament structure itself. This section expands upon the general discussion in Chapter 3.

8.2.1 Disorder Within the Helix

During modelling of the rest structure models, all of the myosin heads were identically oriented and uniformly distributed at their ideal helical positions, save for the regular axial shifts between subsequent head levels required to produce the forbidden myosin meridional reflections. In general, however, the subunits may be disordered positionally and/or orientationally within a single filament: positional disorder refers to the position of the

centre of mass of each myosin head in the filament, whereas orientational disorder refers to the orientation of the heads with respect to the filament backbone. Random isotropic disorder was introduced to several of the key parameters defining the myosin helix, and the effect on the diffraction pattern recorded.

The initial structure in all models was the rest structure in U1a (§7.3), where the axial angles were defined as $\alpha_1=60^\circ$ and $\alpha_2=55^\circ$, the azimuthal angles as $\theta_1=\theta_2=65^\circ$, and the second head was offset vertically by 1.5nm and azimuthally by 2nm from the first. The myosin heads were then randomly allocated an axial orientation in the range $\alpha_0 \pm \Delta\alpha$, where α_0 = the axial angle in the rest model, and the range of disorders tested was $0^\circ < \Delta\alpha < 30^\circ$: at greater ranges than this the myosin heads intruded into the filament backbone. This procedure constrained the average axial angle to α_0 , whilst allowing the individual heads to take a range of values over 60° . As predicted in §3.6.1, the effects on the diffraction pattern were two-fold.

As the myosin heads became more disordered and occupied a wider range of axial angles, all of the myosin meridional reflections decreased in peak intensity and broadened axially. The least affected reflection was the first myosin meridional (1M), whose intensity only dropped slightly (fig. 8.1).

In addition to the meridional effects, disorder in the axial angle was observed to alter the myosin layer line profiles. Random variations in the axial orientation of the myosin heads resulted in the centres of mass of the heads occupying randomly shifted positions, removing to some degree the helical order in the filament. This was transmitted to the diffraction pattern as a partial loss of the underlying Bessel function structure of the layer lines (fig. 8.2). The lost intensity was redistributed into the background to axially smear the layer lines slightly.

In a variation on the introduction of axial disorder to the rest model, a further set of identical models were based on the U1a structure with the axial angles set to $\alpha_1=\alpha_2=0^\circ$ (perpendicular to the filament axis), rather than the previous $\alpha_1=\alpha_2=60^\circ$. The range of disorder tested was increased to $0^\circ < \Delta\alpha < 90^\circ$ without the myosin heads encroaching on the filament backbone. The results were similar to those described immediately above, but the diffraction patterns were more sensitive to the smaller levels of disorder: since the

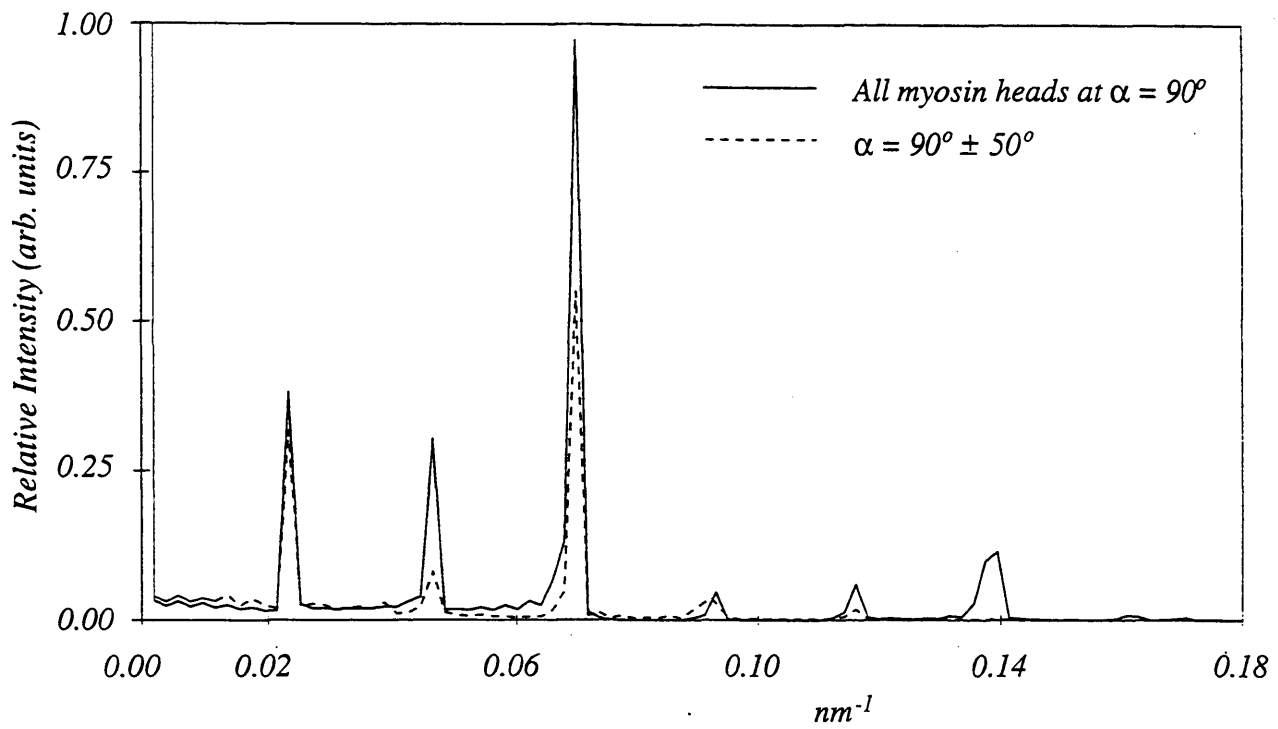


Figure 8.1: Meridional Effects of Randomly Varying the Axial Angle of the Myosin Heads

The introduction of random disorder to the axial angle, α , taken by the myosin heads results in a loss of intensity in all the meridional reflections. The 2M and 3M peaks are most strongly affected.

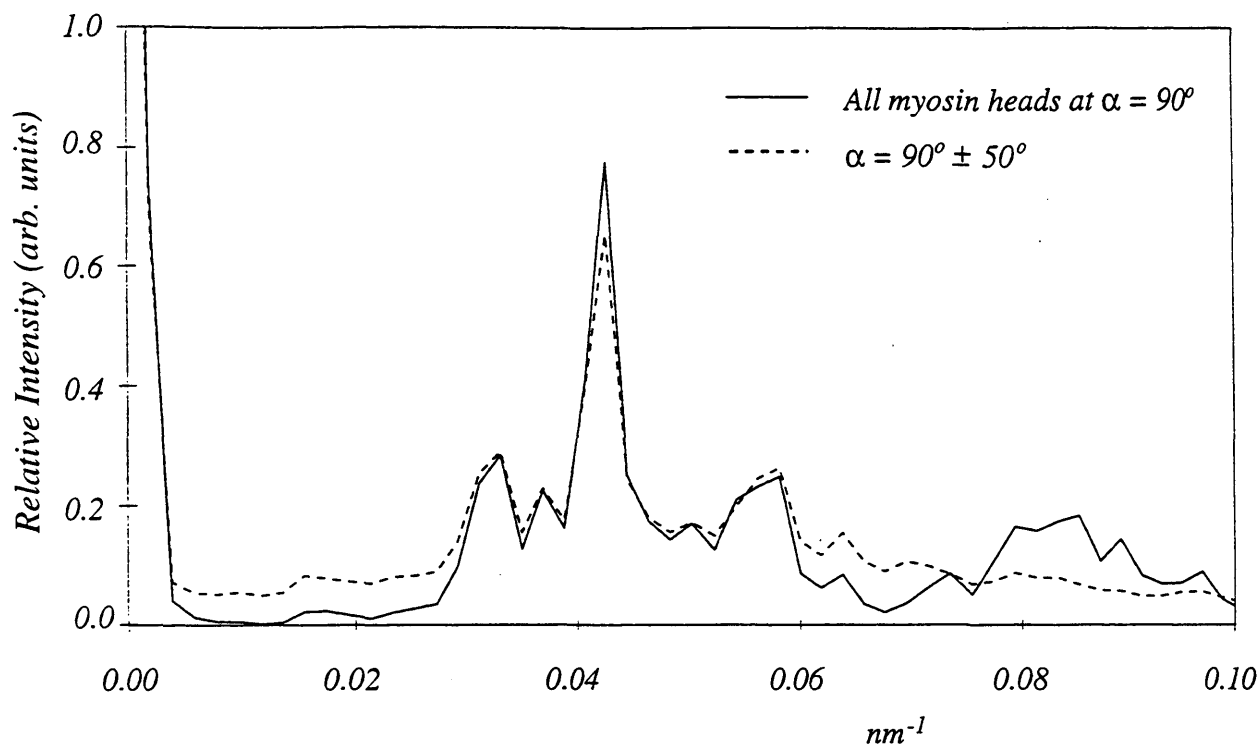


Figure 8.2: *Effect on the First Myosin Layer Line of Randomly Varying the Axial Angle of the Myosin Heads*

The introduction of random disorder to the axial angle, α , results in the partial loss of the Bessel function structure underlying the layer line. The intensity is redistributed axially into the background.

myosin heads were initially perpendicular to the filament axis, a position which resulted in a very sharp axial mass projection, small variations in the axial head orientation in either direction (\pm) detracted from the regularity of the mass projection. Thus the meridional reflections arising from the axial mass projections were more sensitive to the increased angular range about $\alpha_0 = 0^\circ$ than about the higher angle of $\alpha_0 = 60^\circ$.

The second parameter to be disordered was θ , the azimuthal angle of the myosin heads. The heads were randomly allocated azimuthal angles in the range $\theta_0 \pm \Delta\theta$, where θ_0 = the initial angle in the rest model U1a (65°), and $0^\circ < \Delta\theta < 40^\circ$ was the range of disorder extents tested: at greater ranges than this, the myosin heads again encroached upon the filament backbone. A second set of models were built where the undisordered azimuthal angle was set to $\theta_0 = 0^\circ$ (perpendicular to the filament axis), and the range of disorders was increased to $0^\circ < \Delta\theta < 90^\circ$.

Since the axial mass projection plane is insensitive to such variations, which are observed only in the equatorial plane, the azimuthal angle variation did not affect the meridional myosin reflections. Conversely, the layer line profiles were strongly affected: the loss of helical order, caused primarily by the shifting radius of centre of mass of myosin heads fixed at one end to the backbone as their azimuthal angles changed, largely destroyed the Bessel function structure underlying the layer lines, leaving a very different shape to the profile (fig. 8.3). The row line profile in the region of the [10] and [11] equatorial reflections revealed that the intensity is redistributed between the layer lines, adding to the background in these regions (fig. 8.4).

For a given radius of centre of mass, random variations in the azimuthal angles taken by individual heads had little effect on the equatorial intensities. Although a cross sectional slice through a single azimuthally disordered filament clearly showed the random orientations, the averaging effect of the equatorial mass projection along the filament axis rendered the corresponding diffraction features largely insensitive to the disorder.

It is important to differentiate between those effects which are due to the change of orientation, and those which are secondary effects due to the way in which changing the orientation of heads attached at one end to the filament backbone alters the radius of the centres of mass of the heads. In both cases of angular disorder, the disordering of the

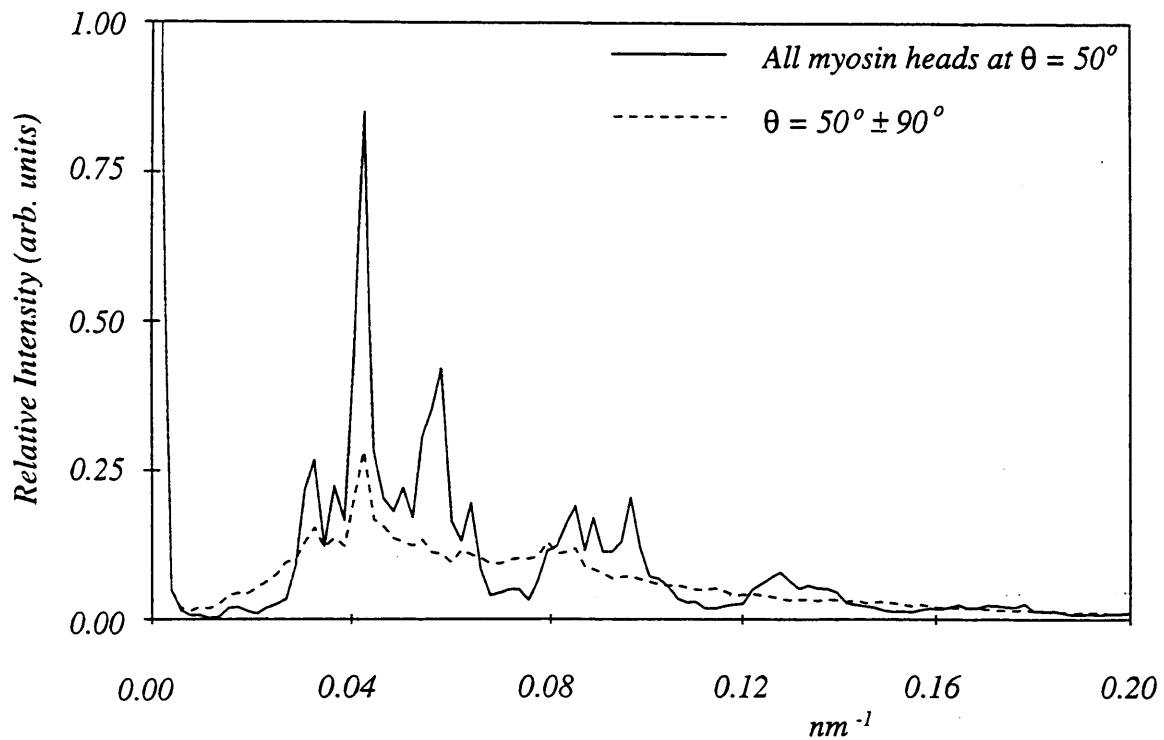


Figure 8.3: *Effect of Randomly Varying the Azimuthal Angle of the Myosin Heads*

Introducing random disorder to the azimuthal angle, θ , taken by the myosin heads results in a definite change of shape of the layer lines. The underlying Bessel structure is destroyed.

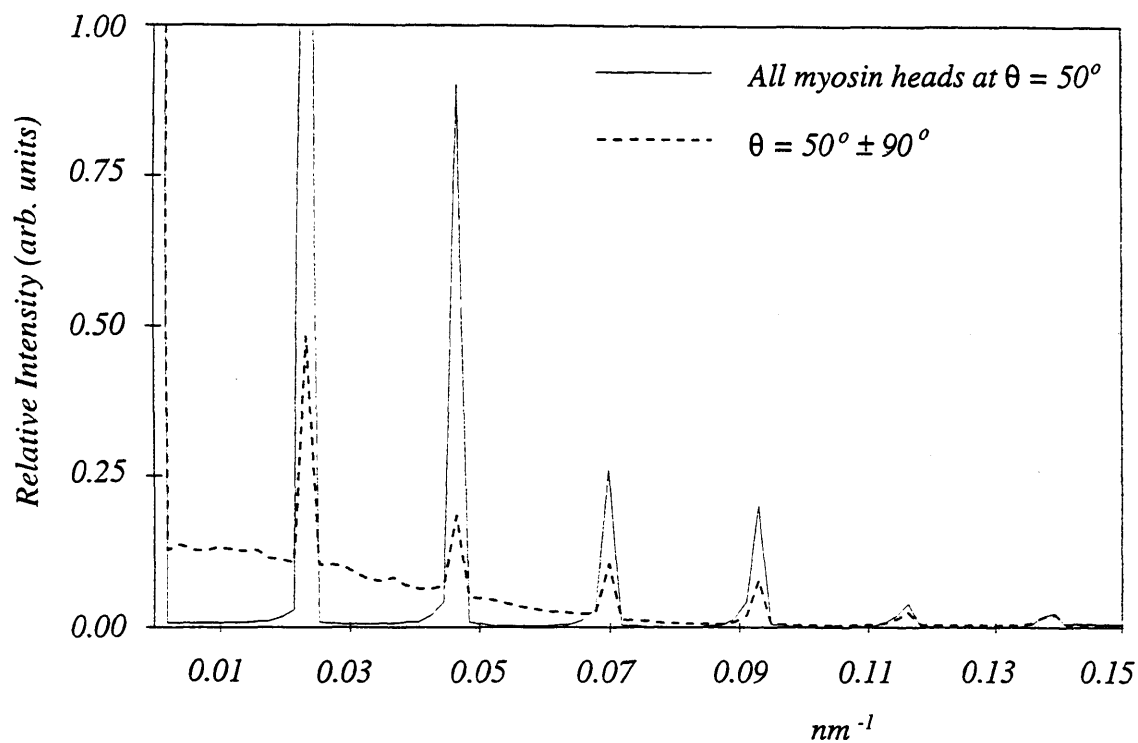


Figure 8.4: *Redistribution of the Intensity Lost by Introducing Random Disorder to the Azimuthal Angle of the Myosin Heads*

Randomising the azimuthal angle, q , causes the background between the myosin layer lines to increase due to the redistribution of the intensity lost from the Bessel structure of the layer line profile.

centres of mass of the myosin heads was not enough to explain the significant changes observed in the diffraction pattern. A set of models where the radius of centre of mass was allowed to vary randomly by up to $\pm 2\text{nm}$ without altering the azimuthal or axial orientation of the individual heads showed that such disorder did indeed remove some sampling from the layer lines, but on a much smaller scale than was observed with orientational changes.

Regular axial shifts of the myosin head levels were introduced to the rest model structures to reproduce the forbidden meridional reflections, as described in some detail in Chapter 7. The key point here is that the shifts were regularly repeated displacements, repeated along the thick filament structure in the form of a distortion group. The introduction of random axial shifts, without altering the orientations of the myosin heads, had markedly different results to the presence of regular axial shifts.

Random displacements of the axial positions of the myosin heads in a range of up to $\pm 4\text{nm}$ were introduced to the already regularly displaced head levels. The meridional intensity distribution was most significantly affected, evidenced in particular by a large decrease in the 3M myosin meridional reflection: even a $\pm 0.5\text{nm}$ range about the rest distribution caused the 3M and 6M reflections to lose intensity. At $\pm 4\text{nm}$, the intensity of the first layer line dropped by around 10%, and the higher order layer lines were even more strongly affected.

Eventually, the axial disorder is enough to effectively remove the regular perturbations from the axial distribution of head levels, and the forbidden reflections disappear. The intensity was redistributed to raise the background on either side of the layer lines (fig. 8.5). The equatorial reflections remained unaffected, the equatorial plane being insensitive to strictly axial changes.

In this set of models, the source of the axial displacement was a shifting of the entire myosin head, without change to its orientation. However, it was noted that the effects were similar to those observed with disordered axial myosin head angles. This was a side effect of fixing the myosin heads to the backbone at one end, and then allowing the axial angles to change: the axial position of the head's centre of mass would then be highly dependant on the axial angle taken by the head. Axial shifts of $\pm 0.5\text{nm}$ had a comparable effect on the meridian to introducing an axial angular distribution of $\alpha = 60^\circ \pm 10^\circ$.

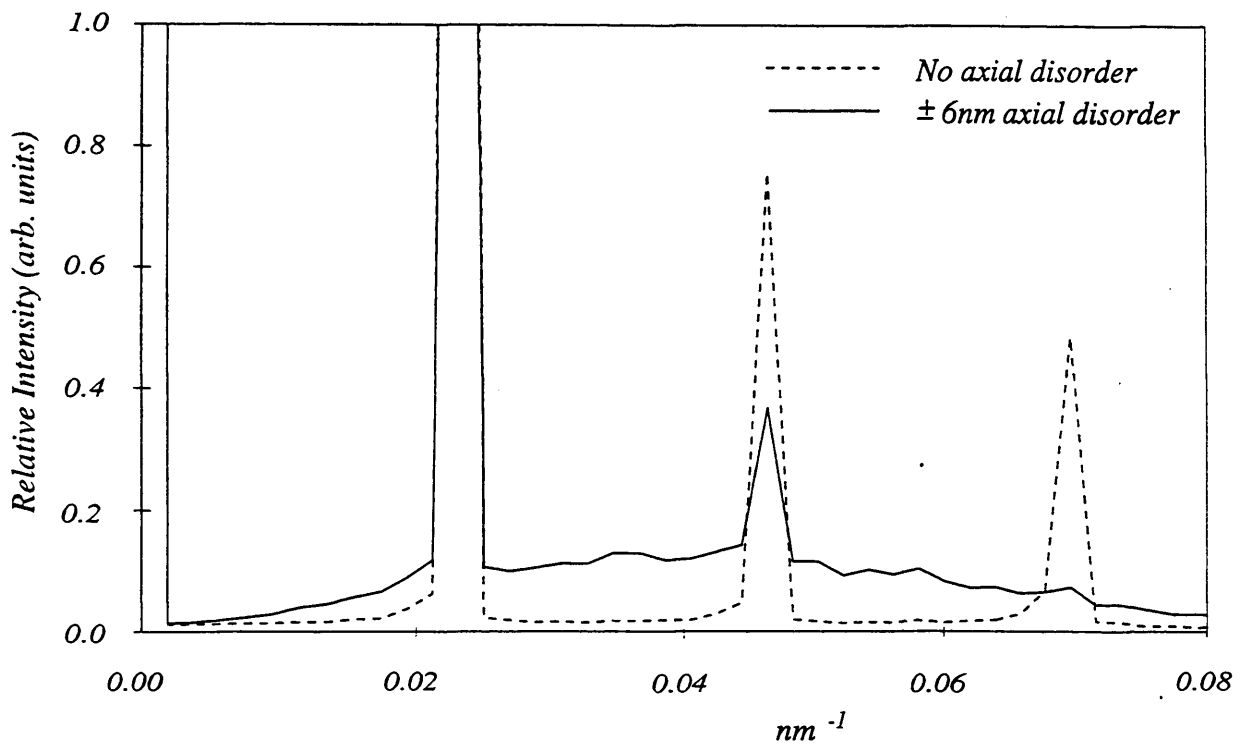


Figure 8.5: *Effect of Introducing Random Axial Shifts to the Position of the Myosin Heads on the Axial Layer Line Profile*

Introducing random disorder to the axial positions of the myosin heads results in the loss of helical order, and the intensity lost from the layer lines is redistributed axially on either side of the layer line. This figure shows an integrated strip running parallel to the meridian in the region of the [10] and [11] equatorial reflections.

The angular position of the base of the myosin heads was determined by the angle between adjacent myosin head pairs: in the ideal triple-start helix, the angular separation was 40° . Here, the separation was randomly chosen in a given range about the $\phi_0 = 40^\circ$ value. The range maximum varied from $\pm 1^\circ$ up to $\pm 20^\circ$: in the latter case, any point on the filament circumference may have been the site of a myosin head pair. Both non-cumulative and cumulative angular distortions were tested.

In the case of non-cumulative angular disorder, a range of $\pm 10^\circ$ caused a decrease in the integrated intensity of the first myosin layer line of around 5%. The intensity was redistributed axially into the background between layer lines, causing it to rise near the centre of the diffraction pattern (fig. 8.6). Radially, the sampling of the layer lines was greatly reduced.

Cumulative angular disorder had a much more significant effect: a range of $\pm 10^\circ$ caused a decrease of around 45% in the first myosin layer line. However, the intensity was redistributed axially in a more localised way on either side of the reduced layer line (fig. 8.7), rather than evenly into the background. For large disorders, the forbidden layer lines corresponding to $n=1, 2, 4, 5$ etc. were clearly visible in addition to the $n=0, 3, 6$ etc. ($l=0,1,2$ etc.) layer lines. These layer lines were forbidden by the triple helix structure, which removed all layer lines except those corresponding to $n = 3 \times \text{integer}$ (§3.5.1). Their return indicated that the triple helix structure was destroyed by the cumulative disorder.

In practice, any combination of the disorders discussed here may be observed, and modelling such combinations illustrated some serious problems. When two or more types of disorder were included in a model, the effects of each were combined in such a way that some features were masked and some were accentuated. It became impossible, with this relatively simple modelling procedure, to distinguish the effects of the individual disorders.

As an example, figure 8.8 shows the result of introducing disorder into both the azimuthal and axial orientation of the myosin heads. Although introducing axial disorder had a significant effect on the diffraction patterns, as seen above, when combined with azimuthal disorder, little additional effect was observed. In practice, this means that when trying to determine the contributing factors to the diffraction pattern, the level of axial disorder is at best an unknown quantity, and at worst may be overlooked entirely.

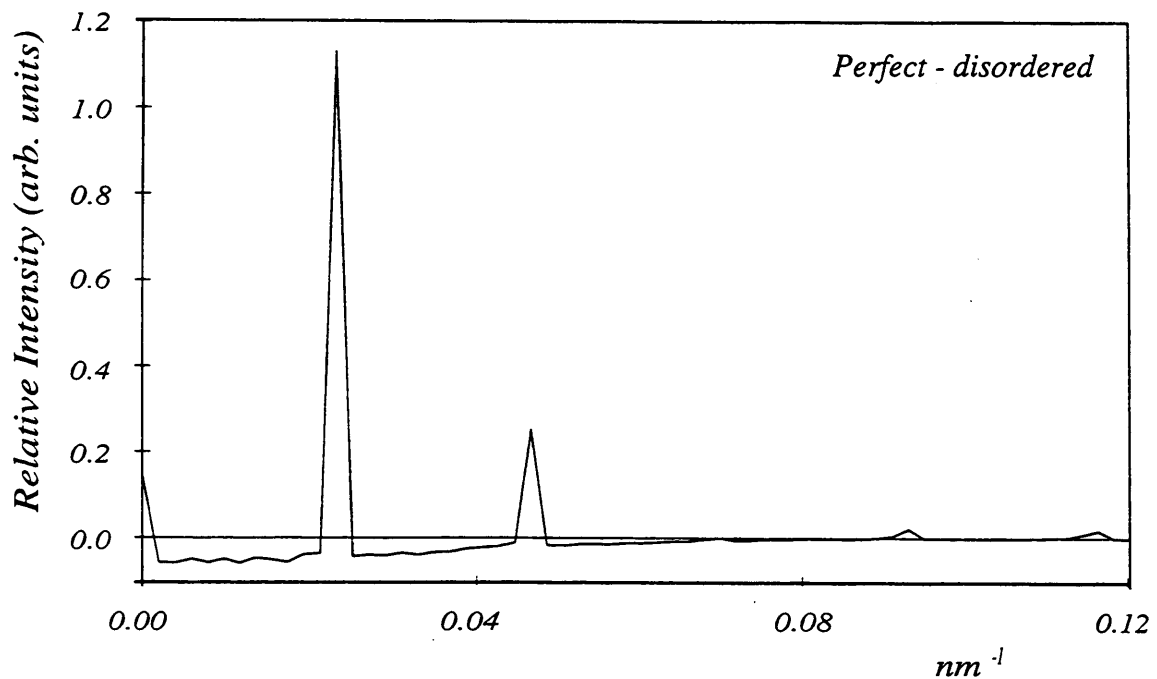


Figure 8.6: *Effect of Non-Cumulative Angular Disorder on the Axial Layer Line Profile*

This figure shows a difference plot of an axial strip parallel to the meridian in the region of the [10] and [11] equatorial reflections. The difference is between the perfect case with no angular disorder (i.e. the angular rotation between adjacent myosin head pairs is 40°) and the case with $\pm 10^\circ$ non-cumulative random isotropic disorder in the angular separation. The non-cumulative disorder causes the intensity lost from the layer lines to be redistributed into the background of the pattern. Compare with figure 8.7 for cumulative disorder.

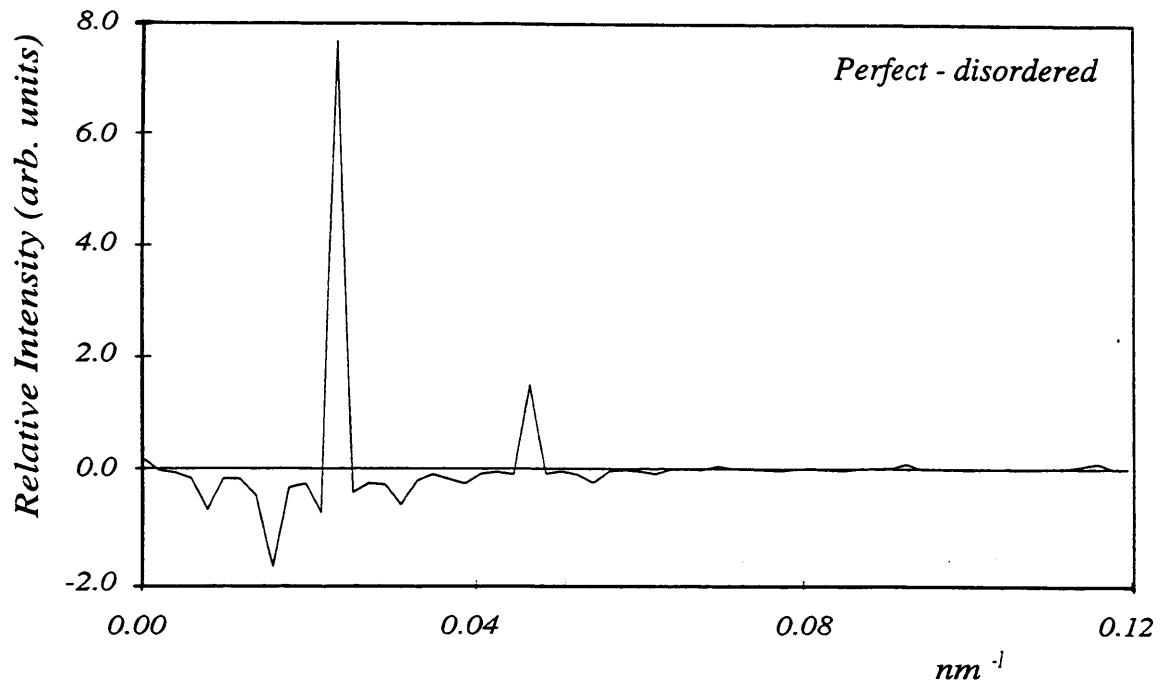


Figure 8.7: *Effect of Cumulative Angular Disorder on the Axial Layer Line Profile*

This figure shows a difference plot of an axial strip parallel to the meridian in the region of the [10] and [11] equatorial reflections. The difference is between the perfect case with no angular disorder (i.e. the angular rotation between adjacent myosin head pairs is 40°) and the case with $\pm 10^\circ$ cumulative random isotropic disorder in the angular separation. The cumulative disorder causes the intensity lost from the layer lines to be redistributed locally on either side of the layer line. Compare with figure 8.6 for non-cumulative disorder.

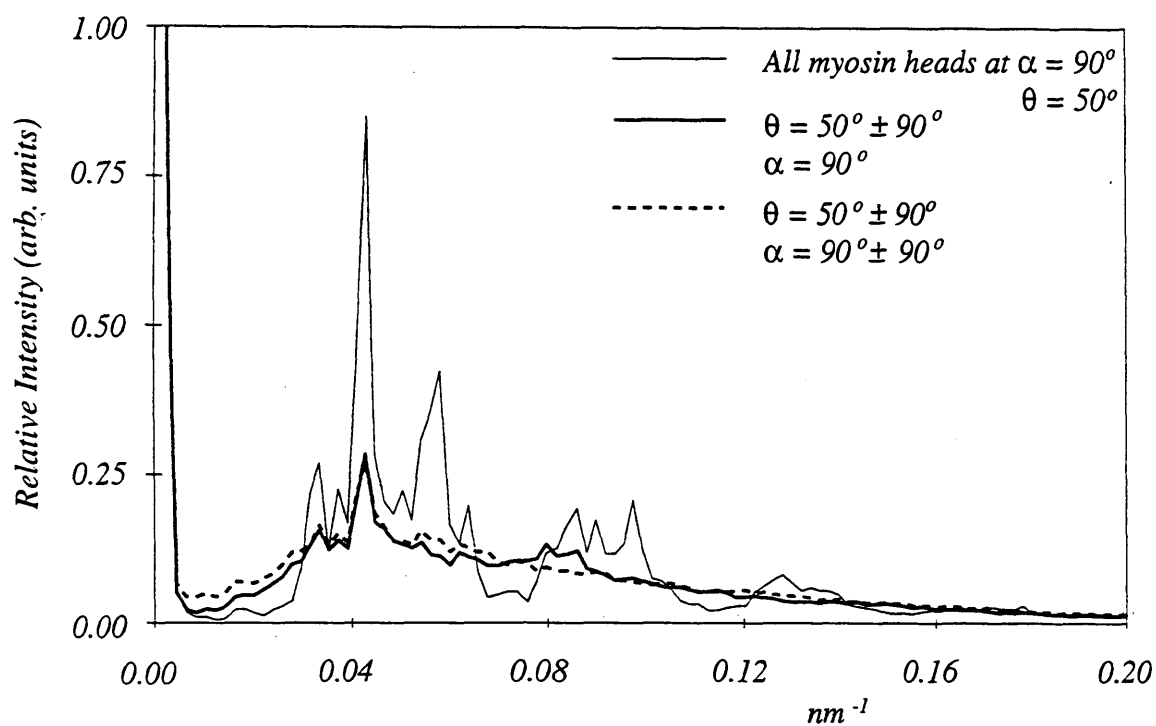


Figure 8.8: Effect of Randomly Varying both the Axial and Azimuthal Angles of the Myosin Heads

Introducing random disorder to the azimuthal angle, θ , taken by the myosin heads results in a significant loss of the Bessel structure of the first Myosin layer Line. However, introducing further disorder in the form of randomising the axial head angle, α , adds little to the structure loss. Once the structure is disordered in some manner, further disorder has a much less significant effect.

8.2.2 Disorder Between Helices

The main source of disorder between filaments in a polycrystalline material is lattice disorder, or net distortions, as described in §3.5.2. In the lattice plane, net distortions are seen as an increase in the effective cross-section of the filaments. The displacements from the ideal lattice points are averaged over the whole model cross section, resulting in a poorer filament definition compared to the average of the ordered filaments. The main result of this is seen in the equatorial reflections.

As the averaged mass projection spreads out radially, the mass in the [10] planes and the corresponding [10] equatorial intensity decreases rapidly. The mass in the [11] planes and the corresponding [11] intensity also decrease slightly, but not as rapidly as the [10] intensity. The ratio of $I_{10} : I_{11}$ correspondingly decreases, resulting in an equatorial intensity reversal similar to that observed during isometric contraction. Random displacements of up to $\pm 10\text{nm}$ from the ideal thick filament positions resulted in a decrease of I_{10} to 45% of the perfectly ordered case, and of I_{11} to 65% of the ordered case. The overall drop in the $I_{10} : I_{11}$ ratio was to 70% of the ordered intensity ratio.

When both the thick and thin filaments were disordered, the reverse occurred and the intensity ratio actually increased. Disordering the thin filaments reduced the I_{11} intensity and slightly increased I_{10} . When the effects of disordering both sets filaments were combined, I_{10} decreased a little, but I_{11} decreased far more rapidly to increase the overall intensity ratio.

In §7.5, a ratio of 1.6 for the amount of thick:thin filament disorder in the rest model was estimated, which resulted in the $I_{10} : I_{11}$ ratio doubling for displacements of up to 2nm and 3.2nm from the ideal thick and thin filament positions respectively. This small amount of random isotropic lattice disorder was included to reduce the Bragg peak sampling appearing on the layer line profiles, but disorder was not covered in any great depth. In this more detailed approach, lattice disorder was introduced as random isotropic disorder, disorder of the first kind, and disorder of the second kind (§3.6.2).

The expected differences between the three types of lattice disorder were not observed in practice. The results were very similar in each case: a broadening of the Bragg diffraction peaks radially, and redistribution of the intensity along the continuous helical

transform of the corresponding layer line (fig. 8.9). Disorder of the second kind should have had a much stronger effect on the higher order layer lines, compared to a similar effect on all layer lines for the other two types, but no significant difference was seen. This is likely to be due to the limited scale of the models involved: over a small area, the differences between cumulative and non-cumulative disorders are almost negligible.

An interesting observation is that the lattice disorder also removed the underlying Bessel structure of the layer lines, indicating that a side effect of lattice disorder is the loss of helical order. This is not unexpected because in shifting the filaments away from their ideal positions, the helical planes across the model as a whole are disturbed.

In addition to net distortions in the lattice plane, whole filaments can be shifted axially with respect to each other, which has a much more immediate effect on the helical order. The introduction of axial net distortions to the rest model U1a revealed that, logically, the axial disorder had a strong effect on the meridional reflections: the whole meridian decreased in intensity, whilst maintaining a similar intensity ratio between peaks. Random axial shifts of between $\pm 5\text{nm}$ resulted in an intensity decrease over most of the meridian of almost 90%. The lower order peaks appeared to be slightly less affected than the higher orders, and the 1M peak became progressively more dominant for shifts between $\pm 3\text{nm}$ and greater. However, the peak to peak ratio along the meridian remains remarkably similar to the rest values considering the immense overall intensity drop.

In the off-meridional pattern, axial shifts resulted in the loss of the Bragg peaks on all layer lines. The only exemption was the equator, which is insensitive to such axial modifications. The overall intensities of the layer lines were not affected much, as the intensity lost from the sampling peaks is redistributed along the layer lines.

The filaments can also be randomly rotated about the filament long axis: the orientation of the filaments gave rise to the superlattice structure in §7.3.2, and illustrated that the precise distribution of filament orientations had a strong effect on the Bragg peaks of the layer lines. Random variations in the orientations of the filaments resulted in the redistribution of the Bragg diffraction peaks into the layer lines, leaving the meridional and equatorial projections largely unaffected.

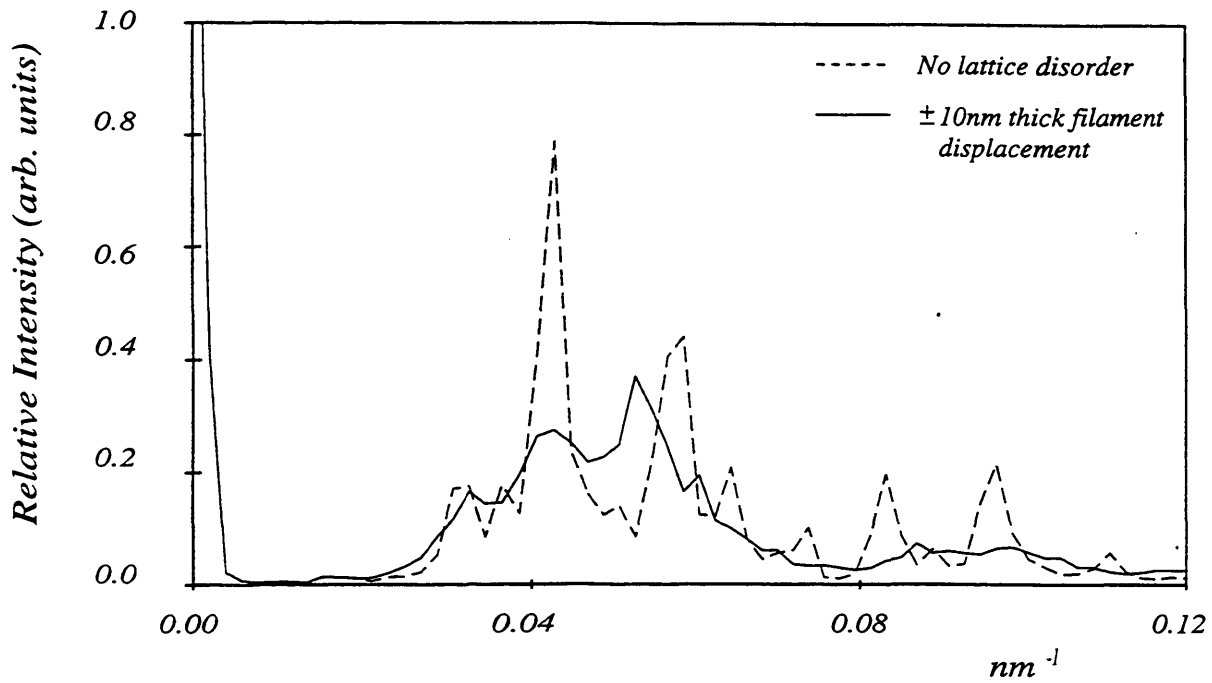


Figure 8.9: *Effect of Lattice Disorder on the First Layer Line Profile*

The sharp Bragg peaks on the layer line are lost with the introduction of lattice disorder. The example shown is for the case of $\pm 10\text{nm}$ random isotropic disorder. At this scale of modelling, little difference is seen with disorders of type 1 (non-cumulative) or type 2 (cumulative).

8.3 Isometrically Contracting Muscle

At the peak of isometric contraction, muscle is in a state of dynamic equilibrium. The diffraction pattern obtained from muscle in this state represents the average structure during the period of exposure to the x-rays. So it is important to remember that in effect, these models are trying to reproduce a structure which has been doubly averaged; over the whole structure and over time.

A “snapshot” image of any structure in dynamic equilibrium might be expected to capture various stages of the dynamic processes involved. For example, a high degree of disorder in the axial angles taken by the myosin heads would support the tilting head model, capturing myosin heads at various points in the tilting cycle. Thus we can interpret the results of the disorder study to the isometric contraction diffraction pattern to provide insight into the dynamic contraction process.

8.3.1 Meridional Intensity Distribution

The meridional changes observed during contraction were significant: the forbidden meridional reflections all but disappeared, and the remaining 3M and 6M reflections broadened axially and increased in intensity. This left just two myosin peaks to model, rather than the six peaks in the rest model, which inevitably resulted in a less confident fit to the data.

The meridional changes could be directly reproduced without resorting to disorder, by simple structural changes. The forbidden reflections arising from the regular axial perturbations in the thick filaments were greatly reduced by lowering the size of the axial perturbations to about half of their values at rest. The myosin head levels within the distortion group were then separated by 13.7nm. This sort of change indicated a structural change, perhaps in the backbone structure itself, which was transferred to the position of the centre of mass of the myosin head level.

Another possibility was that the axial arrangement was disordered such that the average distortion group was the same as that at rest, whilst the actual perturbations varied randomly about the rest positions. This had the same effect on the meridian as reducing the

regular perturbations, reducing the forbidden meridionals. This type of axial disorder is less likely to call for structural changes in the backbone structure. In both cases, the reduced and disordered axial perturbations, the remaining 3M and 6M meridional reflections were augmented by the intensity which had made up the forbidden reflections.

The similarity between the reduction of the axial perturbation and the introduction of axial disorder was to be expected, since both remove the regular axial perturbations: one directly, removing the perturbations themselves; and one indirectly, removing the regularity of the perturbations through disorder, without significantly altering their average size.

A similar increase in the 3M and 6M reflection intensity was observed when the axial angle of the myosin heads was changed so that the main mass of the head was perpendicular to the thick filament backbone. The peaks in the axial mass projection became sharper, resulting in well defined meridional reflections. An axial change of this type did not in itself remove the forbidden meridional reflections, but in combination with a lowering of the axial perturbations as described above, it had the desired effect.

Since similar results were observed for both the reduction of axial perturbation and the change of axial angles described above, this study does not support either the tilting head model or the axial shift model. Further detailed modelling of the meridional region including sarcomere effects may reveal more subtle differences between the two cases, though these differences are likely to be reproducible by a more than one combination of factors, given the scarcity of data to fit.

There is some question as to whether the axial broadening of the meridional peaks is due to the presence of disorder, or to the removal of interference effects brought about by sarcomere misalignment during contraction. Sarcomere studies were beyond the scope of this thesis, so this query could not be addressed at this time. However, if sarcomere effects were neglected, axial broadening was observed when the thick filaments were axially shifted by random amounts relative to one another. There was no need to change the internal structure of the thick filaments to reproduce this change.

The increased spacing of the myosin meridional reflections from 14.3nm to 14.5nm corresponds to an extension of the thick filaments of the order of 1.5%. Such an extension in the modelled filaments reproduced the spacing change as expected. However, 1.5% is a

much larger increase than expected from other studies. A value of 0.3% was calculated for the thin filament extension, using studies of the spacing change of the 2.73nm actin meridional reflection during isometric contraction [159, 75]. Similarly, the myosin extension was estimated by spacing changes during length change experiments to be 0.2-0.3%. Recent work has suggested that nearly all of the elasticity in the sarcomere in fact resides in the thin filaments, which alter their helical structure during contraction to allow a maximum extension of 0.42% [176].

Given the large discrepancy between the calculated and required values of extension, it is highly likely that there is another cause for the spacing change other than simple filament extension. In §7.5, it was suggested that at rest some weak interaction may take place between the actin monomers and myosin heads such that a 5-5-6 model was formed (fig 7.24). Such a model, where the three pairs of myosin heads in a distortion group might attach to the fifth, tenth and sixteenth actin monomers of a sixteen monomer group, produces an average myosin head separation of 14.58nm, which would produce the required spacing change in the myosin meridionals. However, sarcomere interference has a significant effect on the exact spacings of the meridional reflections, and confirmation of this theory cannot be made until such interference effects are accounted for in more complex models.

This section has shown that the observed changes in the meridional region of the diffraction pattern could largely be explained with minimum reference to structural disorder, though without any great degree of accuracy because of the scarcity of data available in the isometric contraction meridian. However, the changes in the rest of the pattern indicate that more subtle motions are taking place, calling for further investigation.

In the rest muscle diffraction patterns, the meridian was the best defined part of the pattern. It was sensible to initially model this region, before moving on to the rest of the pattern. In the case of isometrically contracting muscle, this is not so. The whole diffraction pattern is poorly defined, including the meridian.

8.3.2 Spatial Considerations

Having deduced the effects of various types of forced disorder on the diffraction patterns (§8.2), the next step involved investigating the physical likelihood of such disorders occurring; were they physical possibilities, or, conversely, were they prohibited by the physical arrangement of the molecules within the structure.

Initial models based on the U1a rest structure were built, and each myosin head was assigned a 'favoured' bond, chosen by set criteria. The primary criterion was that the distance between the outer surfaces of the myosin head and the chosen actin monomer was minimal. The choice was further limited by specifying the range of values that the key parameters could take to fulfil the minimum distance criterion. The axial and azimuthal angles corresponding to the favoured bonds were calculated and the distribution of these parameters was analysed. This process of selecting favoured bonds was based on the assumption that there is an electrostatic interaction between the myosin head and the actin filaments, which would therefore depend on their separation.

The key finding of this spatial study was that the minimum distance criterion invariably resulted in a wide distribution of azimuthal angles in the range $\theta=0^\circ\pm 90^\circ$. Figure 8.10 illustrates a typical distribution, for the case where the initial model was the ideal rest structure U1a, and no limits were set on the axial or azimuthal angles. The previous disorder study indicated that such a wide distribution of azimuthal angles would be required to reproduce the myosin layer line profiles during isometric contraction. Similar distributions were also obtained when the initial rest model was modified by changing the axial angles to $\alpha=0^\circ$, and when the axial position of each individual myosin head was allowed to vary by up to 15Å to mimic the flexibility of the S2 section of chain attaching the head S1 section to the backbone. In all cases, the favoured bonds took on a wide distribution of azimuthal angles.

In all these statistical models, an important consideration was how to deal with the second myosin head in each pair: the two companion heads often selected an identical actin monomer, since the compact rest structure of the thick filaments means that the two heads lie very close to each other. The concept of a *spare bond* was introduced, which also accounted for the times when a myosin head selected an actin monomer which was already bound by another myosin head from a different filament. Determining the spare bond meant taking

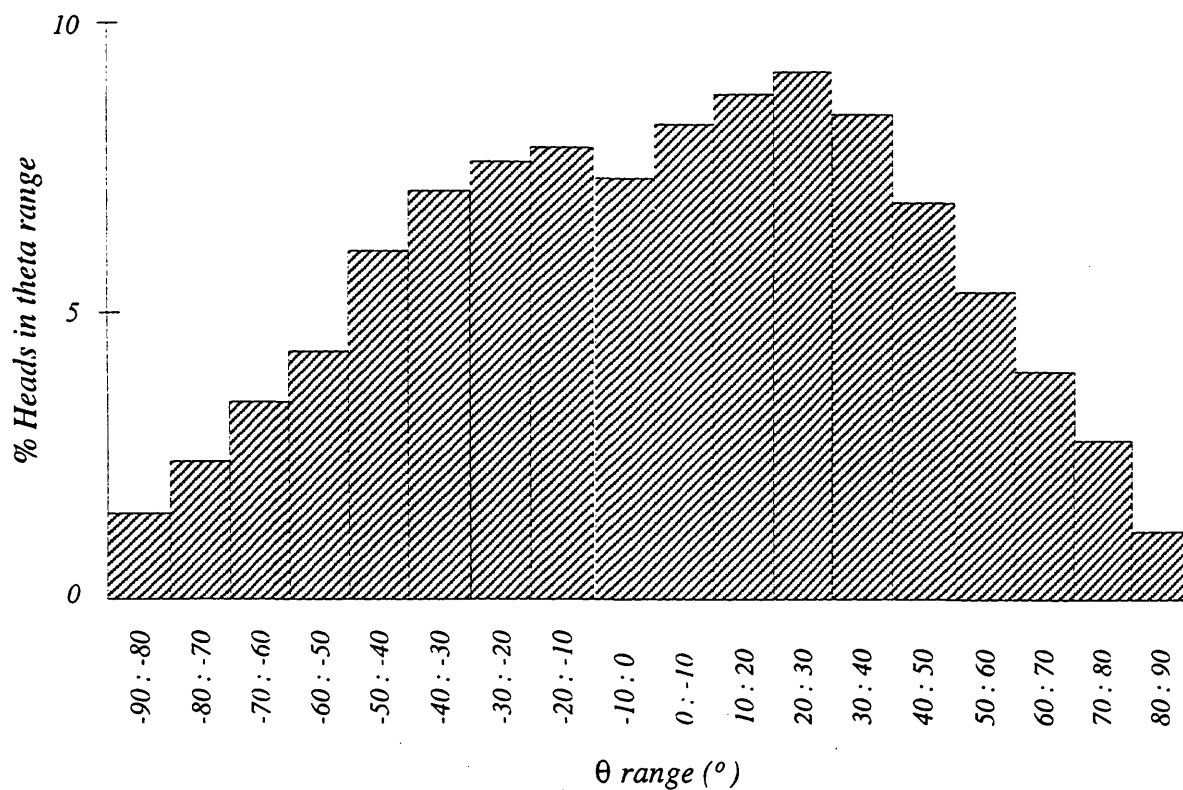


Figure 8.10: Typical θ Distribution Produced by Spatial Bonding Routines

If actin-myosin bonds are assigned on a nearest neighbour basis, the azimuthal angles automatically take on a wide range of values, giving rise to the disordered azimuthal angle arrangement whose effect is shown in figure 8.3.

into account the recent evidence that each myosin head in fact binds to two adjacent actin monomers. This was not a serious problem because the adjacent monomer was usually on the other side of the actin helix to the myosin head, and so was discounted by the minimal distance criterion.

The spare bonds were selected in one of two ways, both involving the minimum distance criterion and the adjacent actin limitation described above. The first was to select the next nearest actin to the outer surface of the myosin head, regardless of which actin chain it was found in. The second was to force the myosin head to remain on the same actin chain as the original favoured bond it selected, and put the head under strain by moving it up or down to the next nearest actin monomer. This is physically more likely if the myosin head is drawn to the actin monomer through an electrostatic interaction, since it is unlikely to overcome such an electrostatic attraction and move away from that actin filament to another. In this initial study, if the actin monomers selected by both the favoured and spare bonds were already bound, that myosin head was left unbound.

In the first case, where the spare bond was selected by distance considerations alone, investigation of a sample thin filament showed that the bound actin monomers approached a repeating 5-5-5-6 pattern: the fifth, tenth and fifteenth and twenty-first actin monomers in a group of twenty-one were bound. Such a pattern resulted in an average spacing between bonds of 14.3nm, comparable to the rest spacing of the myosin heads. In these models, typically 87% of the myosin heads were bound.

However, the second case, where the myosin heads were constrained to select spare bonds in the same actin filament as the rejected favoured bond, the same thin filament showed a pattern approaching a 5-5-6 pattern: the fifth, tenth, and sixteenth actin monomers of a group of sixteen were bound. This pattern gave an average spacing between bound monomers of 14.5 nm, comparable to the new spacing of the myosin meridional reflections in isometrically contracting muscle. The fraction of heads bound was lower than in the unconstrained case at 79%, and was closer to the predicted values of around 70% discussed in §2.7.3.

The patterns observed in the thin filaments are not exact 5-5-6 or 5-5-5-6 repeats as depicted in figure 7.24. Rather, the statistical separation of the bound actin monomers

within a given thin filament represents the pattern. Such a statistical variation supports the presence of significant disorder in the arrangement of the bound myosin heads. Table 8.1 illustrates this point by showing the statistical distribution of actin monomers between successive bound monomers in the two cases described here, compared with the expected statistical distribution for the perfectly repeating 5-5-6 and 5-5-5-6 cases. The unconstrained case has a much clearer 5-5-6 pattern than the constrained case has a 5-5-5-6 pattern, and the constrained case relies more heavily on the statistical separation of bound actin monomers.

| Number of actin monomers separating successively bound monomers | Number of occurrences of the given separation | | | |
|---|---|-------------------------|---------------------------|-----------------------|
| | Case 1 - unconstrained case | Perfect 5-5-5-6 pattern | Case 2 - constrained case | Perfect 5-5-6 pattern |
| 1 | | | 1394 | |
| 2 | | | 634 | |
| 3 | 127 | | 760 | |
| 4 | 1647 | | 2028 | |
| 5 | 8491 | 11025 | 2028 | 9800 |
| 6 | 4689 | 3675 | 2535 | 4900 |
| 7 | 253 | | 3041 | |
| 8 | | | 759 | |
| 9 | | | 1521 | |
| 10 | | | | |
| 11 | | | | |
| average | 5.22 | 5.25 | 5.40 | 5.33 |

Table 8.1: Statistical distribution of the number of actin monomer between successively bound monomers

The results presented here are by no means conclusive, but they do indicate the usefulness of further investigation in such a statistical manner. Several interesting hints have been given about the source of the disorder in the isometrically contracting muscle structure.

8.4 Unloaded Shortening at Zero Tension

Modelling of the structure during unloaded shortening should take into account that the meridional region of the pattern is very similar to the rest pattern, differing only in

absolute intensity, whilst the layer line intensity is reminiscent of the isometric peak pattern. Having observed that axial filament shifts caused the overall intensity of the meridional reflections to drop sharply in intensity without disturbing the relative intensities between peaks, it seems a reasonable explanation for the unloaded shortening pattern.

When the muscle shortens rapidly under very low tensions, it is highly likely that the filaments are forced into disorder relative to each other, until the shortening stops, and tension begins to rebuild, realigning the filaments through sarcomere shortening.

The fact that the meridional reflections are very well preserved despite the drop in intensity implies that the disorder is very specific. The forced slide of filaments past each other rips the bound myosin heads away from their bound positions attached to the thin filaments. They are thus not attached to the thin filaments, but remain in the vicinity of the thin filaments, constantly trying to bind and being ripped away again. Thus the equatorial behaviour during unloaded shortening can be interpreted as the heads remaining in the vicinity of the thin filaments without actually being so close as when they are bound.

8.5 Summary

Lattice disorders generally smear out the sampling Bragg diffraction peaks and redistribute the intensity into the continuous helical transforms; helical disorders tend to broaden the underlying helical transforms themselves, redistributing intensity into the background. Similar effects are observed from several types of disorder, which causes much difficulty in pinpointing the main sources of disorder in contracting muscle.

However, indications are that the primary source of disorder in isometrically contracting muscle lies in the azimuthal angles taken by the myosin heads, when they form bonds based on the distance between the outer surfaces of the selected actin monomer and the myosin head. Such disorder results in a layer line profile similar to that in the diffraction pattern from isometrically contracting muscle. At this stage, no firm conclusions can be drawn on the axial changes taking place in the thick filaments during contraction, but several possibilities have been investigated, and further modelling is suggested in the next chapter.

Similarly, the loss of meridional intensity in the diffraction pattern from shortening muscle appears to be largely due to axial shifts between the thick filaments during shortening, which is physically quite likely to occur in such a large length change.

This disorder study has illustrated the problems encountered when trying to model disordered muscle; namely that although it is quite possible to model the disorders and observe the effects on the diffraction pattern, determining the type of disorder from the effects alone is complex and ambiguous.

Chapter 9: Conclusions and Further Work

The work described in this thesis has provided valuable insight into the structure of frog sartorius muscle at rest, resulting in a suggested molecular arrangement which produces a theoretical x-ray diffraction pattern close to the experimental rest muscle pattern. In addition, a study of disorder in the molecular arrangement has revealed the difficulties inherent in modelling other muscle states during the contraction cycle. The modelling programs written for this work form a sound basis on which to build more complex models.

The simple uniform myosin head model (U), consisting of seven overlapping spheres (fig. 6.7b), was a useful representation in building the initial model, and confirming the correct working of the programs. However, it was too simple to accurately reproduce the myosin diffraction pattern. Although some success was obtained in modelling the axial structure of the thick filaments in relaxed muscle, reproducing the meridional region of the rest diffraction pattern, the inability to model the full pattern to any degree of accuracy indicated the need for a more complex head model.

Still, this simple model was a good starting place to investigate the superlattice arrangement, which depended more on the arrangement of the whole filaments than the molecules within them. A superlattice unit cell of the dimensions previously suggested by Huxley & Brown [70] and Squire [133] was confirmed (fig. 7.9). The corner thick filaments in the unit cell took one orientation, and the central filaments were randomly distributed between this orientation and another 60° apart. The random element in this distribution proved to be a significant factor in producing the correct layer line profiles. The orientations themselves were determined to be offset by about $\sim 10^\circ$ from the [10] lattice planes, in agreement with earlier work by Luther & Squire [175] which determined an offset of $5\text{-}15^\circ$ from the [10] planes.

The success in modelling the thick filament structure at rest was mainly possible because of the large amount of order present. The complex myosin head model (C) (fig 6.7c) was used to determine the thick filaments as compact structures at rest. The myosin heads were wrapped tightly around the thick filament backbone, and axially, most of the head mass lay parallel to the backbone (fig 7.17).

During contraction, the introduction of disorder was seen to be the driving factor in deducing the muscle structure. Some success was had at modelling various types of disorder to the system, including distortions of the lattice and within the filaments themselves. Useful insights into the role the various types might play during contraction were obtained: disorder in the azimuthal angles taken by the myosin heads was determined to be the primary source of the loss of the myosin layer lines from isometrically contracting muscle. A good match to the isometric plateau layer line profile was obtained by distributing the myosin heads at random azimuthal angles between $\pm 90^\circ$ from the normal to the thick filament backbone. This type of disorder was found to occur spontaneously when the bonds between the myosin heads and the actin monomers were assigned according to the initial distance between the two surfaces.

However, this approach was unable to unambiguously tie specific disorders to the isometrically contracting state: many disorders gave rise to similar results, which combined with the lack of sharp features in the corresponding diffraction pattern to produce a high level of ambiguity in the results. In particular, models investigating disorder in the orientation of the myosin heads (i.e. in the azimuthal and axial angles taken by the heads) indicate that once the helical arrangement of heads within the thick filaments has been disturbed, successive disruptions have a far less significant effect and in some cases are all but indistinguishable on top of the original disorder. The level of difficulty in modelling the isometrically contracting state is reflected by the lack of comparison studies carried out on this subject.

No conclusion could be drawn as to the source of the axial structural changes during contraction. The primary features of the meridional region of the isometric contraction diffraction pattern were reproducible by a number of modelling methods, including disordering the axial angles taken by the myosin heads, and introducing random axial shifts to the head arrangement. Thus the possibility exists for both swinging of heads, in support of the tilting head model, and for axial displacements without swinging.

The final state, unloaded shortening at zero tension, had its own particular features which this modelling study suggested was the result of large amounts of axial disorder introduced between the thick filaments whilst the basic filament structure returns towards the structure at rest. Again, little explicit modelling of this state has been performed in the past,

so a comparison cannot be made with other work. However, several reports have suggested theoretically that axial shifts between filaments may be the primary cause of lack of layer lines in what appears to be a structure with a reasonable degree of axial order.

Whilst modelling at this level of accuracy provides much useful information, the basic work carried out in this thesis has opened the way for more complex modelling of the protein arrangements. The models built here cover a filament length of about one overlap region (fig. 6.4), and make no effort to introduce a sarcomere structure: the introduction of longer filaments incorporating such a structure would enable detailed modelling of the meridional region of the pattern to confirm the initial results obtained here. Similarly, the cross-sectional area corresponds to a single cell, and the disorder studies in particular would benefit from an area containing many cells. The main problem with increasingly complex modelling is the limit set by available computer resources, but detailed modelling is possible, as illustrated by Hudson et al with fish muscle [61].

In the same vein, the introduction of the more significant of the minor protein components, troponin, tropomyosin, and C-protein, would be a useful modification. Numerous studies have modelled the troponin and tropomyosin components in detail, and their results could be transferred to these models without too much effort. The return would be a greater degree of confidence in the accuracy of the relative layer line intensities, and the appearance of the familiar meridional reflections.

As a final point, it would be helpful to look at time resolved data during the contraction cycle. Although such data is necessarily less accurate than the high quality data obtained at the comparatively static states of rest and isometric contraction, the changes in the diffraction patterns will give some insight into the structural changes taking place: in particular, certain types of disorder may appear at slightly different stages of the contraction cycle, allowing some degree of distinction between them.

PUBLICATIONS

- 1) X-ray diffraction studies of elastic length changes in the actin and myosin filaments of contracting frog sartorius muscle.

J.Gandy, J.Bordas, A.Svensson, G.Diakun, E.Towns-Andrews, J.Lowy, P.Boesecke and C. Miles

Biophys.J.
Accepted and awaiting publication

- 2) X-ray evidence that in contracting muscle there exist two distinct populations of myosin heads.

J. Bordas, J.Lowy, A.Svensson, J.E.Harries, G.P.Diakun, J.Gandy, C.Miles, G.R.Mant and E.Towns-Andrews

(1995) Biophys.J. **66** Pp. 99-102

- 3) Modelling of rest muscle structure using x-ray diffraction.

C.V.Miles et al.
In preparation.

- 4) Modelling of disorder in muscle structures using x-ray diffraction.

C.V.Miles et al.
In preparation.

REFERENCES

- 1) Al-Khayat H.A., Yagi N., Squire J.M. (1995) *J.Mol.Biol.* **252** p.611-632
- 2) Amemiya Y. (1995) *J.Synch.Rad.* **2(1)** p.13-21
- 3) Amemiya Y., Matsushita T., Nakagawa A., Satow Y., Miyahara J., Chikawa J. (1988) *Nuc.Instrum.Meth.Phys.Res.* **A266** p.645-653
- 4) Amemiya Y., Wakabayashi K. (1991) *Adv.Biophys.* **27** p.115-128
- 5) Amos L.A., Huxley H.E., Holmes K.C., Goody R.S., Taylor K.A. (1982) *Nature* **299** p.467-469
- 6) Andreev O.A., Borejdo J. (1991) *Biochem.Biophys.Res.Comm.* **177(1)** p.350-356
- 7) Asakura S., Taniguchi M., Oosawa F. (1963) *J.Mol.Biol.* **7** p.55-69
- 8) Bagshaw C.R. (1993) "Muscle Contraction" Chapman & Hall
- 9) Bendall P., Koch M.H.J., Bordas J., Mant G. Personal Communication
- 10) Bilsborrow R.L., Bliss N, Bordas J., Cernik R.J., Clark G.F., Clark S.M., Collins S.P., Dobson B.R., Fell B.D., Grant A.F., Harris N.W., Smith W., Towns-Andrews E. (1995) *Rev.Sci.Instrum.* **66(2)** p.1633-1635
- 11) Bliss N., Bordas J., Fell B.D., Harris N.W., Helsby W.I., Mant G.R., Smith W., Towns-Andrews E. (1995) *Rev.Sci.Instrum.* **66(2)** p.1311-1313
- 12) Bonafe N., Chaussepied P. (1995) *Biophys.J.* **68(4SS)** p.S35-S43
- 13) Bordas J., Diakun G.P., Diaz F.G., Harries J.E., Lewis R.A., Lowy J., Mant G.R., Martin-Fernandez M.L., Towns-Andrews E. (1993) *J.Mus.Res.Cell Mot.* **14** p.311-324
- 14) Bordas J., Koch M.H.J., Clout P.N., Dorrington E., Boulin C., Gabriel A. (1980) *J.Phys.E:Sci.Instrum.* **13** p.938-944
- 15) Burton K. (1992) *J.Mus.Res.Cell Mot.* **13** p.590-607
- 16) Cantino M., Squire J. (1986) *J.Cell Biol.* **102** p.610-618
- 17) Chew M.W.K., Squire J.M. (1995) *J.Struct.Biol.* **115** p.233-249
- 18) Clark E.S. & Muus L.T. (1962) *Z.Kristallogr.* **117** p.108-118
- 19) Cochran W., Crick F.H.C., Vand V. (1952) *Acta Cryst.* **5** p.581-586
- 20) Collins J.H., Potter J.D., Wilshire G., Jackman N. (1973) *FEBS Lett.* **36** p.268-272
- 21) Cooke R., Crowder M.S., Wendt C.H., Barnett V.A., Thomas D.D. (1984) in "Contractile Mechanisms in Muscle" (Ed. Pollack G.H. & Sugi H.) Plenum Press, New York and London p.413-423
- 22) Crowther R.A., Padron R., Craig R. (1985) *J.Mol.Biol.* **184** p.429-439
- 23) Dan-Moor M., Muhlrud A. (1991) *Biochemistry* **30** p.400-405

- 24) Denny R.C. Personal Communication
- 25) Diaz Banos F.G., Bordas J., Lowy J., Svensson A. (1996) *Biophys.J.* **71** p.576-589
- 26) Diaz F.G., Pantos E., Bordas J. (1992) *Rev.Sci.Instrum.* **63(1)** p.859-862
- 27) dos Remedios C.G., Moens P.D.J. (1995) *Biochim.Biophys.Acta* **1228** p.99-124
- 28) Ebashi S., Kodama A. (1966) *Biochem.J.* **59** p.425-426
- 29) Egelman E.H., Francis N., DeRosier D.J. (1982) *Nature* **298** p.131-135
- 30) Egelman E. (1985) *J.Mus.Res.CellMot.* **6** p.129-151
- 31) Egelman E.H., DeRosier D.J. (1982) *Acta Cryst.* **A38** p.796-799
- 32) Egelman E.H., DeRosier D.J. (1983) *J.Mol.Biol.* **166** p.623-629
- 33) Eisenberg E., Green L.E. (1980) *Ann.Rev.Physiol.* **42** p.293-309
- 34) Elliot A., Offer G., Burridge K. (1976) *Proc.R.Soc.Lond.[Biol.]* **249** p.30-41
- 35) Finer J.T., Simmons R.M., Spudich J.A. (1994) *Nature* **368** p.113-119
- 36) Flicker P.F., Phillips G.N. Jr., Cohen C. (1982) *J.Mol.Biol.* **162** p.495-501
- 37) Ford L.E., Huxley A.F., Simmons R.M. (1977) *J.Physiol.(Lond.)* **269** p.441-515
- 38) Gabriel A. (1977) *Rev.Sci.Instrum.* **48(10)** p.1303-1305
- 39) Geeves M.A. (1991) *Biochem.J.* **274** p.1-14
- 40) Geeves M.A. (1992) *Philos.Trans.R.Soc.LondonSer.B* **336** p.63-71
- 41) Griffiths P.J., Ashley C.C., Bagni M.A., Maeda Y., Cecchi G. (1993) *Biophys.J.* **64** p.1150-1160
- 42) Hammersley A.P., Svensson S.O., Thompson A. (1994) *Nuc.Instrum.Meth.Phys.Res.* **A346** p.312-321
- 43) Hanson J. (1967) *Nature* **213** p.353-356
- 44) Hanson J. (1973) *Proc.Roy.Soc.Lond.(Biol.)* **183** p.39-58
- 45) Hanson J., Huxley H.E. (1955) *Symp.Soc.Exp.Biol.* **9** p.228-264
- 46) Hanson J., Lowy J. (1963) *J.Mol.Biol.* **6** p.46-60
- 47) Harford J.J., Chew M.W., Squire J.M., Towns-Andrews E. (1991) *Adv.Biophys.* **27** p.45-61
- 48) Harford J.J., Squire J.M. (1992) *Biophys.J.* **63** p.387-396
- 49) Harries J. Personal Communication
- 50) Haselgrove J.C. (1980) *J.Mus.Res.Cell Mot.* **1** p.177-191
- 51) Haselgrove J.C., Huxley H.E. (1973) *J.Mol.Biol.* **77** p.549-568
- 52) Hendrix J., Koch M.H.J., Bordas J. (1979) *J.Appl.Cryst.* **12** p.467-472

- 53) Hichcock S.E. (1973) *Biochemistry* **12** p.2509-2515
- 54) Hill A.V. (1938) *Proc.Roy.Soc.Lond.(Biol.)* **200** p.807-819
- 55) Hill A.V. (1964) *Proc.Roy.Soc.Lond.(Biol.)* **159** p.297-318
- 56) Hirose K., Franzini-Armstrong C., Goldman Y.E., Murray J.M. (1994) *J.Cell Biol.* **127(3)** p.763-778
- 57) Hirose K., Wakabayashi T. (1993) *J.Mus.Res.Cell Mot.* **14** p.432-445
- 58) Holmes K.C. (1995) *Biophys.J.* **68** p.2s-7s
- 59) Holmes K.C., Popp D., Gebhard W., Kabsch W. (1990) *Nature* **347** p.44-49
- 60) Homsher E. (1987) *Ann.Rev.Physiol.* **49** p.673-690
- 61) Hudson L., Harford J., Denny R., Squire J. (1995) *CCP13 Newsletter Issue 4* December p.20-23
- 62) Huxley A.F. (1957) *Prog.Biophys.Biophys.Chem.* **7** p.255-318
- 63) Huxley A.F., Niedergerke R. (1954) *Nature* **173** p.971-973
- 64) Huxley A.F., Simmons R.M. (1971) *Nature* **233** p.533-538
- 65) Huxley A.F. (1973) *Proc.R.Soc.Lond.B.* **183** p.83-6
- 66) Huxley A.F. (1974) *J.Physiol.* **243** p.1-43
- 67) Huxley H.E. (1957) *J.Biophys.Acta* **12** p.387-394
- 68) Huxley H.E. (1963) *J.Mol.Biol.* **7** p.281-308
- 69) Huxley H.E. (1969) *Science* **164** p.1356-1366
- 70) Huxley H.E., Brown W. (1967) *J.Mol.Biol.* **30** p.383-434
- 71) Huxley H.E., Faruqi A.R., Kress M., Bordas J., Koch M.H.J. (1982) *J.Mol.Biol.* **158** p.637-684
- 72) Huxley H.E., Hanson J. (1954) *Nature* **173** p.973-976
- 73) Huxley H.E., Kress M. (1985) *J.Mus.Res.Cell Mot.* **6** p.153-161
- 74) Huxley H.E., Simmons R.M., Faruqi A.R., Kress M., Bordas J., Koch M.H.J. (1983) *J.Mol.Biol.* **169** p.469-506
- 75) Huxley H.E., Stewart A., Sosa H., Irving T. (1994) *Biophys.J.* p.A191
- 76) Irving M., Lombardi V., Piazzesi G., Ferenczi M.A. (1992) *Nature* **357** p.156-158
- 77) Iwazumi T. (1989) *Physiol.Chem.Phys.Med.NMR* **21** p.187-219
- 78) Jontes J.D. (1995) *J.Struct.Biol.* **115** p.119-143
- 79) Kabsch W., Mannherz H.G., Suck D., Pai E.F., Holmes K.C. (1990) *Nature* **347** p.37-44
- 80) Kensler R.W., Stewart M. (1986) *J.CellBiol.* **96** p.1797-1802

- 81) Klug A., Crick F.H.C., Wyckoff H.W. (1958) *Acta Cryst.* **11** p.199-213
- 82) Knappeis G.G., Carlsen F. (1962) *J.Cell Biol.* **13** p.323-335
- 83) Knight P., Trinick J.A. (1984) *J.Mol.Biol.* **177** p.461-482
- 84) Koch E.E., Eastman D.E., Farge Y. (1983) in "Handbook on Synchrotron Radiation - Volume 1A" (Ed. Koch E.E.) North -Holland Publishing Company
- 85) Kohra K., Ando M., Matsushita T., Hashizume H. (1978) *Nuc.Instrum.Meth.* **152** p.161-166
- 86) Lea K.R., Munro I.H. (1980) "The Synchrotron Radiation Source at Daresbury Laboratory"
- 87) Lehman W., Vibert P., Uman P., Craig R. (1995) *J.Mol.Biol.* **251** p.191-196
- 88) Lewis R. (1989) "Daresbury Delay Line Detectors and Data Aquisition Systems"
- 89) Lewis R. (1994) *J.Synch.Rad.* **1(1)** p.43-53
- 90) Lorenz M., Poole K.J.V., Popp D., Rosenbaum G, Holmes K.C. (1995) *J.Mol.Biol.* **246** p.108-119
- 91) Lorenz M., Popp D., Holmes K.C. (1993) *J.Mol.Biol.* **234** p.826-836
- 92) Lowey S. (1971) in "Subunits in Biological Systems - Part A" (Ed. Timasheff S.N., Fasman G.D.) Marcek Dekker, New York p.201-259
- 93) Lowey S., Cohen C. (1962) *J.Mol.Biol.* **4** p.292-308
- 94) Lymn R.W., Taylor E.W. (1971) *Biochem.* **10** p.4617-4624
- 95) Malinchik S., Yu L.C. (1995) *Biophys.J.* **68** p.2023-2031
- 96) Malinchik S.B., Lednev V.V. (1992) *J.Mus.Res.Cell Mot.* **13** p.406-419
- 97) Mant G.R., Bordas J. Personal Communication
- 98) Martin-Fernandez M.L., Bordas J., Diakun G., Harries J., Lowy J., Mant G.R., Svensson A., Towns-Andrews E. (1994) *J.Mus.Res.Cell Mot.* **15** p.319-348
- 99) Matsubara I., Yagi N. (1985) *J.Physiol.* **361** p.151-163
- 100) Mendelson R.A., Morris E. (1994) *J.Mol.Biol.* **240** p.138-154
- 101) Millane R.P. & Stroud W.J. (1991) *Int.J.Biol.Macromol.* **13** p.202-208
- 102) Millane R.P. & Stroud W.J. (1995) *Acta Cryst.* **A51** p.360-365
- 103) Miller A., Tregear R.T. (1972) *J.Mol.Biol.* **70** p.85-104
- 104) Milligan R.A., Flicker P.F. (1987) *J.Cell Biol.* **105** p.29-39
- 105) Milligan R.A., Whittaker M., Safer D. (1990) *Nature* **348** p.217-221
- 106) Miyahara J., Takahashi K., Amemiya Y., Kamiya N., Satow Y. (1986) *Nuc.Instrum.Meth.Phys.Res.* **A246** p.572-578
- 107) Morgan M., Perry S.V., Ottaway J. (1976) *Biochem.J.* **157** p.687-697

- 108) Offer G., Moos C., Starr R. (1973) *J.Mol.Biol.* **74** p.653-676
- 109) Offer G., Knight P., Alamo L., Padron R. (1996) '9th London Muscle Conference'
- 110) Oosawa F. (1980) *Biophys.Chem.* **11** p.443-446
- 111) Pearlstone J.R., Carpenter M.R., Johnson P., Smillie L.B. (1976) *Proc.Natl.Acad.Sci.USA* **73** p.1902-2906
- 112) Pearlstone J.R., Smillie L.B. (1983) *J.Biol.Chem.* **258** p.2534-2542
- 113) Phillips G.N. Jr, Fillers J.P., Cohen C. (1980) *Biophys.J.* **32** p.485-502
- 114) Phillips G.N. Jr, Fillers J.P., Cohen C. (1986) *J.Mol.Biol.* **192** p.111-131
- 115) Phillips G.N. Jr., Lattman E.E., Cummins P., Lee K.Y., Cohen C. (1979) *Nature* **278** p.413-417
- 116) Piazzesi G., Lombardi V., Ferenczi M.A., Thirlwell H., Dobbie I., Irving M. (1995) *Biophys.J.* **68(4SS)** p.S92-S98
- 117) Podolsky R.J., Norman A.C. (1971) in *Contractility of Muscle Cells and Related Processes* (Ed. Podolsky R.J.) New Jersey :Prentice-Hall p.247-260
- 118) Podolsky R.J., Nolan A.C. (1973) *Cold Spring Harbor Symp.Quant.Biol.* **37** p.661-668
- 119) Pollard T.D., Bhandari D., Maupin P., Wachsstock D., Weeds A.G., Zot H.G. (1993) *Biophys.J.* **64** p.454-471
- 120) Poole K.V., Holmes K.C., Rayment I., Lorenz M. (1995) *Biophys.J.* **68** p.S348
- 121) Potter J.D., Gergely J. (1974) *Biochemistry* **13** p.2697-2700
- 122) Poulsen F.R., Lowy J. (1984) *J.Mol.Biol.* **174** p.239-247
- 123) Rayment I., Holden H.M., Whittaker M., Yohn C.B., Lorenz M., Holmes K.C., Milligan R.A. (1993) *Science* **261** p.58-65
- 124) Rayment I., Rypniewski W.R., Schmidt-Base K., Smith R., Tomchick D.R., Benning M.M., Winkelmann D.A., Wesenberg G., Holden H.M. (1993) *Science* **261** p.50-58
- 125) Rome E., Offer G., Pepe F.A. (1973) *Nature (New Biol)* **244** p.152-154
- 126) Ross J. & Smith K. (1992) *Rev. Sci.Instrum.* **63** p.309-312
- 127) Sanders C., Smillie L.B. (1984) *Canad.J.Biochem.Cell Biol.* **62** p.443-448
- 128) Schroder R.R., Manstein D.J., Jahn W., Holden H., Rayment I, Holmes K.C., Spudich J.A. (1993) *Nature* **364** p.171-174
- 129) Schutt C.E., Lindberg U. (1992) *Proc.Natl.Acad.Sci.USA* **89** p.319-323
- 130) Schutt C.E., Lindberg U. (1993) *FEBS Lett.* **325(1,2)** p.59-62
- 131) Schutt C.E., Lindberg U., Myslik M., Strauss N. (1989) *J.Mol.Biol.* **209** p.735-746
- 132) Sherwood D. (1976) "Crystals, X-rays and Proteins" Longman Group Ltd., London

- 133) Squire J. (1981) "The Structural Basis of Muscle Contraction" Plenum Press, New York and London
- 134) Squire J. (1981) *Nature* **291** p.614-615
- 135) Squire J.M. (1971) *Nature* **233** p.457-462
- 136) Squire J.M. (1972) *J.Mol.Biol.* **72** p.125-138
- 137) Squire J.M. (1975) *Ann.Rev.Biophys.Bioeng.* **4** p.291-323
- 138) Squire J.M. (1994) *J.Mus.Res.Cell Mot.* **15** p.227-231
- 139) Squire J.M., Al-Khayat H.A., Yagi N. (1993) *J.Chem.Soc.Faraday Trans.* **89** p.2717-2726
- 140) Squire J.M., Harford J.J., Edman A.C., Sjostrom M. (1982) *J.Mol.Biol.* **155** p.467-494
- 141) Stanton M, Phillips W.C., Li Y., Kalata K. (1992) *J.Appl.Cryst.* **25** p.549-558
- 142) Stein L.A., Schwarz R., Chock P.B., Eisenberg E. (1979) *Biochemistry* **18** p.3895-3909
- 143) Stewart M., Kensler R.W., Levine R.J.C. (1985) *J.Cell Biol.* **101** p.402-411
- 144) Stewart M., Kensler R.W. (1986) *J.Mol.Biol.* **192** p.831-851
- 145) Stone D., Sodek J., Johnson P., Smillie L.B. (1975) *Proc.9th FEBS Meeting (Budapest)* **31** p.125-136
- 146) Stroud W.J. & Millane W.J. (1995) *Acta Cryst.* **A51** p.771-790
- 147) Stroud W.J. & Millane W.J. (1995) *Acta Cryst.* **A51** p.790-800
- 148) Svensson S.O., Hammersley A.P., Thompson A., Gonzalez A., Ursby T. Nov. (1993) *Joint CCP4 & ESF-EACBM Newsletter on Protein Crystallography No.29*
- 149) Szent-Gyorgyi A.G., Prior G. (1966) *J.Mol.Biol.* **15** p.515-538
- 150) Taylor E.W, Amos L.A. (1981)
- 151) Taylor E.W. (1991) *J.Biol.Chem.* **266** p.294-302
- 152) Tokunaga M., Sutoh K., Wakabayashi T. (1991) *Adv.Biophys.* **27** p.157-167
- 153) Tombouliau D.H. & Hartman P.L. (1956) *Phys.Rev.* **102** p.1423
- 154) Towns-Andrews E., Berry A., Bordas J., Mant G.R., Murray P.K., Roberts K., Sumner I., Worgan J.S., Lewis R. (1989) *Rev.Sci.Instrum.* **60(7)** p.2346-2349
- 155) Toyoshima Y. (1991) *Adv. Biophys.* **27** p.213-220
- 156) Trinick J., Cooper J., Seymour J., Egelman H. (1986) *J.Microscopy* **141** p.349-360
- 157) Vainshtein B.K. (1966) "Diffraction of X-Rays by Chain Molecules" Elsevier Publishing Company, London
- 158) Vazina A.A. (1987) *Nuc.Inst.Meth.Phys.Res.* **A261** p.200-208

- 159) Wakabayashi K., Sugimoto Y., Tanaka H., Ueno Y., Takezawa Y., Amemiya Y. (1994) *Biophys.J.* **67** p.2422-2435
- 160) Wilkinson J.M., Grand R.J.A. (1975) *Nature* **271** p.31-35
- 161) Winick H. (1980) in "Synchrotron Radiation Research" (Eds. Winick H., and Doniach S.) Plenum
- 162) Woods E.F. (1967) *J.Biol.Chem.* **242** 2859-2871
- 163) Worgan J.S., Lewis R., Fore N.S., Sumner I.L., Berry A., Parker B., d'Annunzio F., Martin-Fernandez M.L., Towns-Andrews E., Harries J.E., Mant G.R., Diakun G.P., Bordas J. (1990) *Nuc.Instrum.Meth.Phys.Res.* **A291** p.447-454
- 164) Worthington C.R. & Elliott G.F. (1989) *Acta Cryst.* **A45** p.645-654
- 165) Yagi N. (1996) *Acta Cryst.* **D52** p.1169-1173
- 166) Yagi N., O'Brien J., Matsubara I. (1981) *Biophys.J.* **33** p.121-138
- 167) Yagi N., Takemori S. (1995) *J.Mus.Res.Cell Mot.* **16** p.57-63
- 168) Yagi N., Takemori S., Watanabe M. (1993) *J.Mol.Biol.* **231** p.668-677
- 169) Yanagida T. (1981) *J.Mol.Biol.* **146** 539-560
- 170) Yanagida T., Arata T., Oosawa T. (1985) *Nature* **316** p.366-369
- 171) Yanagida T., Harada Y., Kodama T. (1991) *Adv.Biophys.* **27** p.237-257
- 172) Yanagida T., Nakase M., Nishiyama K., Oosawa F. (1984) *Nature (London)* **307** p.58-60
- 173) Moore P.B., Huxley H.E., DeRosier D.J. (1970) *J.Mol.Biol.* **50** p.279-292
- 174) Elliot G.F., Lowy J., Worthington C.R. (1963) *J.Mol.Biol.* **6** p.295-305
- 175) Luther P.K., Squire J.M. (1980) *J.Mol.Biol.* **141** p.409-439
- 176) Gandy J., Bordas J., Svensson A., Diakun G., Towns-Andrews E., Lowy J., Boesecke P., Miles C. (1997) submitted to *J.Biophys.*